ROBUST OPTIMAL MOTION PLANNING FOR MULTI-APERTURE SPACE SYSTEMS VIA PSEUDOSPECTRAL METHODS

DISSERTATION

Brian W. Bishop, Lieutenant Colonel, USSF

AFIT-ENY-21-DS-090

DEPARTMENT OF THE AIR FORCE
AIR UNIVERSITY

AIR FORCE INSTITUTE OF TECHNOLOGY

Wright-Patterson Air Force Base, Ohio

The views expressed in this dissertation are those of the author and do not reflect the official policy or position of the United States Air Force, the Department of Defense, or the United States Government.

AFIT-ENY-21-DS-090

ROBUST OPTIMAL MOTION PLANNING FOR MULTI-APERTURE SPACE SYSTEMS VIA PSEUDOSPECTRAL METHODS

DISSERTATION

Presented to the Faculty

Graduate School of Engineering and Management

Air Force Institute of Technology

Air University

Air Education and Training Command

in Partial Fulfillment of the Requirements for the

Degree of Doctor of Philosophy in Astronautical Engineering

Brian W. Bishop, B.S.M.E., M.S.A.E.

Lieutenant Colonel, USSF

September 2021

AFIT-ENY-21-DS-090

ROBUST OPTIMAL MOTION PLANNING FOR MULTI-APERTURE SPACE SYSTEMS VIA PSEUDOSPECTRAL METHODS

Brian W. Bishop, B.S.M.E., M.S.A.E.
Lieutenant Colonel, USSF

COMMITTEE MEMBERSHIP:

Richard Cobb, PhD
Chairman

Brian Lunday, PhD
Member

Mark Karpenko, PhD
Member

Major Costantinos Zagaris, PhD
Member

Adedeji B. Badiru, PhD
Dean, Graduate School of Engineering and Management

Abstract

For multi-body, flexible systems, the ability to achieve rapid reorientation maneuvers can be impacted by nonlinear dynamics and uncertainty in the model parameters. Trajectory sensitivity to parameter variations increases final pointing error and residual vibrational energy in the system. This dissertation explores using desensitized optimal control and unscented optimal control methods to generate trajectories robust against parameter variations while decreasing total maneuver time, pointing error, and system excitation. A five-body, flexible model representing a communications satellite is developed, and utilizing robust problem formulations solved via pseudospectral techniques, maneuvers are generated decreasing maneuver time by 62% and terminal system energy by up to 60%. Lastly, reduced fidelity, three-body and two-body models are developed achieving similar robust performance to the five-body model but with an up to 99% reduction in computation time.

Acknowledgments

I would like to thank my advisor, Dr. Cobb, for his support throughout my classwork and research journey and for ensuring I achieved my research objectives. I would like to thank Dr. Lunday for being on my research committee and for increasing my knowledge and understand of nonlinear programming. I'd also like to thank Maj. Zagaris for his participation in my research committee and for providing a sounding board for questions and ideas through this process. Finally, I'd like to thank Dr. Karpenko for his committee membership and for originally sparking my interest in utilizing pseudospectral optimal control techniques for space-based applications. Lastly, none of this would be possible without the support of my wife and children who put up with long hours and excessive grumpiness.

Brian W. Bishop

Table of Contents

Page

Page

List of Figures

List of Tables

Table Page

Table Page

List of Acronyms

Acronym	Definition
AT	Auto Track
BVP	Boundary Value Problem
CDF	Cumulative Distribution Function
CMG	Control Moment Gyroscope
CMP	Covector Mapping Principle
DOF	Degrees of Freedom
FEM	Finite Element Method
GEO	Geosynchronous Orbit
HEO	Highly Elliptical Orbit
HST	Hubble Space Telescope
KE	Kinetic Energy
KKT	Karush-Kuhn-Tucker
LEO	Low Earth Orbit
LS	Lebesgue-Stieltjes
LG	Legendre-Gauss
LGL	Legendre-Gauss-Lobatto
LGR	Legendre-Gauss-Radau
LPM	Legendre Pseudospectral Method
MCM	Minimum Control Maneuver
ME	Modal Energy
NASA	National Aeronautics and Space Administration
NLP	Non-Linear Programming
PD	Proportional Derivative

Acronym	Definition
PDF	Probability Density Function
PE	Potential Energy
PMP	Pontryagin's Minimum Principle
PS	Pseudospectral
PSM	Pseudospectral Methods
PSOC	Psuedospectral Optimal Control
PT	Program Track
RF	Radio Frequency
RPM	Radau Pseudospectral Method
RQ	Research Question
RS	Riemann-Stieltjes
SAA	Single Access Antenna
SD	Standard Deviation
SISO	Single-Input-Single-Output
SNOPT	Sparse Nonlinear Optimizer
SQP	Sequential Quadratic Programming
STM	Shortest Time Maneuver
TDRS	Tracking and Data Relay Satellite
TDRSS	Tracking and Data Relay Satellite System
TE	Total Energy
USAT	User Satellites

ROBUST OPTIMAL MOTION PLANNING FOR MULTI-APERTURE SPACE SYSTEMS VIA PSEUDOSPECTRAL METHODS

I. Introduction

1.1 Overview

For many satellite architectures, system utilization is impacted by the ability to access and downlink mission data to ground systems for processing and dissemination. Due to cost and orbital geometry constraints, it is infeasible to employ dedicated ground terminals for every satellite. One method of addressing this constraint is the employment of satellite to satellite crosslinks. Crosslinks allow satellites to pass mission data to neighboring satellite potentially in view of the ground station, allowing the satellites to acts as nodes in a network, transmitting the accumulation of multiple node's data through a single downlink.

With the increasing development of Low Earth Orbit (LEO) mega-constellations such as SpaceX Starlink [6] or DARPA Blackjack [7], the employment of crosslinks is increasing. In a paper by Aguilar [8], the trade space for a next generation communications architecture is explored. Aguilar discusses the use of crosslinks as a way of efficiently passing data through the constellation to the ground. By enabling crosslinks in a mesh configuration (Figure 1.1), a constellation is more robust as it can route around unhealthy nodes, or around bandwidth constrained nodes, thereby achieving more even data loading across the network .

The addition of out-of-plane crosslinks introduces competing objectives when designing control systems. One objective is increasing crosslink aperture slew speed as it transitions between neighboring contacts, increasing link throughput and improving

Figure 1.1: Notional DARPA Blackjack Constellation with Crosslinks [7]

network utilization. It should be noted that while slewing between contacts, there is no croslink data flow, and thus increasing the slew speed would decrease the time the datalink is unavailable. The second objective is minimizing satellite bus disturbances resulting from rapid slewing impacting both payload and adjacent crosslink antenna pointing which in turn impacts achievable data rates. The proposed optimization problem thus has a multiple objectives; minimize antenna slew times, decrease system excitation, and ensure robustness against parameter variation.

1.2 Motivation of Research

The Tracking and Data Relay Satellite System (TDRSS) is a communication crosslink system employed by the National Aeronautics and Space Administration (NASA). TDRSS was envisioned in the 1970s as a method of reducing NASA's reliance on internationally based ground antennas. The TDRSS program was established in 1973 and launched the first spacecraft in 1983. NASA is now in the third generation of the Tracking and Data

Relay Satellite (TDRS) with the most recent spacecraft, TDRS-13, launched in August 2017 [9]. The current active TDRSS fleet is shown in Figure 1.2.

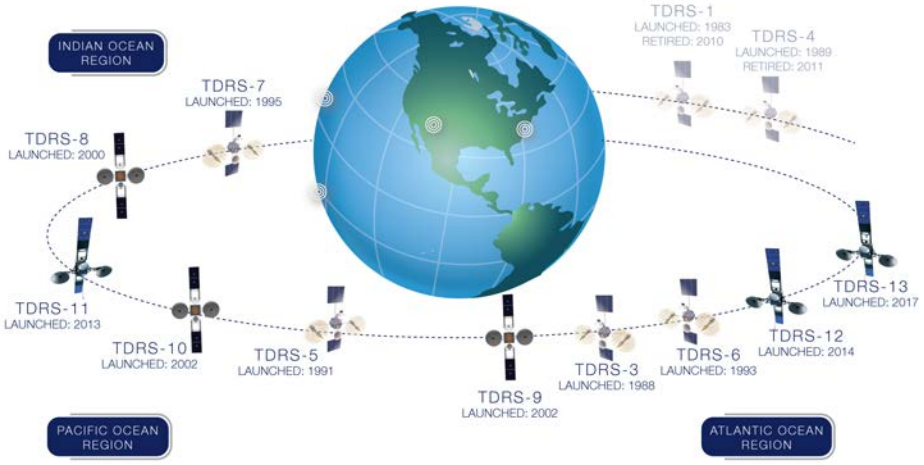

Figure 1.2: Tracking and Data Relay Satellite Fleet [9]

Each TDRS is equipped with an array of antennas maximizing the number of satellites simultaneously serviced, including 47 S-band multi-access antennas and two Single Access Antenna (SAA) capable of high data-rate Radio Frequency (RF) service in S, Ka and Ku-bands (Figure 1.3). Each SAA is independently steerable allowing TDRS to provide simultaneous service to two moving targets in the LEO and Highly Elliptical Orbit (HEO) regime [10]. The movement of each SAA presents a unique multi-body attitude, dynamics and control problem. First and foremost, the satellite bus must maintain a proper attitude in order to maintain link lock with its respective ground station. TDRS must also accommodate one SAA servicing one User Satellites (USAT) while simultaneously slewing the second SAA to achieve line-of-sight lock with a second USAT, all while minimizing disturbances to the bus and adjacent aperture so as not to adversely impact their stringent line-of sight pointing performance [5]. For the Next Generation TDRS,

NASA is investigating the addition of optical crosslinks to service additional satellites as shown in Figure 1.4. The addition of articulated optical payloads further complicates the vehicle dynamics and tightens the pointing requirements [11].

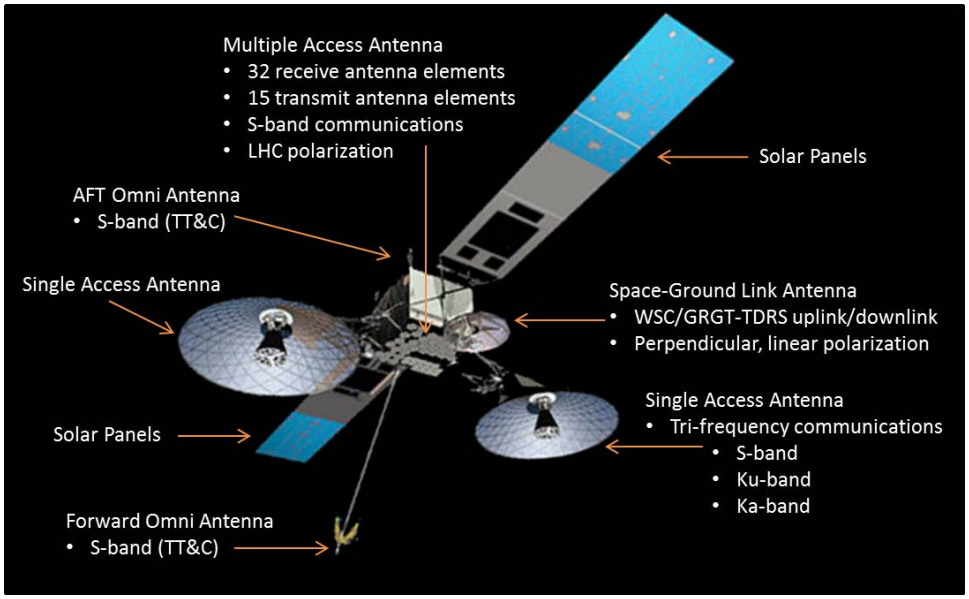

Figure 1.3: TDRS Third Generation Capabilities [9]

The motivation of this research is to increase data throughput of TDRSS and future TDRSS like systems. While there are many factors affecting overall system utilization, some ground and some space-based, this research will limit the scope and only investigate antenna slew maneuvers and their mission impacts. From a system utilization perspective, antenna slew time is non-value-added and when considered across an entire constellation with 100's of slews per day, slew time represents a significant period where communication data is not flowing. Furthermore, with conservatively imposed limits on gimbal motion, this further exacerbates the problem. By reducing antenna slew duration and residual pointing error at maneuver termination, additional time is available for providing communication services.

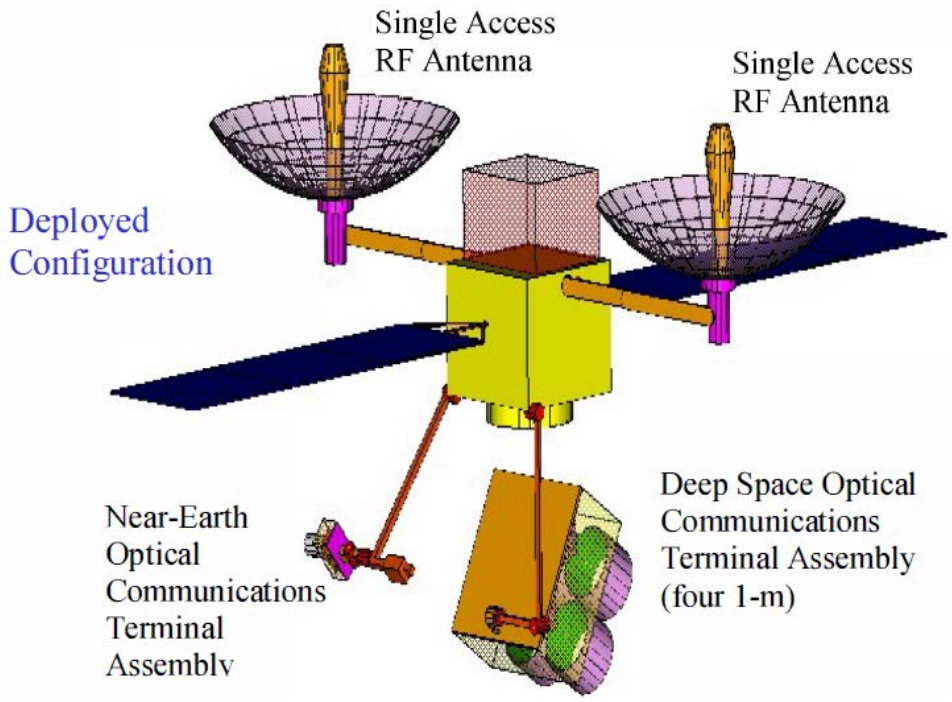

Figure 1.4: Notional Next Generation TDRS in a Deployed Configuration [11]

1.3 Research Problems, Tasks, and Scope

This section reviews the hypothesis and associated questions this research addresses. Specific tasks to be completed in support of the questions as well as the research scope are also defined.

Problem Statement: *Satellite antenna throughput and utilization are negatively affected by long slew durations due to the use of conservative design principles with artificially constrained torque and velocity limits.*

There are many modern tools which can be utilized to increase antenna slew speeds and payload utilization. As will be discussed in Chapter 2, Psuedospectral Optimal Control (PSOC) is one such technique which has been shown to derive optimal maneuvers advantageously leveraging the nonlinear dynamics of the underlying system to increase system performance. There is also a body of research expanding on these optimal control

techniques to increase a maneuvers robustness to parameter variations, in that the desired maneuver can be completed even with uncertainty in a given parameters exact value. The technique of desensitized optimal control is one such method leveraging a sensitivity function and the sensitivity dynamics to derive a robust problem formulation, which is discussed further in Section 2.3. Another techniques is unscented optimal control which leverage the unscented transform to derive multiple, parallel sets of dynamics which are driven towards a zero-mean solution. This method is discussed further in Section 2.4.

1.3.1 Hypothesis and Research Questions.

Hypothesis: *By applying modern optimal control techniques to a free-floating, flexible, multi-body dynamic system, problems including constraints which are highly nonlinear can be formulated and solved, resulting in solutions robust against parameter/configuration uncertainty, realizing faster antenna slew times while simultaneously mitigating system vibrational energy.*

Questions addressed by this hypothesis include the following:

Research Question (RQ) 1: How should an optimal control problem be formulated and solved for a flexible, multi-body spacecraft connected via flexible, revolute joints, performing antenna slew maneuvers between access points while compensating for system vibrational response and adjacent aperture pointing errors?

Research Question 2: How should robust optimal control techniques, accounting for configuration and parameter uncertainty using sensitivity functions, be incorporated into the formulation of RQ 1?

Research Question 3: How should an unscented optimal control problem, accounting for configuration and parameter uncertainty, be incorporated into the formulation of RQ 1?

Research Question 4: How should robust optimal control techniques from RQ 2 and RQ 3 be used as a model reduction techniques to achieve optimal solutions comparable with RQ 1 but with increased computational efficiency?

1.3.2 Research Tasks.

In order to answer the research questions pertaining to this hypothesis, the following tasks were completed:

Task 1: Formulate the dynamics for a flexible, multi-aperture satellite composed of two apertures connected via flexible, revolute joints and develop a feedback controller allowing closed-loop trajectory tracking for antenna and bus maneuvers using kinematic motion planning principles.

Task 2: Use Pseudospectral Methods (PSM) to formulate and solve RQ 1, comparing and contrasting various cost function formulations and the impact on system performance.

Task 3: Using Monte Carlo analysis, compare and contrast the robustness of the standard and optimal maneuvers to parameter uncertainty.

Task 4: Incorporate sensitivity functions into the PSOC problem formulation and derive optimal control trajectories robust against parameter uncertainty (Answering RQ 2).

Task 5: Use unscented optimal control techniques to formualte a new PSOC problem generating solutions robust against parameter uncertainty (Answering RQ 3).

Task 6: Using Monte Carlo Analysis, compare and contrast the solutions from Task 2 with Tasks 4 and 5.

Task 7: Utilize robust optimal control techniques as a method of model reduction. Explore ability to develop lower fidelity models, yielding nearly optimal solutions with a computational efficient manner while maintaining robustness to parameter uncertainty (Answering RQ 4).

1.4 Research Methodology

This research entails multiple overarching engineering fields but is primarily focused on dynamics and optimal control/optimization.

There are many methods of deriving the dynamic equations of motion for rigid and flexible bodies. The research herein focuses on employing Kane's Method which allows

for the derivation of computationally efficient system dynamics [12]. Due to the size and complexity of the dynamics equations for a multi-body system, the symbolic software package *MotionGenesis* is utilized [13]. The incorporation of the primary vibration modes of the spacecraft is done via a hybrid coordinate method, connecting the flexible dynamics derived using Kane's Method to the modal coordinates system representing the vibrational modes [14].

Multiple modern tools are utilized to solve the optimal control or optimization problems. Specifically, custom Matlab code is developed employing the PSM, which is subsequently solved via the Non-Linear Programming (NLP) solver Sparse Nonlinear Optimizer (SNOPT) [15]. Specific details on the employment of these tools is covered in Section 2.2.

For RQ 1, PSM is employed generating an optimal slew trajectory between two points for SAA-2, while SAA-1 maintains pointing at a USAT. Solutions are generated for minimum time, first using rigid body assumptions and simulated with full flexible dynamics. Next, solutions are computed for minimum vibration while decreasing overall maneuver duration. Lastly, additional torque margin is allocated to optimal maneuver design allowing a decrease in slew duration while still solving for a minimum vibration maneuver.

Using the results from RQ 1, a sensitivity function is analytically derived allowing for the generation of trajectories for one SAA that are robust against a changing configuration of the second SAA as well as uncertainty in spacecraft parameters such as bus natural frequencies, and variations in modelled spring coefficients in the flexible joints (RQ 2). RQ 3 follows the same methodology as RQ 2 except using unscented optimal control techniques in place of the sensitivity function. The results of the unscented methods are compared with the sensitivity based robust optimal control methods. RQ 4 explores the trade-space between robust solutions derived using the full-model, and creating reduced

fidelity models and augmenting the sensitivity function to account for the reduction in order.

The efficacy of each result is measured through a validation campaign. For the robust optimal solutions, the resultant maneuver is compared against the standard maneuver planned using linearized equations of motion and kinematic motion principles as well as against the optimal solution solved using full state knowledge from RQ 1.

The trajectories calculated using the PSOC techniques are open-loop solutions that can be used in a feedforward configuration to achieve the desired objectives. However, a feedback controller is still necessary to account for additional uncertainties or noise in the system. In addition to the open-loop validation tests described above, each optimal solution is simulated with a feedback controller and the performance is compared to the standard maneuver (representative of current conservative practices).

1.5 Assumptions and Limitations

Traditionally, satellite slew maneuvers are planned using kinematic motion principles where actuators are treated as a simple double integrator system and all nonlinear/coupling terms are treated as disturbances to be rejected by the controller [16]. In order minimize plant disturbances, allowable torque and slew velocities are conservatively bounded to low values leading to long slew durations. Often, these constraints are not based on true actuator capability but are "soft" constraints intended to minimize un-modeled effects such as system vibrational excitation. TDRS is designed for a worst-case slew of 26-degrees over 2 minutes, or a maximum slew rate of 0.22 deg/sec [3]. However, operationally, most spacecraft only utilize a fraction of available actuator torque. For robustness, MIL-A-83577B specifies a 175% torque margin for predicted worst case static friction torque, but in practice many designers recommend a factor of four or five. Dynamic torque margins are typically specified at 125%, again providing plenty of capability above and beyond what is allocated for nominal operations [17, 18]. While the TDRS maneuver is operationally

constrained to a maximum rate of 0.22 deg/sec, this research assumes additional torque margin is available for optimal trajectory generation, and shows the benefit of optimally utilizing the available torque [17, 18]. In addition to the increased torque allowance, it is assumed that the maximum velocity imposed during traditional motion planning is not based on hardware limitations and is not enforced during optimal maneuvers. Instead of placing artificial restrictions on torque and velocity to minimize bus disturbances, the vibrational modes of the bus are modeled and restricted directly while increasing the allowable torque and velocity envelopes.

Using modern optimization techniques for trajectory planning is advantageous in that non-convex, nonlinear problems, that may contain complex path constraints, can be solved with less simplifying assumptions. As such, they may produce more complex trajectories, but potentially increase overall performance of the system. This research employs non-linear equations of motion with minimal simplifying assumptions.

In a paper by van Woerkom [19], the author discusses the choice of modeling joint and/or link flexibility for on-orbit kinematic chains. For systems like the Canadian Remote Manipulator System (Canadarm) on the Space Shuttle, only joint flexibility is necessary to be modeled, while for the Space Stations Remote Manipulator system, both joint and link flexibility are important. Due to the short lengths of the modeled gimbal linkages, they are assumed to be sufficiently stiff as to neglect link flexibility, however, the flexibility inherent in the joints is modeled.

The primary vibrational modes of the satellite bus can exhibit significant impact on payload performance, and must be modeled. To perfectly capture the vibrational dynamics of a satellite system, an infinite number of modes are necessary, but in practice, a satellite Finite Element Method (FEM) models may only include the first thousand or so modes [2, 20]. This research makes the assumption, satisfied with the use of high frequency attenuation filters, that there exists a point of diminishing return where the inclusion of

additional vibrational modes does not sufficiently improve the optimal trajectory solution. The inclusion of additional flexible gimbal modes adds two additional state variables per mode that must then be modeled and discretized in the NLP solver, increasing computational complexity and algorithm run-time, but may not impact the optimality of the generated solution due to the additional mode being minimally coupled with the slew dynamics. This research investigates the trade space between model complexity, algorithm computation time, and the impact on the optimal results.

Due to the location of TDRS in Geosynchronous Orbit (GEO) and the small timescales of the maneuvers relative to the orbital period, orbital effects, such as gravity and solar wind pressure, are ignored.

Figure 1.5 shows a high level taxonomy for the research questions herein. Green boxes represent assumptions/methods covered in the problem formulation assumptions, white boxes represent assumptions and methods which appear in the literature but are not used herein, and the red text denotes associated RQs investigated. This research assumes TDRS and the two SAA can be modeled as a free-floating, five-body system with motion permissible in a full three dimensional space. Flexibility in the spacecraft bus and gimbal motors are modeled while the gimbaled links are short and assumed to be sufficiently stiff so as to be able to justify neglecting link flexibility. While the optimal control problem can be solved via either direct or indirect methods, this research focuses only on direct methods in general, and the pseudospectral method in particular. While RQ 1 deals with the full dynamic model and complete state and parameter knowledge, the next two research questions consider uncertainty in the parameters (RQ 2-3) and utilize robust optimal control methods as a means of model reduction increasing computational efficiency (RQ 4). On orbit, parameter uncertainty and initial condition uncertainty is a common issue for large spacecraft and finite computational power is always an on-orbit challenge.

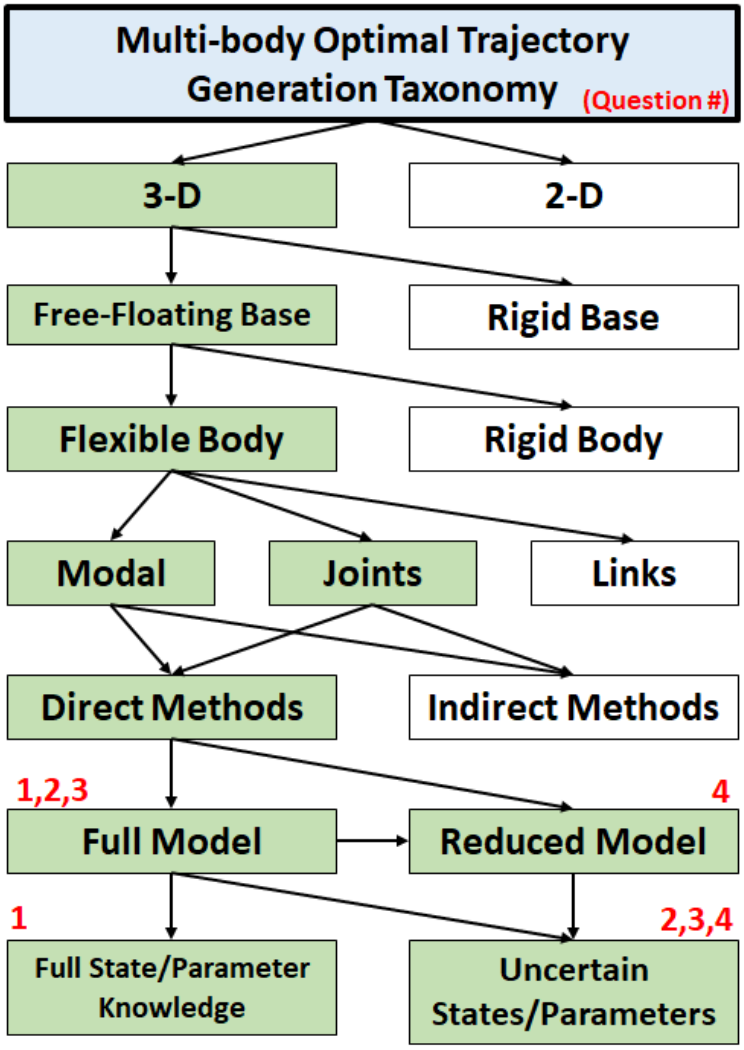

Figure 1.5: Taxonomy of Research Question Formulation

1.6 Research Contributions

This research answers the research questions posed in Section 1.3 using the methodology outlined in Section 1.4. The contributions are to increase and expand the capabilities of optimal path planning algorithms for flexible space structures with multiple apertures, such as TDRS. By utilizing modern pseudospectral optimal control techniques, it is demonstrated that optimal maneuvers can be generated accounting for system flexibility while ensuring residual vibrational energy is simultaneously minimized. The results

affirmatively support the hypothesis, as demonstrated in the document. Additionally, the trade space between solutions with full state and parameter knowledge, and robust optimal solutions, using sensitivity functions and/or unscented optimal control, is explored and compared to demonstrating a computationally efficient method of optimal maneuver generation in the presence of model uncertainties.

1.7 Document Preview

The following chapters expand on the contents presented in this first chapter. Chapter 2 contains the background information and literature review covering recent research in this topic area. It discusses the limitation of the previous research and covers how the research expands in the relevant areas. Chapter 3 develops the dynamic models and simulation environment used in the Monte Carlo simulations. Chapter 4 details the obtained results for each of the four research questions. Chapter 5 summarizes the research contributions of this manuscript and proposes future work to further this field of research.

II. Background

2.1 Overview

The research included herein requires the introduction and discussion of multiple fields of engineering laying the foundation for solving a Psuedospectral Optimal Control (PSOC) problem as outlined in Chapter 1. Section 2.2 provides an introduction to the formulation of an optimal control problem and in particular, how to formulate and discretize the problem for pseudospectral methods. Section 2.3 and Section 2.4 review two methods for formulating robust optimal control problems through the use of sensitivity functions and unscented methods. Section 2.5 covers the development of the dynamic equations of motion for the rigid body system using Kane's Method. These equations are then expanded in Section 2.5.2 and Section 2.5.3 where the dynamics necessary to model joint flexibility and satellite vibrational modes are accounted for. Section 2.6 presents a review of relevant recent research that sets the foundation for this research to expand upon.

2.2 Optimal Control and Pseudospectral Methods

When generating trajectories for multi-body satellite maneuvers, it is desirable to accomplish the maneuvers in an optimal manner. The trajectory/control pair must be chosen such as to minimize a performance index, whether based on time, control effort, or combination of user-defined measures, resulting in an optimal control problem. Optimal control is a vast field with many areas of active research. From surveys by Betts [21], Rao [22], and Conway [23], a variety of solution methods are explored and their relative strengths and weaknesses are discussed. One method in particular, that of PSOC, is utilized in this research. Since 2003, the field of PSOC has advanced rapidly from theory [24–26] to on-orbit flight applications with the International Space Station and other operational satellites [27–29]. Pseudospectral Methods (PSM) differ from finite

element/finite difference methods in that the convergence for N nodes is $O(N^{-m})$ where m is a real number based on the smoothness (regularity) of the underlying function. This is known as spectral convergence. Conversely, a finite element/finite difference method's convergence rates are based on the order of the method, regardless of the underlying function [30].

2.2.1 Problem Formulation.

Problem B: The definition of a Bolza optimal control problem (referred to here as Problem B) is the search for a state-control function pair $[t_0, t_f] \ni t \mapsto (x, u) \in \mathbb{R}^{N_x} \times \mathbb{R}^{N_u}$ for times between t_0 and t_f that minimizes the Bolza cost functional,

$$J[x(\cdot), u(\cdot), t_0, t_f] = E[x_0, x_f, t_0, t_f] + \int_{t_0}^{t_f} F[x(t), u(t), t]\, dt \tag{2.1}$$

subject to the state dynamics

$$\dot{x}(t) = f(x(t), u(t)), \tag{2.2}$$

end-point boundary conditions

$$e(x_0, x_f, t_0, t_f) = 0, \tag{2.3}$$

and mixed control-state path constraints

$$h(x(t), u(t)) \leq 0, \tag{2.4}$$

where $t \in \mathbb{R}$, $x \in \mathbb{R}^{N_x}$, $u \in \mathbb{R}^{N_u}$, $E[\cdot] \mapsto \mathbb{R}$ and $F[\cdot] \mapsto \mathbb{R}$. For brevity, the notation $x_0 = x(t_0)$ and $x_f = x(t_f)$ is used. The lower and upper bounds of the states and controls are denoted as $\{x_l, u_l\}$ and $\{x_u, u_u\}$ respectively. Including state and control bounds, Problem B can be written as:

$$
\begin{aligned}
\text{minimize} \quad & J[x(\cdot), u(\cdot), t_0, t_f] = E[x_0, x_f, t_0, t_f] + \int_{t_0}^{t_f} F[x(t), u(t), t]\, dt \\
\text{subject to} \quad & \dot{x}(t) = f(x(t), u(t), t), \\
& x_l \leq x(t) \leq x_u, \\
& u_l \leq u(t) \leq u_u, \\
& e(x_0, x_f, t_0, t_f) = 0, \\
& h(x(t), u(t)) \leq 0
\end{aligned}
\tag{2.5}
$$

where $E[\cdot]$, $F[\cdot]$, $f[\cdot]$, $e[\cdot]$, $h[\cdot]$ are assumed to be differentiable with respect to their arguments [24].

Problem B^λ: In order to solve Problem B using an indirect method, the necessary conditions for optimality can be derived via the Pontryagin's Minimum Principle (PMP) yielding a two-point Boundary Value Problem (BVP) [31–33]. This process is known as the dualization of Problem B into Problem B^λ [24]. Optimal solutions to this problem represent a vector-covector pair in the primal-dual space. To form Problem B^λ, first form the Pontryagin Hamiltonian (H), the Lagrangian of the Hamiltonian $\bar{H}$, and endpoint Lagrangian, ($\bar{E}$),

$$H(\lambda, x, u) = F(x, u) + \lambda^T f(x, u) \tag{2.6}$$

$$\bar{H}(\lambda, x, u) = H(\lambda, x, ut) + \mu^T h(x, u, t) \tag{2.7}$$

$$\bar{E}(\nu, x_0, x_f) = E(x_0, x_f) + \nu^T e(x_0, x_f) \tag{2.8}$$

where λ, μ, and ν are the adjoint covectors. Formulating the necessary conditions for optimality, Problem B^λ can be summarized as:

$$\text{Find:} \quad [x(\cdot), u(\cdot), \lambda(\cdot), t_0, t_f, \nu] \tag{2.9}$$

$$\text{Such that:} \quad \dot{x}(t) = f(x(t), u(t), t) \tag{2.10}$$

$$e(x_0, x_f, t_0, t_f) = 0 \tag{2.11}$$

$$h(x(t), u(t)) \leq 0 \tag{2.12}$$

$$\dot{\lambda}(t) = -\frac{\partial \bar{H}}{\partial x} \tag{2.13}$$

$$\frac{\partial \bar{H}}{\partial u} = 0 \tag{2.14}$$

$$\frac{\partial \bar{H}}{\partial t} = 0 \tag{2.15}$$

$$\{\lambda_0, \lambda_f\} = \left\{-\frac{\partial \bar{E}}{\partial x_0}, \frac{\partial \bar{E}}{\partial x_f}\right\} \tag{2.16}$$

$$\{\bar{H}_0, \bar{H}_f\} = \left\{\frac{\partial \bar{E}}{\partial t_0}, -\frac{\partial \bar{E}}{\partial t_f}\right\} \tag{2.17}$$

For any optimal solution to Problem B, there exists an adjoint covector λ and endpoint covector ν that satisfy the optimality conditions of Problem B^λ [31].

2.2.2 Pseudospectral Method.

The formulation and employment of PSM is covered extensively in [24–26] and is briefly summarized here for completeness.

PSM are subset of spectral methods utilizing orthogonal basis functions, often Jacobi polynomials, which can be utilized for solving optimal control problems [34]. The goal is to take Problem B and discretize it over carefully chosen nodes into Problem B^N, allowing numerical techniques to determine an optimal solution that commutes with the optimal solution from Problem B^λ via the Covector Mapping Principle (CMP) as shown in Figure 2.1. The CMP provides a way of mapping the Karush-Kuhn-Tucker (KKT) multipliers (or Lagrange multipliers) from the Non-Linear Programming (NLP) solution to Problem B^N with the covectors of the discretized solution to the dualized Problem B^λ, called Problem $B^{\lambda N}$. Thus the optimal solution to Problem B^N can be shown to satisfy the

optimality conditions of the PMP from Problem B^{λ}. For highly complex system, it may be easier to numerically solve Problem B^{N} via direct methods than to analytically derive Problem B^{λ} and solve via indirect methods.

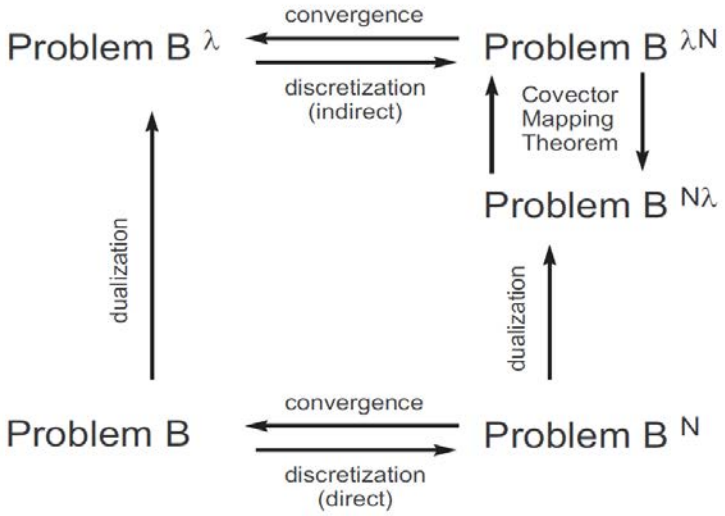

Figure 2.1: Commutative Diagram for Discretization and Dualization (adapted from [24])

Three different types of Gaussian collocation points, or nodes, are traditionally used as the interpolating points in the Legendre Pseudospectral Method (LPM): Legendre-Gauss (LG), Legendre-Gauss-Radau (LGR), or Legendre-Gauss-Lobatto (LGL). One difference between methods is the inclusion of none, one, or both endpoints, respectively, in the collocation points. For brevity, only the LPM, using LGL nodes, is discussed here. Full coverage of all three methods can be found in [24, 35, 36].

The LPM is based on the LGL collocation nodes (τ), distributed in the computational domain $\tau \in [-1, 1]$. Letting $L_N(t)$ be the Legendre polynomial of degree N on the closed interval $[-1, 1]$, the N LGL collocation nodes, τ_l, $l = 1, ..., N$ are chosen as the zeros of $\dot{L}_N(t)$ along with the points $\tau_1 = -1$ and $\tau_N = 1$ where the Legendre polynomial of degree N is defined as,

$$L_N(\tau) = \frac{1}{2^n}\sum_{l=1}^{N/2}(-1)^l \frac{(2N-2l)!}{2^N l!(n-1)!(N-2l)!}\tau^{N-2l}. \tag{2.18}$$

Shifting between the physical domain of $t \in [t_0, t_f]$ to the computation domain of $\tau \in [-1, 1]$ is done via the affine transformation,

$$\tau = \frac{t_f - t_0}{2}\tau + \frac{t_f + t_0}{2} \tag{2.19}$$

The states are then approximated by Lagrange interpolating polynomials of up to the *Nth* degree of the form

$$x(\tau) \approx x^{N+}(\tau) = \sum_{l=1}^{N} x_l \phi_l(\tau) \tag{2.20}$$

where for $l = 1, 2, ...N$

$$\phi_i(\tau) = \prod_{j=1, j\neq i}^{N} \frac{\tau - \tau_j}{\tau_i - \tau_j}, \quad (i = 1, ..., N) \tag{2.21}$$

is the Lagrange interpolating polynomial of order N. Differentiating Equation (2.20) and evaluating the expression at the nodes points, τ_k:

$$\dot{x}^N(t_k) = \left.\frac{dx^N}{d\tau}\right|_{t=t_k} = \left.\frac{dx^N}{dt}\frac{dt}{d\tau}\right|_{t_k} = \frac{2}{t_f - t_0}\sum_{l=1}^{N} D_{kl}x_l \equiv \frac{2}{t_f - t_0}d_k \tag{2.22}$$

where $D_{kl} = \dot{\phi}_l(t_k)$ are the entries defined in the Lobatto Pseudospectral (PS) differentiation matrix D [30]:

$$\boldsymbol{D} = [D_{kl}] = \begin{cases} \frac{L_N(\tau_k)}{L_N(\tau_l)}\frac{1}{\tau_k - \tau_l} & k \neq l \\ -\frac{N(N+1)}{4} & k = l = 1 \\ \frac{N(N+1)}{4} & k = l = N \\ 0 & \text{otherwise.} \end{cases} \tag{2.23}$$

The state dynamics $\dot{x} = f(x, u)$ can now be approximated by,

$$\frac{t_f - t_0}{2} f(x_k, u_k) - \sum_{l=1}^{N} D_{kl} x_l \approx 0 \qquad k = 1, ..., N \tag{2.24}$$

Defining the discretized state and controls as $X = [x_0, x_1, ..., x_N]$ and $U = [u_0, u_1, ..., u_N]$ respectively, the Bolza cost function (Equation (2.1)) can be approximated as

$$J[X, U, t_0, t_f] = E(x_0, x_N, t_0, t_f) + \frac{t_f - t_0}{2} \sum_{k=0}^{N} F(x_k, u_k) w_k \tag{2.25}$$

where w_k are the LGL quadrature weights given by

$$w_k = \frac{2}{N(N+1)} \frac{1}{(L_N(\tau_k))^2}, \quad k = 1, ..., N. \tag{2.26}$$

The optimal control Problem B is now discretized into a static optimization Problem B^N and is formulated as a NLP problem finding the vector $X_{NP} = (X; U; t_0; t_f)$

$$\begin{aligned} \text{minimize} \quad & J[X_{NP}] = E(x_0, x_N, t_0, t_f) + \frac{t_f - t_0}{2} \sum_{k=1}^{N} F(x_k, u_k) w_k \\ \text{subject to} \quad & \frac{t_f - t_0}{2} f(x_k, u_k) - \sum_{l=0}^{N} D_{kl} x_l = 0 \quad k = 1, ..., N, \\ & \boldsymbol{e}(x_0, x_N, t_0, t_f) = 0, \\ & \boldsymbol{h}(x_k, u_k) \leq 0 \quad k = 1, ..., N \end{aligned} \tag{2.27}$$

2.2.3 Pseudospectral Optimal Control Solvers.

To generate and solve Problem B^N, one must choose the method of discretizing and solving. While commercial solvers exists, such as DIDO and GPOPS II, this research employed custom Matlab scripts to transcribe the problem. The LGL collocation points, associated weights and differentiation matrix are computed via scripts from Shen [30] and Trefethan [37]. A custom script is then used to transcribe the dynamic optimization problem into a static NLP problem and submitted to the Sequential Quadratic Programming

(SQP) solver SNOPT [15, 38] which returns the respective state and control trajectories along with the associated KKT multipliers.

2.3 Sensitivity Based Robust Optimal Control

The dynamics of many real-world systems are often defined by various parameters which may represent spring and damper coefficients, system natural frequencies, or various other properties impacting the behavior of the system. For a vector of parameters p, the dynamics defined in Equation (2.2) can be rewritten implying the dependence on p as,

$$\dot{x}(t) = f(x(t), u(t); p). \tag{2.28}$$

For many systems, the actual parameter values may not be know, or may vary over time such as due to temperature effects. It may then be desired to derive optimal maneuvers achieving the desired objective while remaining robust against variation in these parameters. One method of increasing maneuver robustness is through the use of desensitized optimal control techniques. For this technique, the optimal control problem is augmented with sensitivity dynamics describing the time-varying sensitivity of the states to variations in the parameters. For uncertain parameters $p \in \mathbb{R}^{N_p}$ with nominal value $\bar{p}$, and state trajectory $x(t, u; \bar{p}) \in \mathbb{R}^{N_x}$, the sensitivity function is defined as [39],

$$s(t) = \left.\frac{\partial x(t)}{\partial p}\right|_{\bar{x},\bar{u},\bar{p}} = \begin{bmatrix} \frac{\partial x_1}{\partial p_1} & \cdots & \frac{\partial x_1}{\partial p_n} \\ \frac{\partial x_2}{\partial p_1} & \cdots & \frac{\partial x_2}{\partial p_n} \\ \vdots & \vdots & \vdots \\ \frac{\partial x_n}{\partial p_1} & \cdots & \frac{\partial x_n}{\partial p_n} \end{bmatrix}, \tag{2.29}$$

where for a first-order sensitivity function, all terms higher than first order are truncated. The nominal parameter vector is denoted as $\bar{p}$ while $\bar{x}$ and $\bar{u}$ are the state and control trajectories calculated assuming the nominal parameters. Considering a small perturbation

of the uncertain parameters (Δp) from $\bar{p}$, the state trajectory can be augmented with the sensitivity states

$$x(t, u; \bar{p} + \Delta p) \approx x(t, u; \bar{p}) + s(t)(\Delta p). \tag{2.30}$$

Taking the time derivative yields the dynamics of the system,

$$\dot{x}(t, u; \bar{p} + \Delta p) \approx f(x, t, u; \bar{p}) + \dot{s}(t)(\Delta p), \tag{2.31}$$

with the initial conditions $s(0) = 0$. The dynamics of the sensitivity function are then [39, 40]

$$\dot{s}(t) = A(t, \bar{p})s(t) + B(t, \bar{p}), \quad s(t_0) = 0 \tag{2.32}$$

$$A(t, \bar{p}) = \left.\frac{\partial f}{\partial x}\right|_{\bar{x},\bar{u},\bar{p}} \tag{2.33}$$

$$B(t, \bar{p}) = \left.\frac{\partial f}{\partial p}\right|_{\bar{x},\bar{u},\bar{p}}, \tag{2.34}$$

where $A(t, \bar{p})$ is the Jacobian of the dynamics along the nominal trajectory, $x(t, \bar{p})$, and $B(t, \bar{p})$ is a matrix describing the specific dependence of the dyanmics of the uncertain parameters.

The derived sensitivity dynamics can are then appended to the system dynamics, augmenting the original optimal control problem formulation. The optimal control problem formulation can now be updated to take advantage of the sensitivity states within the cost functional to derive robust maneuvers,

$$
\begin{aligned}
\text{minimize} \quad & J[x(\cdot), u(\cdot), s(\cdot), t_0, t_f] = E[x_0, x_f, s_f, t_0, t_f] + \int_{t_0}^{t_f} F[x(t), u(t), s(t), t]\, dt \\
\text{subject to} \quad & \dot{x}(t) = f(x(t), u(t), s(t), t, \bar{p}), \\
& \dot{s}(t) = A(s)\Big|_{\bar{x},\bar{u},\bar{p}} s(t) + B(s)\Big|_{\bar{x},\bar{u},\bar{p}}, \\
& e(x_0, x_f, s_0, t_0, t_f) = 0, \\
& h(x(t; \bar{p}), u(t)) \leq 0
\end{aligned}
\tag{2.35}
$$

The objective of Research Question (RQ) 2 is to utilize the desensitized optimal control problem formulation of Equation (2.35) to derive antenna slew maneuvers which not only decrease total slew time, but also minimize the sensitivity of the maneuver to parameter variation.

2.4 Unscented Optimal Control

For a given $\bar{p}$, Equation (2.5) provides a deterministic formulation for solving for a trajectory with nominal parameter values. However, it does not account for parameter variability nor incorporate methods to improve robustness against that variability. Unscented optimal control is another method of designing robust, open-loop control for systems with parametric uncertainty [41–43].

The unscented transform was originally developed by Julier and Uhlmann [44] as a method of filtering nonlinear systems by approximating a Probability Density Function (PDF) rather than linearizing a nonlinear function. A generalized representation of the unscented transform is shown in Figure 2.2 where a deterministic algorithm is used to carefully select a number of points which are then subjected to a nonlinear transformation. The resulting mean and covariance of the transformed points capture the statistical information of the distribution where high-order information about the distribution can be captured with few points.

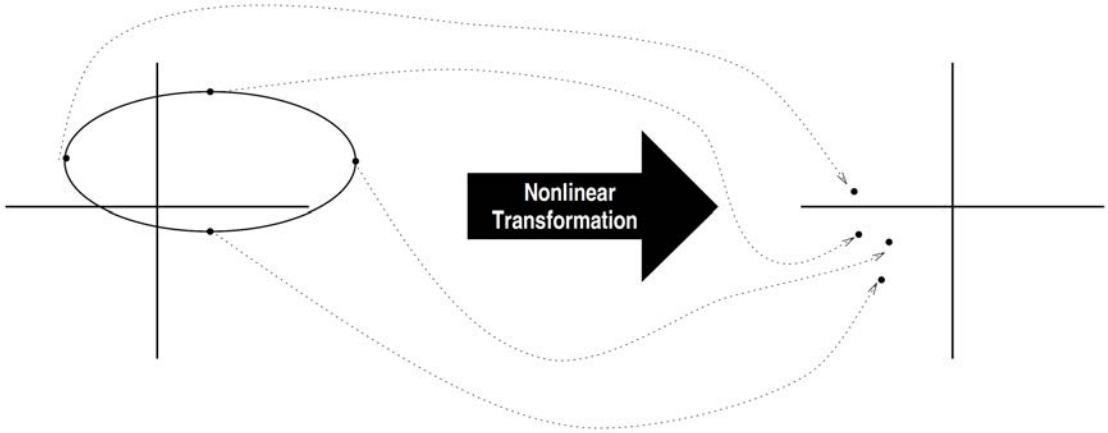

Figure 2.2: Generalized Unscented Transform (from [44])

Unscented optimal control relies on this same principle by combining the unscented transform with standard optimal control techniques to manage uncertainty in the resultant open-loop solutions. This is done by formulating the cost functional as a Riemann-Stieltjes integral [39, 45]. The system with dynamics

$$\dot{x} = f(x, u; p), \quad x(0) = x_0, \tag{2.36}$$

with states $x \in \mathbb{R}^{N_x}$ and uncertain parameters $p \in \mathbb{R}^{N_p}$ can be modified to shift uncertainty in the parameters to uncertainty in the dynamics by defining an explicit dependence on p,

$$\dot{x} = f(x, u; p)$$

$$\dot{p} = 0.$$

The cost functional $J[x(t), u(t)]$ can then be updated to include the uncertain parameters,

$$J_{uns}[x(t, p), u(t); p]. \tag{2.37}$$

For any value (p), a real-valued cost (J_{uns}) can be generated, but the cost functional must be modified further to account for the uncertainty in the parameters. This is done via the Riemann-Stieltjes (RS) integral, which is an integral of a real function with respect to a real measure

$$\int f(x)dg(x). \tag{2.38}$$

With regards to the initial uncertainty, this is written as

$$\int_{\Omega} \dots d\alpha(x_0), \tag{2.39}$$

where Ω is the support of the uncertainty PDF of the parameters and $\alpha(p)$ is a joint Cumulative Distribution Function (CDF) of the uncertainties [45, 46]. Combining the RS integral and the uncertain cost functional J_{uns} yields the functional of a functional

$$\int_{\Omega} J_{uns}[x(t,p), u(t); p]d\alpha(p). \tag{2.40}$$

The RS integral of Equation (2.40) can then be used to define an optimal control problem which generates a state/control pair $[x(t), u(t)]$ minimizing the uncertain cost functional J_{uns} over the support of the uncertain parameters p.

Considering the uncertain cost functional

$$J_{uns} = E(x_0, x_f) + \int_{t_0}^{t_f} F(x(t,p), u(t); p)\, dt, \tag{2.41}$$

the unscented cost functional can tehn be written as,

$$J[\boldsymbol{x}(\cdot,\cdot), \boldsymbol{u}(\cdot), t_f] = \int_{\Omega} J_{uns}[\boldsymbol{x}(\cdot,\boldsymbol{p}), \boldsymbol{u}(\cdot), t_f; \boldsymbol{p}]d\alpha(\boldsymbol{p}), \tag{2.42}$$

where, $\int_{supp(\boldsymbol{p})}$ is an N_p-dimensional integral over $supp(p)$. This new functional is deterministic and as such can be minimized by various means. From Equation (2.42), a new unscented optimal control problem can be given by:

$$
\begin{aligned}
\text{minimize} \quad & J[\boldsymbol{x}(\cdot,\cdot),\boldsymbol{u}(\cdot),t_f] = \int_{supp(\boldsymbol{p})} J_{uns}[\boldsymbol{x}(\cdot,\boldsymbol{p}),\boldsymbol{u}(\cdot),t_f;\boldsymbol{p}]d\alpha(\boldsymbol{p}) \\
\text{subject to} \quad & \dot{\boldsymbol{x}}(t) = f(\boldsymbol{x}(t),\boldsymbol{u}(t);\boldsymbol{p}), \\
& (\boldsymbol{x}(t_0;\boldsymbol{p}),t_0) = (\boldsymbol{x}^{\boldsymbol{0}},t^0), \\
& \|\boldsymbol{u}(t)\|_\infty \leq \boldsymbol{u}_{max}, \\
& \int_{supp(\boldsymbol{p})} \boldsymbol{e}(\boldsymbol{x}(t_f;\boldsymbol{p}),t_f)\alpha(\boldsymbol{p}) - \boldsymbol{x}^{\boldsymbol{f}} \leq \boldsymbol{\mu_x}, \\
& \int_{supp(\boldsymbol{p})} h(\boldsymbol{x},t)\alpha(\boldsymbol{p}) - \boldsymbol{h_{max}} \leq \boldsymbol{\mu_h}, \\
& t_0 \leq t \leq t_f.
\end{aligned}
\tag{2.43}
$$

To apply the concepts from Equation (2.43) to formulate an unscented optimal control problem, define $p \in \mathbb{R}^{N_p}$ to be a tychastic set of parameters of the nonlinear dynamical system with mean and covariance of μ_p and Σ_p. Using the unscented transform, a series of sigma vectors of parameters are calculated, $p_1, p_2, \ldots, p_{N_\Sigma}$. For dynamics of the form in Equation (2.2) with $u \in \mathbb{R}^{N_u}$ and $f(x,u,t;p) \mapsto \mathbb{R}^{N_x}$ that is differentiable with respect to $x \in \mathbb{R}^{N_x}$ [41], the dynamics of the N_Σ dynamics systems are,

$$
\dot{\chi}_i = f(\chi_i,u,t;p_i) \tag{2.44}
$$

Defining the $N_\sigma N_x$ dimensional vector X as

$$
X = \begin{bmatrix} \chi_1 \\ \chi_2 \\ \vdots \\ \chi_{N_\sigma} \end{bmatrix} \in \mathbb{R}^{N_\sigma N_x} \tag{2.45}
$$

$$
\tag{2.46}
$$

the dynamics of the sigma vector are given by

$$\dot{X} = \begin{bmatrix} f(\chi_1, u, t; p_1) \\ f(\chi_2, u, t; p_2) \\ \vdots \\ f(\chi_{N_\Sigma}, u, t; p_{N_S igma}) \end{bmatrix} = f(X, u, t). \tag{2.47}$$

For the initial sigma vector

$$X(t_0) = X^0 = \begin{bmatrix} \chi_1^0 \\ \chi_2^0 \\ \vdots \\ \chi_{N_\sigma}^0 \end{bmatrix} \tag{2.48}$$

the unscented optimal control objective is to find a control trajectory, $t \mapsto u$ that drives X^0 towards a desired end state while minimizing a cost functional and controlling for the statistics of the final propagated position of the sigma vector. For $X \in \mathbb{X}^{N_\sigma} \subseteq \mathbb{R}^{N_\sigma N_x}$, a standard unscented optimal control problem can be formulated as [42]

$$\begin{aligned} \underset{u \in \mathbb{U} \subseteq \mathbb{R}^{N_u}}{\text{minimize}} \quad & J[X(\cdot), u(\cdot), t_0, t_f] = E[X_0, X_f, t_0, t_f] + \int_{t_0}^{t_f} F[X(t), u(t), t]\, dt \\ \text{subject to} \quad & \dot{X}(t) = f(X(t), u(t), t), \\ & e(X_0, X_f, t_0, t_f) \leq 0, \\ & h(X(t), u(t)) \leq 0 \end{aligned} \tag{2.49}$$

Using this problem formulation, a new set of endpoint conditions can be derived based on the statistics of the sigma vector, such that the mean of the final error ($\mu_\chi(t_f)$) can be driven towards zero while enforcing the final covariance of each state to be within a user-defined value. The endpoint constraints for this formulation are then,

$$e_1(X(t_f)) = \mu_\chi(t_f) - x^f = 0 \tag{2.50}$$

$$e_2(X(t_f)) = diag[\Sigma_\chi] \leq [\sigma_1^2, \sigma_2^2 ... \sigma_{N_x}^2]^T \tag{2.51}$$

where x^f is the desired endpoint condition of the states, Σ_χ is the calculated covariances at the terminal point, and $\sigma_{1,...,N_x}$ are the user specified bounds of the respective variances [47].

Discretizing the parameter space of Equation (2.49) using sigma vector based on the unscented transform allows for a low number of sample nodes, capturing the underlying PDF of the uncertain parameters, while limiting the computational growth of the problem formulation. For the N_p uncertain parameters with known distributions, $N_\Sigma = 2N_p + 1$ sigma vector are necessary[48]. For model parameters p with mean $\bar{p}$ and covariance P_p, the matrix of sigma vector is formed according to the following,

$$\begin{aligned}
p^1 &= \bar{p} \\
p^i &= \bar{p} + \left(\sqrt{(L+\lambda)P_p}\right)_i \quad i = 2, ..., N_p + 1 \\
p^i &= \bar{p} - \left(\sqrt{(L+\lambda)P_p}\right)_{i-N_p} \quad i = N_p + 2, ..., 2N_p + 1 \\
w^1 &= \lambda/(N_p + \lambda) \\
w^i &= 1/(2(N_p + \lambda)) \quad i = 2, ..., 2N_p + 1,
\end{aligned} \tag{2.52}$$

where $\lambda = \alpha^2(N_p + \kappa) - N_p$ is a scaling parameter with α determining the spread of the sigma vector about the mean. κ is a secondary scaling parameter and β is a parameter used to incorporate prior knowledge of the distribution of p [48].

Based on the selected cubature scheme (or multi-dimensional quadrature), the discretized formulation of Equation (2.49) is then

$$\chi_i \in \mathbb{R}^{N_x}, \quad u \in \mathbb{R}^{N_u}, \quad i = 1, 2, ..., N_\Sigma, \quad p \in supp(p)$$

$$
\begin{aligned}
\text{minimize} \quad & J[\chi_1(\cdot), ..., \chi_{N_\Sigma}(\cdot), u(\cdot), t_f] = \sum_{i=1}^{N_\Sigma} w_i J_{uns}[\chi(\cdot, p_i), u(\cdot), t_f; p_i] \\
\text{subject to} \quad & \dot{\chi}_1(t) = f(\chi_1(t, p_1), u(t); p_1), \\
& \vdots, \\
& \dot{\chi}_{N_\Sigma}(t) = f(\chi_{N_\Sigma}(t, p_{N_\Sigma}), u(t); p_{N_\Sigma}), \\
& (\chi_i(t_0; p_i), t_0) = (\chi^0, t^0), \\
& \chi_{low} \leq \chi_i(t; p_i) \leq \chi_{upp}, \\
& |u(t)| \leq u_{max}, \\
& \sum_{i=1}^{N_\Sigma} w_i e(\chi_i(t_f, p_i); p_i) - \chi^f \leq \mu_\chi, \\
& \sum_{i=1}^{N_\Sigma} w_i h(\chi_i(t_f, p_i); p_i) - h_{max} \leq \mu_h, \\
& t_0 \leq t \leq t_f.
\end{aligned}
\tag{2.53}
$$

Equation (2.53) is now a fully deterministic optimal control problem which can be minimized via traditional methods, albeit sized according to the choice of N_Σ sigma vector.

2.5 Dynamics of a Flexible, Multi-Body Spacecraft

When considered at a high level, all methods of deriving equations of motion are similar, however, each method has varying complexity with regards to application of the method and simplicity of the resultant equations. Due to the impact of code complexity on computation time for NLP solvers, care should be taken to generate the most computationally efficient dynamical equations possible.

Two of the most common methods of deriving equations of motion are the Newton-Euler method, and Lagrange's method. When deriving the dynamics of a multi-body system, the Newton-Euler formulation requires a force and moment balance for each body separately, requiring the derivation of internal constraint forces (work-less constraints)

that do not perform work. This leads to a large but sparse system of equations which requires much algebraic work to eliminate these internal constraint forces. Additionally, for a system with n Degrees of Freedom (DOF), the Newton-Euler methods results in a system of order $O(n^4)$ computational complexity [49].

Lagrange's Equations provide a method of eliminating work-less constraint forces, but has the disadvantage of needing to derive complicated Lagrangians of the energy functions. It does, however, yield a system with $O(n^3)$ computational complexity, which is an improvement over the Newton-Euler method [50].

Kane's method offers the advantages of the two previous methods with none of the disadvantages, in that the use of generalized forces eliminates the need to calculate work-less constraint forces, and because it does not use energy functions, the calculation of complex Lagrangians is avoided while still yielding equations with complexity of $O(n^3)$ [12, 51, 52].

2.5.1 Kane's Equations.

For a system of N_b bodies composed of n-DOF, Kane's equation is defined as the sum of the generalized active forces (F_r) and generalized inertia forces (F_R^*)[12],

$$F_r + F_r^* = 0, \quad r = 1, ..., n \tag{2.54}$$

$$F_r = \sum_{k=1}^{N_b} (\vec{\omega}_r^k \cdot \vec{T}_k) + \sum_{k=1}^{N_b} (\vec{v}_r^k \cdot \vec{F}_k) \tag{2.55}$$

$$F_r^* = \sum_{k=1}^{N_b} [\vec{\omega}_r^k \cdot (-I_k \vec{\alpha}_k - \vec{\omega}_k \times \vec{H}_k)] + \sum_{k=1}^{N_b} [\vec{v}_r^k \cdot (-m_k \vec{a}_k)] \tag{2.56}$$

where $\vec{\omega}_r$ and $\vec{v}_r$ are the partial angular velocities and partial velocities respectively. To gather further insight into the equation, it can be recast into the following form,

$$\sum_{k=1}^{N_b} [\vec{\omega}_r^k \cdot (\vec{T} - I\vec{\alpha} - \vec{\omega} \times \vec{H})_k] + \sum_{k=1}^{N_b} [\vec{v}_r^k \cdot (\vec{F} - m\vec{a})_k] = 0 \tag{2.57}$$

which is easily identifiable as Euler's Equation and Newton's Second Law of Motion. For a system with N_b bodies, there are $6N_b$ DOF requiring $6N_b$ differential equations. Considering the set of constraints N_c, there are then $N_u = 6N_b - N_c$ DOF remaining. Kane's method arrives at a minimum dimension system of equations by first defining N_u generalized speeds. The $6N_b$ space of motion is then partitioned into an N_u-dimension space of permissible motion and a N_c-dimension space of impermissible motion. Using the partial velocities and partial angular velocities, Kane's method then projects Euler's and Newton's Equations into the permissible subspace [53]. Kane's method results in the scalar multiplication of the vector entities of partial velocities, which is easily cast into matrix form for use with numerical computer packages. There are many commercial software packages that have been developed over the past few decades automating the formation of the dynamical equations. One such software package is *MotionGenesis* [13], which is utilized for this research.

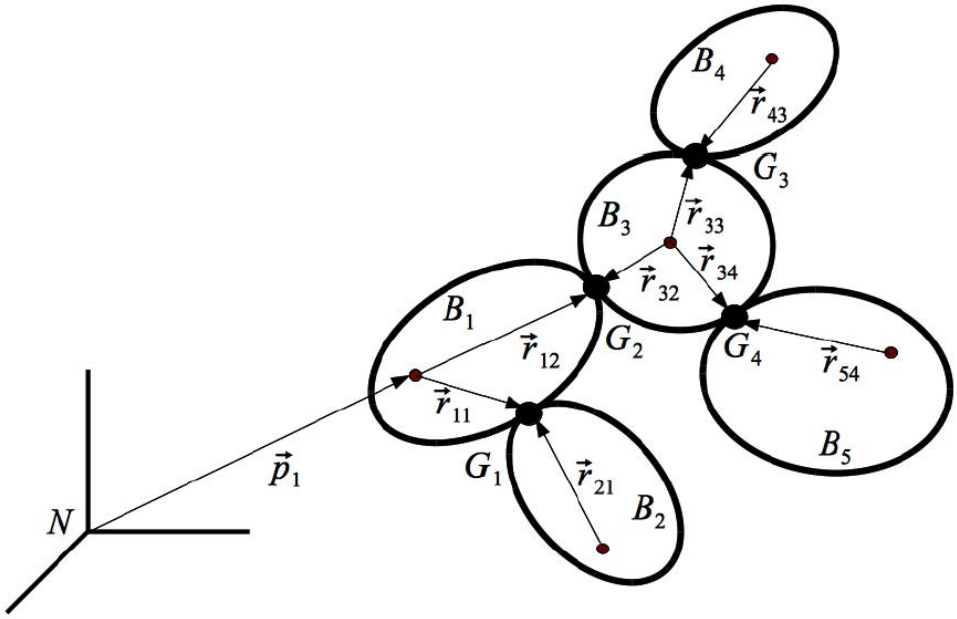

Figure 2.3: Tree topology of a Notional Multi-body System (from [53])

For a multi-body system connected via revolute joints, such as the notional five body system shown in Figure 2.3, the mass and inertia properties of each body (B) are individually defined. Vectors from the body's respective mass center to each connected joints ($\vec{r}$) are defined, along with the number of DOF inherent in each joint (G) and any external forces and torques (F, τ). Based on the defined parameters, *MotionGenesis* automates the application of Kane's method and outputs a function file containing the system's complete nonlinear equations of motion. The resultant equations of motion in second-order form are

$$M(x)\ddot{x} = N(\dot{x}, x, F, \tau) \tag{2.58}$$

where $\ddot{x}$ is a vector of accelerations, M is a symmetric, generalized coordinate dependent mass matrix and $N(\cdot)$ is a vector of all remaining linear and nonlinear terms including external forces/torques.

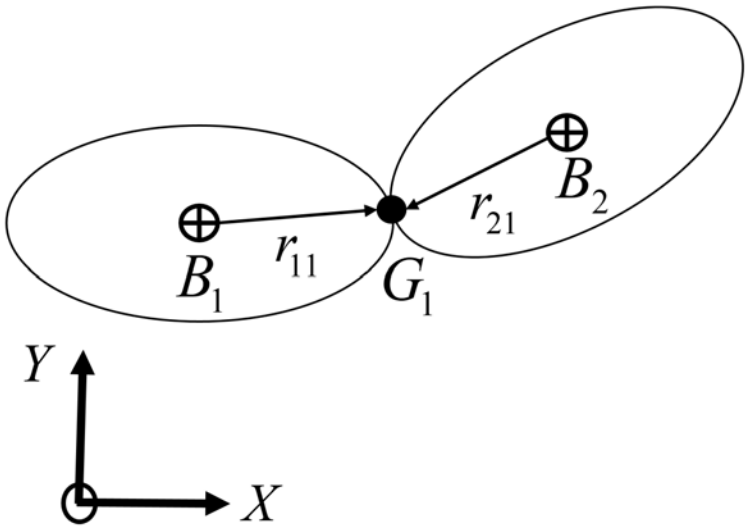

Figure 2.4: Generic Two-Body Planar System

Consider two rigid bodies (B_1, B_2), free-floating in inertial space but restricted to planar motion in the (x, y)-plane, connected via a 1-DOF revolute joint with rotation about the z-axis as shown in Figure 2.4. The states $[x_1, x_2]$ represent the generalized angles and the dot-notation represents their derivative with respect to time (Table 2.1)

Table 2.1: Parameters for Two-Body Rigid Model

Symbol	Description	Ref. Frame
I_i	central moment of inertia, body i	body local
m_i	mass, body i	–
$(x, \dot{x}, \ddot{x})_1$	Body 1 angle/rate/acceleration	inertial
$(x, \dot{x}, \ddot{x})_2$	Body 2 angle/rate/acceleration	body local
r_{ij}	Vector from mass center, body i, to gimbal j	body local
τ_j	External torque, gimbal j	body local

Utilizing MotionGenesis, a script is generation where each rigid body is defined with its own reference frame. The various reference frame are then connected via a chain of vectors starting from the origin of the inertial frame and concluding with the outer most body. After defining the mass and inertial properties, MotionGenesis employs Kane's method to symbolically derive the equations of motion. The second-order dynamics derived utilizing MotionGenesis and Kane's method are,

$$\begin{bmatrix} I_1+I_2+m_2\left(r_{11y}{}^2+2\cos(x_2)\, r_{11y}\, r_{21y}+r_{21y}{}^2\right) & I_2+m_2\, r_{21y}\left(r_{21y}+r_{11y}\cos(x_2)\right) \\ sym & m_2\, r_{21y}{}^2+I_2 \end{bmatrix} \begin{bmatrix} \ddot{x}_1 \\ \ddot{x}_2 \end{bmatrix} = \begin{bmatrix} \tau_1 + m_2\, r_{11y}\, r_{21y}\, \sin(x_2)\left((\dot{x}_1+\dot{x}_2)^2 - \dot{x}_1^2\right) \\ \tau_2 - m_2\, r_{11y}\, r_{21y}\, \dot{x}_1^2\, \sin(x_2) \end{bmatrix} \quad (2.59)$$

2.5.2 Joint Flexibility.

Robotic systems in industrial applications are often built with high rigidity to simplify their dynamics, as the tip position is often measured only using sensors in the actuator. This rigidity requires links which are thicker and heavier than strictly necessary, a design practice that is not practical for space systems where weight savings are critical. Due to the inherent rigidity, motion planning is performed assuming the forces are applied directly to each link, as shown in Figure 2.5.

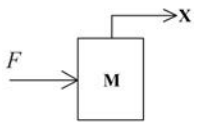

Figure 2.5: Simplified One-Body System

Due to the lightweight nature of space systems, it is difficult to achieve this high level of link/motor rigidity. To account for the flexibility inherent within satellite gimbal joints, the elastic properties of the actuator must be modeled.

In this research, the satellite gimbal actuators are assumed to be direct current motors, rigidly mounted to the inner link and elastically coupled to the outer link. It is further assumed that the kinetic energy of the rotor is due to its own rotation. The rotor/gearing inertia is assumed to be symmetric about the rotation axis and gravitational potential is ignored. It has been shown that these simplifying assumptions amount to neglecting higher-order terms and have little impact on computational results [54]. Each gimbal motor/link pair is then treated as a two-body, mass-spring-damper system as shown in Figure 2.6.

For a system of n-links, this yields additional gimbal motor states, $x_g \in \mathbb{R}^{N_g}$ modeled as rigidly connected to the inner link. Control forces are introduced into the gimbal bodies

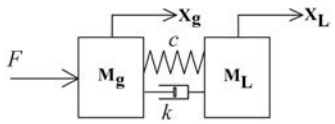

Figure 2.6: Simplified Two-Body System for Motor Shaft Flexibility

which are elastically coupled to the outer link, $x_L \in \mathbb{R}^{N_g}$ [54, 55]. Equations of motion for the gimbal motors are then,

$$I_g \ddot{x}_g + C(\dot{x}_L - \dot{x}_g) + K(x_L - x_g) = \tau_g \tag{2.60}$$

where x_g is the vector of motor states, x_L the vector of link angles, I_g is a diagonal matrix of motor inertia, C and K are diagonal matrices of corresponding damping and spring coefficients, and τ_g is the gimbal motor torque vector.

The previous two-body example in Equation (2.59) can now be revised with an additional state for the gimbal motor (x_G), with the updated parameters shown in Table 2.2. In the first example, x_2 represented the generalized coordinate associated with the pointing of Body 2. In this formulation, x_2 represents the generalized coordinate representing the angle between motor angle (x_G) being driven by the controller, and the link angle due to flexibility in the joint, so the actual link angle with respect to Body 1 is $x_C = x_G + x_2$. The updated parameter table is shown in Table 2.2 with the resultant equations of motion in Equations (2.61) and (2.62). The appearance of the elastic coupling terms between Body 2 and the gimbal motor can be seen in Equations (2.62i) and (2.62j).

$$\begin{bmatrix} m_{11} & m_{12} & m_{13} \\ & m_{22} & m_{23} \\ & & m_{33} \end{bmatrix} \begin{bmatrix} \ddot{x}_1 \\ \ddot{x}_2 \\ \ddot{x}_G \end{bmatrix} = \begin{bmatrix} n_1(\dot{x}, x, \tau) \\ n_2(\dot{x}, x, \tau) \\ n_3(\dot{x}, x, \tau) \end{bmatrix} \tag{2.61}$$

Table 2.2: Parameters for Two-Body Model with Flexible Joint

Symbol	Description	Ref. Frame
I_i	central moment of inertia, body i	body local
m_i	mass, body i	–
$(x, \dot{x}, \ddot{x})_1$	Body 1 angle/rate/acceleration	inertial
$(x, \dot{x}, \ddot{x})_2$	Body 2 angle/rate/acceleration	body local
$(x, \dot{x}, \ddot{x})_G$	Gimbal motor angle/rate/acceleration	body local
r_{ij}	Vector from mass center, body i, to gimbal j	body local
τ_j	External torque, gimbal j	body local
$(k, c)_j$	Gimbal motor (j) spring and damping coefficient	body local

$$m_{11} = I_1 + I_2 + I_G + m_G {r_{11y}}^2 + \tag{2.62a}$$

$$m_2 \left({r_{11y}}^2 + 2 \cos(x_2 + x_G)\ r_{11y} r_{21y} + {r_{21y}}^2 \right) \tag{2.62b}$$

$$m_{12} = I_2 + m_2 r_{21y} \left(r_{21y} + r_{11y} \cos(x_2 + x_G) \right) \tag{2.62c}$$

$$m_{13} = I_2 + I_G + m_2 r_{21y} \left(r_{21y} + r_{11y} \cos(x_2 + x_G) \right) \tag{2.62d}$$

$$m_{22} = m_2 {r_{21y}}^2 + I_2 \tag{2.62e}$$

$$m_{23} = m_2 {r_{21y}}^2 + I_2 \tag{2.62f}$$

$$m_{33} = m_2 {r_{21y}}^2 + I_2 + I_G \tag{2.62g}$$

$$n_1 = \tau_1 + m_2 r_{11y} r_{21y} \sin(x_2 + x_G) \left((\dot{x}_1 + \dot{x}_2 + \dot{x}_G)^2 - \dot{x}_1^2 \right) \tag{2.62h}$$

$$n_2 = -m_2 r_{11y} r_{21y} \sin(x_2 + x_G)\ \dot{x}_1^2 - c_2 \dot{x}_2 - k_2 x_2 \tag{2.62i}$$

$$n_3 = \tau_B - m_2 r_{11y} r_{21y} \sin(x_2 + x_G)\ \dot{x}_1^2 + c_2 \dot{x}_2 + k_2 x_2 \tag{2.62j}$$

2.5.3 Hybrid Coordinate Method.

To model the interaction between the spacecraft control system and (as of yet unmodeled) bus structural flexibility, the hybrid coordinate method is used. This method produces coordinates describing the modal response of elastic appendages of the vehicle such as the solar array, while the coordinates modeling the attitude of the rigid body remain discrete. This method assumes the modeled flexibility only undergo "small", linearly elastic deformations [14, 20]. Defining the modal coordinates as $\eta \in \mathbb{R}^{N_\eta}$, the modal dynamics are described by,

$$\ddot{\eta} + 2\zeta\omega_n\dot{\eta} + \omega_n^2\eta + \delta\ddot{x} = 0 \tag{2.63}$$

where ζ is a passive modal damping ratio, ω_n is a diagonal matrix of modal frequencies, δ is the rigid-elastic coupling matrix, and $\ddot{x}$ is a vector of appropriate accelerations from the rigid body equations [2, 56]. Combining the concepts from Equation (2.63) with Equation (2.61) yields the matrix differential equation,

$$\begin{bmatrix} M(x) & 0 & \delta \\ 0 & I_g & 0 \\ \delta^T & 0 & I \end{bmatrix} \begin{bmatrix} \ddot{x} \\ \ddot{x}_g \\ \ddot{\eta} \end{bmatrix} = \begin{bmatrix} N(\dot{x}, x, \tau_1) + C(\dot{x}_L - \dot{x}_g) + K(x_L - x_g) \\ -C(\dot{x}_L - \dot{x}_g) - K(x_L - x_g) + \tau_g \\ -\omega_n^2\eta - 2\zeta\omega_n\dot{\eta} \end{bmatrix}, \tag{2.64}$$

where I is taken to be an appropriately sized identity matrix. Control inputs $\tau = [\tau_1, \tau_g]$, are divided into root body torques (τ_1) and gimbal torques (τ_g) such that root body torques act directly on the body while gimbal torques are introduced through the gimbal bodies and elastically coupled through the diagonal stiffness and damping matrices, K and C, into the appropriate links in accordance with Equation (2.60).

The kinematics of the root body are then modeled via the quaternion, where defining the rotation rate about the $x/y/z$ body axes as $(\omega_x, \omega_y, \omega_z)$, the quaternion ($q \in \mathbb{R}^4$) dynamics are defined as,

$$\begin{bmatrix} \dot{q}_1 \\ \dot{q}_2 \\ \dot{q}_3 \\ \dot{q}_4 \end{bmatrix} = \frac{1}{2} \begin{bmatrix} 0 & \omega_3 & -\omega_2 & \omega_1 \\ -\omega_3 & 0 & \omega_1 & \omega_2 \\ \omega_2 & -\omega_1 & 0 & \omega_3 \\ -\omega_1 & -\omega_2 & -\omega_3 & 0 \end{bmatrix} \begin{bmatrix} q_1 \\ q_2 \\ q_3 \\ q_4 \end{bmatrix}. \tag{2.65}$$

2.6 Literature Review

Motion control of articulated systems can be loosely broken into the three tasks of trajectory planning, feedforward control, and system compensation via feedback control. Based on system constraints, the desired system performance is initially designed into the planned trajectory while feedforward control reduces trajectory tracking errors and feedback control provides system robustness and stability. For traditional space system, these tasks are performed independently for individual actuators, treating each link as a simple mass articulated about a single degree of freedom. While these assumptions simplify trajectory planning, they increase the reliance on system compensation to ameliorate disturbance torques arising from coupling between motion axes and dynamic nonlinearities. To minimize the magnitude of these disturbances, maneuvers are planned using conservative constraints on maximum allowable link acceleration (torque) and velocity. Often, these constraints are not based on hardware capabilities but are "soft" constraints intended to minimize un-modeled second-order effects such as system vibrational excitation [18]. If the planned trajectory were executed open-loop, these un-modeled effects can lead to large position and velocity errors, requiring a large percentage of available control authority be reserved for feedback control. Similarly, terminal pointing errors and residual velocity can require additional pull-in maneuvers to achieve the desired position/velocity, further increasing maneuver execution length.

To address the shortcomings of simplified trajectory planning methods, a multitude of advanced control techniques have been proposed. Many feedback control design methods

have been considered to decrease errors during trajectory tracking such as adaptive control [57], fuzzy control [58], H_2/H_∞ control [59, 60], and predictive control [61]. While these methods can decrease tracking errors during and after a maneuver, they do not increase the performance of the maneuver beyond what is already inherent to the trajectory profile being considered. Meaning, for a given planned trajectory final time, t_f, the referenced feedback techniques do not provide a framework for decreasing t_f, and thus increasing payload availability. Likewise, improvements can also be made in feedforward control methodology, such as those based on plant inversion [62, 63], which similarly may decrease tracking errors, but do not provide a means for reducing maneuver length. The smoothing or shaping of trajectories is another method of minimizing unwanted coupling and vibrational excitation of flexible systems whether by increasing the polynomial order used for designing the trajectory [64, 65] or through input shaping [66, 67]. While these methods can be successful at suppressing unwanted dynamic interactions, it typically comes at the expense of an increase in trajectory execution time.

While improvements in feedforward and feedback control can reduce trajectory tracking errors, decrease settling times, and increase robustness to disturbances, they lack the capability to decrease maneuver execution time beyond what is inherent in the trajectory. Therefore, if one desires to significantly increase payload availability, the best candidate is through improved trajectory design, such as through the use of PSOC techniques.

Now that the basics of PSOC and robust optimal control have been reviewed, the following section focuses on relevant research as it relates to RQ 1 through 4. Previous work is reviewed where PSM are used to develop optimal trajectories, to include multi-body systems exhibiting flexibility and parametric uncertainty.

2.6.1 Previous Work Pertaining to Research Question 1.

There is a large body of work regarding the application of PSOC to the reorientation of rigid body, free-floating systems. Bedrossian developed a zero-propellant maneuver for the International Space Station [27] while Karpenko et al. developed a Shortest Time Maneuver (STM) for the National Aeronautics and Space Administration (NASA) TRACE and Lunar Reconnaissance Orbiter satellites [28, 29]. These techniques were expanded to include path constraints such as managing singularity measures during Control Moment Gyroscope (CMG) control [68] or avoiding keep-out zones [69]. However, in each of these papers, the target satellite is modeled as a single rigid body, where flexibility inherent in the system, such as from solar arrays, is un-modeled during optimal trajectory generation. While the assumption of a single rigid body may be appropriate for the satellite reorientation maneuvers investigated, the RQ posed in this dissertation require the modeling of a multi-body system and the relevant vibrational dynamics.

The proposed multi-body system can be modeled similarly to a multi-link robotic arm, such as proposed for on-orbit servicing missions. Considerable research has been performed on path planning for space-based robotic servicing platforms which present unique problems as compared to terrestrial applications, as they are free-floating, so any linkage movement impacts the entire system due to the conservation of angular momentum. Considering a free-floating multi-body system, Papadopoulos showcased the ability to achieve a desired manipulator endpoint while also achieving a desired bus attitude, but the approach assumes no bus control and was restricted to a 3-body, planar problem without flexibility. While the solution was determined to be feasible, no measure of optimality was discussed [70]. Xu et al. explored a similar problem that expanded beyond a planar restriction to a full 6 DOF model with a single robotic arm using polynomial and sinusoidal basis functions for path generation, however, the proposed solution only accounts for the

final end conditions of the single manipulator and leaves the spacecraft bus in a perturbed state [71].

Wang investigated time-fuel optimal attitude maneuver of a flexible spacecraft where the dynamics were derived using the Newton-Euler method while using hybrid-coordinate method to model the modal vibration. The optimal maneuver was solved using PMP but the dynamics were simplified to a simple double-integrator system for the optimization and restricted to rotation about a single axis. Additionally, the optimal maneuver did not account for the vibration in the system directly, but suppressed the modes through a notch filter in the control system [56].

Crain and Ulrich used PSM to optimally slew a three-body system where a two-bar linkage is attached to a free-floating base [72]. While the problem formulation was restricted to planar dynamics and did not account for system flexibility, the dynamics were formulated so as to model the reaction torque imposed into the base by the motion of the linkage assembly. In this way, the system dynamics were simplified as only two bodies of the three-body system needed to be modeled. This technique is a motivating example to be used to address RQ 4 in that judicious choice of model simplification can lead to optimal results in a computational efficient manner. In [72], Crain expands the previous work to a four-body model, with a free-floating base and a 3-bar linkage system, however the problem is still restricted to planar motion without modeled flexibility. Using PSM, he derived an optimal trajectory for deploying the three-linkage robotic arm while minimizing the total angular displacement of the base body. The results were then experimentally validated using a robot floating on an air-bearing table which were shown to match well with the simulated results. Xu et al. studied vibration suppressive control for a two-link flexible manipulator using LPM. The paper showed that the PSM was able to calculate a maneuver of the link that minimized residual vibration, however, the problem formulation was restricted to only two links, with planar motion and a fixed base [73].

Expanding the multi-body concept into three dimensions, Bishop et al. demonstrated the optimal slewing of a three-body system in which a Tracking and Data Relay Satellite (TDRS) Single Access Antenna (SAA) performed a STM while accounting for attitude disturbances imposed on the spacecraft bus [16]. It was shown that maneuver speedups of 11-29% were achievable while ensuring the peak rotation rate realized in the bus were maintained less than or equal to that induced by a traditionally planned maneuver. While this problem formulation begins to approach that proposed in this dissertation, it models the TDRS bus and second SAA as a single rigid body and does not account for gimbal flexibility or vibrational modes of the bus. Wojdakowski [74] and Atwood [55, 75] progressed the previous work for optimal trajectory generation by expanding the dynamics to include joint flexibility in the manner discussed in Section 2.5.2. Both authors showed that when the joint flexibility is modeled in the formulation of the PSOC problem, the method is able to account for the impacts of flexibility and generate optimal solutions capable of suppressing excitation of those modes.

Research Question 1 requires the modeling of not only joint vibration, but also the impacts of the satellite's primary modes, often driven by other un-modeled bodies such as solar arrays. Likins and Fleischer used a hybrid coordinate scheme to couple the rigid body dynamics with the modal coordinates of flexible space structures [20, 76] which was later used by Wie to develop robust feedback control for a flexible satellite [2]. This method allows the primary modes of the spacecraft bus to be coupled to multi-body dynamics with flexible joints, such as implemented by Zarafshan [77]. While these papers have a more complete model of the multi-body, flexible system, they do not utilize the dynamics equations to develop optimal trajectories, but instead rely on robust feedback control of the linearized system to achieve the desired endpoint conditions.

2.6.2 Previous Work Pertaining to Research Questions 2 and 3.

Banerjee et al. investigated robust optimal attitude tracking for a rigid spacecraft. It was first shown that the LPM could be used to generate an optimal trajectory for the spacecraft [78], which was then expanded to account for uncertainty in the inertial properties [79]. The author however, does not account for the uncertain parameter directly in the PSM, but instead implements a sliding mode controller to account for the uncertainty while following the optimal trajectory.

Sensitivity analysis and the sensitivity function have been established as a means of increasing the robustness of a system given uncertain parameters. Sensitivity analysis was utilized by Dai to reduce plant sensitivity to parameter variation [80]. Seywald et al. [81, 82] generated desensitized optimal control trajectories, however, the analysis was restricted the Zermelo problem with a single uncertain parameters. The analysis does not extend the technique to more complex dynamics, multiple uncertain parameters, and assumes the sensitivity function can be derived explicitly, which does not necessarily hold for more complex systems. Using a robustness constraint, Liu et al. solved a time-optimal control problem minimizing endpoint vibration for a rest-to-rest maneuver of a flexible satellite [83, 84]. This was later expanded upon by Ansari for robust path planning, creating trajectories insensitive to small variations in system parameters [85, 86]. Shaffer expanded upon the technique by combining the sensitivity function dynamics with the dynamics of a flexible double gimbal assembly. The combined dynamics were utilized in a PSOC method where open-loop trajectories were generated exhibiting robustness against variations in system parameters, such as joint stiffness [39, 87]. Through Monte Carlo analysis, Shaffer was able to demonstrate an 88% decrease in mean residual energy and a 99% decrease in the final position variance as compared to the optimal solution assuming nominal parameters.

Unscented optimal control is a relatively new method, having been pioneered for spaceflight application by Ross et al. within the last decade [41, 42, 47]. The first

applications of the method were with regards to trajectory generation for the classical Zermelo navigation problem of crossing a body of water with uncertain winds and currents [42]. In their paper, an uncertain Zermelo problem is formulated, and by first solving the deterministic problem and performing a Monte Carlo analysis about the uncertain parameters, Ross showed the target error distribution was non-zero mean. The first ancillary Lebesgue-Stieltjes (LS) optimal control formulation loosened the endpoint condition to encourage a zero-mean solution for the subsequent optimal trajectory. This solution resulted in a nearly zero-mean distribution but with unchanged standard deviations. The second LS optimal control problem was to place constraints on and minimize the endpoint standard deviations. Ross' results demonstrated the (x, y) mean and covariance being reduced from $\mu_{x,y} = (0.0305, 0.0181)$ and $\Sigma_{x,y} = (0.2454, 0.1590)$ to $\mu_{x,y} = (-0.0018, 0.0005)$ and $\Sigma_{x,y} = (0.1139, 0.1112)$. The Zermelo problem was then extended by Ross et al. to the space domain where the optimal rendezvous of a spacecraft with an asteroid was analyzed allowing for uncertainty in the asteroid angular velocity and gravitational potential [47]. While the dynamics associated with the Zermelo and associated orbital rendezvous problem are different than that of the multi-body spacecraft, the techniques for formulating successive LS relaxations of the deterministic optimal control problem will be applied in this research.

The unscented method has also been applied to the optimal reorientation of the Hubble Space Telescope (HST) using reaction wheel control. Assuming perfect pointing knowledge at the start of a STM, Ross et al. [41] demonstrated the derivation of a HST maneuver robust against variations in the inertia tensor, gravity gradient and atmospheric drag. Successive unscented problem formulations were solved first focusing on ensuring a nearly zero-mean solution, while the second formulation imposed constraints on the standard deviation of the stochastic results. The paper demonstrated a posteriori Monte Carlo results with zero mean and a ten-fold reduction in the covariance of the target state

variables. This paper showed the application of the unscented method to the reorientation maneuver of a satellite with uncertain parameters, but did not account for path constraints such as minimization of vibration modes or saturation of momentum management devices. The unscented optimal control method was later applied to generating reorientation maneuvers for agile imagine satellites [45] which was then experimentally validated by Karpenko et al. [88] against a Honeywell CMG test bed . It has been shown [89] that an optimal STM for a vehicle under CMG control may result in singular gimbal configurations which render the space vehicle uncontrollable. A deterministic optimal control formulation starts with a known, initial state for the CMG gimbal angles (δ), which may not always be true. The unscented approach is used to generate an optimal trajectory based on uncertainty in the initial gimbal angles, while adhering to a path constraint governed by a singularity measure which ensures the CMG is sufficiently far from a singularity to ensure controllability due to system disturbances [90].

In research by Shaffer et al., the robust maneuver generation of a flexible double gimbal mechanism is considered with uncertainty in the stiffness parameter of the flexible joint (k). Shaffer demonstrated the nonlinear relationship between the residual energy in the double gimbal system where k varied from the value used in the optimal solution. Shaffer goes on to formulate two different robust solution methods for a Minimum Control Maneuver (MCM) of the double gimbal assembly including the use of a sensitivity function as detailed in Section 2.3 as well as an unscented formulation. Shaffer showed that both methods could produce robust trajectories and minimized residual vibrational energy. However, this research was limited to a two-body system with a fixed base, and only accounted for the uncertainty of a single parameter [39, 87].

Mathavaraj et al. [91] applied a similar unscented method along with model predictive static programming to solve the Zermelo problem with uncertain wind, as well as the inverted-pendulum problem with uncertainty in the initial conditions. Ozaki [92] similarly

applies the unscented transform in conjunction with differential dynamics programming to solve a low-thrust trajectory design for an Earth-Mars transfer orbit. While the numerical methods of solving the optimal control problems different from the pseudospectral method utilized herein, these papers demonstrate the ability of the unscented transform to capture parameter uncertainty and cast a stochastic dynamic problem into a deterministic form.

Based on the previous work related to RQ 2-3, this research intends to extend the complexity of the models and reduce the number of simplifying assumptions in order to analyze the applicability to a more representative satellite system. RQ 2 and 3 will utilize the same five-body flexible model as RQ 1, but will apply robust and unscented optimal control techniques as a method of accounting for initial state and parameter uncertainty. As a motivating example, TDRS requirements state the controller must be robust against modal frequency variations of ±20% [3]. While RQ 1 will investigate the ability to exactly suppress a known modal frequency, RQ 2 and 3 will extend the analysis to include uncertainty and ensure the resultant solution is robust against frequency variability. Similarly, for RQ 1, the initial state of the modal variables are assumed to be identically zero in the PS problem formulation, while in practice there will always be some level of modal excitation exhibited in the system. Using robust and unscented methods, optimal maneuvers suppressing additional modal excitation will be investigated while starting from an unknown modal state.

2.6.3 Previous Work Pertaining to Research Question 4.

Robust optimal control methods as a means of model reduction is a topic that has not been explicitly explored in the literature, though the underlying concepts are implicit in all optimal control problem formulations. The choice of dynamical equations for a flexible, multi-body system exist on a continuum of complexity. On one end could be considered the Finite Element Method (FEM), where in the limit as the number of elements approaches infinity, the model more precisely models the real-world system. On the other

end of the continuum are heritage methods of motion planning, where a double gimbal mechanism is treated as a decoupled, linearized system, and interactions between gimbals and the satellite bus are un-modeled and suppressed via conservative design principles and feedback control. There are infinite variations of complexity between the ends of the continuum and the controls engineer must make judicious decisions on what elements to include, linearize, or exclude all together. These choices not only impact the resultant optimal solution, but also the computational time necessary to reach that solution. While computation times on the order of minutes to hours may have little impact in an academic environment, real-world systems may only have milliseconds allocated to motion planning. In order to move towards implementing real-time optimal control, the computational efficiency of the problem formulation must be evaluated and improved.

RQ 1 builds a satellite model including the primary spacecraft modes and flexible joints, and assuming full state and parameter knowledge, develops optimal trajectories for an antenna slew maneuver. RQ 2 and 3 take that model and implement techniques to calculate trajectories robust against parameter and state uncertainties. RQ 4 will explore the trade-space between solving the exact, high-order model and using sensitivity functions and/or unscented methods in conjunction with model reduction techniques to develop trajectories nearly as optimal as the full-model solution but with reduced computational complexity.

2.7 Conclusion

In this chapter, the foundational topics of PSOC were reviewed, including problem formulation, discretization the dynamic problem using the Radau Pseudospectral Method (RPM) into a static optimization problem, and solving via NLP solvers. Two different methods of increasing optimal solution robustness were reviewed. In Section 2.3, a first-order sensitivity function defined by a linearization about the nominal model parameters was derived, while in Section 2.4 the unscented transform was used to discretize and

propagate the full nonlinear errors. Section 2.5 reviewed Kane's method of deriving systems of dynamic equations along with methods used to incorporate joint flexibility and the use of the hybrid coordinate method to account for the primary vibration modes of the satellite bus. Section 2.6 provided an overview of relevant recent research and it was shown how the proposed topic would advance each area in a novel manner.

III. Model Development and Simulation Environment

This chapter covers the development of the full system model and simulation environment utilized during this research. It outlines standard maneuver planning techniques and provides and overview of standard maneuver performance, which acts as the baseline to which the optimal maneuvers are compared.

3.1 Spacecraft Model

The five-body spacecraft model utilized in this dissertation is developed utilizing Kane's method defining a kinematic chain as detailed in Stoneking [53] and is represent as a five-body tree-topology as shown in Figure 3.1.

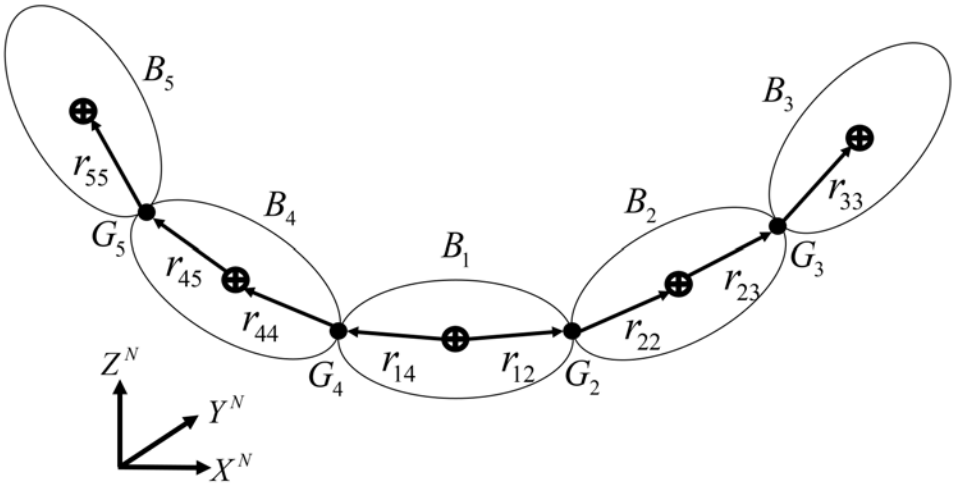

Figure 3.1: Generic Five-Body Dynamic System

For the five-body system with Body 1 (B_1) representing the spacecraft bus, bodies B_2 and B_4 represent the inner elevation gimbals of the two Single Access Antenna (SAA), each rotating about the x-axis of the B_1 relative frame. Bodies B_3 and B_5 represent the outer azimuth gimbal and respective antenna assemblies rotating about the y-axis of their inner

gimbal's body-fixed frame. The inertia matrices for the five bodies are defined in their body fixed frames are,

$$I_1 = \begin{bmatrix} 6234 & 50 & -61 \\ 50 & 5400 & 958 \\ -61 & 958 & 8328 \end{bmatrix} kg\ m^2 \tag{3.1a}$$

$$I_{2,4} = \begin{bmatrix} 2 & 0 & 0 \\ 0 & 2 & 0 \\ 0 & 0 & 2 \end{bmatrix} kg\ m^2 \tag{3.1b}$$

$$I_{3,5} = \begin{bmatrix} 58.4 & -0.07 & -1.8 \\ -0.07 & 58.4 & 1.95 \\ -1.8 & 1.95 & 112 \end{bmatrix} kg\ m^2. \tag{3.1c}$$

The inertia tensor I_1 representing the spacecraft bus is taken directly from Shunli [1]. The inertia matrix for the inner gimbal (I_2) is a rough estimate based on the weight of the Tracking and Data Relay Satellite (TDRS) gimbal drive assembly of (4.2 pounds). The outer gimbal and antenna assembly is based off the mass of the TDRS antenna (217 pounds) and is modeled as a cylinder with a radius of 1.5m and a length of 0.5m [4]. The resulting matrix ($I_{3,5}$) is then rotated 2-degrees about each axis in order to introduce products of inertia (which inevitably exist in real-world systems).

Attitude control of the TDRS bus (B_1) is modeled as a pyramid array of four reaction wheels, $\tau_1 \in \mathbb{R}^4$, where the control torque about the respective bus axes ($\tau_{x,y,z}$) are calculated as,

$$Z = \begin{bmatrix} -a & a & a & -a \\ -a & -a & a & a \\ a & a & a & a \end{bmatrix}, \qquad a = \frac{1}{\sqrt{3}} \tag{3.2}$$

$$\tau_{x,y,z} = Z\tau_1.$$

The generalized coordinates for the complete system are then as follows: The quaternion $q = [q_1, q_2, q_3, q_4]$ describes the attitude of the root body, B_1, with attitude rates $\omega = [\omega_x, \omega_y, \omega_z]$. The generalized coordinates $x_L = [x_2, x_3, x_4, x_5]$ describe the orientation of the four links (B_{2-5}) while $x_G = [x_{G2}, x_{G3}, x_{G4}, x_{G5}]$ describe the gimbal motor angles. Figure 3.2 shows a generic schematic for B_{1-3} and the nature of the gimbal motor versus respective link states which are shown as coaxial for convenience, which need not be the case.

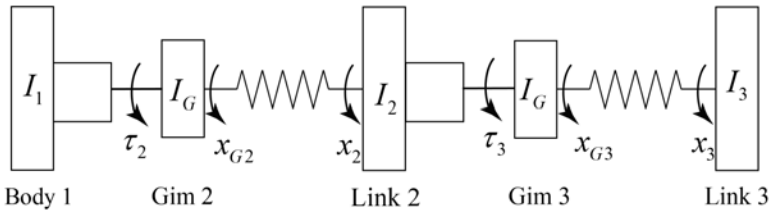

Figure 3.2: Generalized Schematic of a Flexible Two-link Arm Connected to Root Body (B_1)

Bus flexibility modeled by nine modal coordinates are denoted as η_{1-9}. with bus reaction wheel torques $\tau_1 = [\tau_{11}, \tau_{12}, \tau_{13}, \tau_{14}]$ and gimbal torques τ_{2-5}. The complete system is then composed of 41 states and 8 controls,

$$\begin{aligned} \boldsymbol{x} &= [q_1, q_2, q_3, q_4, x_L, x_G, \eta]^T \in \mathbb{R}^{21} \\ \dot{\boldsymbol{x}} &= [\omega, \dot{x}_L, \dot{x}_G, \dot{\eta}]^T \in \mathbb{R}^{20} \\ \boldsymbol{\tau} &= [\tau_1, \tau_2, \tau_3, \tau_4, \tau_5]^T \in \mathbb{R}^8. \end{aligned} \tag{3.3}$$

The modal frequencies and dynamic coupling terms shown in Table 3.1 and Equation (3.7) are modified from those used in [1, 2] while the remaining physical parameters in Table 3.2 are based on engineering judgement.

The general form of the full dynamics is shown in Equation (3.4) with symmetric mass matrix $\boldsymbol{M} \in \mathbb{R}^{20\times20}$, dynamics coupling matrix δ in Equation (3.7), gimbal inertia matrix I_G in Equation (3.6) and identity matrix $I \in \mathbb{R}^9$.

$$\boldsymbol{M}\ddot{x} = N(\dot{x}, x) + \tau \tag{3.4}$$

$$\boldsymbol{M} = \begin{bmatrix} M(x) & 0 & \delta \\ 0 & I_g & 0 \\ \delta^T & 0 & I \end{bmatrix}, \tag{3.5}$$

$$I_G = \begin{bmatrix} 200 & 0 & 0 & 0 \\ 0 & 200 & 0 & 0 \\ 0 & 0 & 200 & 0 \\ 0 & 0 & 0 & 200 \end{bmatrix} kg\ m^2 \tag{3.6}$$

$$\delta = \begin{bmatrix} 35 & 5 & 2.75 & 0 & 0 & 0 & 0 & 0 & 0 \\ 0 & 0 & 0 & 8.5 & 1.75 & 0.7 & 0 & 0 & 0 \\ 0 & 0 & 0 & 0 & 0 & 0 & 22.45 & 6.9 & 3.5 \end{bmatrix} kg\ m^2 \tag{3.7}$$

The rigid body mass matrix $M(x) \in \mathbb{R}^{7\times7}$ is shown in Equation (3.8) where the subscripts of M_{ij} denote the configuration dependent mass interaction of the i-th and j-th bodies.

$$M(x) = \begin{bmatrix} M_{11} & M_{12} & M_{13} & M_{14} & M_{15} \\ M_{21} & M_{22} & M_{23} & 0 & 0 \\ M_{31} & M_{32} & M_{33} & 0 & 0 \\ M_{41} & 0 & 0 & M_{44} & M_{45} \\ M_{51} & 0 & 0 & M_{54} & M_{55} \end{bmatrix} \tag{3.8}$$

where $M_{11} \in \mathbb{R}^{3x3}$, $M_{12,13,14,15} \in \mathbb{R}^{3x1}$, $M_{22,33,44,55} \in \mathbb{R}$ and $M_{23,45} \in \mathbb{R}$. Due to $M(x)$ being symmetric, $M_{ji} = M_{ij}^T$.

The parameters are then defined in a custom script and executed in the software package MotionGenesis generating the nonlinear dynamic equations via Kane's method. MotionGenesis is used to auto-code a Matlab function file containing the dynamic equations which is leveraged in further Matlab scripts to employ the Pseudospectral Methods (PSM). An excerpt of the five-body dynamics function file is included in the appendix for reference.

Table 3.1: Modal Parameters for Five-Body Model with Flexible Joint [Derived from[1, 2]]

Parameter	Description
$\zeta = 0.0025$	Modal damping ratios
$\dot{\omega}_{1-3} = (0.628, 4.398, 7.854) rad/sec$	X-modal frequencies
$\dot{\omega}_{4-6} = (0.942, 12.566, 31.416) rad/sec$	Y-modal frequencies
$\dot{\omega}_{7-9} = (1.571, 3.142, 6.283) rad/sec$	Z-modal frequencies

As discussed in Section 2.5, the natural frequencies of the modal variables are derived utilizing the Finite Element Method (FEM) and assumes a nominal gimbal angle. For a system such as TDRS exhibiting a large ratio of antenna to bus inertia, the frequency response of the bus can vary with SAA gimbal angle and solar array panel angle (which remains un-modeled). To measure the robustness of the derived optimal maneuvers,

Table 3.2: Parameters for Five-Body Model with Flexible Joint [Derived from[1, 3–5]]

Parameter	Description
$m_1 = 3,249kg$	B_1 mass
$m_{2,4} = 2kg$	$B_{2,4}$ mass
$m_{3,5} = 100kg$	$B_{3,5}$ mass
$r_{12} = [4, 0.1, 1.5]^T\ m$	B_1 CM to G_2
$r_{14} = [-4, 0.1, 1.5]^T\ m$	B_1 CM to G_4
$r_{22} = [0.05, 0.05, 0.05]^T\ m$	G_2 to B_2 CM
$r_{23} = [0.1, 0.05, 0.05]^T\ m$	B_2 CM to G_3
$r_{33} = [0.2, 0.05, 0.05]^T\ m$	G_3 to B_3 CM
$r_{44} = [-0.05, 0.05, 0.05]^T\ m$	G_4 to B_4 CM
$r_{45} = [-0.1, 0.05, 0.05]^T\ m$	B_4 CM to G_5
$r_{55} = [-0.2, 0.05, 0.05]^T\ m$	G_5 to B_5 CM
$[k, c] = [460Nm/rad, 117Nms/rad]$	Gimbal elastic coefficients
$\tau_1 = 1Nm$	B_1 Maximum Torque
$\tau_{2-5} = 0.23Nm$	G_{2-5} Maximum Torque

uncertainty is applied to 13 parameters for Monte Carlo simulations, and seven parameters for the robust optimal control problem formulations where the parameter vector p is defined as,

$$\begin{aligned} p &\approx \mathcal{N}(\bar{p}, \sigma^2) \\ p_{MC} &= [k_{2-5}, \omega_{1-9}] \\ p_{opt} &= [k_{2-5}, \omega_1, \omega_4, \omega_7] \\ \sigma_p^2 &= [0.2\bar{p}]^2 \end{aligned} \tag{3.9}$$

3.1.1 Optimal Control Model Dynamics.

All of the optimization results from Research Question (RQ) 1-4 are simulated against the full dynamic model detailed above. However, in order to reduce the number of states and decrease the computation time of the PSM, various reduced fidelity models were generated. Likin et al. [93] detailed a variety of methods that can be utilized to truncate modal coordinates for hybrid-coordinate method models. Additionally, further model truncations were implemented decreasing the number of rigid bodies included within the dynamics, further reducing the number of states in the optimal control problem formulation, but at the expense of reducing the optimality of the solutions when simulated against the complete model.

The five body optimal control model is based on truncating the two highest modal coordinates about each spacecraft bus axis such that only three modal coordinates are simulated. This reduced the total number of states from 41 to 29 as shown in Equation (3.10) while the dynamics coupling matrix is truncated accordingly as shown in Equation (3.11). Equation (3.5) remains unchanged in this problem formulation as it is dependent only on the rigid body states (x_L, x_G).

$$\begin{aligned} \boldsymbol{x} &= [q_1, q_2, q_3, q_4, x_2, x_3, x_4, x_5, x_{G2}, x_{G3}, x_{G4}, x_{G5}, \eta_1, \eta_4, \eta_7]^T \in \mathbb{R}^{15} \\ \dot{\boldsymbol{x}} &= [\omega_x, \omega_y, \omega_z, \dot{x}_2, \dot{x}_3, \dot{x}_4, \dot{x}_5, \dot{x}_{G2}, \dot{x}_{G3}, \dot{x}_{G4}, \dot{x}_{G5}, \dot{\eta}_1, \dot{\eta}_4, \dot{\eta}_7]^T \in \mathbb{R}^{14} \\ \boldsymbol{\tau} &= [\tau_1, \tau_2, \tau_3, \tau_4, \tau_5]^T \in \mathbb{R}^8. \end{aligned} \tag{3.10}$$

$$\delta = \begin{bmatrix} 35 & 0 & 0 \\ 0 & 8.5 & 0 \\ 0 & 0 & 22.45 \end{bmatrix} kg\ m^2 \tag{3.11}$$

3.1.2 Reduced Fidelity Models.

Utilizing historical methods of motion planning, each gimbal axis is modeled as a single, independent rigid body requiring only two states representing position and velocity

yielding a problem size of $x \in \mathbb{R}^2$ and where $u \in \mathbb{R}$. Utilizing the methods outlined in Section 2.5, the flexible five-body model of the TDRS spacecraft were developed incorporating additional states for joint and bus flexibility. As shown in Equation (4.3), this new problem formulation leads to a model with $x \in \mathbb{R}^{37}$, $u \in \mathbb{R}^8$. Assuming the RQ 1 problem is discretized utilizing 20 Legendre-Gauss-Lobatto (LGL) nodes, the resulting problem submitted to the Non-Linear Programming (NLP) solver Sparse Nonlinear Optimizer (SNOPT) yields 901 optimization variables and 827 constraints. The subsequent increase in problem size, while yielding significant improvement in maneuver performance, comes at the cost of computation time.

The computational burden is further complicated in Research Questions 2 and 3 which incorporate additional states for the implementation of the sensitivity and unscented optimal control methods. RQ 2 derived a sensitivity function for an uncertain parameter space of $p \in \mathbb{R}^7$, yielding a sensitivity state matrix $s \in \mathbb{R}^{N_x \times N_p}$, which for the problem considered herein results in 203 additional dynamic states. Again assuming 20 LGL nodes, the resulting desensitized optimal control problem results in 4961 optimization variables and 5090 constraints.

Another factor increasing the computation burden of the sensitivity based method for this analysis is the means by which the sensitivity dynamics are calculated, particularly the matrices $A(\cdot)$ and $B(\cdot)$ from Equation (2.32). For many systems previously considered, such as by Shaffer [39] and Seywald et al. [82], the considered dynamical equations are such that the partial derivatives of the dynamics with respect to the state variables and parameters can be calculated by hand and coded directly in software. For complex multi-body systems with highly nonlinear dynamics, the direct derivation of $A(s)$ and $B(s)$ may not be possible or practical. In this manuscript, the sensitivity matrices are calculated through perturbing the system dynamics. For a generic system defined by $\frac{dx}{dt} = f(x; p)$, where $\Delta x = x + \epsilon$ and

$\Delta p = p + \epsilon$ represent a small perturbation of $i-th$ element of x and p by ϵ, the $i-th$ column of $A(x; p)$ and $B(x; p)$ can be calculated as,

$$\begin{aligned} A_i(x; p) &= \frac{\partial f}{\partial x} = \frac{f(x : p) - f(\Delta x; p)}{\epsilon}, \quad \text{for: } i = 1, ..., N_x \\ B_i(x; p) &= \frac{\partial f}{\partial p} = \frac{f(x; p) - f(x; \Delta p)}{\epsilon}, \quad \text{for: } i = 1, ..., N_p. \end{aligned} \tag{3.12}$$

where ϵ is a sufficiently small perturbation where $\epsilon = 1e^{-8}$ is utilized for this analysis.

Calculating the sensitivity matrices in this manner removes the burden of deriving explicit equations for $A(\cdot)$ and $B(\cdot)$ but at the expense of an additional $N_x + N_p$ calculations of the system dynamics for each collocation point. Assuming 20 LGL nodes, the RQ 1 problem formulation is composed of 37 states requiring 20 evaluations of the system dynamics function each time an optimal trajectory is generated. For the desensitized optimal control problem considered in RQ 2, the computational space is increased to 240 states requiring 740 evaluations of the dynamics function for each trajectory calculation.

The parameter space of the unscented optimal control problem proposed in RQ 3 increases in a similar manner. Considering the uncertain parameters $p \in \mathbb{R}^7$, the unscented transform yields, $N_\Sigma = 2N_p + 1 = 15$, Σ-points requiring N_Σ independent trajectory calculations. This increases the number of optimization states from $N_x = 37 \rightarrow 443$ which for 20 LGL nodes requires 300 calls to the dynamics function. For the system concerned herein, the desensitized optimal control formulation contains less optimization variables, but requires more calls to the dynamics function as compared to the unscented optimal control method.

It should be noted that the limitation on the direct computation of the sensitivity function matrices is not inherent to the problem formulation or technique utilized to solve the proposed optimal control problem so much as a reflection of the tools and techniques available to the author. The flexible five-body dynamics represents approximately 500 lines of Matlab code which is auto-generated by MotionGenesis. To increase the computational

speed, the Matlab dynamics are then auto-coded into the C-language providing an order of magnitude decrease in computational time. MotionGenesis is also capable of deriving the sensitivity matrices symbolically, however the resultant file is 10,000 lines of code. Matlab is unable to auto-code this expanded dynamics file into C-code. Bench-marking was performed comparing the calculation of the matrices directly via the 10k line Matlab m-file, versus estimating the matrices utilizing the 500 line C-code. The matrices derived via Equation (3.12) provide significant improvements in computation time. This is more a reflection on the efficiency of C-code versus Matlab m-files than on the method of matrix derivation, so comparisons of computation time are somewhat hampered. It is assumed that given the appropriate mathematical tools and coding practices, this limitation can be overcome and the direct computation of the sensitivity matrices would yield improvements in computation time.

The results in Sections 4.2 and 4.3 demonstrated that both robust optimal control methods can be utilized to generate trajectories robust against parameter variations, albeit at increased computational compared to the standard maneuver. The objective of RQ 4 is then to determine how the methods leveraged in RQ 2-3 can be used with reduced order models as a means of deriving robust maneuvers but at a reduced computational cost. The complexity of the mathematical model exists on a continuum, where on one end is the single-body planning methods utilized for standard maneuver planning. The other end of the continuum could be a FEM model with 1000's of elements. In theory, assuming the model is accurate, the more complex the model, the more accurate and optimal the results. However, there is a computational cost for each additional included state and there exists a point of diminishing returns where performance improvements from an expanded model are outweighed by the increased computation time.

Research Question 4 explores utilizing a 3-body and 2-body models to derive SAA-2 maneuvers which are robust against parameter variations and still minimize impacts to

SAA-1 even though the corresponding SAA-1 bodies are no longer modeled as distinct states within the dynamics. For optimal maneuvers derived utilizing the five-body model, the dynamic interaction between each of the bodies is fully accounted for and the subsequent control profiles to ameliorate the interaction is incorporated into each bodies optimal control profile τ_{opt}. This negates the necessity of the bus controller incorporating counter-steering torques for the antenna maneuver into the bus feedforward control as shown in Equation (3.20).

3.1.2.1 Three Body Optimal Control Model.

The baseline maneuver simulated herein consists of a reorientation maneuver of SAA-2 while SAA-1 maintains nadir pointing, simulating providing communication services to a User Satellites (USAT). For the three body model, the SAA-1 dynamics are assumed to be neglected, or static, effectively fixing the associated degrees of freedom of bodies $B_{2,3}$ and gimbals $G_{2,3}$. Locking those four degrees of freedom can be accomplished by either removing the respective row/columns from $\boldsymbol{M}$ and the respective rows from $N(\cdot)$ in Equation (3.4), or using MotionGenesis, the dynamics can be re-derived where the locked degrees of freedom are changed from a variable to an assigned value. This effectively subsumes bodies $B_{2,3}$ into B_1 creating a new rigid-body $\bar{B}_1$ as shown in Figure 3.3.

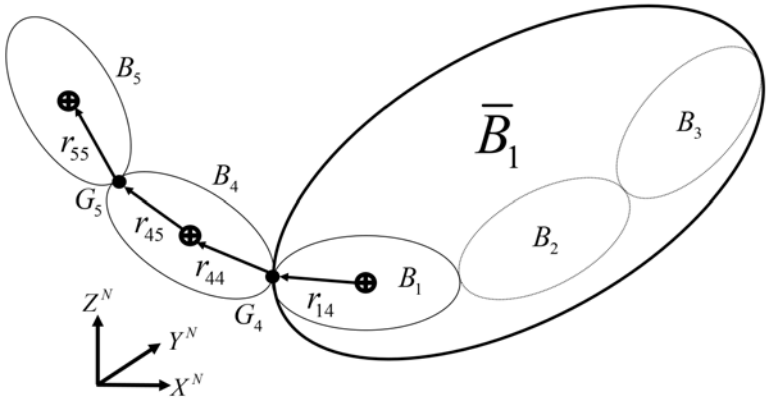

Figure 3.3: Generic Three Body System

This model reduction further reduces the number of optimization variables from 29 in the five body case to 21 for the three body case as shown in Equation (3.13), with a similar reduction in control variables from eight to six.

$$\begin{aligned} \boldsymbol{x} &= [q_1, q_2, q_3, q_4, x_4, x_5, x_{G4}, x_{G5}, \eta_1, \eta_4, \eta_7]^T \in \mathbb{R}^{11} \\ \dot{\boldsymbol{x}} &= [\omega_x, \omega_y, \omega_z, \dot{x}_4, \dot{x}_5, \dot{x}_{G4}, \dot{x}_{G5}, \dot{\eta}_1, \dot{\eta}_4, \dot{\eta}_7]^T \in \mathbb{R}^{10} \\ \boldsymbol{\tau} &= [\tau_1, \tau_4, \tau_5]^T \in \mathbb{R}^6. \end{aligned} \tag{3.13}$$

The results of this model reduction is that optimal feedforward control profiles for SAA-1 are not computed, increasing the reliance on feedback control to maintain antenna pointing. Similarly, the optimal bus control profiles are calculated assuming a static SAA-1, which need not be the case.

3.1.2.2 Two Body Optimal Control Model.

While the three body model detail in Section 3.1.2.1 incorporates the spacecraft bus as a free-floating body in inertial space, the two body model makes the further reduction of truncating the model at gimbal 4 (G_4) and assumed G_4 is translationally fixed in inertial space while allowing rotation about its respective x-axis as shown in Figure 3.4. This results in a further reduction to 14 states and two control variables as seen in Equation (3.14).

$$\begin{aligned} \boldsymbol{x} &= [x_4, x_5, x_{G4}, x_{G5}, \eta_1, \eta_4, \eta_7]^T \in \mathbb{R}^7 \\ \dot{\boldsymbol{x}} &= [\dot{x}_4, \dot{x}_5, \dot{x}_{G4}, \dot{x}_{G5}, \dot{\eta}_1, \dot{\eta}_4, \dot{\eta}_7]^T \in \mathbb{R}^7 \\ \boldsymbol{\tau} &= [\tau_4, \tau_5]^T \in \mathbb{R}^2. \end{aligned} \tag{3.14}$$

A core objective of this research is to derive maneuvers that simultaneously reduce maneuver time while accounting for system flexibility and minimizing vibrational excitation. After the initial truncation of B_1, the flexibility of the remaining gimbals is still accounted for, but the dynamic interaction between the bus and modal variables (η) has

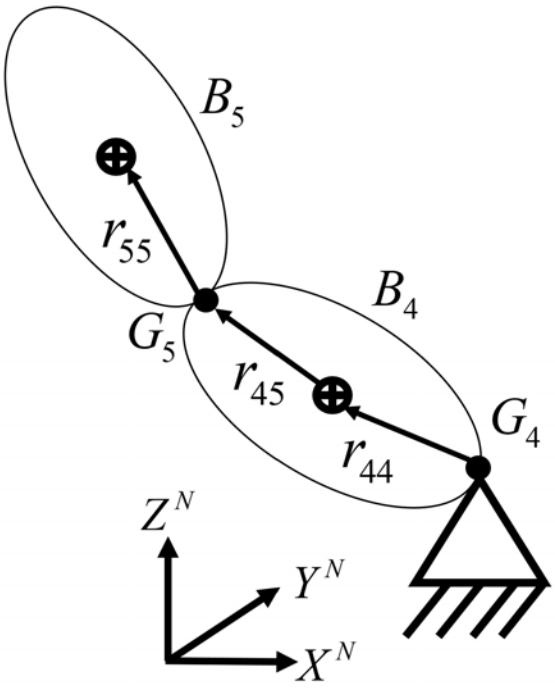

Figure 3.4: Generic Two Body System

been eliminated. To provide a measure of the bus excitation due to the antenna maneuver, an estimation of the bus acceleration must be reintroduced.

Defining $\bar{x}$ as the nominal system configuration at the start of the maneuver, $\bar{M}(\bar{x})$ is the system mass matrix from Equation (3.8). Taking the inverse of $\bar{M}$ and extracting the appropriate sub-elements relating to $B_{1,4,5}$, the bus acceleration due to SAA motion can be estimated as,

$$\dot{\omega}_1 \approx \begin{bmatrix} \bar{M}_{14}^{-1} & \bar{M}_{15}^{-1} \end{bmatrix} \begin{bmatrix} \ddot{x}_4 \\ \ddot{x}_5 \end{bmatrix}. \tag{3.15}$$

Denoting the sub-elements of the inverse mass matrix from Equation (3.15) as $\bar{M}^{-1}$, the two body dynamics can now be represented as,

$$\begin{bmatrix} M(x) & 0 & 0 \\ 0 & I_g & 0 \\ \delta\bar{M}^{-1} & 0 & I \end{bmatrix} \begin{bmatrix} \ddot{x}_L \\ \ddot{x}_G \\ \ddot{\eta} \end{bmatrix} = \begin{bmatrix} N_L(\dot{x}, x) \\ N_G(\dot{x}, x, \tau) \\ N_\eta(\dot{x}, x) \end{bmatrix}, \tag{3.16}$$

where $x_L = [x_4, x_5]^T$ and $x_G = [x_{G4}, x_{G5}]^T$. This estimation of bus acceleration due to gimbal maneuvers then drives the modal dynamics. In the five and three body models, the modal coordinates are an integral part of the system dynamics with the rigid body and modal coordinates coupled together through the matrix δ. In the two body model, the coupling between the modal coordinates and the rigid body states has been eliminated, however, the excitation of the modal coordinates as shown in Equation (3.16) provides a measure of vibrational excitation, without the computational burden of modeling the root body. These states can still be leveraged in the optimal control cost functional as a means of quantifying bus vibrational excitation due to the antenna maneuver.

3.2 Standard Maneuver Planning

To quantify the performance improvements possible utilizing the robust optimal control techniques contained herein, a standard maneuver must be designed and simulated. For a standard TDRS antenna maneuver, each linkage is treated as an independent, decoupled system with motion planned using kinematic principles and second-order feedforward planning is utilized to generate the point-to-point trajectories defined by,

$$\bar{M}_{ii}\ddot{x}_i = \tau_i, \quad i = 1, ..., 4. \tag{3.17}$$

where assuming a nominal gimbal configuration ($\bar{x}$), the linkage mass ($\bar{M}_{ii} = M(\bar{x})$) is the diagonal element for the i-th row of the mass matrix from Equation (3.8). This second-order planning results in a three phase trajectory composed of an acceleration phase, a constant rate phase (coast phase), and a deceleration phase.

Due to the simplified nature of the trajectory planning model, variability in joint stiffness and structural frequency response are un-modeled and cannot be minimized directly. As such, dynamic nonlinearities and coupling between motion axes enter the system as disturbance torques to be ameliorated by the controller. To reduce these disturbance magnitudes, artificial "soft" constraints are placed on maximum acceleration ($\hat{a}$) and velocity ($\hat{v}$) during trajectory planning. These constraints are not necessarily based on hardware limitations, but arise due to limitations in maneuver planning model fidelity. For example, the two-axis antenna trajectory of a TDRS SAA is rate limited to $\hat{v} = 0.25$ deg/s leading to a 5 second acceleration and deceleration phases. These conservative planning principles lead to slew times of up to 2 minutes for large maneuvers during which the SAA is not providing communication services [3, 94].

Given a desired change in slew angle (Δx), with maximum allowable velocity ($\hat{v}$) and acceleration ($\hat{a}$), the acceleration/deceleration time interval is calculated as $t_a = \sqrt{\Delta x/\hat{a}}$ where the maximum velocity obtained is $v_{max} = \hat{a} \cdot t_a$. From these maximum accelerations and rates, the distance covered during the acceleration/deceleration phases is calculated at $x_a = \hat{a}t_a^2$ and the coast phase time can then be calculated as $t_c = (\Delta x - x_a)/\hat{v}$. Defining x_0 as the initial gimbal angle, the desired trajectory is defined by,

$$t_{\Delta x} = 2t_a + t_c, \quad x_{Des} = \hat{a}t_a^2 + \hat{v}t_v + x_0. \tag{3.18}$$

This planning is performed for each gimbal joint independently. The joint with the longest slew duration is denoted as the "major" axis the shorter maneuver the "minor" axis. The maximum acceleration and velocity of the minor axis is then adjusted so as to complete its maneuver simultaneously with the major axis.

In this manner, system flexibility is partially mitigated through conservative upper bounds on joint velocities. These bounds reduce the magnitude of coupling between

axes and disturbance torques while acceleration/torque constraints ensure sufficient control authority within the compensator to counteract the disturbances.

Once the desired acceleration trajectories are calculated for each body, the feedforward control torques can be calculated by,

$$\begin{bmatrix} \tau_{x,y,z} \\ \tau_2 \\ \tau_3 \\ \tau_4 \\ \tau_5, \end{bmatrix} = \begin{bmatrix} \bar{M}_{11} & \bar{M}_{12} & \bar{M}_{13} & \bar{M}_{14} & \bar{M}_{15} \\ \bar{M}_{21} & \bar{M}_{22} & \bar{M}_{23} & 0 & 0 \\ \bar{M}_{31} & \bar{M}_{32} & \bar{M}_{33} & 0 & 0 \\ \bar{M}_{41} & 0 & 0 & \bar{M}_{44} & \bar{M}_{45} \\ \bar{M}_{51} & 0 & 0 & \bar{M}_{54} & \bar{M}_{55} \end{bmatrix} \begin{bmatrix} \dot{\omega}^{Des} \\ \ddot{x}_2^{Des} \\ \ddot{x}_3^{Des} \\ \ddot{x}_4^{Des} \\ \ddot{x}_5^{Des} \end{bmatrix}. \tag{3.19}$$

While each gimbal trajectory is planned independently, by utilizing the linearized mass matrix ($\bar{M}$) to calculate the system control inputs, a counteracting torque is applied to the spacecraft bus based on the estimation of the reaction torque from the antenna slew maneuver. For example, the counter-steering torque component (τ_{cs}) of $\tau_{x,y,z}$ necessary to maintain $\dot{\omega}^{Des}$ due to the SAA-1/2 maneuvers is,

$$\tau_{cs} = \begin{bmatrix} \bar{M}_{12} & \bar{M}_{13} & \bar{M}_{14} & \bar{M}_{15} \end{bmatrix} \begin{bmatrix} \ddot{x}_2^{Des} \\ \ddot{x}_3^{Des} \\ \ddot{x}_4^{Des} \\ \ddot{x}_5^{Des} \end{bmatrix}. \tag{3.20}$$

3.3 Simulation Environment and Control System

The control system utilized in this manuscript is based on independent joint control where each rotational axis is treated as an independent Single-Input-Single-Output (SISO) system, which is a common method of control for many space-borne systems due to its simplicity, ease of design, and space flight heritage [16]. This method allows the attitude control of each appendage to be designed completely independent of one another. To

analyze the system, the portion of Equation (3.4) relating to the rigid-body dynamics is extracted and partitioned as,

$$\begin{bmatrix} \bar{M}_{11} & \bar{M}_{12} & \bar{M}_{13} & \bar{M}_{14} & \bar{M}_{15} \\ \bar{M}_{21} & \bar{M}_{22} & \bar{M}_{23} & 0 & 0 \\ \bar{M}_{31} & \bar{M}_{32} & \bar{M}_{33} & 0 & 0 \\ \bar{M}_{41} & 0 & 0 & \bar{M}_{44} & \bar{M}_{45} \\ \bar{M}_{51} & 0 & 0 & \bar{M}_{54} & \bar{M}_{55} \end{bmatrix} \begin{bmatrix} \dot{\omega} \\ \ddot{x}_2 \\ \ddot{x}_3 \\ \ddot{x}_4 \\ \ddot{x}_5 \end{bmatrix} = \begin{bmatrix} N_1(x, \dot{x}) \\ N_2(x, \dot{x}) \\ N_3(x, \dot{x}) \\ N_4(x, \dot{x}) \\ N_5(x, \dot{x}) \end{bmatrix} + \begin{bmatrix} \tau_1 \\ \tau_2 \\ \tau_3 \\ \tau_4 \\ \tau_5 \end{bmatrix} \tag{3.21}$$

where $\bar{M} = M(\bar{x})$ is the configuration dependent mass matrix computed about nominal system configuration $\bar{x}$ and the matrix/vector subscripts refer to the rigid body number from Figure 3.1. A generalized block diagram for such a system is shown in Figure 3.5 utilizing a Proportional Derivative (PD) controller for each channel with proportional gain K_p, derivative gain K_D, and narrowband notch filter N_f.

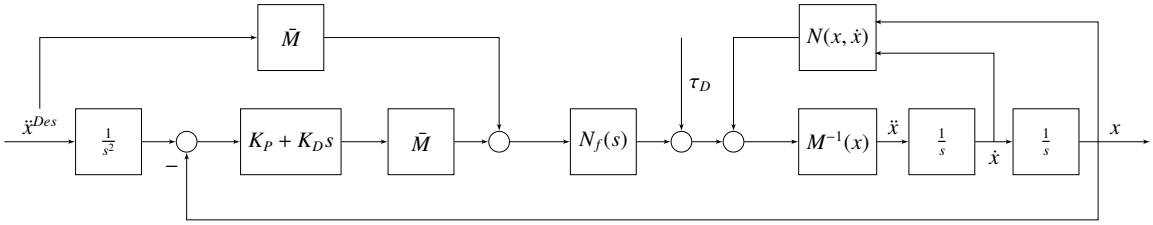

Figure 3.5: Generalized Controller for Standard Maneuvers

For multi-aperture satellites with fine pointing requirements, it is necessary to ensure the movement of one aperture does not negatively impact adjacent aperture pointing which can arise due to unintended excitation of spacecraft vibrational modes. To minimize these impacts, the simulation further employs a bank of notch filters. For $i = 1, ..., N_q$ frequencies to be filtered, the narrowband notch filter is defined as,

$$
\begin{aligned}
Q(\omega, \zeta) &= s^2 + 2\zeta\omega s + \omega^2 \\
N_f(s)_i &= \prod \frac{Q(\omega_i, \zeta_i)}{Q(\omega_i, 0.2)},
\end{aligned}
\tag{3.22}
$$

where ω is the frequency of the filter in rad/s and ζ is the damping ratio [3]. For the five-body model considered herein, $N_q = 9$ modal frequencies are included where modes $i = 1, 4, 7$ represent the lowest frequency modes about the x, y, and z axes respectively of the root body (B_1). The corresponding damping ratios for Equation (3.22) are then,

$$
\zeta_i = \begin{cases} 0.005, & i = 1, 4, 7 \\ 0.01, & \text{otherwise.} \end{cases}
\tag{3.23}
$$

By modeling and leveraging system flexibility directly in the optimal control problem formulation, the derived optimal control trajectories are such that system modes can be suppressed without necessitating the use of notch filters. As such, for simulation of results derived from PSM, optimal control profiles (τ_{opt}) are fed directly into the model plant as shown in Figure 3.6, bypassing the notch filter utilized by the standard maneuver.

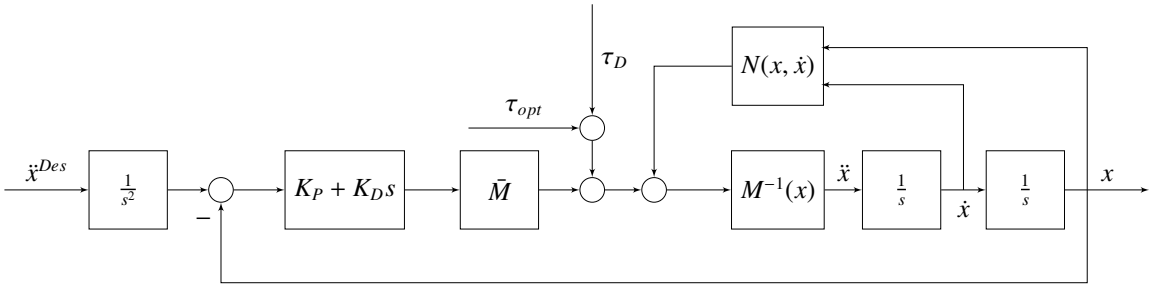

Figure 3.6: Generalized Controller for Optimal Maneuvers

Figure 3.7 provides further breakout of the controller portion responsible for SAA-2 and bus control for a standard maneuver, where the SAA-1 control loops have been omitted for brevity. This diagram demonstrates that each gimbal control channel experiences a

configuration dependent loop gain ($\bar{M}M(x)$) as well as a time-varying disturbance input ($N(x, \dot{x})$) whose overall magnitude depends on the nonlinear coupling terms. The effects of these nonlinear and configuration dependent terms must be ameliorated by the controller by allocating a sufficient portion of torque for feedback control, versus feedforward control.

The simulation model used herein contains two sets of controller gains for the SAA controllers; a high-gain mode and a low-gain mode (Table 3.3). For the standard maneuver, high-gain mode is utilized for any antenna in an Auto Track (AT) mode, where it is providing communication services to a USAT. In Program Track (PT) mode, when an antenna is transitioning between USAT, the controller is switched into a low-gain mode to avoid exciting unwanted system excitation. If a PT antenna's controller is operated in high-gain mode during a standard maneuver, as will be shown later, unwanted affects due to the configuration dependent loop gain and nonlinear effects increase the total energy in the system and lead to longer settling times. In contrast, for optimal maneuvers, the antenna in PT mode is controlled using the high-gain mode with little impact, because the nonlinear and configuration dependent nature of the maneuvers is accounted for in the optimal control profile.

Table 3.3: Single Access Antenna PD Controller Gains

	High Gain		Low Gain	
Gimbal	Inner	Outer	Inner	Outer
K_P	10.1	9.92	1.1	1.09
K_D	90	89.2	30	29.7

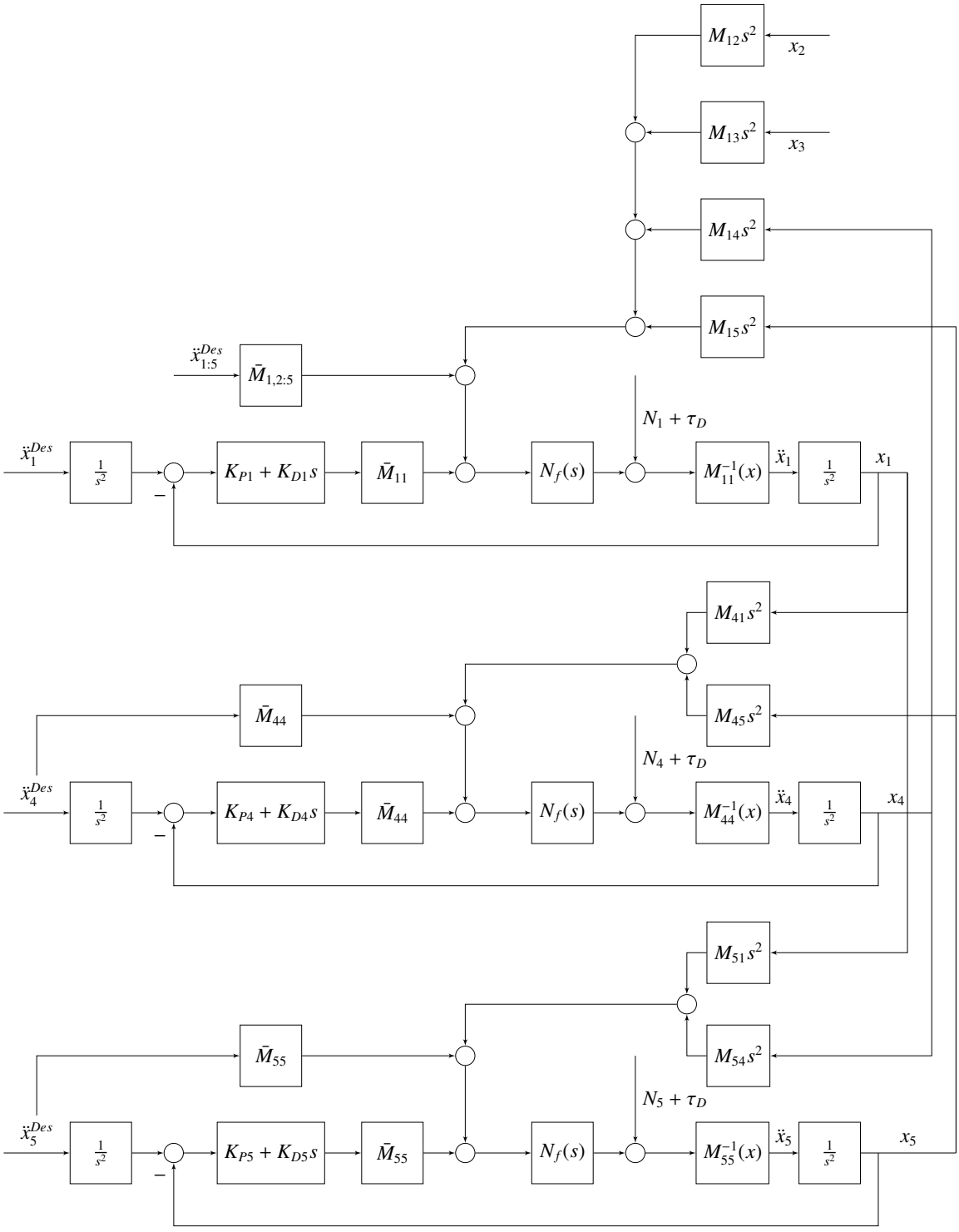

Figure 3.7: Block Diagram for Independent Joint Control of Bus and SAA-2 for Standard Maneuver

3.3.1 System Performance Measures.

There are multiple measures that will be utilized in this manuscript to compare the relative performance of the various maneuvers. As one of the driving objectives of this research is to increase payload availability through decreased slew durations, the final maneuver time (t_f) is a primary measures.

Particularly when simulated open-loop, the final pointing error of the bus and payloads is important, as the larger the terminal pointing error, the longer the respective pull-in maneuver will be, further decreasing the amount of time the payload is not performing mission. The bus pointing error is derived from error quaternion, where given a commanded attitude quaternion $q_c = [q_{1c}, q_{2c}, q_{3c}, q_{4c}]$ and current attitude $q = [q_1, q_2, q_3, q_4]$, the error quaternion (q_e) and Body 1 pointing error θ_1^{err} are calculated by,

$$\begin{bmatrix} q_{1e} \\ q_{2e} \\ q_{3e} \\ q_{4e} \end{bmatrix} = \begin{bmatrix} q_{4c} & q_{3c} & -q_{2c} & -q_{1c} \\ -q_{3c} & q_{4c} & q_{1c} & -q_{2c} \\ q_{2c} & -q_{1c} & q_{4c} & -q_{3c} \\ q_{1c} & q_{2c} & -q_{3c} & -q_{4c} \end{bmatrix} \begin{bmatrix} q_1 \\ q_2 \\ q_3 \\ q_4 \end{bmatrix} \tag{3.24}$$

$$\theta_1^{err} = 2cos^{-1}(q_{4e})$$

Similarly, another important measure is the pointing error for each of the payloads at maneuver termination. Defining the antenna boresight in the outer body frame (B_o) as $v = [0, 0, 1]^T$, and a rotation matrix from the outer link frame to the inertial frame (N) as ${}^N C^{B_o}$, the angular pointing error (θ^{err}) between the actual (v^N) and desired boresight (v_{Des}^N) for Body i is computed as,

$$\begin{aligned} v_{Des}^N &= {}^N C^{B_o}(x_{Des})[0, 0, 1]^T \\ v^N &= {}^N C^{B_o}(x)[0, 0, 1]^T \\ \theta_i^{err} &= atan\left(\frac{\|v_{Des}^N \times v^N\|}{v_{Des}^N \cdot v^N}\right). \end{aligned} \tag{3.25}$$

Due to the rotation matrix ${}^{N}C^{B_o}$ being dependent on the bus attitude, Equation (3.25) ensures the payload pointing error calculation encompasses any bus pointing errors, which should nominally remain nadir pointing.

A further measure of maneuver performance is the amount of control necessary to achieve the desired maneuver, defined as the control cost,

$$F_u(x,t) = \int_0^{t_f} u^T u \, dt. \tag{3.26}$$

Another important measure of maneuver optimality is the total energy in the system at maneuver completion. For flexible systems such as TDRS, ensuring the system vibrational modes are not "rung up" during an antenna maneuver is of upmost importance, and is a primary goal of this research. The Total Energy (TE) in the system is then the sum of Kinetic Energy (KE) and Potential Energy (PE) calculated as,

$$\begin{aligned} TE &= KE + PE \\ KE &= \frac{1}{2}\left([\omega, \dot{x_L}]M[\omega, \dot{x_L}]^T + \dot{x_G} I_G \dot{x_G} + \dot{\eta}^T \dot{\eta}\right) \\ PE &= \frac{1}{2}\left((x_L - x_G)^T K (x_L - x_G) + \eta^T \Omega^2 \eta\right) \end{aligned} \tag{3.27}$$

where M is the mass matrix from Equation (2.64), I_G is the diagonal matrix of gimbal inertia (Equation (3.6)), K is a diagonal matrix of the gimbal spring coefficients, Ω is a diagonal matrix of modal frequencies, KE: $\mathbb{R}^{N_x+N_\eta} \mapsto \mathbb{R}$, PE: $\mathbb{R}^{N_G+N_\eta} \mapsto \mathbb{R}$. The kinetic energy is then composed of the rigid body, gimbal, and modal components, while the potential energy is composed of the elastic energy storage of the gimbal joints as well as the modal coordinate component. The Modal Energy (ME) can then be calculated as the components of Equation (3.27) arising from the modal variables (η) as,

$$ME = \frac{1}{2}(\eta^T \Omega^2 \eta + \dot{\eta}^T \dot{\eta}), \tag{3.28}$$

where ME: $\mathbb{R}^{N_\eta} \mapsto \mathbb{R}$. The ME provides a means of quantifying the vibrational energy in the root body arising during maneuver execution which nominally should be maintained as low as possible.

3.4 Baseline Maneuvers

In order to provide a baseline with which to compare the optimal maneuvers generating in RQ 1-4, a standard maneuver was selected and simulated using traditional motion planning principles. The simulated antenna maneuver selected from Schmeichel et al. [4] represents a SAA-2 maneuver from 0 to -20 degrees in azimuth and 0 to 19 degrees in elevation. SAA-1 is assumed to maintain target pointing at a USAT located at (0,0) degrees in azimuth/elevation. The objective is to perform a slew maneuver of SAA-2 while minimizing the impacts to SAA-1 which is attempting to maintain the fine pointing requirements. For this maneuver, all other initial and final conditions are identically zero. The initial conditions and desired final conditions are then $x_L^0 = x_G^0 = [0, 0, 0, 0]^T$ and $x_L^F = x_G^F = [0, 0, 19, -20]^T$. This will be referred to as Case 1.

3.4.1 Case 1: Standard Maneuver Planning.

The Case 1 standard maneuver was planned in accordance with Equation (3.18) resulting in the three-phase, second-order trajectory as seen in Figure 3.8. The SAA-2 trajectory has a 5 second acceleration phase up to the maximum allowable gimbal velocity of 0.25 deg/s, a subsequent constant rate phase followed by a deceleration phase. Due to the "soft" constraint on maximum gimbal velocity, the resulting maneuver has a planned completion of 83.4 seconds and was simulated open loop against the model out outlined in Section 3.1.

The resulting bus trajectory is shown in Figure 3.9, where the quaternion has been converted into Euler angles $[\phi, \theta, \psi]$ representative of a Body-321 rotation. In accordance with Equation (3.19), counter-steering torques are applied to the bus to attempt to maintain

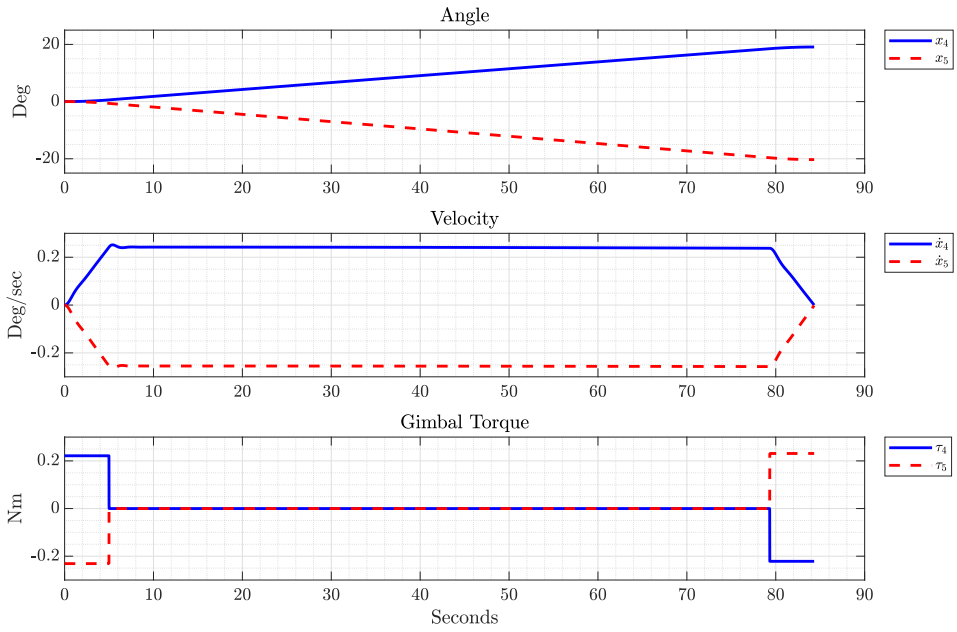

Figure 3.8: Case 1 Open-loop Baseline Maneuver: SAA-2 States and Control

the desired orientation, assuming a stationary bus of $\omega^{Des} = [0, 0, 0]$. The bus counter-steering torques necessary to compensate for the antenna maneuver are then,

$$\tau_1 = Z^{-1} \begin{bmatrix} \bar{M}_{14} & \bar{M}_{15} \end{bmatrix} \begin{bmatrix} \ddot{x}_4^{Des} \\ \ddot{x}_5^{Des} \end{bmatrix},$$

where Z^{-1} is the Moore-Penrose inverse of matrix Z from Equation (3.2). Figure 3.9 shows that even accounting for the antenna maneuver with pre-calculated bus counter-steering torques, the maneuver still exhibits 0.065 degrees of bus pointing error due to the counter-steering controls being calculated based on a linearization of the nonlinear dynamics and not evolving in time as the gimbal orientation changes the system inertia properties. Similarly, the perturbation of the bus attitude due to the SAA-2 maneuver couples into SAA-1 as seen in Figure 3.10, exhibiting a final pointing error of 0.026 degrees.

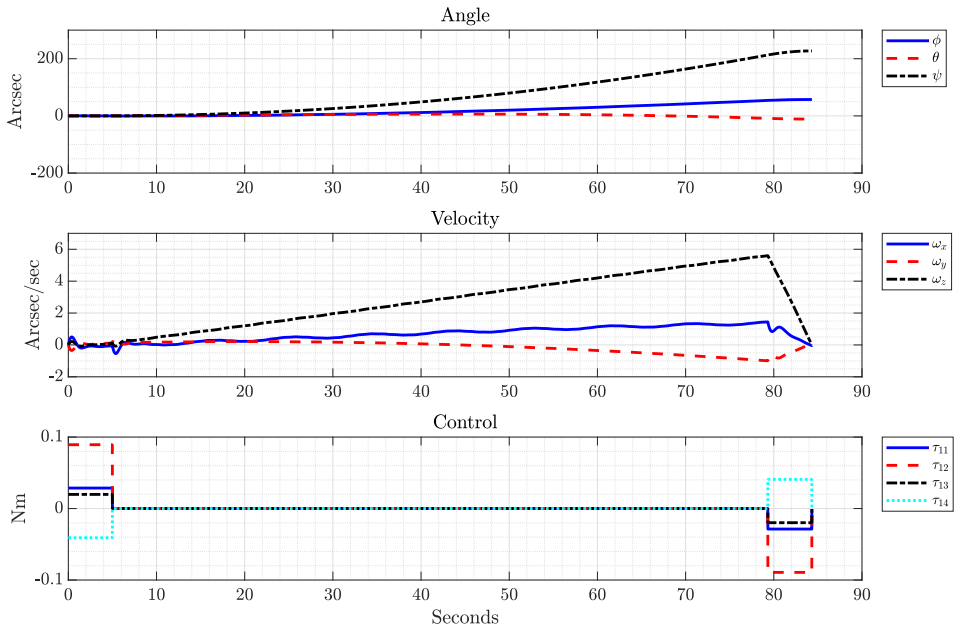

Figure 3.9: Case 1 Open-loop Baseline Maneuver: Bus States and Control

The standard maneuver was simulated a second time with the notch filter outlined in Equation (3.22) enabled and is denoted as Case 1a, with the summary results for both open-loop maneuvers shown in Table 3.4. Figures 3.11 and 3.12 show the time histories of the three primary modal coordinates about the x/y/z axes of the spacecraft bus ($\eta_{1,4,7}$) for Cases 1 and 1a, showing the impact notch filtering the control trajectory has on the excitation of the modes. Without notch filtering, the maximum magnitude of the modal variables η is $\approx$ 42 arcseconds while the notch filter decreases the maximum value to $\approx$ 25 arcseconds.

These results demonstrate the notch filter reduces the modal energy by 63.4% but at the expense of a three orders of magnitude increase in total system energy. The increase in total energy is due to residual velocity in SAA-2, so while the pointing error at maneuver termination is lower for the notch solution, in operations, further control is necessary in order for the payload to begin its mission. The pull-in time necessary to counteract the

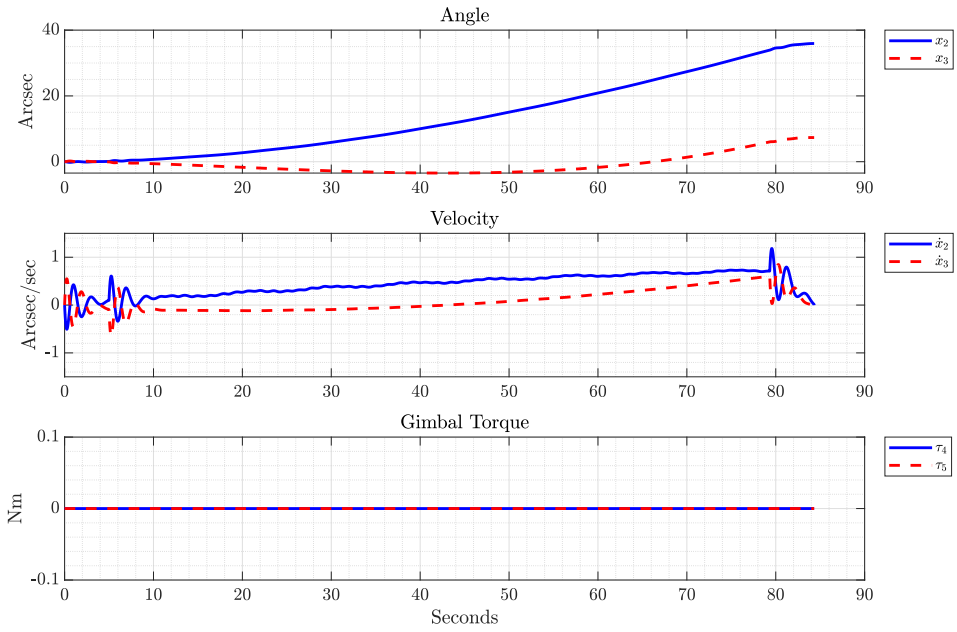

Figure 3.10: Case 1 Open-loop Baseline Maneuver: SAA-1 States and Control

Table 3.4: Case 1 Open-Loop Simulation Results for Standard Maneuver with and without Notch Filtering

			Error (deg)			Energy (J)		Control
Case #	Filter	t_f (s)	Bus	SAA-1	SAA-2	Total	Modal	Cost
1	n/a	84.3	0.065	0.026	0.32	6.7e-6	1.9e-8	1.024
1a	Notch	84.3	0.064	0.026	0.19	1.3e-3	6.9e-9	0.557

additional gimbal velocity serves to increase the length of time the antenna is not in mission, further reducing payload operational availability.

To illustrate this point, Cases 1 and 1a are simulated closed-loop. The convergence time for each maneuver is measured, where pointing convergence corresponds to the amount of time it takes to achieve antenna pointing error of less than 0.02 degrees while the

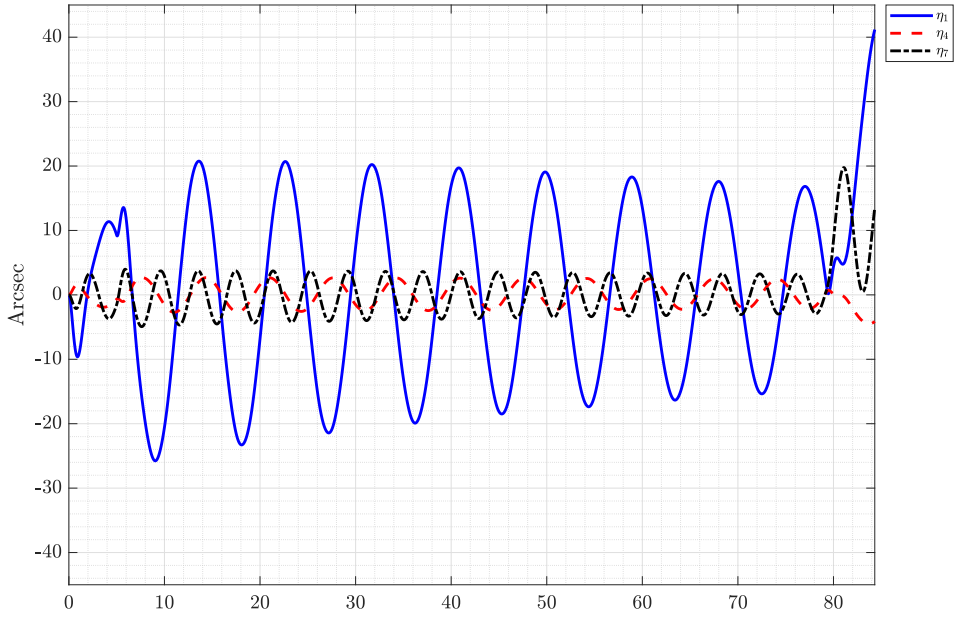

Figure 3.11: Case 1 Open-loop Baseline Maneuver: Primary Modal States about the B_1 x/y/z Axes

total system energy convergence time is is taken when total system energy remains below $1x10^{-7}$ joules. A value of "––" denotes the respective measure always being within the convergence tolerance.

Table 3.5: Case 1 Close-Loop Convergence Results for Standard Maneuver with and without Notch Filtering

			Convergence Time (s)			
Case #	Filter	Gain	Bus	SAA-1	SAA-2	Total Energy
1	n/a	Low	86.0	–	84.4	250.3
1a	Notch	Low	89.3	–	131.6	145.2
1b	Notch	High	89.72	–	109.3	421.5

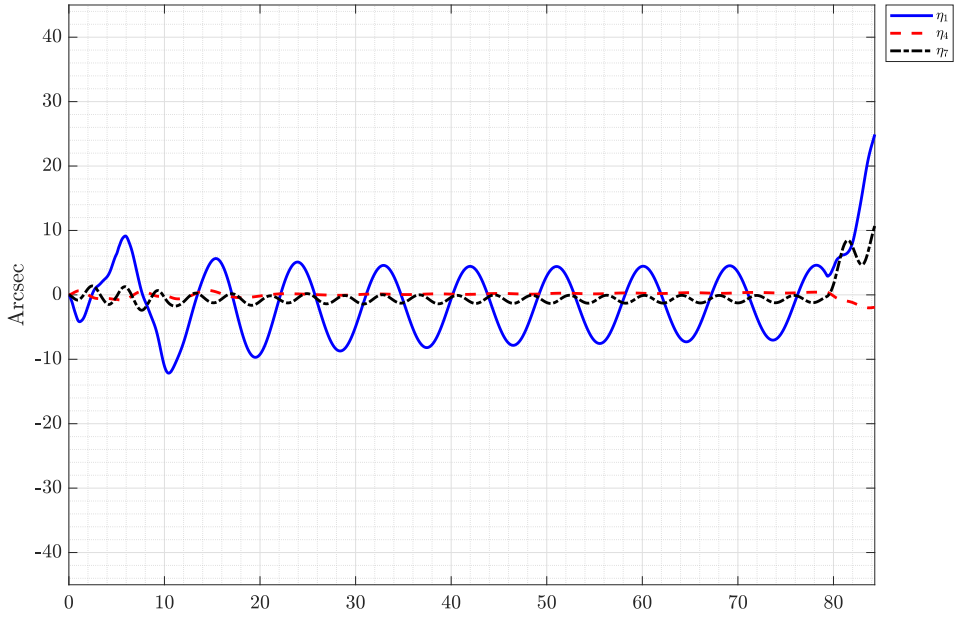

Figure 3.12: Case 1 Open-loop Baseline Maneuver with Notch Filter: Primary Modal States about the B_1 x/y/z Axes

The results for both simulations are shown in Table 3.5 demonstrating the standard maneuver without notch filtering achieving SAA-2 pointing convergence in 84.4 seconds, but due to excitation of the spacecraft vibrational modes, it takes 250 seconds for the vibration to damp out. Conversely, the notch filtered only takes 145 seconds for the vibrational energy to converge to acceptable levels, but the pointing error doesn't converge for 131.6 seconds. In neither case does the pointing error of SAA-1 exceed 0.02 degrees, indicating the SAA-2 maneuver has negligible impact to SAA-1 pointing. It should be noted that a convergence time for the satellite is not necessarily indicative of a poorly performing maneuver, so long as there is no corresponding convergence issues for SAA-1. The standard maneuvers all exhibit bus pointing errors in excess of 0.02 degrees, albeit with no impact to SAA-1 pointing performance.

Table 3.5 also includes results for a third case, Case 1b, which is identical to Case 1a except the SAA-2 controller is operated in high-gain mode from Table 3.3. While the SAA-2 pointing convergence is decreased by 17%, the energy convergence time is increased by 190%, demonstrating that increasing controller bandwidth for the standard maneuver can amplify unwanted system excitations.

For the subsequent analysis of the optimal maneuvers, Case 1a is utilized as the baseline with which all performance metrics are compared. Case 1a represents standard, one-body maneuver planning, utilizing notch filtering of the control profiles to reduce unwanted excitation, with all closed-loop analysis performed with both antenna controllers in low-gain mode.

These cases illustrates the trade-off of standard maneuver design practices. Using simplified one-body planning necessitates the enforcement of conservative "soft" constraints in order to minimize the magnitude of unwanted interaction between antenna gimbals, the bus, and neighboring apertures. The conservatism leads to long maneuver times and excessive system excitation reducing payload availability. Notch filters can be applied within the control system to reduce system excitation, but comes at the expense of increased antenna pointing error and additional settling time. This then presents a trade-off between controller gain, which can be increased to improve antenna settling time, but can have an adverse effect on system energy and amplify vibrational modes.

Notch filtering, much like the use of trajectory shaping, can be successful at decreasing system excitation, but comes at the expense of maneuver length. Neither filtering or input shaping techniques provide a framework for addressing the negative impacts arising due to system flexibility while simultaneously decreasing maneuver length. The shortcomings of these techniques leads to the desire of utilizing optimization techniques to derive maneuvers which increase payload availability.

3.4.2 Case 2: Minimum-Time Maneuver with Rigid Body Assumptions.

One method of increasing system performance through reduced maneuver time is the use of PSM to solve minimum-time optimal control problems. The intent of Case 2 is to demonstrate the impact of solving such a problem using rigid body assumptions for highly flexible systems. While the "soft" constraints of maximum gimbal velocity are eliminated from this problem formulation, the underlying issue of system flexibility is un-modeled and thus not constrained during maneuver planning.

By setting $\delta = [0]$ and $k_i, c_i \rightarrow \infty$, for $i = 1, ..., N_G$, the flexible dynamics from Equation (2.64) reduce to rigid-body dynamical equations from Equation (2.58). A minimum-time optimal control problem can be formulated as,

Given:

$$\boldsymbol{x} = [q_1, q_2, q_3, q_4, x_2, x_3, x_4, x_5, \omega_x, \omega_y, \omega_z, \dot{x}_2, \dot{x}_3, \dot{x}_4, \dot{x}_5]^T \in \mathbb{R}^{15}$$
$$\boldsymbol{\tau} = [\tau_1, \tau_2, \tau_3, \tau_4, \tau_5]^T \in \mathbb{R}^8.$$

$$\begin{aligned} \text{minimize} \quad & J = t_f \\ \text{subject to} \quad & 0 = \dot{x}(t) - f(x(t), u(t)), \\ & x_L^0 = [0, 0, 0, 0] deg, \\ & x_L^f = [0, 0, 19, -20] deg, \\ & |\tau_1| \leq 1 \; Nm, \\ & |\tau_{2-5}| \leq 0.23 \; Nm, \\ & h(x, t) \leq 0.02 \; deg, \\ & 0 \leq t \leq 84.3 \; s \end{aligned} \tag{3.29}$$

where $h(x, t)$ is a path constraint associated with the pointing error of the SAA-1 in inertial space using Equation (3.25). While the standard maneuver trajectory takes 84.3 seconds, the minimum-time maneuver, rigid-body maneuver takes 42.6 seconds to achieve

the desired antenna pointing objective. The resulting state and control trajectories for the bus and SAA-1/2 are shown in Figure 3.13 and Figure 3.14, while the terminal open-loop pointing error and terminal energies are shown in Table 3.6.

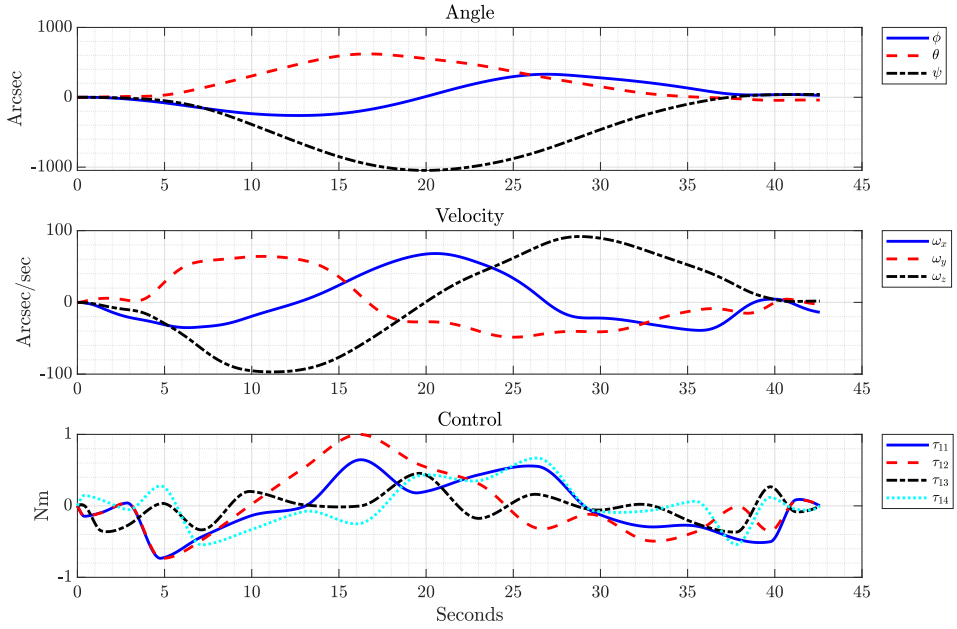

Figure 3.13: Case 2 Open-loop Baseline Maneuver: Bus States and Control

Table 3.6: Case 2 Open-Loop Simulation Results for Minimum-Time Maneuver with Rigid-Body Dynamics

			Error (deg)			Energy (J)		Control
Case #	Filter	t_f (s)	Bus	SAA-1	SAA-2	Total	Modal	Cost
1a	Notch	84.3	0.064	0.026	0.19	1.3e-3	6.9e-9	0.557
2	n/a	42.6	0.018	0.055	0.089	3.2e-3	1e-4	23.0

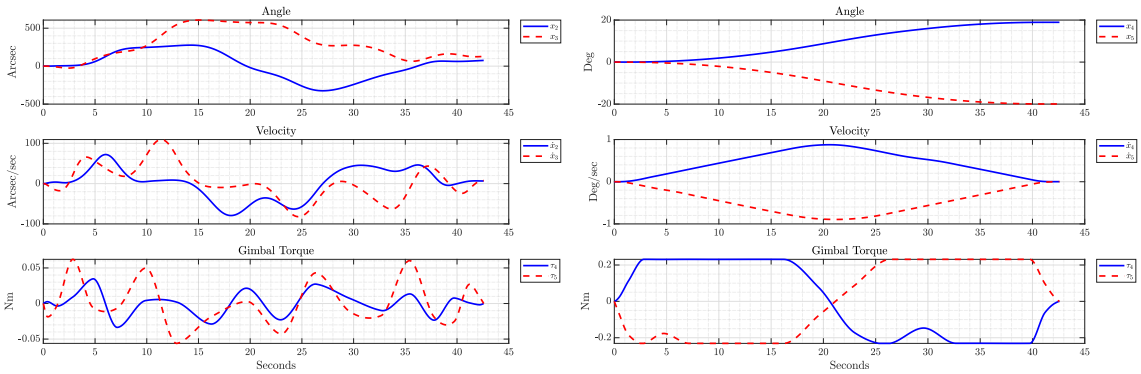

(a) SAA-1 (b) SAA-2

Figure 3.14: Case 2 Open-loop Baseline Maneuver: SAA States and Controls

These results demonstrate the rigid-body, minimum time maneuver achieves desirable pointing results for both SAA while decreasing maneuver length by 49%, resulting in a large increase in payload availability. However, due to the rigid-body nature dynamics used for planning, the vibrational modes of the system are un-accounted for leading to a four order-of-magnitude increase in modal energy. The point is further accentuated when the rigid-body, minimum-time maneuver is simulated closed-loop, where the convergence of the total system energy takes 1403 seconds, an almost ten-fold increase from Case 1a.

Table 3.7: Case 2 Close-Loop Convergence Results for Standard Maneuver with and without Notch Filtering

		Convergence Time (s)			
Case #	Filter	Bus	SAA-1	SAA-2	Total Energy
1a	Notch	89.3	–	131.6	145.2
2	n/a	–	–	42.6	1404

These Case 2 results shown the possible limitations of solving for optimal solutions that minimize slew times for flexible systems while making rigid-body assumptions with the system dynamics. Large improvements can be made in the reduction of pointing error and decreasing maneuver length, but at the expense of large increases in vibrational excitation. A posterior techniques such as filtering and input shaping could be applied to this new trajectory, but there are no guarantees the resulting maneuver will maintain system vibrational energy magnitude in family (or less) than the standard maneuver.

This research investigates methods of utilizing the full, nonlinear, flexible dynamics of the multi-body system to generate antenna slew maneuvers that not only decrease maneuver time, but simultaneously account for and minimize system vibrational excitation.

IV. Optimal Maneuvers for Flexible, Multi-body Systems

In the following chapter, each of the Research Questions proposed in Chapter 1 are reviewed and the relevant results are presented and discussed. For convenience, the four Research Question (RQ) are restated below:

Research Question 1: How should an optimal control problem be formulated and solved for a flexible, multi-body spacecraft connected via flexible, revolute joints, performing antenna slew maneuvers between access points while compensating for system vibrational response and adjacent aperture pointing errors?

Research Question 2: How should robust optimal control techniques, accounting for configuration and parameter uncertainty using sensitivity functions, be incorporated into the formulation of RQ 1?

Research Question 3: How should an unscented optimal control problem, accounting for configuration and parameter uncertainty, be incorporated into the formulation of RQ 1?

Research Question 4: How should robust optimal control techniques from RQ 2 and RQ 3 be used as a model reduction techniques to achieve optimal solutions comparable with RQ 1 but with increased computational efficiency?

4.1 Multi-body Trajectories with Vibration Compensation

The objective of RQ 1 is to derive an optimal control problem formulation utilizing the full nonlinear dynamics of the system, including system flexibility, and design a maneuver decreasing maneuver execution time while simultaneously suppressing the system's vibrational modes. By utilizing the full nonlinear dynamics, configuration dependent terms and nonlinear effects are accounted for and leveraged when minimizing the cost functional. System nonlinearities are then embedded within the derived control and joint profiles. These control trajectories are thus based on dynamics and kinetics and not

just kinematics as with the standard maneuver, reducing pointing error during maneuver execution and decreasing reliance on feedback control to maintain the desired trajectories. By leveraging the flexible dynamics within the optimal control formulation, the desired vibrational response of the system can be addressed and the corresponding control response embedded within the computed profiles. By addressing the system frequency response a priori during trajectory planning, it negates the necessity of using notch filtering for the feed-forward control profiles, as was used in the the baseline maneuver.

As shown in Figure 3.7 and Equation (3.20), the standard maneuvers requires computation of bus counter-steering torques due to the Single Access Antenna (SAA) maneuver, where based on the pre-planning gimbal acceleration profiles, the bus counter-steering torques are calculated as,

$$\tau_{cs} = \bar{M}_{1,2:5}\ddot{x}_{2:5}. \tag{4.1}$$

Due to the five-body optimal control formulation computing the required control trajectories for all bodies simultaneously, the control necessary for the bus to achieve its desired trajectory includes the component of control necessary to counteract motion induced by the SAA maneuver. As such, the bus controller is not required to compute feedforward counter-steering controls. For the five-body optimal control problems considered in this section, each controller is in the form of Figure 3.6 where the totality of the necessary control is represented in τ_{opt} and the notch filter is not utilized.

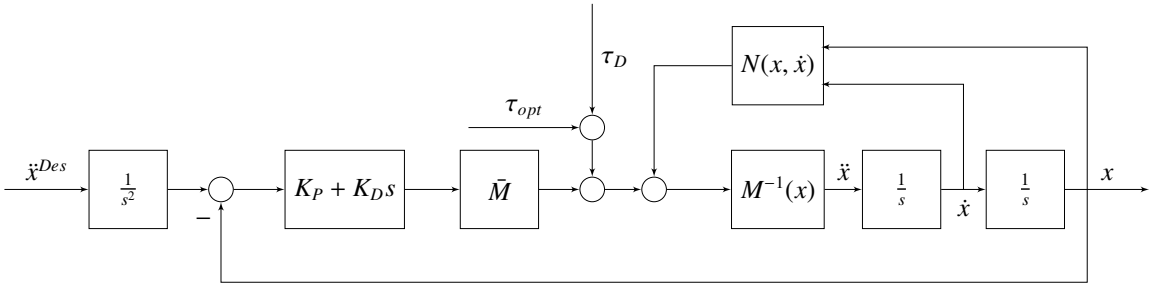

4.1.1 Case 3: Five Body, Minimum Modal Cost.

The objective of Case 3 is to roll back the conservative "soft" constraint of maximum gimbal velocity from Case 1 of 0.25 deg/s, and directly bound the magnitude of vibrational excitation in the system. To accomplish this, the maximum magnitude of the modal variables $|\eta|$ during the standard maneuver are used to bound the η states in the optimal control problem. To further support this objective, the cost functional is constructed so as to minimize the integral of the square of the modal variables as shown in Equation (4.2). In addition to enforcing absolute bounds on the modal state magnitudes, the cost functional effectively penalizes maneuvers inducing excessive bus vibration.

$$F_\eta(x,t) = \int_0^{t_f} \eta^T \eta \, dt. \tag{4.2}$$

For the optimal control problem formulation considered in this dissertation, the state vector (x) from Equation (3.3) is augmented with the torque vector (τ) and the time derivative of torque, or jerk, is used as the control input ($u(t)$). Utilizing jerk as the control input to the optimal control problem provides an amount of smoothing to the resulting torque profiles making them easier to interpolate for use in the subsequent simulation. The state and control vectors are then defined as,

$$\begin{aligned} x = [&q_1, q_2, q_3, q_4, x_2, x_3, x_4, x_5, x_{G2}, x_{G3}, x_{G4}, x_{G5}, \eta_1, \eta_4, \eta_7, ... \\ &\omega_x, \omega_y, \omega_z, \dot{x}_2, \dot{x}_3, \dot{x}_4, \dot{x}_5, \dot{x}_{G2}, \dot{x}_{G3}, \dot{x}_{G4}, \dot{x}_{G5}, \dot{\eta}_1, \dot{\eta}_4, \dot{\eta}_7, ... \\ &\tau_1, \tau_2, \tau_3, \tau_4, \tau_5]^T \in \mathbb{R}^{37} \\ u = [&\dot{\tau}_1, ..., \dot{\tau}_5] \in \mathbb{R}^8 \end{aligned} \tag{4.3}$$

From the Case 2 results, it was shown that a rigid-body minimum-time solution completes the desired maneuver in 42.6 seconds providing a reasonable lower bound for the flexible optimal solution. The Case 3 time bound is then set to be $t_f \leq 50s$ which

provides for an improvement in overall maneuver length over the 84.4 seconds of the standard maneuver. The optimal control problem in standard format is then,

$$
\begin{aligned}
\text{minimize} \quad & J = \int_0^{t_f} \eta^T \eta \, dt \\
\text{subject to} \quad & 0 = \dot{x}(t) - f(x(t), u(t); \bar{p}), \\
& q^0 = q^f = [0, 0, 0, 1], \\
& x_L^0 = [0, 0, 0, 0] \; deg, \\
& x_L^f = [0, 0, 19, -20] \; deg, \\
& |\eta| \leq 36 \; arcsec, \\
& |\tau_1| \leq 1 \; Nm, \\
& |\tau_{2-5}| \leq 0.23 \; Nm, \\
& |\dot{\tau}_{1-5}| \leq 0.3 \; Nm/s, \\
& h(x, t) \leq 0.02 \; deg, \\
& 0 \leq t \leq 50 \; s
\end{aligned}
\tag{4.4}
$$

where the variable $\bar{p}$ represents the nominal values of the vector of uncertain parameters p from as defined in Equation (3.9).

Figure 4.1 and Figure 4.2 show the computed bus and SAA-2 controls and resulting state trajectories when simulated open-loop and terminated at the computed final maneuver time with the terminal pointing errors and energy displayed in Table 4.1. The Case 1a notch filtered solution is shown for reference.

Due to the maneuver being generated based on nonlinear dynamics and kinematics, and not simply kinematics as with the standard maneuver, the open-loop terminal pointing errors of SAA-1/2 are reduced by 98% and 80% respectively while the bus pointing error is reduced by 99.7%. Similarly, by modeling the vibrational response of the bus and minimizing it within the cost functional, terminal system energy is reduced by almost

Table 4.1: Case 3 Terminal Open-Loop Simulation Results for Minimum Modal Cost Maneuver

			Terminal Error (deg)			Total	Control
Case #	Filter	t_f (s)	Bus	SAA-1	SAA-2	Energy (J)	Cost
1a	Notch	84.3	0.064	0.026	0.19	1.3e-3	0.56
3	n/a	50	1.7e-4	4.8e-4	0.038	2.5e-7	11.9

four orders of magnitude. These results demonstrate that even when executed open-loop, the optimal solution is able to nearly achieve the pointing objectives while exhibiting significant reductions in system excitation.

Table 4.2 shows the closed-loop convergence times for the Case 3 maneuver executed in high-gain mode. Unlike the standard maneuver, neither the bus nor SAA-1 pointing error ever exceeds 0.2 degrees, and the SAA-2 pointing error is converged immediately at maneuver termination. Additionally, due to the reduced excitation of the bus, energy convergence is achieved 95 seconds faster than the standard maneuver.

Table 4.2: Case 3 Closed-Loop Convergence Results for Minimum Modal Cost Maneuver

		Planned	Convergence Time (s)			
Case #	Filter	t_f (s)	Bus	SAA-1	SAA-2	Total Energy
1a	Notch	84.3	89.3	–	131.6	145.2
3	n/a	50	–	–	50	50.5

These results demonstrate how conservative "soft" constraints on maximum gimbal velocity, originally enforced to reduce the magnitude of disturbance torques, can be eliminated so long as the primary concern of system flexibility is modeled within the optimal control dynamics. By directly bounding the modal variables and utilizing a cost functional penalizing system vibrations, closed-loop maneuver convergence time

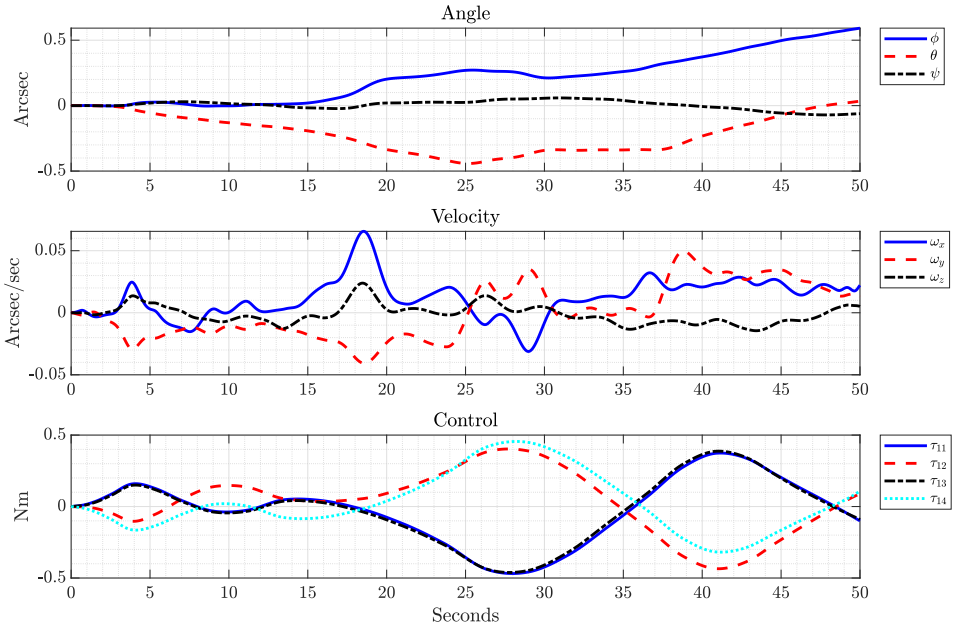

Figure 4.1: Case 3 Open-loop Baseline Maneuver: Bus States and Control

is improved by 62% while the magnitude of modal excitation is significantly reduced. Leveraging the nonlinear dynamics leads to more optimal control trajectories for the slewing antenna as well as the counter-steering torques necessary for the bus to maintain proper pointing, all while accounting for and minimizing vibrational excitation.

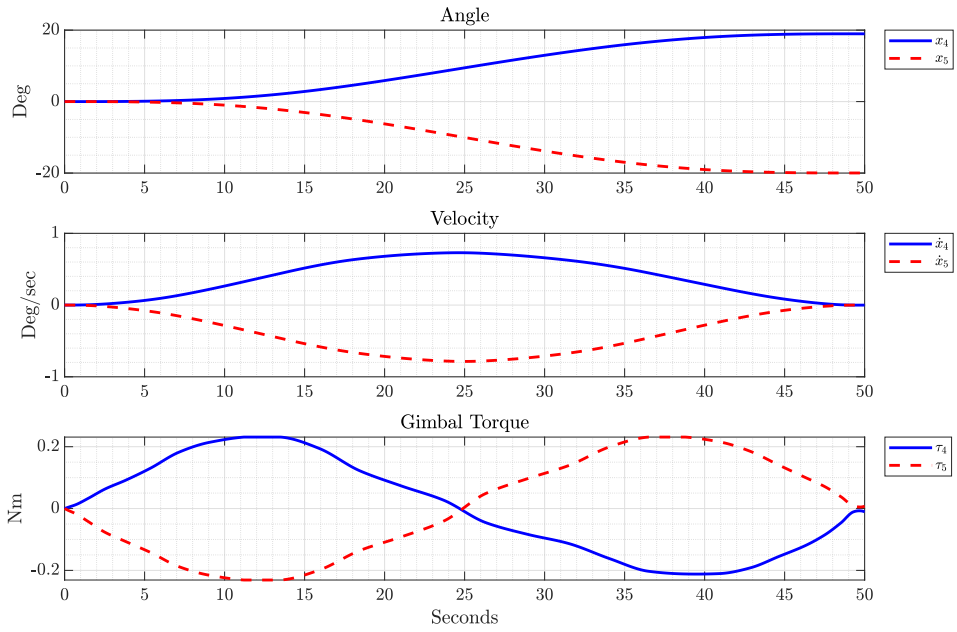

Figure 4.2: Case 3 Open-loop Maneuver: SAA-2 States and Control

4.1.2 Case 4: Five Body, Minimum Modal Cost, 2x Payload Torque.

For standard maneuver planning, a certain percentage of available actuator torque must be set aside for feedback control. The amount of actuator torque set aside is influenced by the peak joint rates as well as the configuration dependent portion of the loop gain for each gimbal channel. By utilizing the nonlinear dynamics during optimal trajectory generation, Case 3 removed constraints on peak gimbal velocity. Case 4 goes one step further and assumes that further actuator torque capacity can be allocated from feedback control, to feedforward control, to further reduce maneuver time and increase payload availability. Case 4 assumes the maximum allowable gimbal torque is doubled from $|\tau_{2-4}| \leq 0.23\ Nm$ to $|\tau_{2-4}| \leq 0.46\ Nm$. Furthermore, the maximum allowable maneuver time is reduced to $t_f \leq 40s$. The Case 4 optimal control problem in standard format is then,

$$
\begin{aligned}
\text{minimize} \quad & J = \int_0^{t_f} \eta^T \eta \, dt \\
\text{subject to} \quad & 0 = \dot{x}(t) - f(x(t), u(t); \bar{p}), \\
& q^0 = q^f = [0, 0, 0, 1], \\
& x_L^0 = [0, 0, 0, 0] \; deg, \\
& x_L^f = [0, 0, 19, -20] \; deg, \\
& |\eta| \leq 36 \; arcsec, \\
& |\tau_1| \leq 1 \; Nm, \\
& |\tau_{2-5}| \leq 0.46 \; Nm, \\
& |\dot{\tau}_{1-5}| \leq 0.3 \; Nm/s, \\
& h(x, t) \leq 0.02 \; deg, \\
& 0 \leq t \leq 40 \; s
\end{aligned}
\tag{4.5}
$$

The resulting open-loop control profile and state trajectories are shown in Figure 4.3 and Figure 4.4 while the resulting terminal pointing error and energies are shown in Table 4.3. While the open-loop bus pointing error has increased by an order of magnitude as compared to Case 3, it still represents an approximately 96% improvement as compared to Case 1, while the terminal pointing error of SAA-2 is reduced by 99.5%.

Table 4.3: Case 4 Open-Loop Simulation Results for Minimum Modal Cost Maneuver with 2x Allowable Payload Torque

			Error (deg)			Total	Control
Case #	Filter	t_f (s)	Bus	SAA-1	SAA-2	Energy (J)	Cost
1a	Notch	84.3	0.064	0.026	0.19	1.3e-3	0.56
4	n/a	40	2.7e-3	0.031	0.1493	5.9e-6	12.3

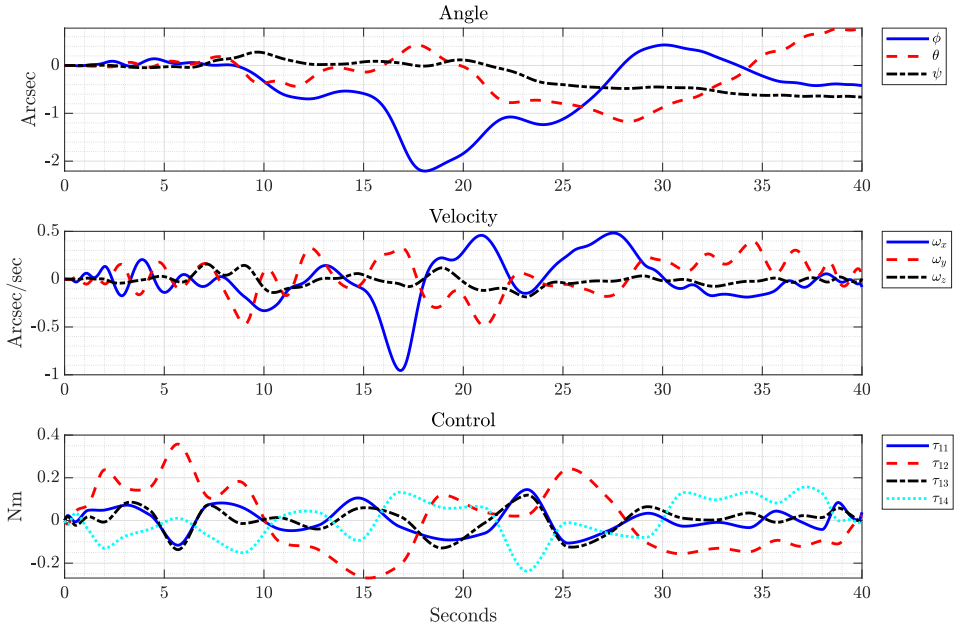

Figure 4.3: Case 4 Open-loop Baseline Maneuver: Bus States and Control

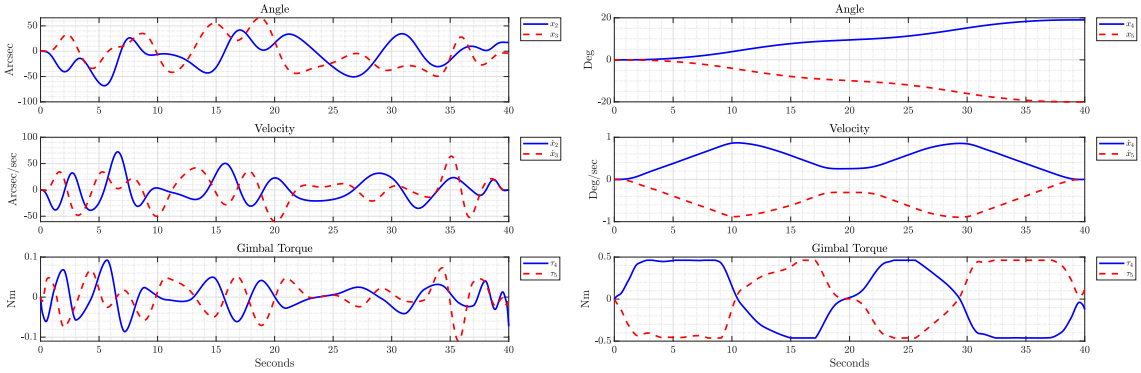

(a) SAA-1

(b) SAA-2

Figure 4.4: Case 4 Open-loop Baseline Maneuver: SAA States and Controls

While the open-loop pointing error for SAA-1 is worse for Case 4 than Case 1a, when simulated closed-loop as shown in Table 4.4, pointing convergence for SAA-1 is achieved and maintained immediately at maneuver termination. As with the closed-

loop performance of Case 3, energy convergence is improved and converges within 42 seconds. The closed-loop performance for Case 4 demonstrates that even when removing "soft" constraints on maximum gimbal velocity and allocated additional torque capacity for trajectory design, by utilizing Pseudospectral Methods (PSM), optimal maneuvers can be generated improving payload pointing convergence by 70% while simultaneously improving energy convergence by 71%.

Table 4.4: Case 4 Closed-Loop Convergence Results for Minimum Modal Cost Maneuver with 2x Allowable Payload Torque

		Planned	Convergence Time (s)			
Case #	Filter	t_f	Bus	SAA-1	SAA-2	Total Energy
1a	Notch	84.3	89.3	–	131.6	145.2
4	n/a	40	–	–	40	42.2

4.1.3 Research Question 1 Summary.

Research Question 1 demonstrates that Psuedospectral Optimal Control (PSOC) techniques, when coupled with a highly nonlinear, flexible, multi-body system, can derive control trajectories which first and foremost decrease maneuver execution time while simultaneously addressing unwanted system excitation. As discussed in Section 2.6, previous research limited problem formulations to a small number of flexible bodies, planar motion, or often a single flexible mode. The results of RQ 1 are novel in that they demonstrates how the PSM can generate optimal trajectories for a nonlinear, free-floating, five-body model, with multiple flexible modes and gimbal joints

Summary open-loop results for RQ 1 maneuvers are shown in Table 4.5 and Table 4.6, where 4.6 shows percentage improvement of the maneuvers as compared to the Case 1a standard maneuver. Closed-loop results are shown in Table 4.7 with percentage

Table 4.5: Research Question 1: Open-Loop Maneuvers Results Compared to Standard Maneuvers

Case #	Filter	t_f (s)	Error (deg) Bus	SAA-1	SAA-2	Total Energy (J)
1	n/a	84.3	0.066	0.026	0.32	6.7e-6
1a	Notch	84.3	0.064	0.026	0.19	1.3e-3
3	n/a	50	1.7e-4	4.8e-4	0.038	2.5e-7
4	n/a	40	2.7e-3	0.031	0.1493	5.9e-6

Table 4.6: Research Question 1: Percent Improvement of Open-Loop Maneuvers Compared to Standard Maneuver

Case #	Filter	t_f (%)	Error Reduction (%) Bus	SAA-1	SAA-2	Total Energy Reduction(%)
3	n/a	40.7	99.7	98.2	80.1	100
4	n/a	52.6	95.8	(-21.0)	21.4	99.5

improvements shown in Table 4.8. In Case 1, motion planning is performed on a per-gimbal basis, where each rigid body is modeled as an independent, uncoupled system. When the corresponding maneuver is executed closed-loop, the controller has to ameliorate unwanted disturbance torques due to the configuration dependent loop gain and un-modeled nonlinear terms which excited unwanted vibrational modes in the system. To decrease the magnitude of these disturbances, the maximum gimbal torque and corresponding maximum velocity are artificially restricted. Table 4.6 shows that by employing the notch filter from Equation (3.22), open-loop pointing error for the bus and SAA-2 are both reduced, while modal excitation of the system is improved by 64%. However, due to the notch filter reducing the amount of control applied to the system, total system energy is increased. The trade-off presented by the notch filter is more apparent in the closed-loop results where the

pointing convergence time for SAA-2 increases by 56%, but energy convergence improved by 42%.

Table 4.7: Research Question 1: Closed-Loop Convergence Times

Case #	Filter	Planned t_f(s)	Convergence Time (s) Bus	SAA-1	SAA-2	Total Energy
1a	Notch	84.3	89.3	–	131.6	145.2
3	n/a	50	–	–	50	50.5
4	n/a	40	–	–	40	42.2

Table 4.8: Research Question 1: Percent Improvement of Closed-Loop Maneuvers Convergence Compared to Standard Maneuver (Case 1a)

Case #	Filter	Convergence Time Reduction (%) Bus	SAA-1	SAA-2	Total Energy
3	n/a	–	–	62.0	65.2
4	n/a	–	–	69.6	71.0

The Case 3 maneuver, which removed constraints on maximum gimbal velocity and derived trajectories minimizing modal excitation, decreases SAA-2 pointing error by 80.1% and unlike the standard maneuver, requires no additional time to achieve pointing convergence. Similarly, energy convergence is achieved in 51 seconds compared to 145 seconds for Case 1a, a 65% improvement. Case 4 goes one step further and allocates additional torque margin to trajectory generation and achieves a 70% improvement in pointing convergence time while improving energy convergence by time 71%.

The time history of total system energy for Cases 1, 3 and 4 are shown in Figure 4.5 where the total energy is calculated using Equation (3.27). Due to doubling allowable torque for Case 4 and the removal of gimbal velocity constraints for both cases 3 and 4, the

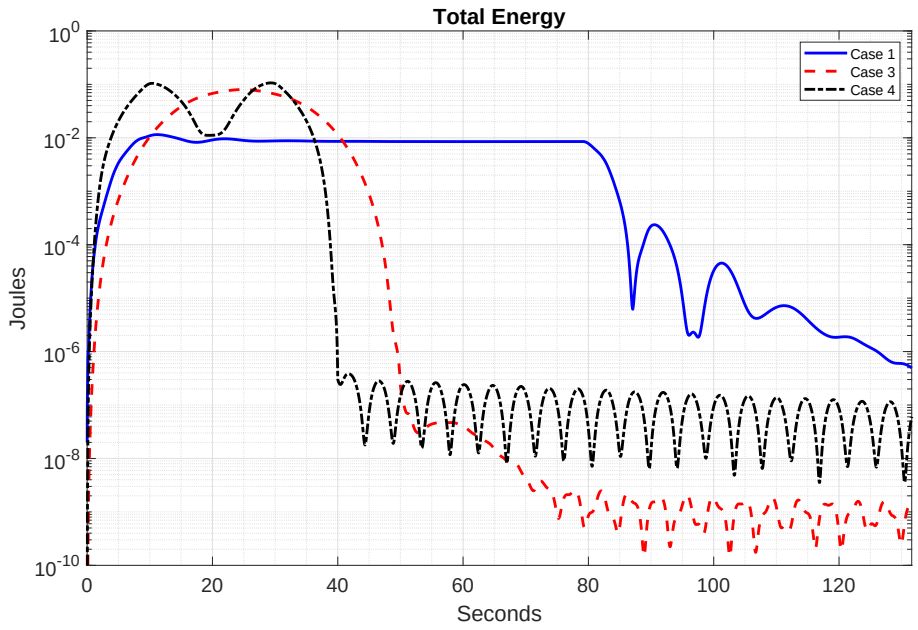

Figure 4.5: Comparison of Total Energy for RQ 1 Closed-Loop Maneuvers

system achieves a higher total energy allowing maneuver completion in 50 and 40 seconds respectively compared to 84.3 seconds for the standard maneuver. By accounting for the nonlinear dynamics and minimizing the modal excitation, both maneuvers terminal with a lower total energy than the Case 1 maneuver.

4.2 Sensitivity Based, Robust Optimal Control

The objective of RQ 2 is three-fold. As with the results of RQ 1, the first objective is to derive a trajectory decreasing the overall slew time of SAA-2, thereby increasing payload availability. The second objective is to increase trajectory robustness against variations in system parameters (p) and ensure the increased gimbal velocities do not negatively impact SAA-1 pointing. The last objective is to reduce the total energy in the system at the termination of each maneuver, which serves as a means of reducing the vibrational excitation of the bus, further reducing impacts to antenna pointing. While the previously outlined model can be used to formulate deterministic optimal control problems

using nominal parameter values $\bar{p} = [\bar{k}, \bar{\omega_n}]$, these parameters can be difficult to measure precisely, may change on orbit due to environmental impacts, or in the case of the natural frequencies ω_n, are derived via Finite Element Method (FEM) assuming a nominal gimbal configuration. For systems such as Tracking and Data Relay Satellite (TDRS), exhibiting a large ratio of antenna to bus inertia, the gimbal configuration can have significant impacts on the system's inertia values and the vibrational response. These variations in parameters can yield unwanted residual energy and gimbal pointing error at the conclusion of a maneuver derived using the nominal values.

Utilizing the sensitivity dynamics derived in Equation (2.32), RQ 2 formulates a desensitized optimal control problem which minimizes, or otherwise constrains, the systems sensitivity to parameter variations. In this manner, robust maneuvers can be generated which decrease terminal system pointing error and residual energy when subjected to variations in system parameters.

Using the previously developed flexible satellite model from Section 3.1.1, an optimal control problem is formulated where the dynamics from Equation (2.64) are denoted as $\dot{x} = f(x(t), u(t); \bar{p})$ and p is a vector of uncertain parameters where $\bar{p}$ represents the nominal values from Equation (3.9). The general optimal control problem is defined as,

$$\begin{aligned}
\text{minimize} \quad & J_P = E[x^f, t_f] + \int_{t_0}^{t_f} F[x(t), u(t); \bar{p}]\, dt \\
\text{subject to} \quad & 0 = \dot{x}(t) - f(x(t), u(t); \bar{p}), \\
& (x(t_0), t_0) = (x^0, t^0), \\
& x(t_f) = x^f, \\
& |u| \leq u_{max}, \\
& |h(x,t)| \leq h_{max},
\end{aligned} \tag{4.6}$$

where $E[\cdot]$ is the endpoint cost, $F[\cdot]$ is the running cost, x^0 and x^f are the initial and final states and $h(x,t)$ incorporates path constraints.

The sensitivity dynamics from Equation (2.32) are then appended to the flexible system dynamics, introducing an additional $N_x \times N_p$ optimization variables. The cost function for the desensitized optimal control problem is then formulated by defining a performance objective $P[\cdot]$ and a Robustness objective $R[\cdot]$ where the variable $\alpha \in [0, 1]$ is a risk-aversion parameter allowing tuning between the objectives. The choices of $P[\cdot]$ and $R[\cdot]$ are specific to each case and will be detailed in the following subsections. The general problem formulation is then,

$$\begin{aligned}
\text{minimize} \quad & J_R = (1-\alpha)P[\cdot] + \alpha R[\cdot] \\
\text{subject to} \quad & 0 = \dot{x}(t) - f(x(t), u(t); \bar{p}), \\
& 0 = \dot{s}(t) - f(s(t); \bar{p}), \\
& (x(t_0), s(t_0), t_0) = (x^0, [0], t^0), \\
& x(t_f) = x^f, \\
& |u| \leq u_{max}, \\
& |h(x,t)| \leq h_{max},
\end{aligned} \tag{4.7}$$

where the initial value of the sensitivity states are set to identically zero.

4.2.1 Case 5: Minimal Terminal Sensitivity.

Equation (4.9) shows the desensitized, robust optimal control formulation where the "soft" constraint of the standard maneuvers, namely maximum link velocity, are unconstrained and the underlying issues of vibrational excitation of the system is directly constrained based on the maximum values measured from the standard maneuver. To minimize terminal sensitivity of the optimal trajectory to parameter uncertainty, the robustness objective can be set to the norm of the sensitivity matrix at the maneuver final time ($R[\cdot] = \|s(t_f)\|$), where the 2-norm is utilized in this analysis [81]. The risk-aversion parameter is then defined by $\alpha = 1$ and the optimal control problem formulation is,

Given:

$$
\begin{aligned}
x = [&q_1, q_2, q_3, q_4, x_2, x_3, x_4, x_5, x_{G2}, x_{G3}, x_{G4}, x_{G5}, \eta_1, \eta_4, \eta_7, ... \\
&\omega_x, \omega_y, \omega_z, \dot{x}_2, \dot{x}_3, \dot{x}_4, \dot{x}_5, \dot{x}_{G2}, \dot{x}_{G3}, \dot{x}_{G4}, \dot{x}_{G5}, \dot{\eta}_1, \dot{\eta}_4, \dot{\eta}_7, ... \\
&\tau_1, \tau_2, \tau_3, \tau_4, \tau_5]^T \in \mathbb{R}^{37} \\
s \in \mathbb{R}^{29x7} \\
u = [\dot{\tau}_1, ..., \dot{\tau}_5] \in \mathbb{R}^8
\end{aligned}
\tag{4.8}
$$

$$
\begin{aligned}
\text{minimize} \quad & J = \|s(t_f)\| \\
\text{subject to} \quad & 0 = \dot{x}(t) - f(x(t), u(t); \bar{p}), \\
& 0 = \dot{s}(t) - f(x(t), s(t); \bar{p}), \\
& q^0 = q^f = [0, 0, 0, 1], \\
& x_L^0 = x_G^0 = [0, 0, 0, 0]\ deg, \\
& x_L^f = x_G^f = [0, 0, 19, -20]\ deg, \\
& |(\eta, \dot{\eta})| \leq (36, 27)\ arcsec, arcsec/s, \\
& |\tau_1| \leq 1\ Nm, \\
& |\tau_{2-5}| \leq 0.23\ Nm, \\
& |\dot{\tau}| \leq 0.3\ Nm/s, \\
& h(x, t) \leq 0.02\ deg, \\
& t_f \leq 50s.
\end{aligned}
\tag{4.9}
$$

The resulting open-loop bus and payload control and state trajectories are shown in Figure 4.6 and Figure 4.7. To quantify the impacts of parametric uncertainty on the performance and robustness of the derived maneuver, Monte Carlo analysis is performed with $n = 500$ realizations where the unknown parameter vector p is distributed per Equation (3.9). Each realization is simulated open-loop and terminated at the pre-calculated

maneuver end-time. The resultant mean terminal pointing errors and mean total energy are shown in Table 4.9 while the histogram distributions are shown in Figure 4.8 where the distribution values are normalized by the Case 1a means. These results demonstrate the minimum terminal sensitivity maneuver improves maneuver execution time by 40.7% while improving mean open-loop bus pointing error by 99% and SAA-1/2 pointing error by 79 and 64% respectively. As with previous cases, by leveraging the nonlinear dynamics during trajectory planning, total system energy is reduced by 100%.

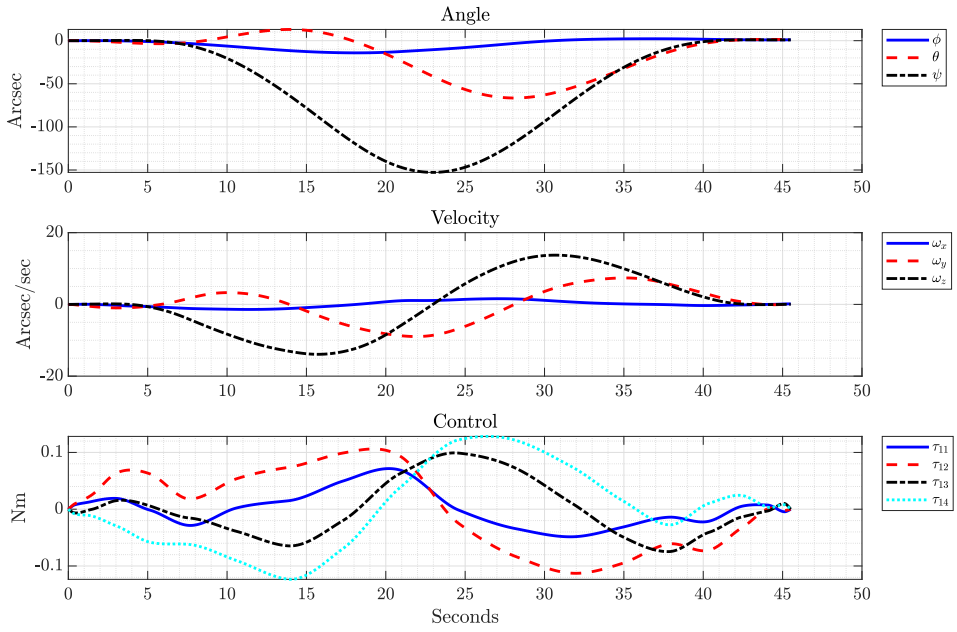

Figure 4.6: Case 5 Open-loop Baseline Maneuver: Bus States and Control

Table 4.10 contains the closed-loop simulation results where the Case 5 maneuver maintains pointing convergence for SAA-1 and attains SAA-2 convergence at the planned maneuver termination time with energy convergence being achieved in 58 seconds, an improvement of 60% over the standard maneuver.

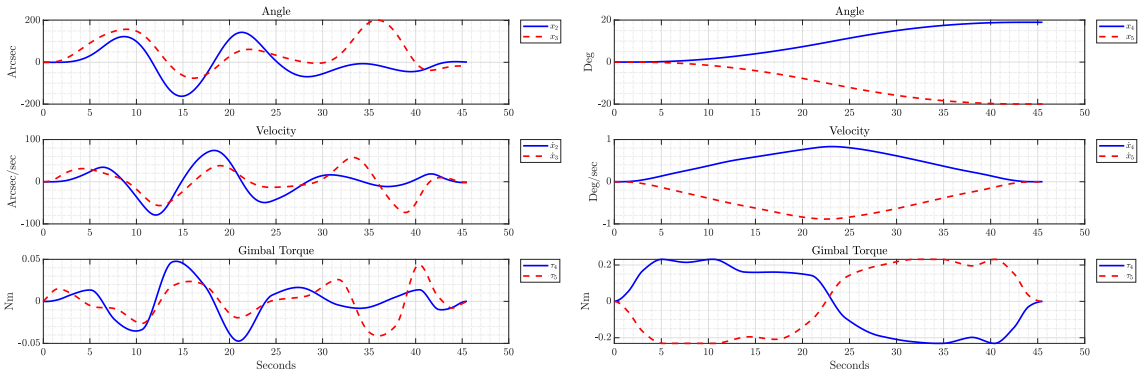

(a) SAA-1 (b) SAA-2

Figure 4.7: Case 5 Open-loop Baseline Maneuver: SAA States and Controls

Table 4.9: Case 5 Terminal Open-Loop Monte Carlo Results for Minimum Terminal Sensitivity

Case #	Filter	t_f (s)	Mean Error (deg) Bus	SAA-1	SAA-2	Mean Total Energy (J)	Control Cost
1a	Notch	84.3	0.064	0.026	0.19	1.3e-3	0.56
5	n/a	50	5.6e-4	5.5e-3	0.068	3.7e-7	3.75

Table 4.10: Case 5 Closed-Loop Convergence Times for Minimum Terminal Sensitivity

Case #	Filter	Planned t_f	Convergence Time (s) Bus	SAA-1	SAA-2	Total Energy
1	Notch	84.3	89.3	–	131.6	145.2
5	n/a	50	37.2	–	50	57.8

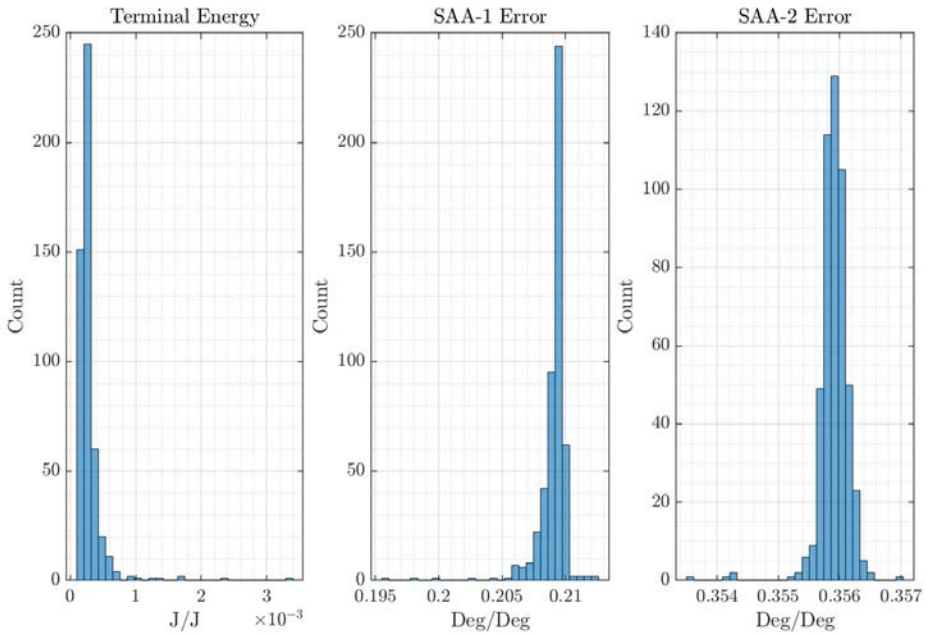

Figure 4.8: Case 5 Distribution of Normalized Terminal Residual Energy and SAA Pointing Error

4.2.2 Cases 6-7: Minimal Jerk and Terminal Sensitivity.

Cases 6 and 7 explore the impact of adding an additional performance objective to the desensitized optimal control cost function to further improve maneuver performance and robustness. Previous research has shown that jerk-limited profile generation can be a successful method of reducing excitation of flexible structures [95, 96]. For cases 6 and 7, an additional performance objective is added into the optimal control problem cost functional in accordance with Equation (4.7) minimizing the jerk into the system where the performance objective $P[\cdot] = \int \dot{\tau}^T \dot{\tau}\, dt$. By varying the value of the risk aversion parameter α, the relative weighting of the performance versus robustness objectives can be altered.

The new desensitized optimal control problem formulation is,

$$
\begin{aligned}
\text{minimize} \quad & J = (1-\alpha)\int \dot{\tau}^T \dot{\tau}\, dt + \alpha \|s(t_f)\| \\
\text{subject to} \quad & 0 = \dot{x}(t) - f(x(t), u(t); \bar{p}), \\
& 0 = \dot{s}(t) - f(x(t), s(t); \bar{p}), \\
& q^0 = q^f = [0, 0, 0, 1], \\
& x_L^0 = x_G^0 = [0, 0, 0, 0]\ deg, \\
& x_L^f = x_G^f = [0, 0, 19, -20]\ deg, \\
& |(\eta, \dot{\eta})| \leq (36, 27)\ arcsec, arcsec/s, \\
& |\tau_1| \leq 1\ Nm, \\
& |\tau_{2-5}| \leq 0.23\ Nm, \\
& |\dot{\tau}| \leq 0.3\ Nm/s, \\
& h(x,t) \leq 0.02\ deg, \\
& t_f \leq 50s.
\end{aligned}
\tag{4.10}
$$

where $\alpha = 0.91$ for Case 6 and $\alpha = 0.5$ for Case 7. This equates to a 10x weighting on the robustness cost versus the performance cost for Case 6 and equal weighting for Case 7.

Figure 4.9 and 4.10 contain the resulting Case 6 bus and antenna trajectories while the Case 7 trajectories are shown in Figure 4.11 and 4.12. The impacts of penalizing jerk can be seen in the bus trajectories of the two cases, where for Case 6, a maximum rotational velocity of $\approx$ 5 arcsec/s is achieved while for Case 7 the maximum is $\approx$ 0.5 arcsec/s with a similar reduction of SAA-1 velocity for both cases. The impacts of the reduction in velocity are seen in the open loop Monte Carlo results in Table 4.11 and the normalized Monte Carlo distributions in Figure 4.13 and 4.14.

As the cost weighting is increased on the performance objective, the open-loop mean pointing error for the antennas are decreased, however, the closed-loop performance in Table 4.12 shows that Case 7 requires an additional 6 seconds to achieve SAA-2 pointing convergence than Cases 5 and 6. While the terminal sensitivity is a direct measure of a maneuvers robustness against parameter variation, minimizing control jerk is an indirect method of reducing the high-frequency content of a maneuver which previous research has shown to have the effect of reducing residual vibrations. The Case 6/7 results shows that when simulated closed-loop, adding an additional indirect method of robustness does not necessarily translate to more robust maneuvers as compared to the Case 5 results relying solely on terminal sensitivity.

Table 4.11: Cases 6-7 Terminal Open-Loop Monte Carlo Results

			Mean Error (deg)			Mean Total	Control
Case #	Filter	t_f (s)	Bus	SAA-1	SAA-2	Energy (J)	Cost
1	Notch	84.3	0.064	0.026	0.19	1.3e-3	0.56
6	n/a	50	7.6e-4	0.017	0.051	2.8e-7	15.1
7	n/a	50	9.8e-4	6.6e-3	0.027	9.7e-7	4.3

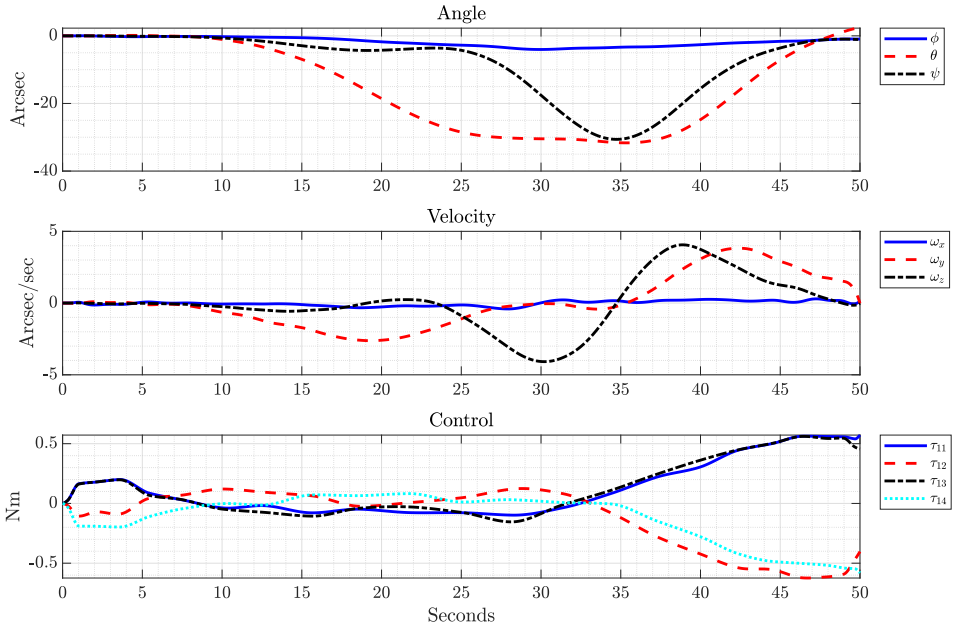

Figure 4.9: Case 6 Open-loop Maneuver: Bus States and Control

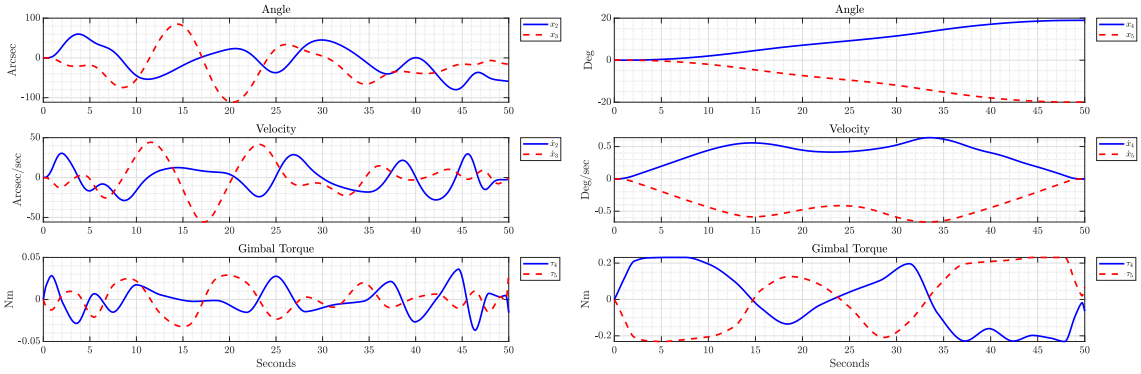

(a) SAA-1

(b) SAA-2

Figure 4.10: Case 6 Open-loop Maneuver: SAA States and Controls

Table 4.12: Cases 6-7 Closed-Loop Convergence Times

		Planned	Convergence Time (s)			
Case #	Filter	t_f(s)	Bus	SAA-1	SAA-2	Total Energy
1	Notch	84.3	89.3	–	131.6	145.2
6	n/a	50	–	–	50	59.52
7	n/a	50	–	–	56.1	64.34

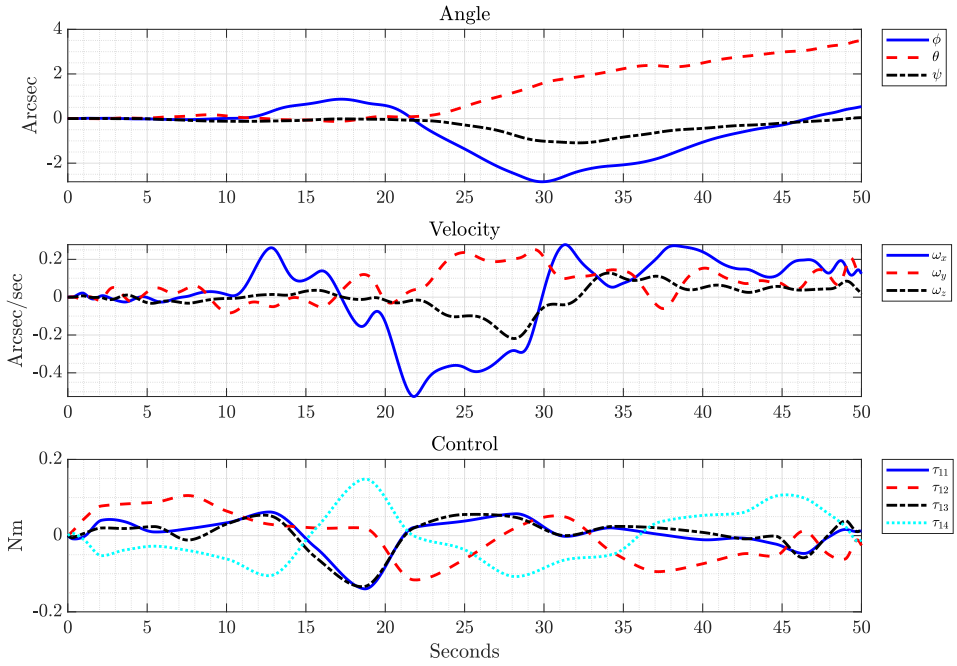

Figure 4.11: Case 7 Open-loop Maneuver: Bus States and Control

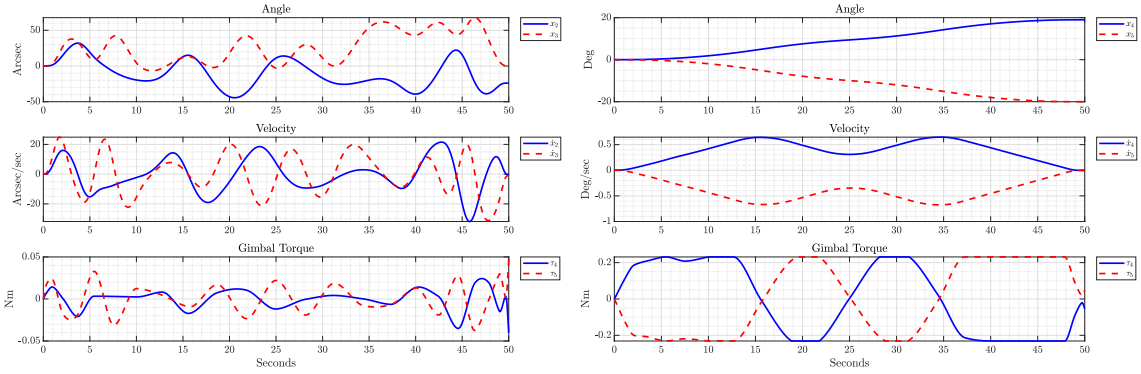

(a) SAA-1

(b) SAA-2

Figure 4.12: Case 7 Open-loop Maneuver: SAA States and Controls

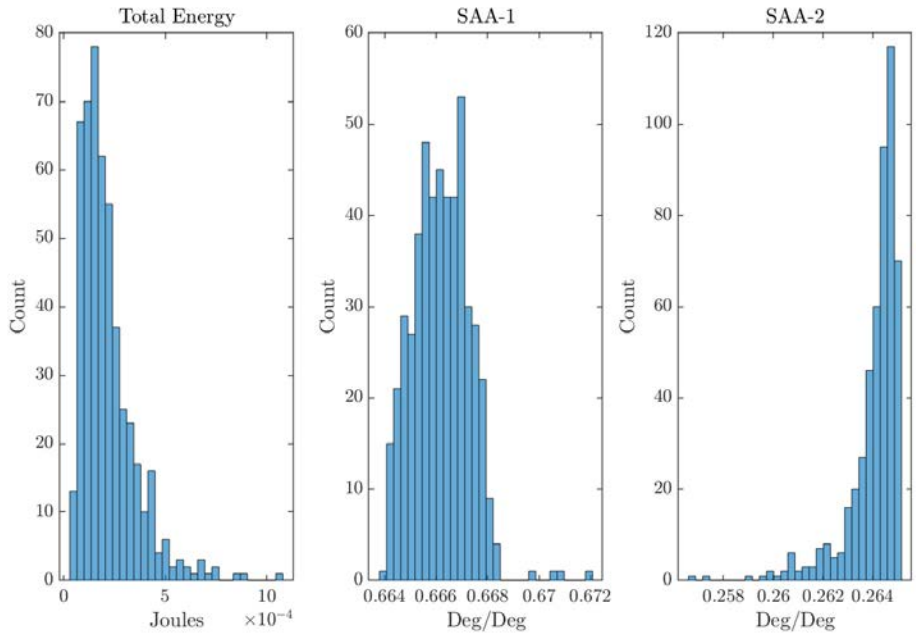

Figure 4.13: Case 6 Distribution of Normalized Terminal Residual Energy and SAA Pointing Error

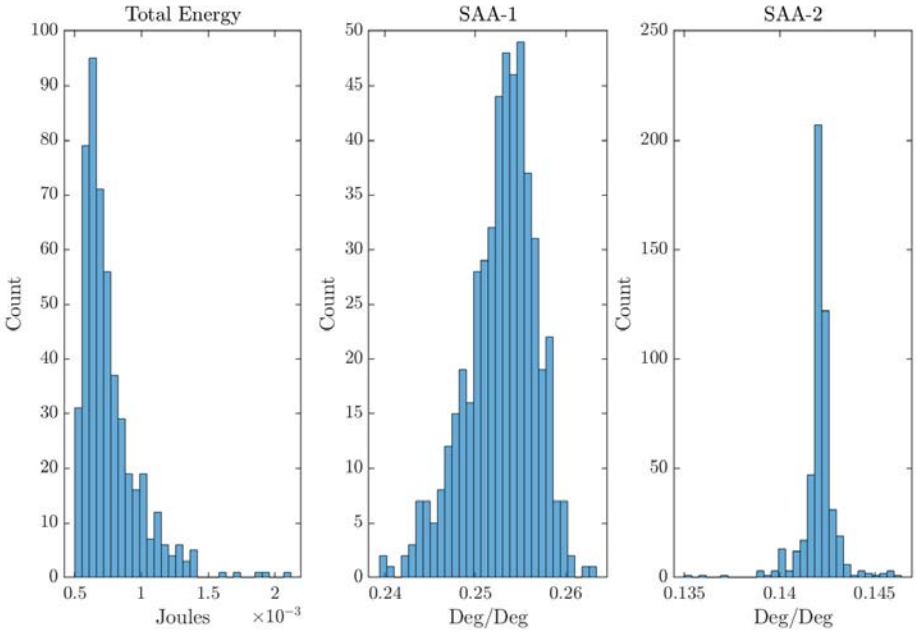

Figure 4.14: Case 7 Distribution of Normalized Terminal Residual Energy and SAA Pointing Error

4.2.3 Research Question 2 Summary.

Research Question 1 focused on deriving optimal control problem formulations utilizing the full, nonlinear equations of motion for the five-body system, while rolling back "soft" constraints on maximum gimbal velocity and torque to derive maneuvers simultaneously decreasing maneuver time while accounting for unwanted system vibrational excitation. These maneuver are derived with the assumption of perfect knowledge of system parameters. RQ 2 extends this concept in an attempt to increase system robustness by utilizing a sensitivity function to minimize maneuver sensitivity due to unknown variations in system parameters. The cost functional for the desensitized optimal control problems with risk aversion parameter α is summarized as,

$$J = (1-\alpha)\int_{t_0}^{t_f} \dot{\tau}^T \dot{\tau}\, dt + \alpha \|s(t_f)\|$$
$$\text{Case \#} \begin{cases} 5: & \alpha = 1 \\ 6: & \alpha = 0.91 \\ 7: & \alpha = 0.5. \end{cases} \tag{4.11}$$

As with cases 3 and 4, Case 5-7 maneuvers achieve a higher total system energy due to the removal of gimbal speed restrictions, allowing the maneuvers to complete in less time than with standard planning, thereby increasing payload availability. Likewise, by modeling and utilizing the nonlinear dynamics, the optimal maneuvers compensate for system flexibility and achieve the desired end condition with less residual energy, reducing vibrational settling time by 56 to 60%.

Table 4.13 contains the summary Monte Carlo results for RQ 2 cases showing percent improvement compared to Case 1a standard maneuver. All three desensitized maneuvers achieve the open-loop pointing objective 41% faster than the standard maneuver while showing significant improvements terminal pointing error. While the mean SAA-

Table 4.13: Research Question 2: Percent Improvement of Open-loop Mean Pointing Error and Terminal Energy for RQ 2 Maneuvers

	Mean Error (%)			Mean Total
Case #	Bus	SAA-1	SAA-2	Energy (%)
5	99.1	79.3	78.6	94.7
6	98.8	34.1	84.1	95.7
7	98.5	75.0	91.5	85.8

Table 4.14: Research Question 2: Percent Improvement of Closed-Loop Desensitized Maneuvers Compared to Standard Maneuver Without Notch Filtering

	Convergence Time Reduction (%)			
Case #	Bus	SAA-1	SAA-2	Total Energy
5	58.4	–	62	60.2
6	–	–	62	59.0
7	–	–	57.4	55.7

2 pointing error is improved with the additional weighting applied to the minimal jerk performance objective, when the control loop is closed, the Case 7 maneuver exhibits a longer convergence time than the Case 5 and 6 maneuvers. While minimizing jerk has been shown to create maneuver inherently robust against unwanted system excitation, it does not provide a direct measure of maneuver robustness that can be minimized[95, 96]. While minimizing jerk is a method of providing inherent robustness for a flexible system, for the model considered herein, better results are obtain by utilizing terminal sensitivity as a direct measure of maneuver robustness.

4.3 Unscented Optimal Control

While the desensitized optimal control problem utilized in RQ 2 assumes nominal parameter values and utilizes a first order sensitivity function to minimize the maneuver's

terminal sensitivity to parameter variation, RQ 3 employs the unscented method to directly model the underlying parameter distribution via the unscented transform as outlined in Section 2.4. For this RQ, the uncertain parameter space includes the primary mode about each bus axis along with the uncertain joint stiffness coefficients yielding the parameter vector $p = [\omega_1, \omega_4, \omega_7, k_1, k_2, k_3, k_4] \in \mathbb{R}^7$. Applying the unscented transform in accordance with Equation (2.52) leads to $N_\Sigma = 15$ sigma points. The optimal control problem then contains N_Σ independent sets of dynamics driven by a common control profile. In this manner, a single control profile can be calculated minimizing the unscented cost functional. By placing bounds on the mean state error for the N_Σ independent systems, the mean error can be driven towards zero, thereby increasing the robustness of the maneuver.

4.3.1 Case 8: Initial Ancillary Case.

For the initial case, the unscented parameters for Equation (2.52) are selected as $[\alpha, \beta, \kappa] = [1e^{-3}, 2, 0]$ resulting in a small standard deviation for the parameters in $p \in supp(p)$. It should be noted that the this value α is an unscented transform turning parameter from Julier et al. [44] and is different from the risk aversion parameter α outlined in Equation (4.7), though they serve similar purposes. For desensitized optimal control, as the value of α is increased, a higher weighting is placed upon the robustness term within the cost function. For the unscented optimal control problem considered herein, the magnitude of α determines the modeled Standard Deviation (SD) of the parameters within the sigma points, so larger values of α results in larger parameter SD and ideally, maneuvers robust against larger magnitudes of parameter variation.

Similar to the selection of a small value of α, the values of the mean allowable rigid-body state and path constraint errors, μ_x and μ_h, are chosen as $[0.01, 0.05]$ deg respectively allowing for a wider acceptable variation in final state error values. Taken together, the small parameter variance and large allowance on mean final error increases the likelihood of the existence to the proposed problem and serves as a starting pointing for future cases. The

endpoint constraint (μ_x) on the final state errors serves as an outer bound on the decision variables search space of the Non-Linear Programming (NLP) solver, and helps drive the solution towards a zero-mean-error solutions. By providing tight bounds on the search space for the endpoint constraints, the computational time of the NLP solver is reduced. The Case 8 unscented optimal problem formulation is then,

Given:

$$
\begin{aligned}
&\text{For } i = 1, ..., N_\Sigma \\
&\quad x_i = [q_1, q_2, q_3, q_4, x_2, x_3, x_4, x_5, x_{G2}, x_{G3}, x_{G4}, x_{G5}, \eta_1, \eta_4, \eta_7, ... \\
&\qquad \omega_x, \omega_y, \omega_z, \dot{x}_2, \dot{x}_3, \dot{x}_4, \dot{x}_5, \dot{x}_{G2}, \dot{x}_{G3}, \dot{x}_{G4}, \dot{x}_{G5}, \dot{\eta}_1, \dot{\eta}_4, \dot{\eta}_7]^T \in \mathbb{R}^{29} \\
&\quad \tau = [\tau_1, \tau_2, \tau_3, \tau_4, \tau_5]^T \in \mathbb{R}^8 \\
&\quad u = [\dot{\tau}_1, ..., \dot{\tau}_5] \in \mathbb{R}^8
\end{aligned}
\tag{4.12}
$$

$$
\begin{aligned}
\text{minimize} \quad & J[\cdot] = \sum_{i=1}^{N_\Sigma} w_i \left[[x_i(t_f; p_i) - x^f]^T [x_i(t_f; p_i) - x_f] \right] \\
\text{subject to} \quad & \dot{x}_i(t) = f(x_i(t), \tau(t); p_i), \quad i = 1, ..., N_\Sigma, \\
& \dot{\tau}(t) = u(t), \\
& q_i^0 = q_i^f = [0, 0, 0, 1], \\
& x_i^0 = [0, 0, 0, 0]\ deg, \\
& x_i^f = [0, 0, 19, -20]\ deg, \\
& |(\eta_i, \dot{\eta}_i)| \leq (36, 27)\ arcsec, arcsec/s, \\
& |\tau_{1,2-5}| \leq [1, 0.23]\ Nm, \\
& |\dot{\tau}| \leq 0.3\ Nm/s, \\
& \left| \sum_{i=1}^{N_\Sigma} w_i e(x_i(t_f, p_i); p_i) - x^f \right| \leq 0.01\ deg, \\
& \left| \sum_{i=1}^{N_\Sigma} w_i h(x_i(t_f, p_i); p_i) - h_{max} \right| \leq 0.05\ deg, \\
& t_0 \leq t \leq 50s.
\end{aligned}
\tag{4.13}
$$

The resulting control profiles and mean states for the unscented problem formulation are shown in Figure 4.15 through Figure 4.17 while the open loop Monte Carlo results are shown in Table 4.15. Due to the elimination of the maximum gimbal velocity, gimbal control is continuously applied throughout the maneuver allowing for a 41% decrease in total maneuver time, while simultaneously decreasing both SAA-1 & 2 mean pointing error by 33% and 18% respectively, as shown in Figure 4.18 which shows the distribution of normalized, terminal pointing error and total energy.

Table 4.15: Case 8 Open-Loop Monte Carlo Results for Minimum State Error ($\mu_x \leq 0.01$)

Case #	Filter	t_f (s)	Mean Error (deg) Bus	SAA-1	SAA-2	Mean Total Energy (J)	Control Cost
1a	Notch	84.3	0.064	0.026	0.19	1.3e-3	0.56
8	n/a	50	2.6e-3	0.018	0.16	9.6e-5	4.27

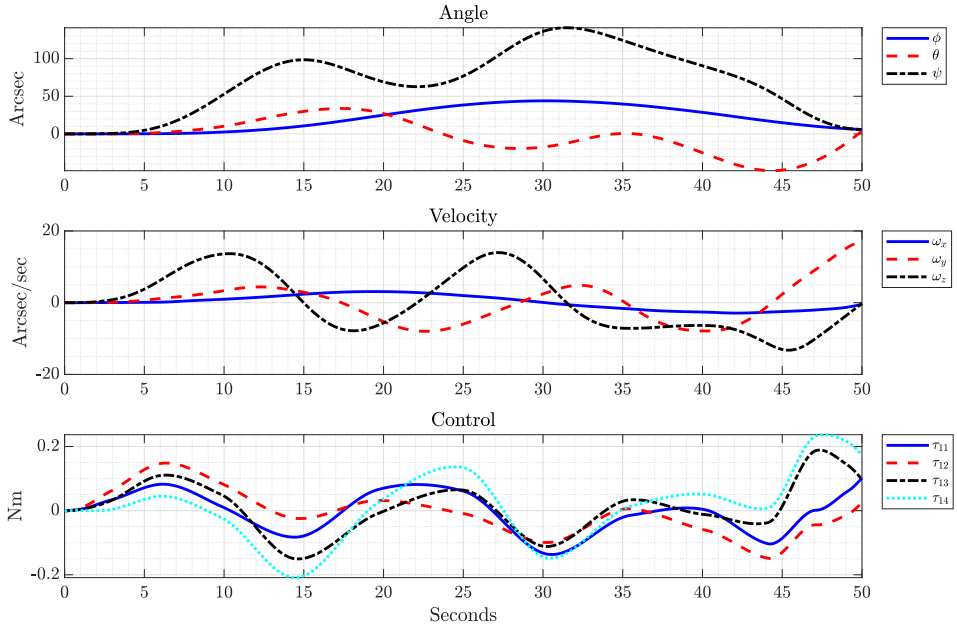

Figure 4.15: Case 8 Open-loop Maneuver: Bus States and Control

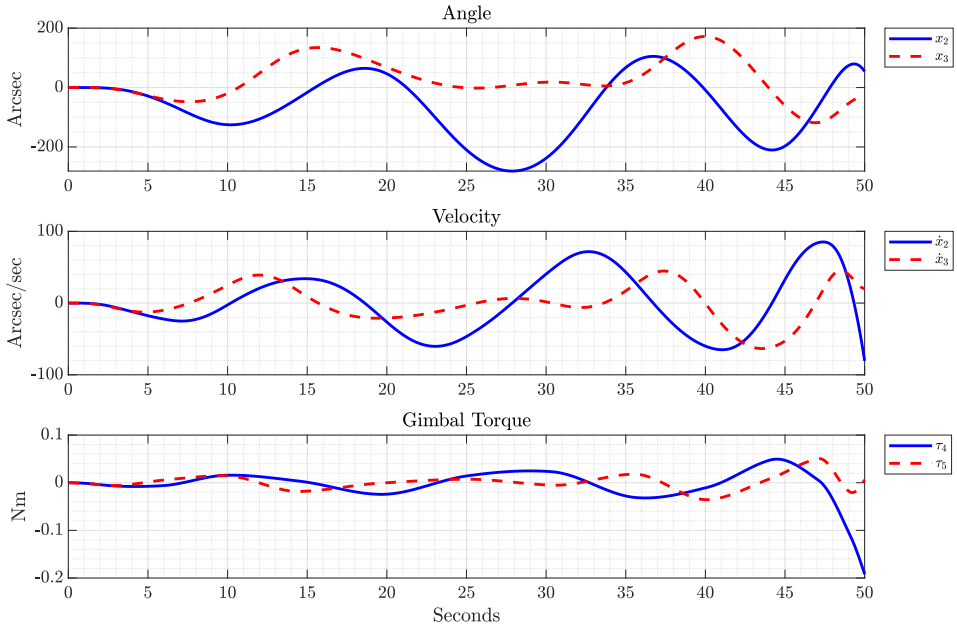

Figure 4.16: Case 8 Open-loop Maneuver: SAA-1 States and Control

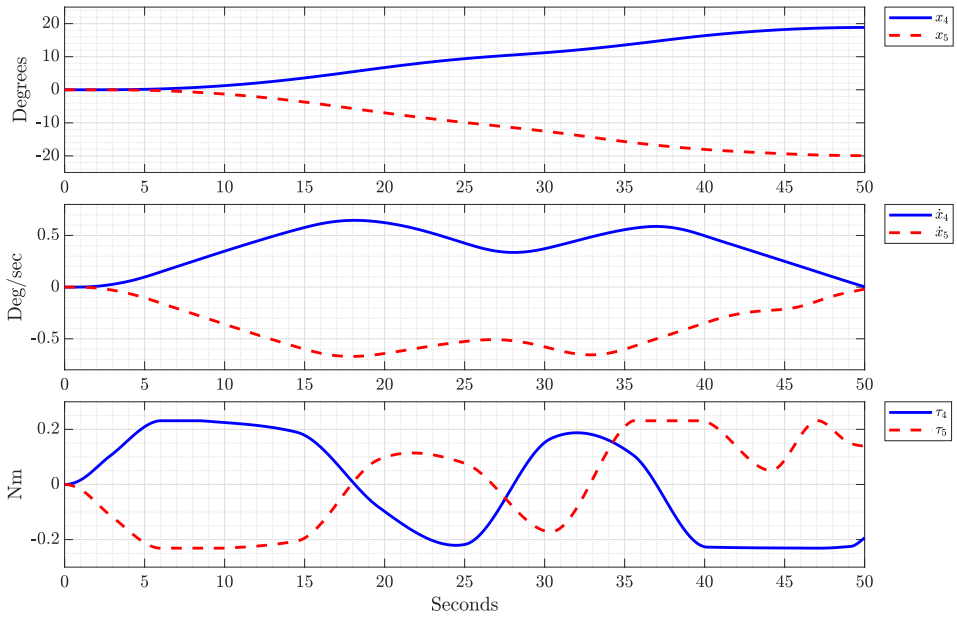

Figure 4.17: Case 8 Open-loop Maneuver: SAA-2 States and Control

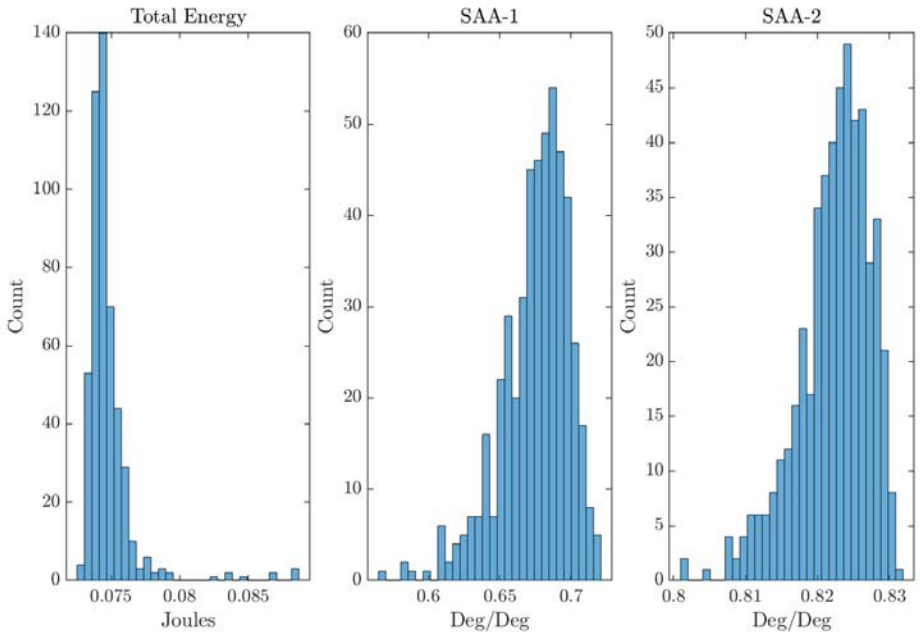

Figure 4.18: Case 8 Distribution of Normalized Terminal Residual Energy and SAA Pointing Error

4.3.2 Case 9: Second Ancillary Case.

From the Monte Carlo simulation of the Case 8 maneuver, the terminal pointing error for the SAA-1/2 antenna are $(0.018, 0.16)$ degrees respectively, however, Case 8 was initially formulated with wide bounds on the allowable mean state error in order to ensure the existence of an optimal solution. For Case 9, the objective is then to drive the optimal trajectory to have closer to zero-mean error in the face of the parametric uncertainty. The Case 9 problem formulation is then identical to Equation (4.13) except the allowable state and path constraint errors are reduced from $\mu_x = 0.01\ deg$ to $\mu_x = 0.005\ deg$.

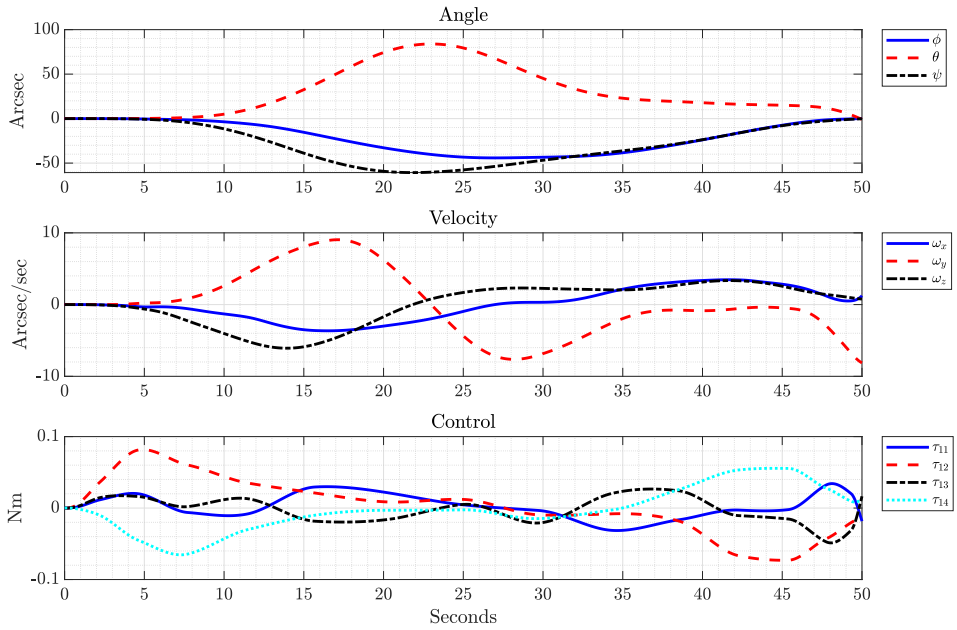

Figure 4.19: Case 9 Open-loop Maneuver: Bus States and Control

Figures 4.19 through 4.21 show the resulting rigid-body states and optimal control profiles when simulated open-loop with nominal parameter values while Table 4.16 shows the terminal open-loop results from the Monte Carlo simulation while Figure 4.22 shows the resulting normalized distributions. While Case 9 does not achieve zero-mean pointing

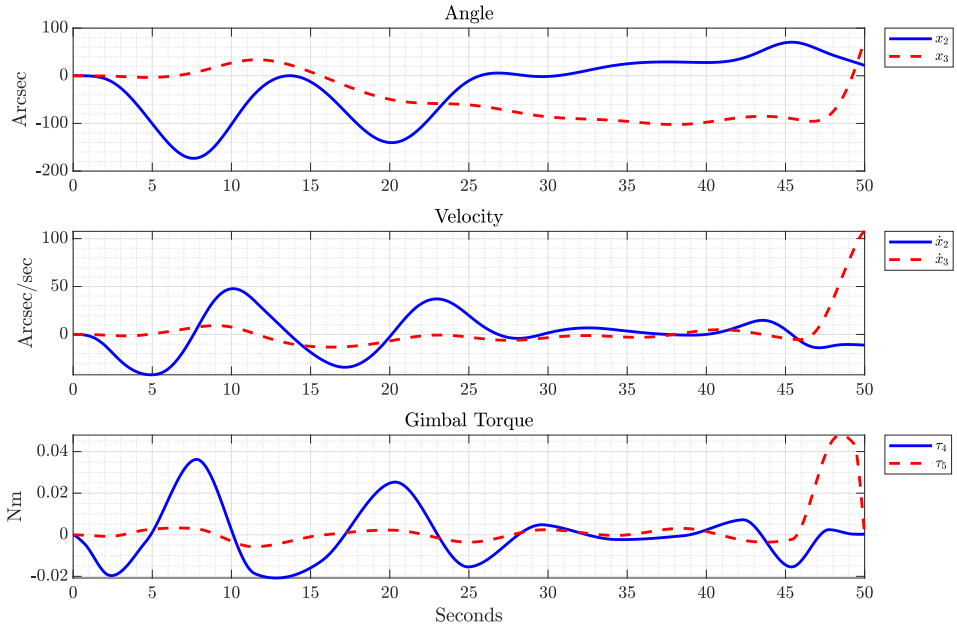

Figure 4.20: Case 9 Open-loop Maneuver: SAA-1 States and Control

error, it is successful in decreasing both SAA-1 and 2 terminal pointing error compared to both Cases 1 and 8, decreasing SAA-1/2 pointing error by 67% and 36% respectively while also decreasing terminal energy by 94% compared to the standard maneuver.

Table 4.16: Case 9 Open-Loop Monte Carlo Results for Minimum State Error ($\mu_x \leq 0.005$)

			Mean Error (deg)			Mean Total	Control
Case #	Filter	t_f (s)	Bus	SAA-1	SAA-2	Energy (J)	Cost
1a	Notch	84.3	0.064	0.026	0.19	1.3e-3	0.56
9	n/a	50	2.9e-4	8.5e-3	0.12	7.51e-5	2.61

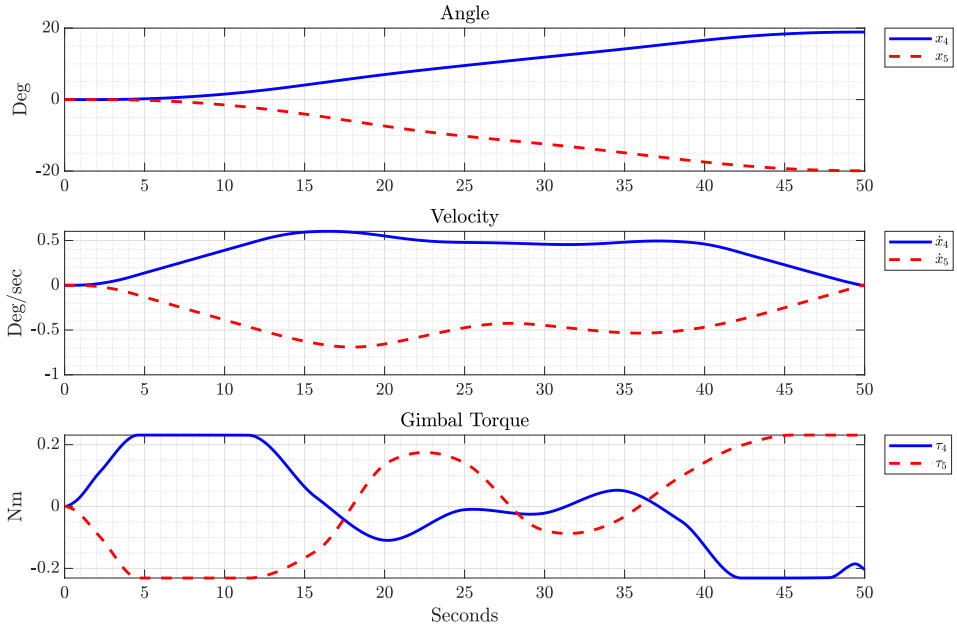

Figure 4.21: Case 9 Open-loop Maneuver: SAA-2 States and Control

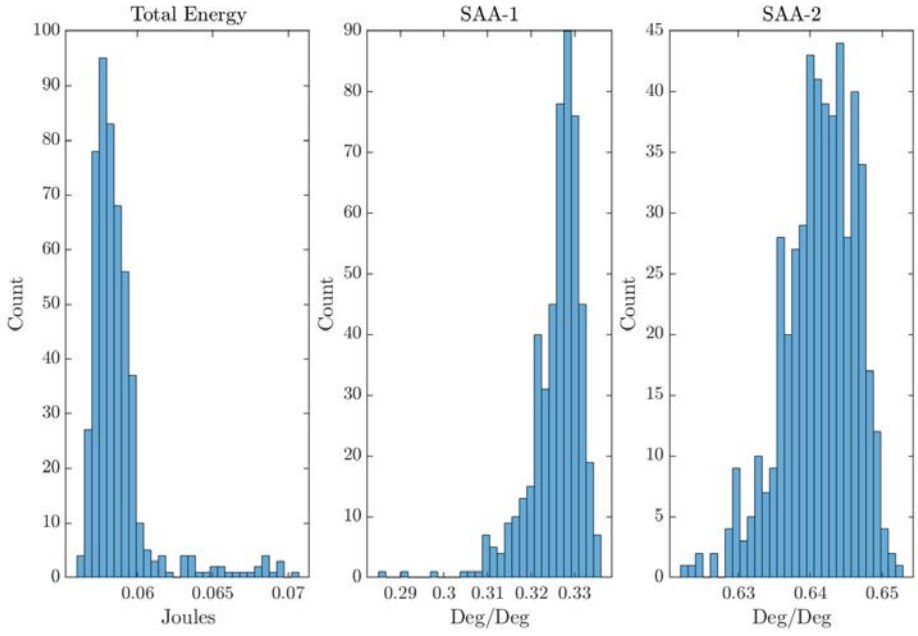

Figure 4.22: Case 9 Distribution of Normalized Terminal Residual Energy and SAA Pointing Error

4.3.3 Case 10: Minimal Mean Energy and State Error.

Cases 8 and 9 served as initial problem formulations where bounds on state error are successively tightened in order to approach a zero-mean error solution. While the modal variables are bounded for each of the sigma points based on the maximum magnitude from the standard maneuver, no further actions have been taken to increase the system robustness against residual vibration and energy in the system. To further increase maneuver robustness, the Case 10 problem formulation incorporates terminal energy (Equation (3.27)) of each sigma point into the cost functional,

$$J[\cdot] = \sum_{i=1}^{N_\Sigma} w_i \left[\gamma_1 TE_i + \gamma_2 \left[[x_i(t_f; p_i) - x^f]^T [x_i(t_f; p_i) - x^f] \right] \right]. \tag{4.14}$$

This new functional is then a weighted sum of each sigma point's terminal energy and final state error. To normalized the relative magnitudes of the two cost components to be of the order 1, the weighting terms $\gamma_{1,2} = [5e^{-5}, 1e^{-7}]$ are introduced. To further increase the robustness of the Case 10 maneuver, the unscented tuning parameter α is changed from $\alpha = 1e^{-3} \rightarrow 1e^{-1}$. Increasing α serves to increase the variance of the modeled parameters from the unscented transform, thereby increasing their spread about the mean and forcing the optimal control problem to deal with increased error compared to nominal parameter values.

Table 4.17: Case 10 Open-Loop Simulation Results for Minimum State Error ($\mu_x \leq 0.005$)

			Error (deg)			Total	Control
Case #	Filter	t_f (s)	Bus	SAA-1	SAA-2	Energy (J)	Cost
1a	Notch	84.3	0.064	0.026	0.19	1.3e-3	0.56
10	n/a	50	0.008	0.017	0.092	3.13e-5	3.83

The resulting terminal control profile is first simulated open-loop assuming nominal parameter values with the resulting state trajectories shown in Figures 4.23 through 4.25

while Table 4.17 shows the results of the Monte Carlo simulation as compared to Case 1a with the normalized distributions shown in Figure 4.26.

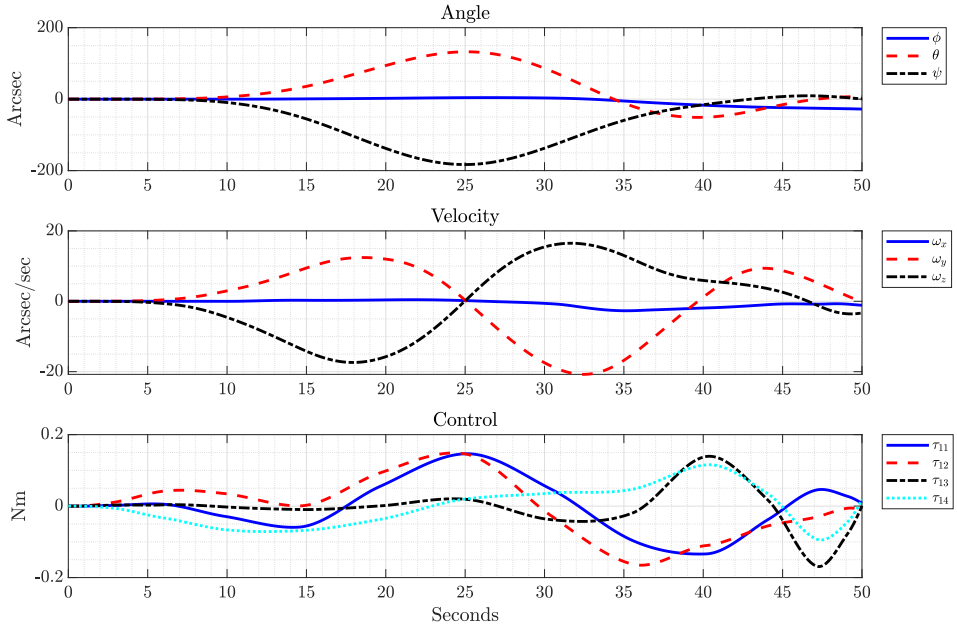

Figure 4.23: Case 10 Open-loop Maneuver: Bus States and Control

The results in Table 4.17 show that open-loop, Case 10 generates a trajectory resulting in mean pointing error improvements of 36 and 52% for SAA-1/2 respectively while decreasing mean terminal energy by 97.5%. Closed-loop simulations shown similar improvements with bus pointing convergence improving by 56% and SAA-2 convergence improving by by 62%. As with the previous optimal maneuver, terminal total energy convergence is achieved 24% faster for Case 10 versus Case 1a.

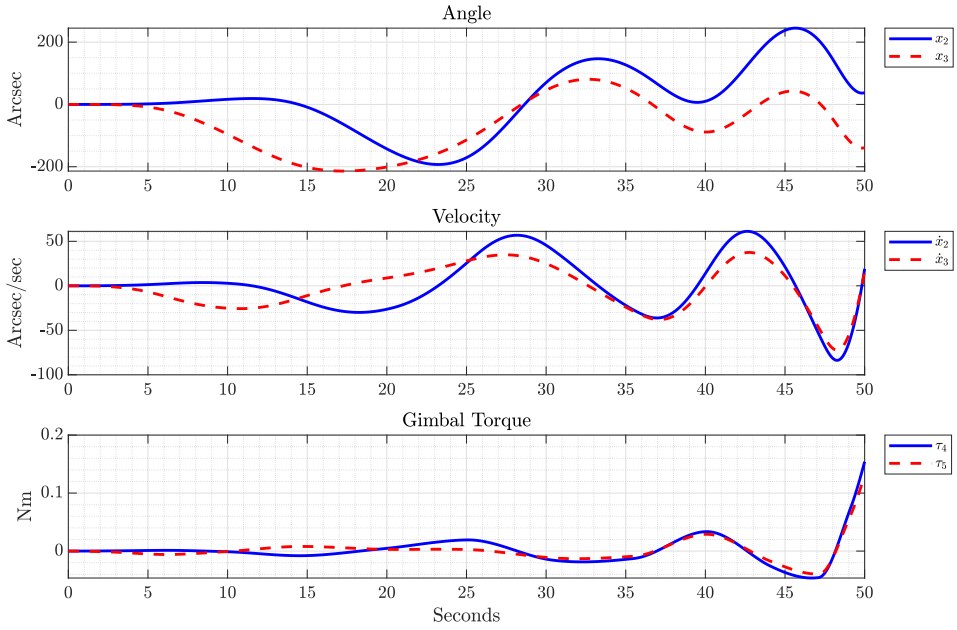

Figure 4.24: Case 10 Open-loop Maneuver: SAA-1 States and Control

Table 4.18: Cases 10 Closed-Loop Convergence Results

		Planned	Convergence Time (s)			
Case #	Filter	t_f(s)	Bus	SAA-1	SAA-2	Total Energy
1a	Notch	84.3	89.3	–	131.6	145.2
10	n/a	50	39.2	–	50	110.3

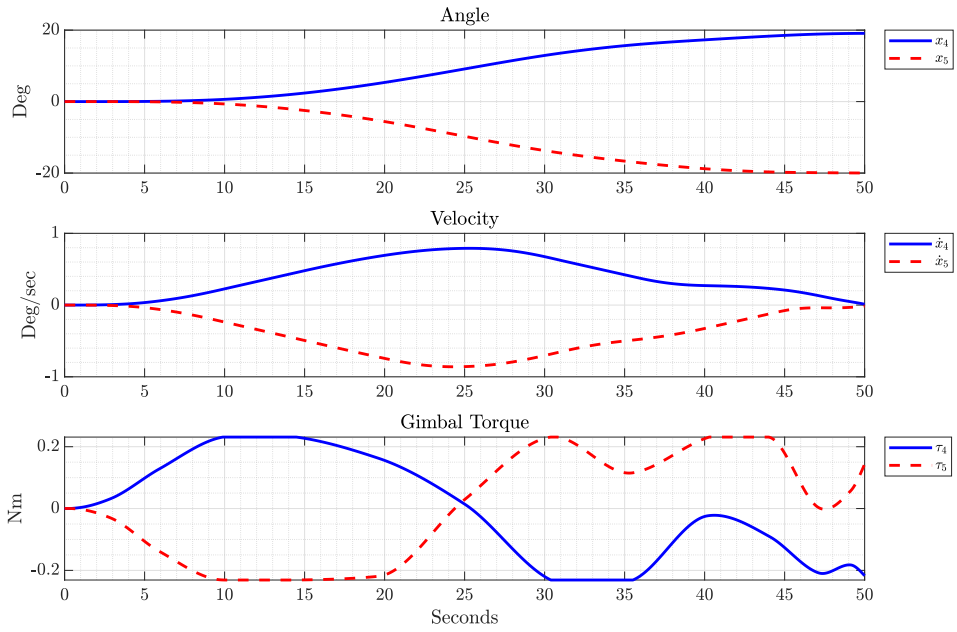

Figure 4.25: Case 10 Open-loop Maneuver: SAA-2 States and Control

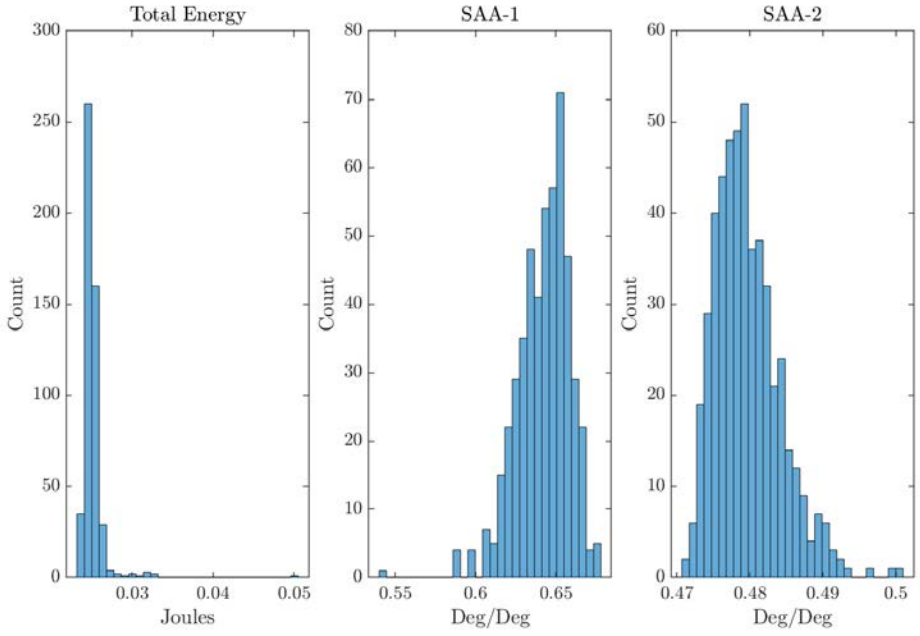

Figure 4.26: Case 10 Distribution of Normalized Terminal Residual Energy and SAA Pointing Error

4.3.4 Research Question 3 Summary.

Research Question 3 derives antenna slew maneuvers decreasing total maneuver time while minimizing system vibrational excitation and impacts to adjacent apertures, while remaining robust against variations in system parameters. While RQ 2 employed a sensitivity based method, which assumes a models nominal parameter values and minimizes the terminal sensitivity of the maneuver, RQ 3 directly models variations in the parameters of concerns through the employment of the unscented transform, and drives multiple parallel dynamics models with a common control input. The method minimizes mean terminal error for the independent sets of dynamics and thus increase the robustness of the derived maneuver.

Table 4.19 contains a summary table of the open-loop Monte Carlo results for Cases 8-10. Cases 8 and 9 represented ancilliary optimal control problems formulated to at first ensure the existence of a solution, and then subsequently tighten bounds to arrive at a maneuver with near zero-mean pointing error. As the allowable mean state error was decreased from $0.01 \rightarrow 0.005$ degrees, the resulting solution's mean SAA-2 pointing error decreased, going from a 17.8% to a 35.9% improvement. Similarly, the mean terminal energy decrease from a 92.5% to a 94.1 % improvement. Case 10 then changed the unscented tuning parameter α to increase the parameter SD of the sigma points, while also updating the cost functional to incorporate and minimize terminal energy. The resulting open-loop Monte Carlo results decrease SAA-2 mean pointing error by a further 16% while reducing mean terminal energy by a further 3.4%.

Table 4.20 contains the percentage improvements for the closed-loop simulations of the optimal maneuvers. As with the open-loop results, as the tuning parameters are tightened on subsequent cases, the convergence time for the optimal maneuvers improve. While Case 10 exhibited lower mean SAA-2 than Case 9, the mean error for both cases is within the convergence criteria utilized for the closed-loop analysis and thus exhibit

Table 4.19: Research Question 3: Percent Improvement of Open-loop Mean Pointing Error and Terminal Energy

	Mean Error (%)			Mean Total
Case #	Bus	SAA-1	SAA-2	Energy (%)
8	96.0	32.5	17.8	92.5
9	99.6	67.4	35.9	94.1
10	87.5	35.8	52.0	97.5

Table 4.20: Research Question 3: Percent Improvement of Closed-Loop Unscented Maneuvers Compared to Standard Maneuver Without Notch Filtering

	Convergence Time Reduction (%)			
Case #	Bus	SAA-1	SAA-2	Total Energy
8	48.5	–	55	15.9
9	59.3	–	62	20.8
10	56.2	–	62	24.0

identical convergence time improvements. Due to the inclusion of terminal energy is the cost functional of Case 10, the open-loop mean terminal error is lower than the other cases which is also the case when the control loop is closed exhibiting a 24% improvement over the standard maneuver as seen in Figure 4.27. Due to the removal of the "soft" constraints on maximum gimbal velocity, the dynamic energy of Case 10 is an order of magnitude larger than the standard maneuver in Case 1a, allowing the optimal maneuver to achieve the pointing objectives 62% faster and still achieves energy convergence 24% faster.

Figure 4.28 visualizes the azimuth and elevation trajectories for Case 1a and cases 8-10 where the time axis has been normalized to be between $t \in [0, 1]$ allowing a better comparison of the maneuver shape. While the standard maneuver is restricted to a straight-line maneuver in gimbal space, the optimal trajectories are not subjected to such artificial

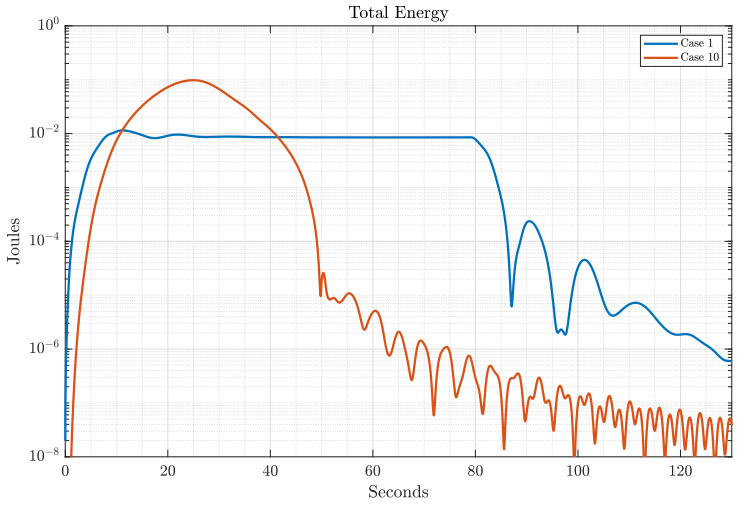

Figure 4.27: Mean System Energy for Cases 1 and 10 (Mean of Eq. 3.27)

restrictions and are allowed to traverse any allowable gimbal angle. This allows the pseudospectral optimal control trajectories to take advantage of the nonlinear dynamics, and advantageously utilize coupling between the slewing gimbals as well as the root body to not only achieve a faster maneuver, but through the robust formulation, decrease excitation of the system's flexible modes and complete the maneuver with less pointing error and lower total system energy, even when subjected to parameter uncertainty.

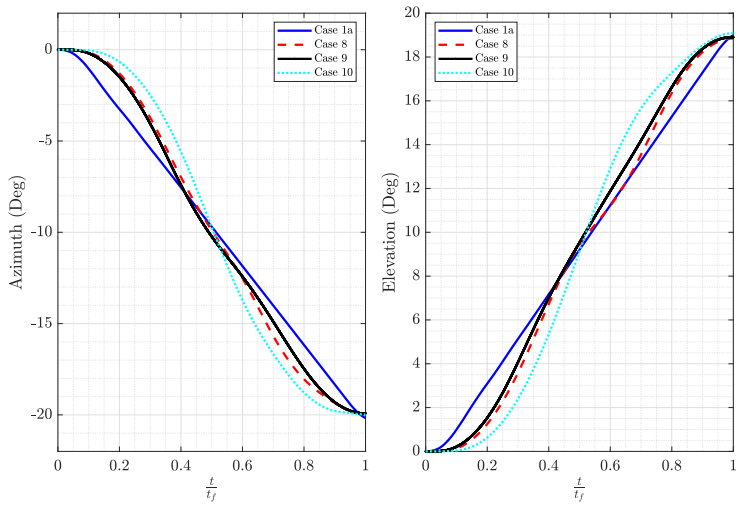

Figure 4.28: Comparison of Mean Azimuth and Elevation Trajectories versus Normalized Time

4.4 Robust Maneuvers Utilizing Reduced Order Models

Previous results have shown how PSOC techniques can be utilized to compute TDRS antenna slew maneuvers that increase payload availability through decreased maneuver length. By utilizing a more complete dynamics model of the flexible system, RQ 1 showed that conservative "soft" constraints could be eliminated so long as the true underlying problem of system flexibility is modeled and bounded within the optimal control problem formulation. The implication of this method is a rapid increase in the number of modeled states which impacts the computational time necessary for the NLP solver to converge to an optimal solution.

The results in Sections 4.2 and 4.3 demonstrated that both robust optimal control methods can be utilized to generate trajectories robust against parameter variations, albeit at increased computational compared to the standard maneuver. The objective of RQ 4 is then to determine how the methods leveraged in RQ 2-3 can be used with reduced order models as a means of deriving robust maneuvers but at a reduced computational cost. The

complexity of the mathematical model exists on a continuum, where on one end is the single-body planning methods utilized for standard maneuver planning. The other end of the continuum could be a FEM model with 1000's of elements. In theory, assuming the model is accurate, the more complex the model, the more accurate and optimal the results. However, there is a computational cost for each additional included state and there exists a point of diminishing returns where performance improvements from an expanded model are outweighed by the increased computation time.

Research Question 4 explores utilizing a 3-body and 2-body models to derive SAA-2 maneuvers which are robust against parameter variations and still minimize impacts to SAA-1 even though the corresponding SAA-1 bodies are no longer modeled as distinct states within the dynamics. For optimal maneuvers derived utilizing the five-body model, the dynamic interaction between each of the bodies is fully accounted for and the subsequent control profiles to ameliorate the interaction is incorporated into each bodies optimal control profile τ_{opt}. This negates the necessity of the bus controller incorporating counter-steering torques for the antenna maneuver into the bus feedforward control as shown in Equation (3.20).

For the three-body model, the SAA-1 states are no longer modeled within the dynamics and thus the bus control torque necessary to maintain SAA-1 pointing are no longer included within the resulting optimal control profiles τ_1^{opt}. For maneuvers derived using the three-body model, SAA-1 bus counter-steering torques are then implemented within the controller as,

$$\tau_{cs} = \begin{bmatrix} \bar{M}_{12} & \bar{M}_{13} \end{bmatrix} \begin{bmatrix} \ddot{x}_2^{Des} \\ \ddot{x}_3^{Des} \end{bmatrix} \tag{4.15}$$

while for optimal solutions derived utilizing the two-body model, bus counter-steering torques for both antenna are calculated in accordance with Equation (3.20).

4.4.1 Case 11: Three Body Minimal Terminal Sensitivity.

For the maneuvers considered herein, SAA-1 is assumed to be in an Auto Track (AT) mode, which for TDRS exhibits a maximum gimbal rate of 0.02 deg/s [4]. When considered against the SAA-2 maneuver duration of 50s, the maximum angular distance covered by SAA-1 is one degree. While TDRS exhibits a high ratio of antenna to bus inertia, a one degree change in gimbal orientation could be considered to have a negligible effect on overall system inertia properties. The three-body problem formulations take advantage of this fact and the SAA-1 states are assumed to be static and the corresponding states representing gimbal position/velocity are eliminated from the dynamic equations. The mass properties of Bodies B_2 and B_3 are then subsumed into B_1 yielding the combined root body $\bar{B}_1$ as shown in Figure 3.3.

In the five-body problem formulation, the maximum angular rate of the bus is unbounded, however, due to the path constraints on SAA-1 pointing, the resultant maneuvers effectively place a maximum bound on the bus trajectory to ensure the path constraint bounds are not violated. For the three-body problem, the states representing SAA-1 are no longer modeled, therefore the path constraint on SAA-1 pointing error is eliminated as well. To ensure the resulting three-body maneuver does not induce excessive bus rotation negatively impacting SAA-1 pointing when simulated against the full model, a maximum bus rate of 0.001 deg/s is enforced, which is derived from the maximum rate exhibited by TDRS during an antenna maneuver [4].

Case 11 then formulates a three-body desensitized optimal control problem seeking to minimize terminal sensitivity of the SAA-2 maneuver due to variations in the remaining gimbal stiffness and bus primary mode frequencies. The remaining system states and controls are given in Equation (4.16) while the optimal control problem formulation in standard format is given as,

Given:

$$
\begin{aligned}
& x = [q_1, q_2, q_3, q_4, x_4, x_5, x_{G4}, x_{G5}, \eta_1, \eta_4, \eta_7, ... \\
& \quad \omega_x, \omega_y, \omega_z, \dot{x}_4, \dot{x}_5, \dot{x}_{G4}, \dot{x}_{G5}, \dot{\eta}_1, \dot{\eta}_4, \dot{\eta}_7, \tau_1, \tau_4, \tau_5]^T \in \mathbb{R}^{27} \\
& s \in \mathbb{R}^{21\times 5} \\
& u = [\dot{\tau}_1, \dot{\tau}_4, \dot{\tau}_5] \in \mathbb{R}^6
\end{aligned} \tag{4.16}
$$

$$
\begin{aligned}
\text{minimize} \quad & J = \|s(t_f)\| \\
\text{subject to} \quad & 0 = \dot{x}(t) - f_x(x(t), u(t); \bar{p}), \\
& 0 = \dot{s}(t) - f_s(x(t), s(t); \bar{p}), \\
& q^0 = q^f = [0, 0, 0, 1], \\
& x^0_{4,5} = x^0_{G4,G5} = [0, 0]\ deg, \\
& x^f_{4,5} = x^f_{G4,G5} = [19, -20]\ deg, \\
& |(\eta, \dot{\eta})| \leq (36, 27)\ arcsec, arcsec/s, \\
& |\omega| \leq 0.001\ deg/s, \\
& |\tau_1| \leq 1\ Nm, \\
& |\tau_{4,5}| \leq 0.23\ Nm, \\
& |\dot{\tau}| \leq 0.3\ Nm/s, \\
& t_f \leq 50s.
\end{aligned} \tag{4.17}
$$

The resulting open-loop trajectories and control profiles for the bus and SAA and shown in Figures 4.29 through 4.31. The corresponding open-loop Monte Carlo results for terminal pointing error and energy are shown in Table 4.21. The results for Case 5 are included as a means of comparing the results of the five-body problem formulation with the three-body results of Case 11. When comparing the optimal bus trajectories of Cases 5 and 11, it is quickly apparent that Case 5 exhibits higher bus slewing rates and maximum Euler angle of approximately 15 arcsec/s and 150 arcsec respectively while the three-body

formulation of Case 11 exhibits a maximum of approximately 0.5 arcsec/s and 3 arcsec. Even though Case 5 exhibits higher maximum angular deviation and velocity, the open-loop terminal pointing errors are lower than Case 11, as seen in Table 4.21 where Case 5 results in 0.068 degrees of error versus 0.13 degrees for Case 11. Likewise, the terminal residual energy for Case 5 is an order of magnitude lower.

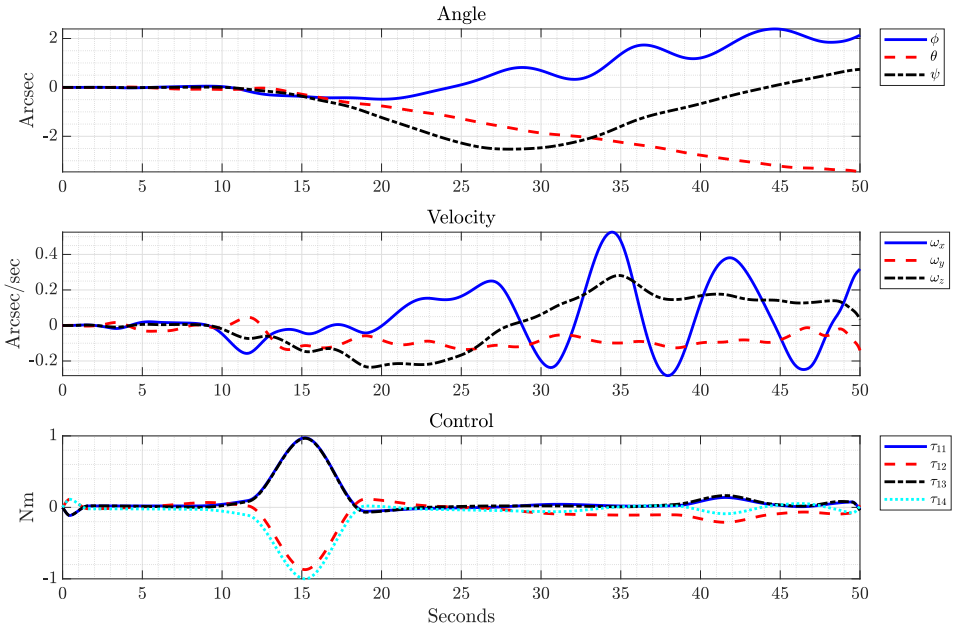

Figure 4.29: Case 11 Open-loop Maneuver: Bus States and Control

Table 4.21: Case 11 Open-Loop Monte Carlo Results for Minimal Terminal Sensitivity

Case #	Filter	t_f (s)	Mean Error (deg) Bus	SAA-1	SAA-2	Mean Total Energy (J)	Control Cost
1a	Notch	84.3	0.064	0.026	0.19	1.3e-3	0.56
5	n/a	50	5.6e-4	5.5e-3	0.068	3.7e-7	3.75
11	n/a	50	0.0012	0.0016	0.13	7.53e-7	13.5

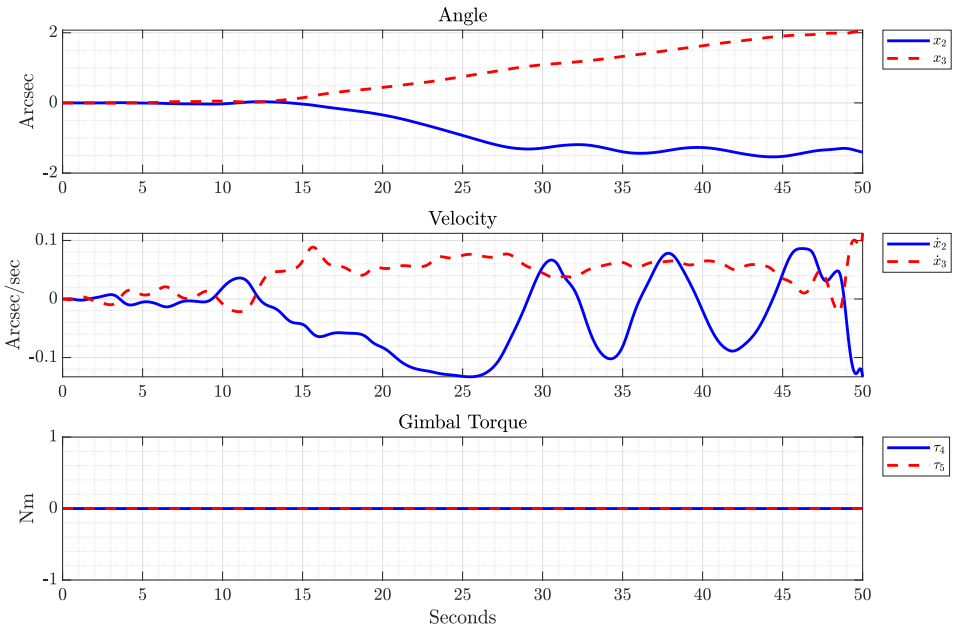

Figure 4.30: Case 11 Open-loop Maneuver: SAA-1 States and Control

While the Case 11 exhibits higher terminal error and residual energy than Case 5, the results still represent a significant improvement over the standard maneuver, as further detailed in the closed-loop convergence times shown in Table 4.22. Similarly to Case 5, Case 11 achieves SAA-2 pointing convergence at maneuver completion while never violating SAA-1 pointing requirements. Case 11 also achieves system energy convergence after 64 seconds, which is approximately 6 seconds longer than Case 5, but still represents an 81 second improvement over the standard maneuver.

An open-loop Monte Carlo analysis was performed for the maneuver where the resulting histogram distributions for terminal energy and SAA pointing errors are shown in Figure 4.32 with results normalized by the Case 1a, standard maneuver results. The results of this analysis show significant improvements in maneuver robustness compared to the standard maneuver with a 34.4% improvement in mean SAA-2 error with a 85.8% reduction in SD. While a 34% improvement is significant, the three-body results still fall

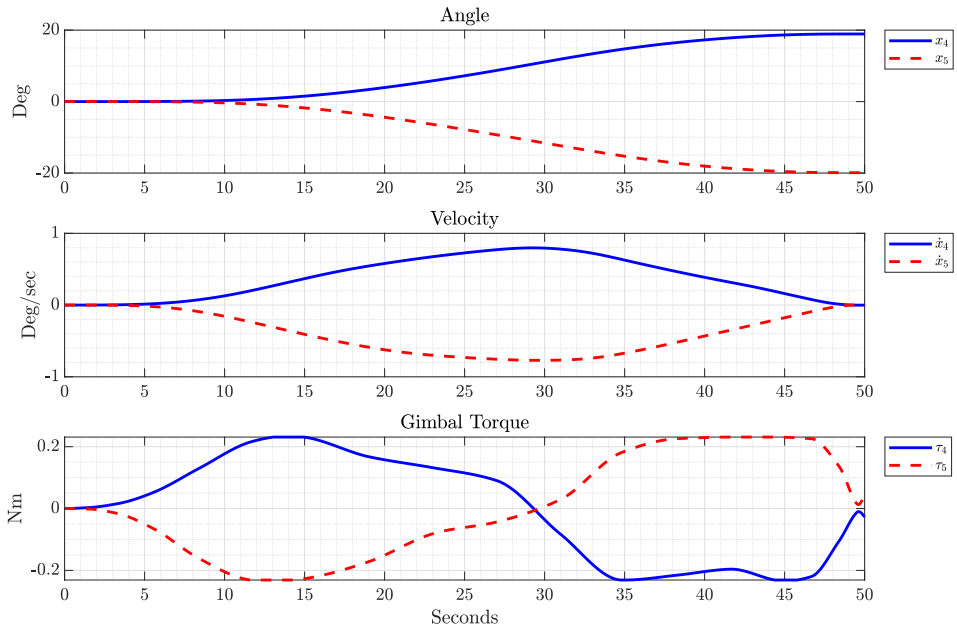

Figure 4.31: Case 11 Open-loop Maneuver: SAA-2 States and Control

Table 4.22: Case 11 Closed-Loop Convergence Results for Three-Body Minimum Terminal Sensitivity

		Planned	Convergence Time (s)			
Case #	Filter	t_f	Bus	SAA-1	SAA-2	Total Energy
1	Notch	84.3	89.3	–	131.6	145.2
5	n/a	50	37.2	–	50	57.8
11	n/a	50	–	–	50	64

short of that achieved with the five-body model of Case 5 exhibiting a 64.4% improvement in SAA-2 pointing error.

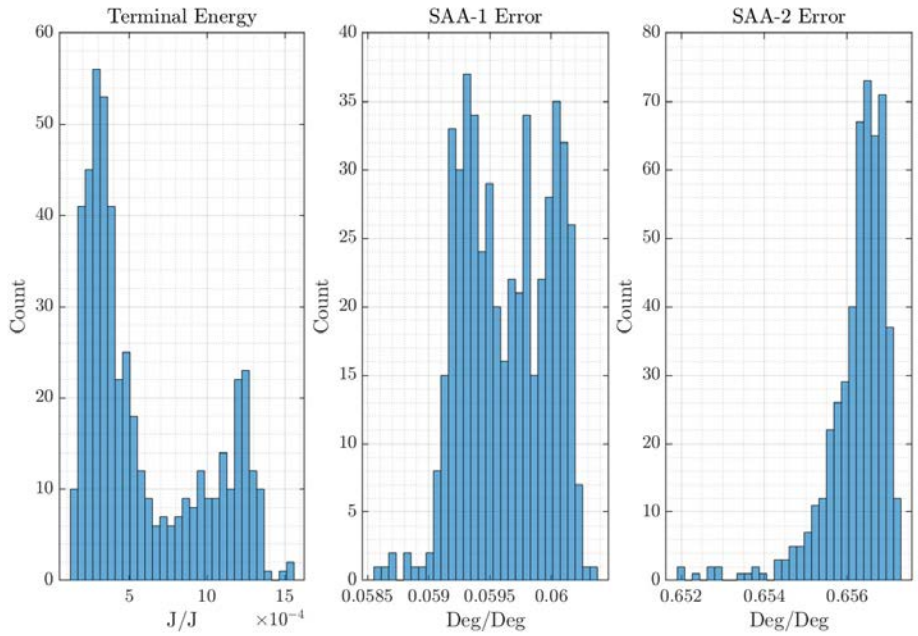

Figure 4.32: Case 11 Distribution of Normalized Terminal Residual Energy and SAA Pointing Error

4.4.2 Cases 12/13: Three Body Minimal Jerk and Terminal Sensitivity.

For Cases 12 and 13, the cost function is modified to be consistent with Equation (4.7) where an additional running cost is added as a performance objective along with the risk aversion parameter α, where for Case 12 $\alpha = 0.91$ and for Case 13 $\alpha = 0.5$, successively increasing the weighting on the performance objective of minimizing control jerk into the system. The three body states are as stated in Equation (4.16) with the problem formulation given as,

$$
\begin{aligned}
\text{minimize} \quad & J = (1-\alpha)\int \dot{\tau}^T\dot{\tau}\,dt + \alpha\|s(t_f)\| \\
\text{subject to} \quad & 0 = \dot{x}(t) - f_x(x(t), u(t); \bar{p}), \\
& 0 = \dot{s}(t) - f_s(x(t), s(t); \bar{p}), \\
& q^0 = q^f = [0,0,0,1], \\
& x^0_{4,5} = x^0_{G4,G5} = [0,0]\ deg, \\
& x^f_{4,5} = x^f_{G4,G5} = [19,-20]\ deg, \\
& |(\eta, \dot{\eta})| \leq (36, 27)\ arcsec, arcsec/s, \\
& |\omega| \leq 0.001\ deg/s, \\
& |\tau_1| \leq 1\ Nm, \\
& |\tau_{4,5}| \leq 0.23\ Nm, \\
& |\dot{\tau}| \leq 0.3\ Nm/s, \\
& t_f \leq 50s.
\end{aligned}
\tag{4.18}
$$

The resultant bus and payload states and control for Case 12 are shown in Figure 4.33 through Figure 4.35 while the results for Case 13 are given in Figure 4.36 through Figure 4.38. Table 4.23 shows the results of the Monte Carlo simulation for Cases 12 and 13 with the corresponding five-body cases for reference while the resulting distributions are shown in Figures 4.39 and 4.40. Comparing the corresponding five and three body cases, mean bus pointing error and SAA-2 error are worse for the three-body problem formulations. When $\alpha = 0.91$, Case 6 achieves a 73.6% improvement in mean SAA-2 error while the three body formulation of Case 12 only achieves 10.4% improvement. Similarly, the SD for cases 6 and 12 are improved by 76.8% and 11% respectively. Comparing the results of cases 7 and 13 yields a similar results where the three-body problem formulation yields a 39.5% improvement when compared to the standard maneuver but does not achieve the 85.8% improvement of the five-body formulation (Case 7).

Table 4.23: Case 12/13 Open-Loop Monte Carlo Results for Minimal Jerk and Terminal Sensitivity

Case #	Filter	α	# Bodies	t_f (s)	Mean Error (deg) Bus	SAA-1	SAA-2	Mean TE (J)	Control Cost
1a	Notch	n/a	1	84.3	0.064	0.026	0.19	1.3e-3	0.56
6	n/a	0.91	5	50	7.6e-4	0.017	0.051	2.8e-7	15.1
7	n/a	0.5	5	50	9.8e-4	6.6e-3	0.027	9.7e-7	4.3
12	n/a	0.91	3	50	3.3e-3	5.0e-3	0.17	1.1e-5	4.0
13	n/a	0.5	3	50	9.4e-4	1.2e-3	0.12	3.1e-7	3.9

The closed-loop convergence results for cases 12 and 13 are shown in Table 4.24 which show favorable results when compared to the standard maneuver. While neither maneuver achieves pointing convergence for SAA-2 at the desired maneuver completion, the additional settling time still represents a 59-62% improvement over the standard maneuver, and a 56-59% improvement in energy convergence. While the open-loop results showed the five-body problems achieving lower mean pointing errors, the control system is closed, the pointing and energy convergence times are nearly identical.

Table 4.24: Case 12/13 Closed-Loop Convergence Results for Three-Body Minimum Jerk and Terminal Sensitivity

Case #	Filter	Planned t_f	Convergence Time (s) Bus	SAA-1	SAA-2	Total Energy
1	Notch	84.3	89.3	–	131.6	145.2
6	n/a	50	–	–	50	59.5
7	n/a	50	–	–	56.1	64.3
12	n/a	50	–	–	53.8	64.6
13	n/a	50	–	–	50.2	59.4

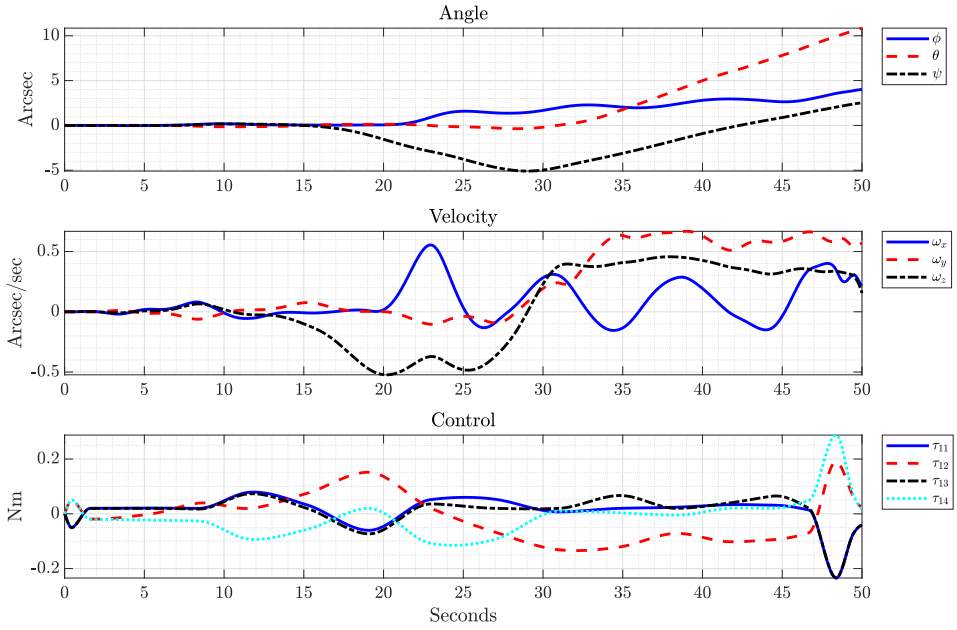

Figure 4.33: Case 12 Open-loop Maneuver: Bus States and Control

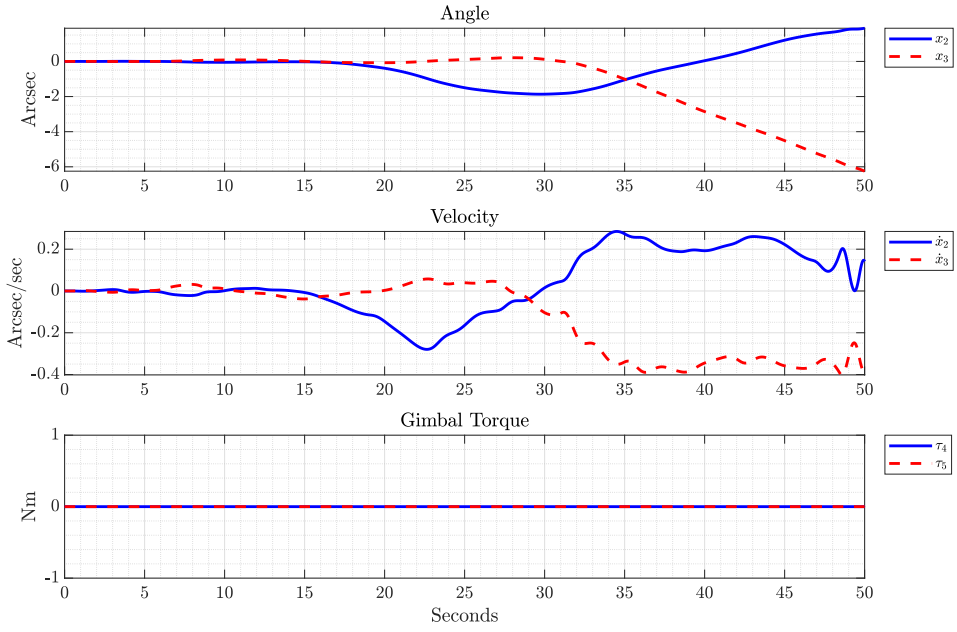

Figure 4.34: Case 12 Open-loop Maneuver: SAA-1 States and Control

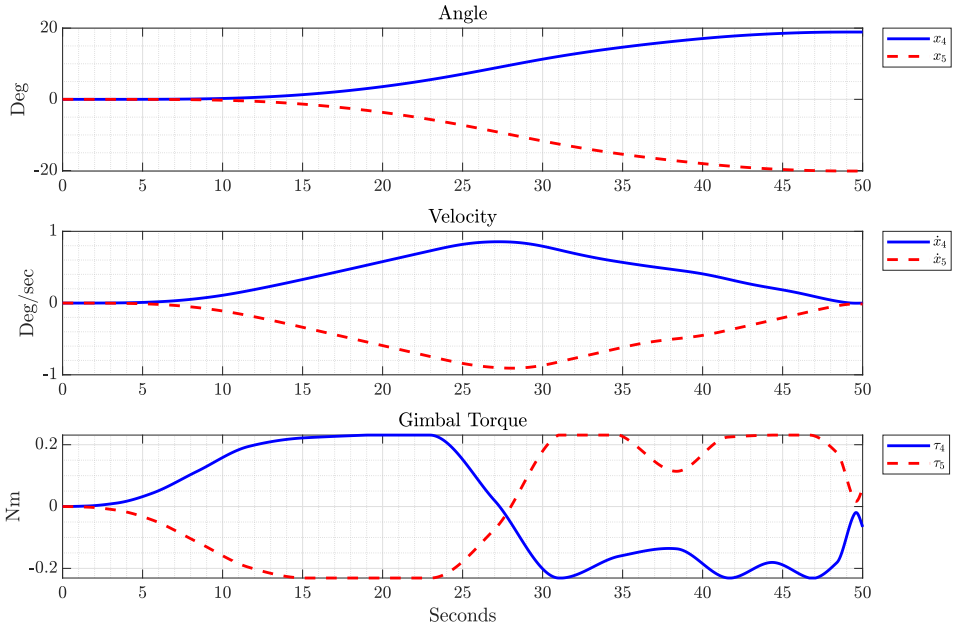

Figure 4.35: Case 12 Open-loop Maneuver: SAA-2 States and Control

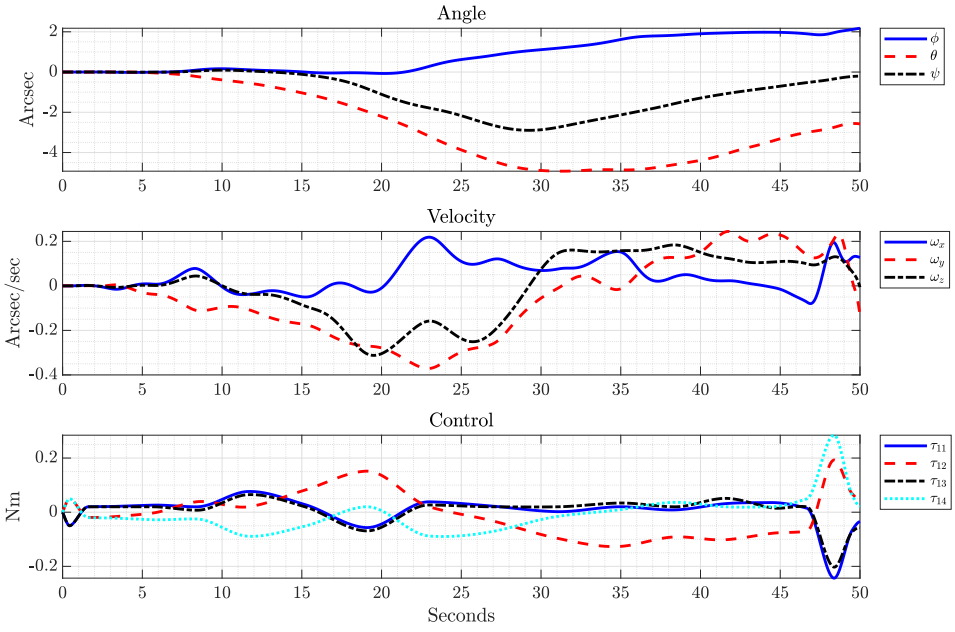

Figure 4.36: Case 13 Open-loop Maneuver: Bus States and Control

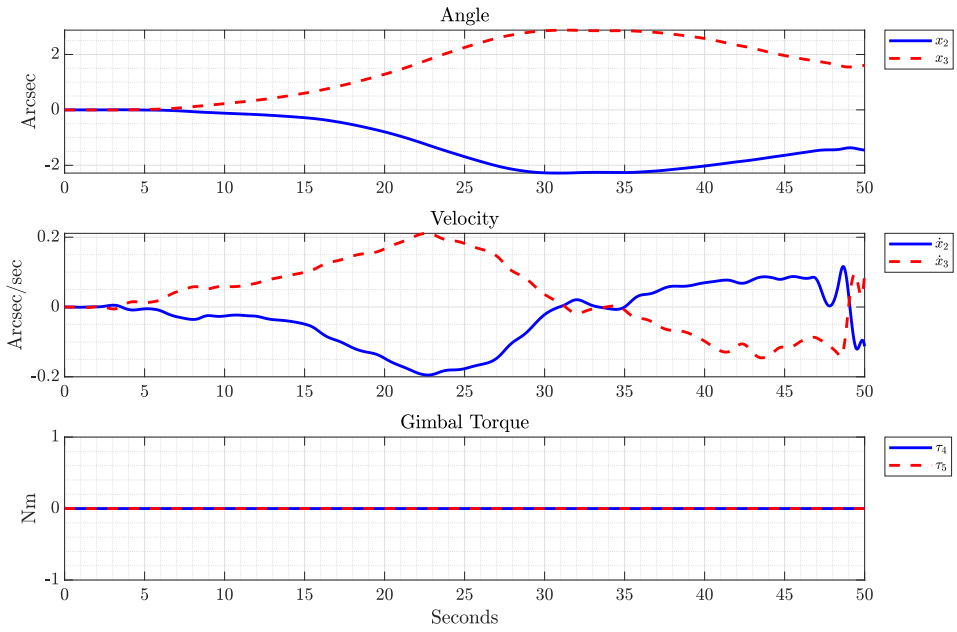

Figure 4.37: Case 13 Open-loop Maneuver: SAA-1 States and Control

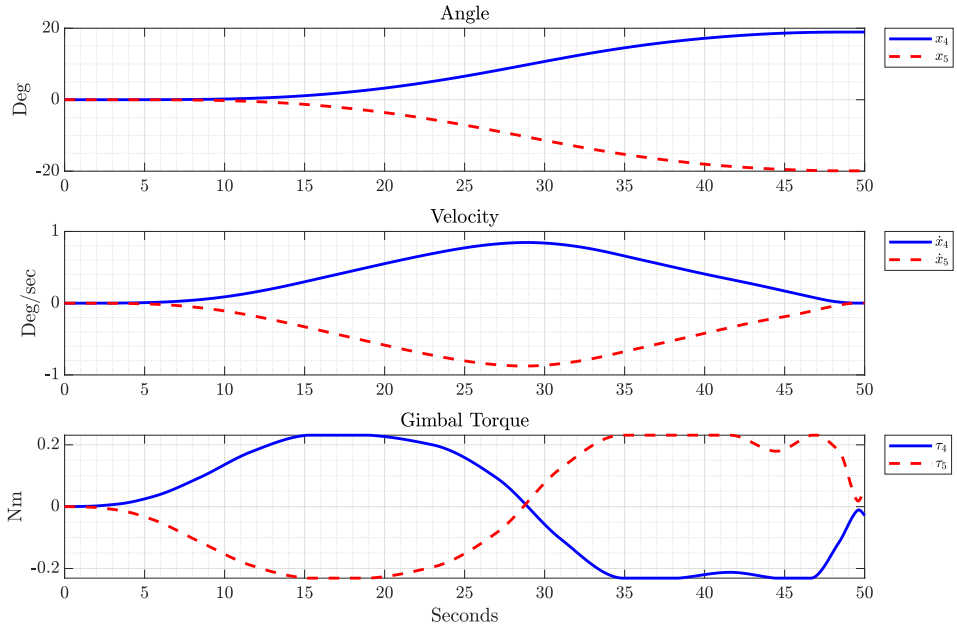

Figure 4.38: Case 13 Open-loop Maneuver: SAA-2 States and Control

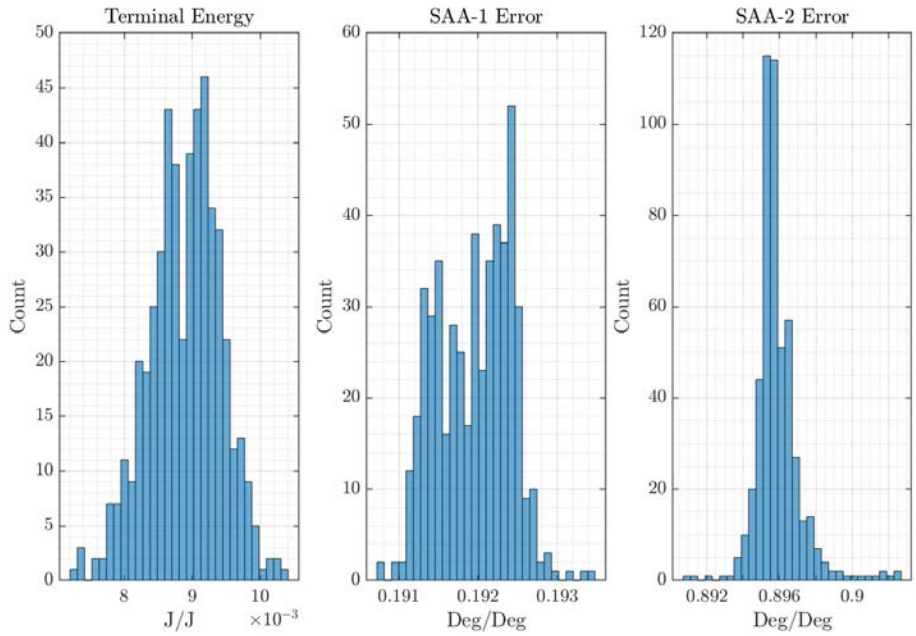

Figure 4.39: Case 12 Distribution of Normalized Terminal Residual Energy and SAA Pointing Error

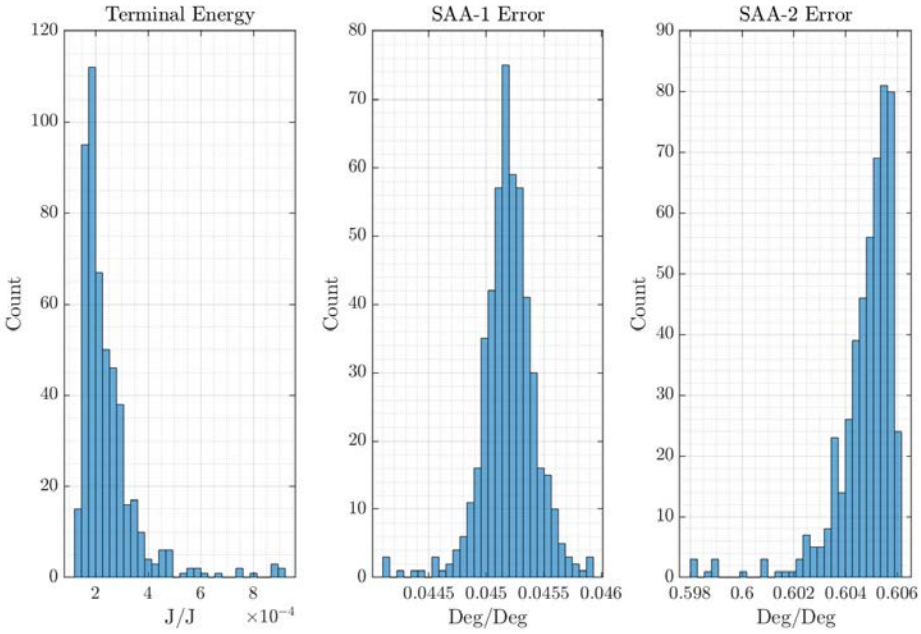

Figure 4.40: Case 13 Distribution of Normalized Terminal Residual Energy and SAA Pointing Error

4.4.3 Case 14: Three Body Unscented Minimal Terminal Energy.

Case 14 leverages the three-body model outlined in Section 3.1.2.1 and formulates an unscented optimal control problem using the reduced model. As with Cases 11-13, the simplified dynamics assume SAA-1 is fixed withing the B_1 frame and exhibits no gimbal flexibility. The remaining states are as detailed in Equation (4.16). Due to the reduced number of states, the stiffness parameters associated with SAA-1 are not modeled within the dynamics, leading to a reduced uncertain parameter space of,

$$\hat{p} = [k_3, k_4, \omega_1, \omega_4, \omega_7], \tag{4.19}$$

leading to a reduction in the number of unscented sigma points to $N_\Sigma = 11$. The resulting unscented optimal control problem formulation is shown in Equation (4.21) where the cost functional is identical to that utilized in Case 10 which is a multi-objective functional seeking to minimize both terminal energy and state error. As with Case 10, the unscented tuning parameters are selected as $[\alpha, \beta, \kappa] = [1e^{-1}, 2, 0]$, however, the allowable mean state error bounds (μ_x) is changed from $\mu_x = 0.01$ to 0.015 degrees. The original bounds on mean state error of 0.01 degrees proved too restrictive for the NLP solver and an optimal solution could not be calculated within the iteration limit. Increasing the bounds to $\mu_x \leq 0.015$ degrees allowed an optimal solution to be reached.

Given:

$$\begin{aligned} &\text{For } i = 1, ..., N_\Sigma \\ &x_i = [q_1, q_2, q_3, q_4, x_4, x_5, x_{G4}, x_{G5}, \eta_1, \eta_4, \eta_7, ... \\ &\quad \omega_x, \omega_y, \omega_z, \dot{x}_4, \dot{x}_5, \dot{x}_{G4}, \dot{x}_{G5}, \dot{\eta}_1, \dot{\eta}_4, \dot{\eta}_7, \tau_1, \tau_4, \tau_5]^T \in \mathbb{R}^{27} \\ &u = [\dot{\tau}_1, ..., \dot{\tau}_5] \in \mathbb{R}^6 \end{aligned} \tag{4.20}$$

$$
\begin{aligned}
\text{minimize} \quad & J[\cdot] = \sum_{i=1}^{N_\Sigma} w_i \left[\gamma_1 TE_i + \gamma_2 \left[[x_i(t_f; \hat{p}_i) - x^f]^T [x_i(t_f; \hat{p}_i) - x^f] \right] \right] \\
\text{subject to} \quad & \dot{x}_i(t) = f(x_i(t), \tau(t); \hat{p}_i), \quad i = 1, ..., N_\Sigma, \\
& \dot{\tau}(t) = u(t), \\
& q_i^0 = q_i^f = [0, 0, 0, 1], \\
& [x_{4,5}^0]_i = [0, 0]\ deg, \\
& [x_{4,5}^f]_i = [19, -20]\ deg, \\
& |(\eta_i, \dot{\eta}_i)| \leq (36, 27)\ arcsec, arcsec/s, \\
& |\tau_1| \leq 1\ Nm, \\
& |\tau_{2-5}| \leq 0.23\ Nm, \\
& |\dot{\tau}| \leq 0.3\ Nm/s, \\
& \left| \sum_{i=1}^{N_\Sigma} w_i e(x_i(t_f, \hat{p}_i); \hat{p}_i) - x^f \right| \leq 0.015\ deg, \\
& t_0 \leq t \leq 50s.
\end{aligned}
\tag{4.21}
$$

The resulting optimal three-body maneuver is then simulated against the full five-body model in a Monte Carlo simulation including variation of all seven parameters in p with the results being shown in Table 4.25 while the optimal control profiles and resulting states from the open-loop simulation are shown in Figures 4.41 through 4.43. The normalized terminal pointing error and residual system energy is shown in Figure 4.44.

The three-body problem formulation has lower mean pointing error for both the bus and SAA-1 while the mean pointing error for SAA-2 is only improved by 39.7% versus 52% for Case 10, which still represents a significant improvement over the standard maneuver.

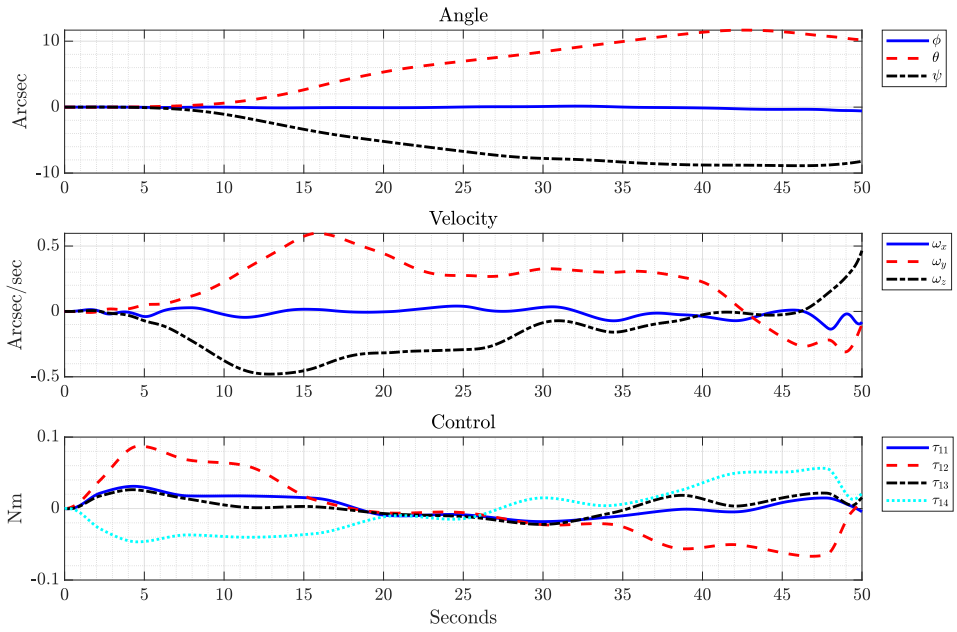

Figure 4.41: Case 14 Open-loop Maneuver: Bus States and Control

Table 4.25: Case 14 Open-Loop Monte Carlo Results

Case #	Filter	# Bodies	t_f (s)	Mean Error (deg) Bus	SAA-1	SAA-2	Mean TE (J)	Control Cost
1a	Notch	1	84.3	0.064	0.026	0.19	1.3e-3	0.56
10	n/a	5	50	8.0e-3	0.017	0.092	3.2e-5	3.82
14	n/a	3	50	3.6e-3	1.5e-3	0.084	8.8e-7	1.96

The closed-loop convergence results for Case 14 are shown in Table 4.26 with results for the standard maneuver and Case 10 are included for reference. Case 14 produces convergence times for the bus and SAA-2 which are equivalent to Case 10, while actually improving SAA-1 pointing convergence. Case 14 falls short however in total energy convergence time where an additional 78 seconds are required for the bus to achieve a quiescent state versus Case 10. The sources of the additional settling time becomes apparent when the modal states for both closed-loop simulations are analyzed. Figure 4.45

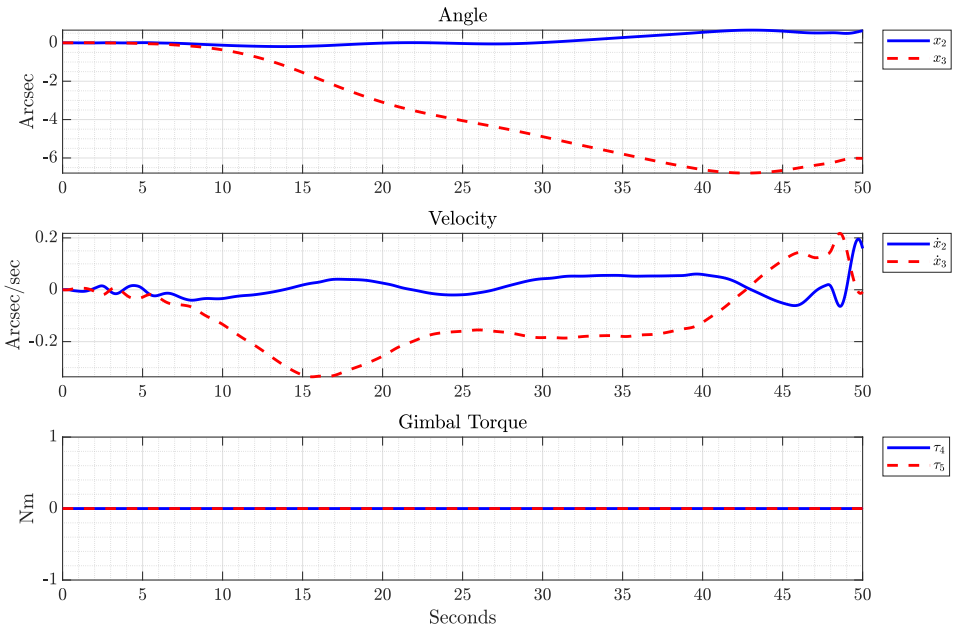

Figure 4.42: Case 14 Open-loop Maneuver: SAA-1 States and Control

shows the time history for the primary modals states about each bus axes. Both cases elicit similar excitation of η_1 about the bus x-axis, however, the Case 14 optimal maneuver has a significant increase in η_7 excitation which takes additional time to damp out. This demonstrates that for certain maneuvers, improvements in system performance during open-loop simulation may not carry forward to closed-loop results.

Table 4.26: Case 14 Closed-Loop Convergence Results

		Planned	Convergence Time (s)			
Case #	Filter	t_f	Bus	SAA-1	SAA-2	Total Energy
1a	Notch	84.3	89.3	–	131.6	145.2
10	n/a	50	39.15	–	50.0	110.3
14	n/a	50	–	–	54.8	65.7

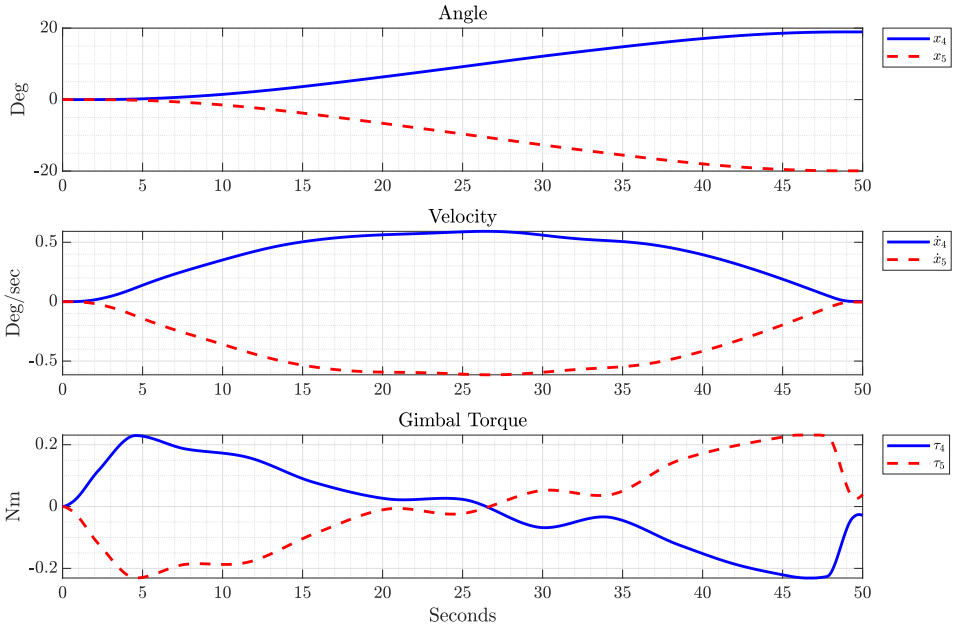

Figure 4.43: Case 14 Open-loop Maneuver: SAA-2 States and Control

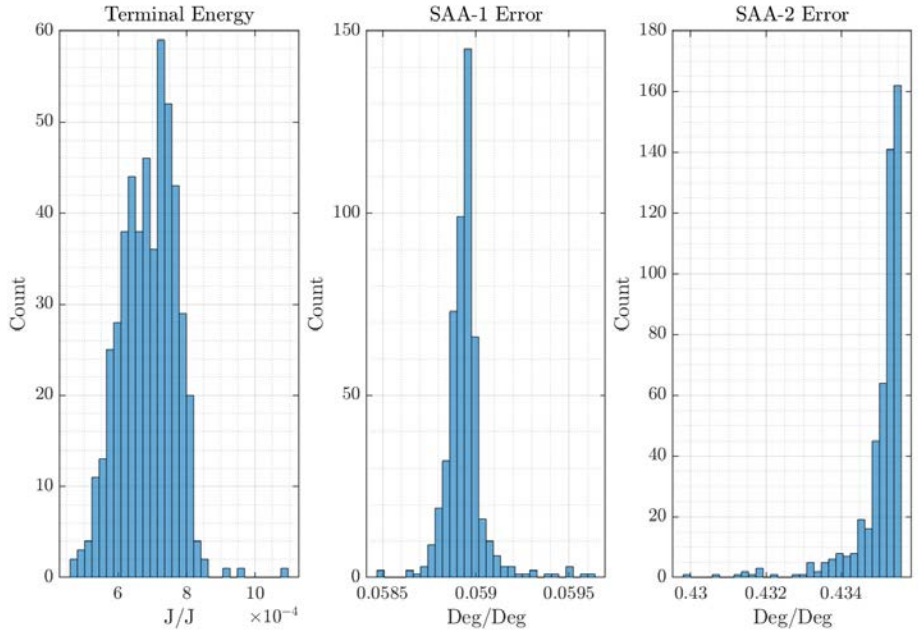

Figure 4.44: Case 14 Distribution of Normalized Terminal Residual Energy and SAA Pointing Error

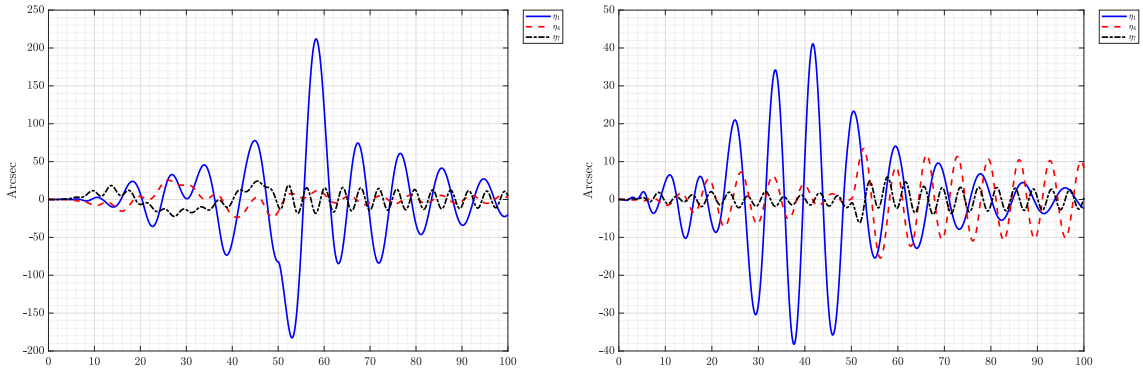

(a) Case 10

(b) Case 14

Figure 4.45: Case 10 vs. Case 14 Primary Modal States for Closed-loop Simulation with Nominal Parameter Values

4.4.4 Case 15: Three Body Unscented Minimal Jerk.

Case 14 sought to derive an optimal maneuver maximizing robustness by minimizing mean state error and terminal system energy. While this was shown to be effective with the five-body model of Case 10, the three-body problem formulation elicited higher modal excitation when the control loop was closed. For Case 15, instead of maximizing robustness through the cost functional, guarantees are placed on maneuver robustness by successively tightening the endpoint constraints on mean terminal error while the cost functional seeks to minimize the amount of jerk into the system. As detailed by Lambrechts et al. [64], increasing the order of trajectory planning decreases high-frequency content and provides trajectories less prone to vibrational excitation. For Case 15, the cost functional then minimizes control jerk while the endpoint constraints provides upper bounds on mean pointing error. The optimal control problem formulation is then,

$$
\begin{aligned}
\text{minimize} \quad & J[\cdot] = \int_{t_0}^{t_f} \dot{\tau}^T \dot{\tau}\, dt \\
\text{subject to} \quad & \dot{x}_i(t) = f(x_i(t), u(t); \hat{p}_i), \quad i = 1, ..., N_\Sigma, \\
& q_i^0 = q_i^f = [0, 0, 0, 1], \\
& [x_{4,5}^0]_i = [0, 0]\ deg, \\
& [x_{4,5}^f]_i = [19, -20]\ deg, \\
& |(\eta_i, \dot{\eta}_i)| \leq (36, 27)\ arcsec, arcsec/s, \\
& |\tau_1| \leq 1\ Nm, \\
& |\tau_{2-5}| \leq 0.23\ Nm, \\
& |\dot{\tau}| \leq 0.3\ Nm/s, \\
& \left| \sum_{i=1}^{N_\Sigma} w_i e(x_i(t_f, \hat{p}_i); \hat{p}_i) - x^f \right| \leq 0.0017\ deg, \\
& t_0 \leq t \leq 50s.
\end{aligned}
\tag{4.22}
$$

The results of an open-loop simulation of the resulting maneuver utilizing nominal parameter values is shown in Figures 4.46 through 4.48 while Monte Carlo simulation results are shown in Table 4.27 with the corresponding histogram distributions in Figure 4.49. From Figure 4.46 it is apparent that Case 15 utilizes less control authority than Case 14 with an order of magnitude decrease in maximum bus slewing velocity These results show that when simulated open-loop, Case 15 exhibits similar mean pointing error for the bus and SAA-1 as Cases 10 and 14 while showing an improvement in SAA-2 pointing error. While the mean terminal energy is higher for Case 15 than Case 14, when the closed-loop simulation results are compared, as shown in Table 4.28, Case 15 achieves energy convergence 116 seconds faster than Case 14 while also eliminating any bus pointing error. The reduced vibrational energy is due to the lower excitation of the bus modes as seen in Figure 4.50 which exhibits a maximum modal deflection of approximately 50 arcseconds versus over 200 or 150 arseconds for Cases 10 and 14.

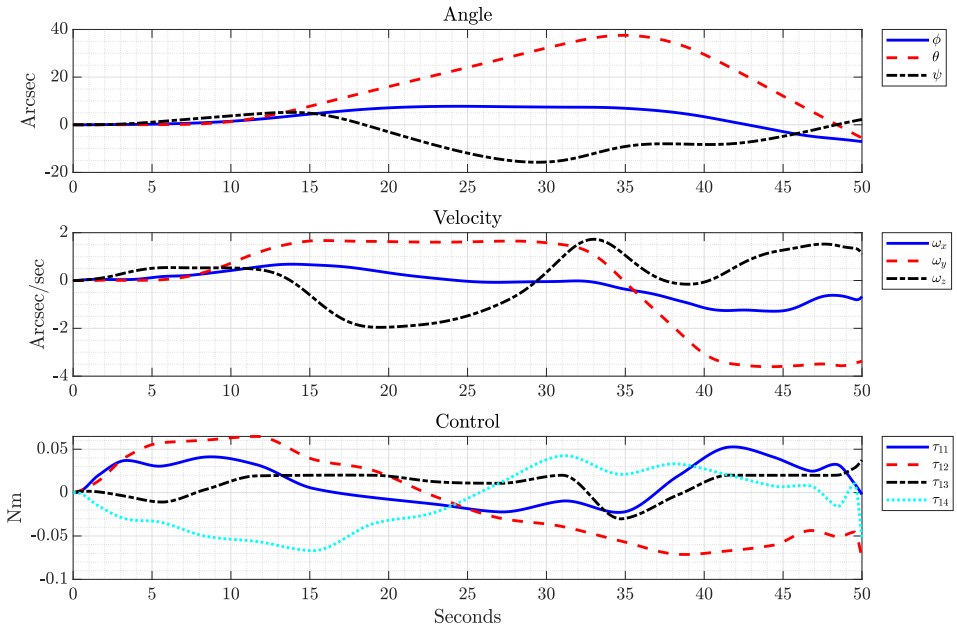

Figure 4.46: Case 15 Open-loop Maneuver: Bus States and Control

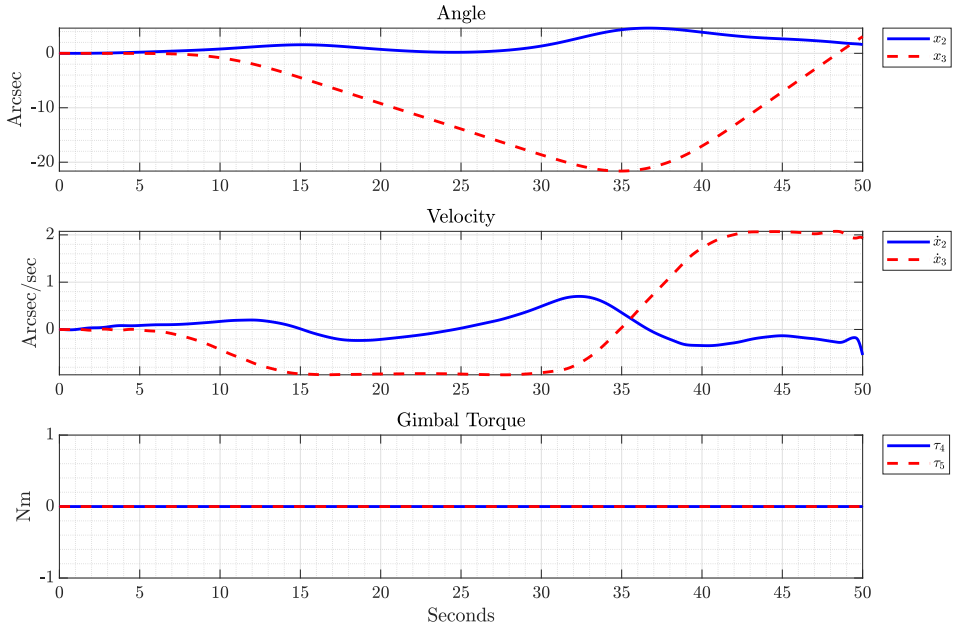

Figure 4.47: Case 15 Open-loop Maneuver: SAA-1 States and Control

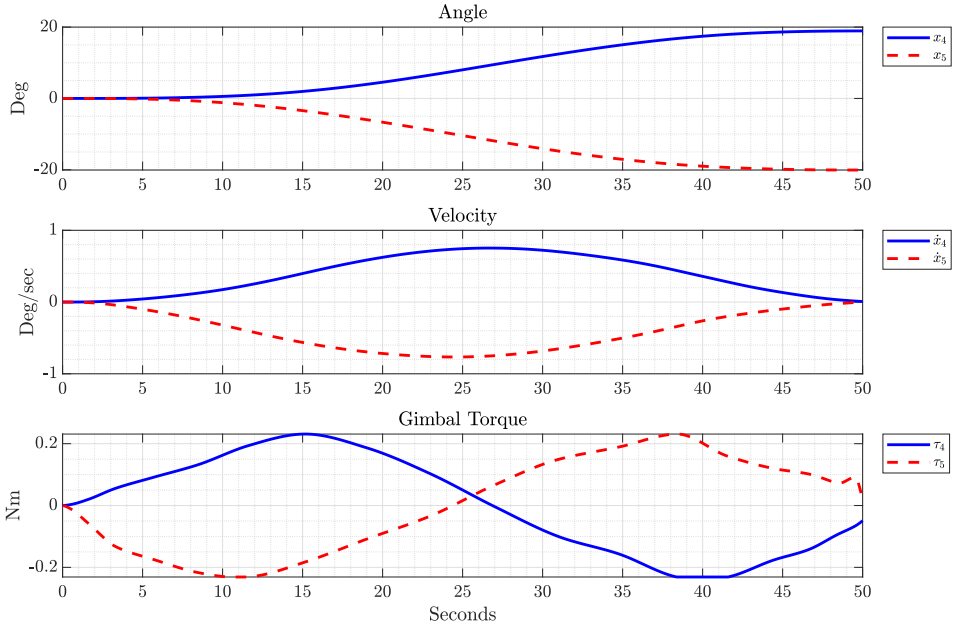

Figure 4.48: Case 15 Open-loop Maneuver: SAA-2 States and Control

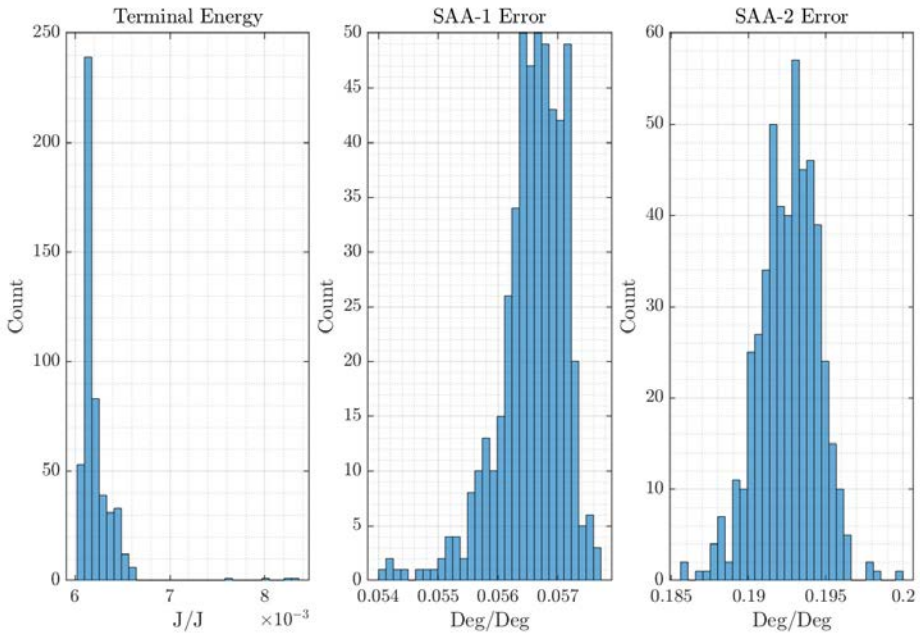

Figure 4.49: Case 15 Distribution of Normalized Terminal Residual Energy and SAA Pointing Error

Table 4.27: Case 15 Open-Loop Monte Carlo Results

Case #	Filter	# Bodies	t_f (s)	Mean Error (deg) Bus	SAA-1	SAA-2	Mean TE (J)	Control Cost
1a	Notch	1	84.3	0.064	0.026	0.19	1.3e-3	0.56
10	n/a	5	50	8.0e-3	0.017	0.092	3.2e-5	3.82
14	n/a	3	50	3.6e-3	1.5e-3	0.084	8.8e-7	1.96
15	n/a	3	50	2.6e-3	1.5e-3	0.037	8.0e-6	3.45

While Cases 10 and 15 differ in the number of bodies simulated as well as the cost functional minimized, Case 15 still demonstrates that the three body problem can still get favorable results as compared to the five body formulation. While the intent of the maneuvers is to decrease maneuver time with building in robustness, the robustness

Table 4.28: Case 15 Closed-Loop Convergence Results

Case #	Filter	Planned t_f	Convergence Time (s) Bus	SAA-1	SAA-2	Total Energy
1a	Notch	84.3	89.3	–	131.6	145.2
10	n/a	50	39.15	–	50.0	110.3
14	n/a	50	–	–	54.8	65.7
15	n/a	50	–	–	64.2	72.3

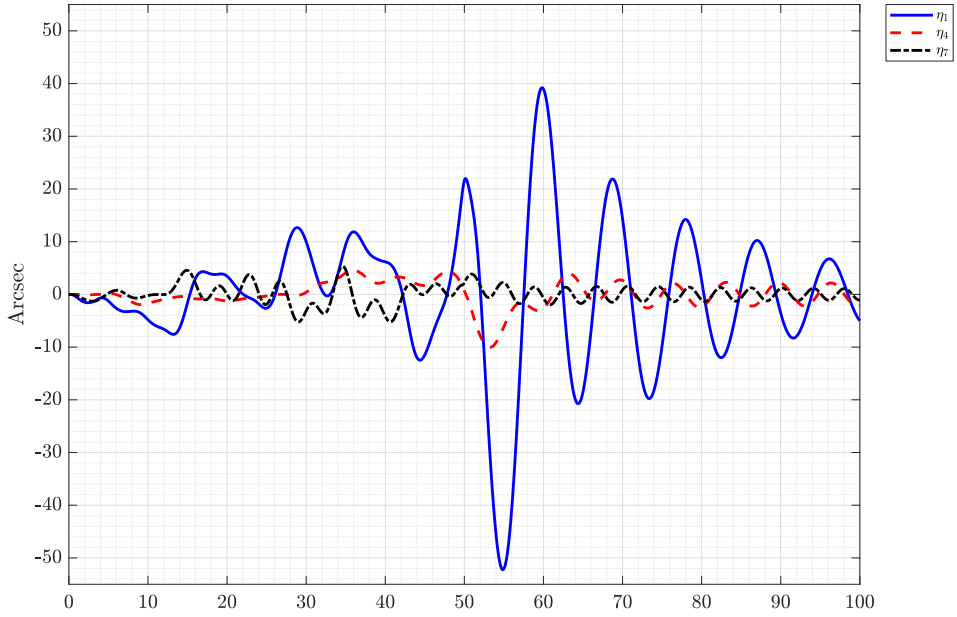

Figure 4.50: Case 15 Primary Modal States for Closed-loop Simulation with Nominal Parameter Values

can be achieved multiple ways. While Case 10 sought to maximum robustness directly by minimizing mean error and terminal energy, Case 15 ensure robustness through the successive tightening of the endpoint constraints on mean state error, and minimized terminal energy through the minimization of control jerk into the system.

4.4.5 Case 16: Two Body Minimal Sensitivity.

For multi-aperture systems such as TDRS, there can be operational advantages to planning maneuvers for each aperture independently. For the five-body system considered herein, the maneuver of SAA-2 accounts for SAA-1 pointing and can leverage bus maneuvers to maintain maintain SAA-1 pointing while meeting SAA-2 objectives. Similarly, with the three-body formulation where SAA-1 is subsumed into B_1 and assumed to be static, the maneuvers generated for SAA-2 can still advantageously maneuver the bus to achieve the objectives. While there are advantages to including additional bodies and more accurate dynamics in the optimal problem formulation, the analysis relies on the assumption that the objectives of adjacent apertures remains constant throughout the maneuver. For example, all the previous cases assumed SAA-1 remained on the same target throughout the SAA-2 maneuver, however, operationally, this need not be the case. SAA-1 may be commanded to transition to a different User Satellites (USAT) at any point during the SAA-2 maneuver. Due to the bus control trajectories accounting for the necessary counter-steering for SAA-1, re-pointing of SAA-1 would mean the bus control profiles are no longer optimal requiring a new optimal control problem be solved.

This constraint can be overcome by deriving optimal control problems for each aperture independently and creating robust maneuvers which attempt to minimize excitation of the bus and thus minimize impacts to adjacent apertures. For multi-aperture space systems, each aperture can then be re-planed in real-time without accounting for neighboring apertures, thus reducing computational complexity.

Case 16 utilizes the two-body dynamics as outlined in Section 3.1.2.2 with the reduced set of states as given in Equation (4.23). For the previous cases, bounds were placed on the magnitude of modal excitation based on the results of the standard maneuver, thus any optimal maneuver must exhibit a lower magnitude of excitation. For the two body problem formulation, the modal dynamics are no longer coupled with the rigid-body dynamics,

thus the previous constraints are no longer valid. The modal coordinates are no longer a components of the satellite dynamics, but act as a decoupled energy monitor which can be utilized in the cost functional and whose excitation can be minimized.

Case 16 formulates a two-body optimal control problem utilizing desensitized optimal control techniques given as,

$$
\begin{aligned}
&\text{Given:} \\
&\quad x = x_4, x_5, x_{G4}, x_{G5}, \eta_1, \eta_4, \eta_7, ... \\
&\qquad \dot{x}_4, \dot{x}_5, \dot{x}_{G4}, \dot{x}_{G5}, \dot{\eta}_1, \dot{\eta}_4, \dot{\eta}_7, \tau_4, \tau_5]^T \in \mathbb{R}^{16} \\
&\quad s \in \mathbb{R}^{14\times 5} \\
&\quad u = [\dot{\tau}_4, \dot{\tau}_5] \in \mathbb{R}^2 \\
&\text{minimize} \quad J = \|s(t_f)\| \\
&\text{subject to} \qquad 0 = \dot{x}(t) - f_x(x(t), u(t); \bar{p}), \\
&\qquad\qquad 0 = \dot{s}(t) - f_s(x(t), s(t); \bar{p}), \\
&\qquad x^0_{4,5} = x^0_{G4,G5} = [0, 0]\ deg, \\
&\qquad x^f_{4,5} = x^f_{G4,G5} = [19, -20]\ deg, \\
&\qquad |\tau_1| \leq 1\ Nm, \\
&\qquad |\dot{\tau}| \leq 0.3\ Nm/s, \\
&\qquad t_f \leq 50s.
\end{aligned}
\tag{4.23, 4.24}
$$

where the resulting control profiles for the bus and antennas are shown in Figures 4.51 through 4.53. Comparing the bus trajectory to the five-body and three-body maneuvers of Cases 5 and 11, the absence of the bus dynamics within the optimal maneuver problem formulation leads to higher resulting bus rates and terminal pointing error when the optimal maneuver is sumulated against the full dynamics. Even applying bus counter-steering torques in accordance with Equation (3.20), due to the mass matrix $\bar{M}$ being based on

a nominal gimbal configuration, time varying disturbances are introduced to the system leading to an increase in bus and SAA-1 pointing errors compared to the five-body and three-body results.

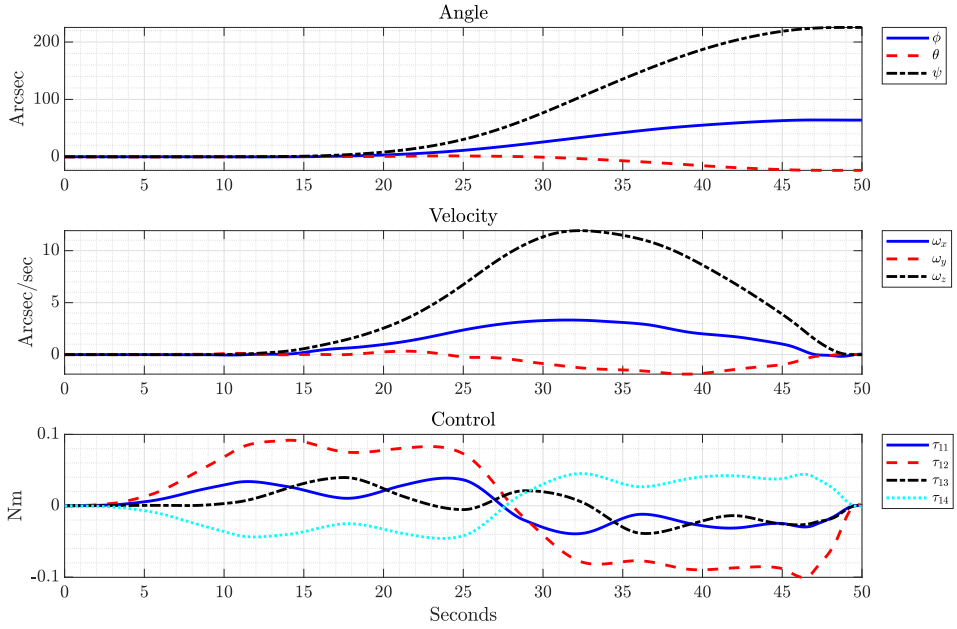

Figure 4.51: Case 16 Open-loop Maneuver: Bus States and Control

Table 4.29: Case 16 Open-Loop Monte Carlo Results

Case #	Filter	# Bodies	t_f (s)	Mean Error (deg) Bus	SAA-1	SAA-2	Mean TE (J)	Control Cost
1a	Notch	1	84.3	0.064	0.026	0.19	1.3e-3	0.56
5	n/a	5	50	5.6e-4	5.5e-3	0.068	3.7e-7	3.8
11	n/a	3	50	1.2e-3	1.6e-3	0.13	7.5e-7	13.5
16	n/a	2	50	0.065	0.028	0.13	4.0e-7	3.4

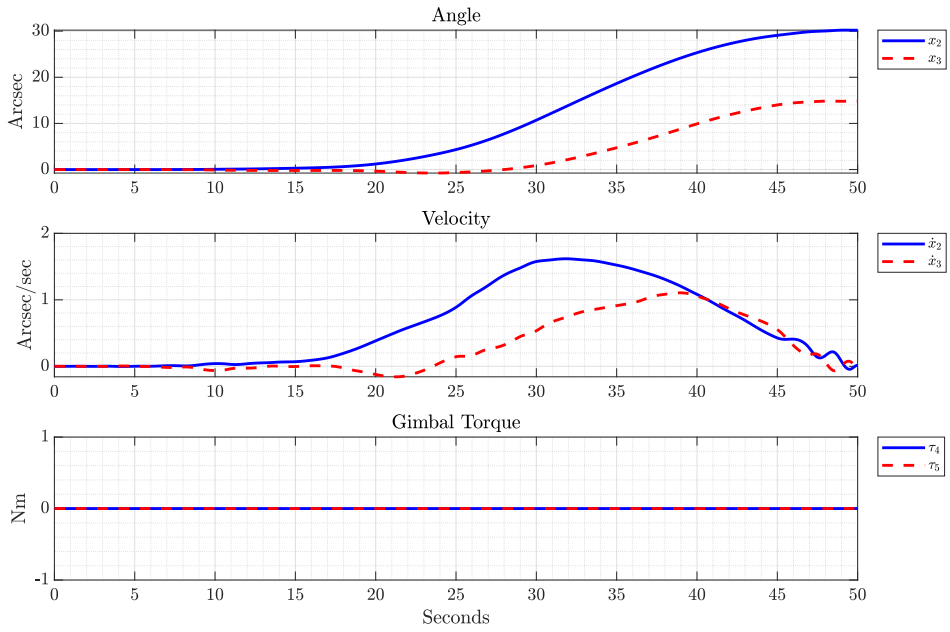

Figure 4.52: Case 16 Open-loop Maneuver: SAA-1 States and Control

Table 4.29 contains the results of the open-loop Monte Carlo analysis comparing Case 16 the standard maneuver as well as the corresponding five and three-body cases. Due to both the standard maneuver and Case 16 utilizing planning methods that do not account for the satellite bus or SAA-1 dynamics, the mean pointing errors are similar, as seen in Figure 4.54, the difference being Case 16 accomplishes the maneuver 40% faster than the standard maneuver. The difference lies in the ability of Case 16 to account for the nonlinear dynamics of the antenna as well as modal excitation of the system resulting in a four order-of-magnitude reduction in mean terminal energy. This demonstrates that even though the modal coordinates are un-coupled from the rigid-body dynamics, the sensitivity of the modal states to parameter variation can still be minimized leading to a lower energy optimal solution.

Closed-loop convergence times for Case 16 are shown in Table 4.30 showing the Case 16 maneuver maintains pointing convergence of the satellite bus and SAA-1 throughout the

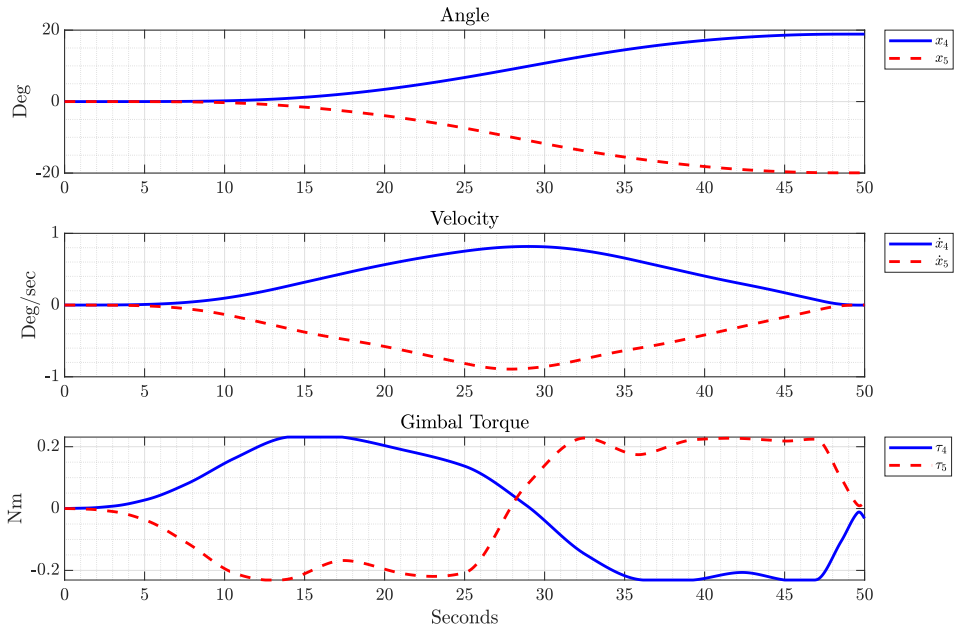

Figure 4.53: Case 16 Open-loop Maneuver: SAA-2 States and Control

Table 4.30: Case 16 Closed-Loop Convergence Results

		#	Planned	Convergence Time (s)			
Case #	Filter	Bodies	t_f	Bus	SAA-1	SAA-2	Total Energy
1a	Notch	1	84.3	89.3	–	131.6	145.2
5	n/a	5	50	37.2	–	50	57.8
11	n/a	3	50	–	–	50	64
16	n/a	2	50	–	–	50	68.7

entire maneuver while SAA-2 achieves and maintains pointing convergence at maneuver termination. Energy convergence is achieved in 69 seconds, which is 11 seconds longer than the five-body maneuver of Case 5 but still represents a 77 second improvement over the standard maneuver. These results demonstrate that even when the dynamics of the bus and SAA-1 are neglected, a desensitized optimal control problem can be formulated that

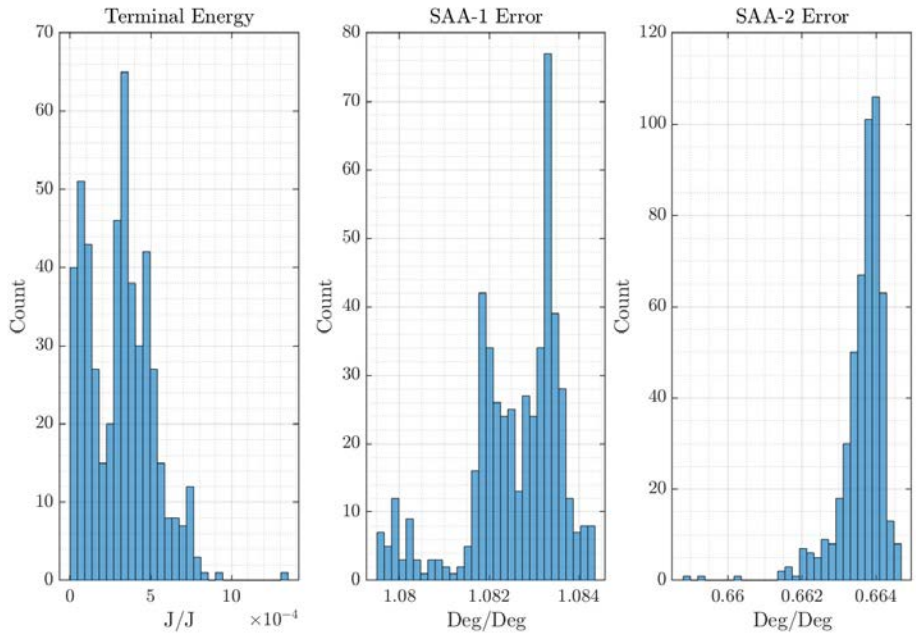

Figure 4.54: Case 16 Distribution of Normalized Terminal Residual Energy and SAA Pointing Error

generates a maneuver decreasing slew time, while still resulting in a maneuver more robust against parameter variation than the standard maneuver.

4.4.6 Case 17: Two Body Unscented - Minimum Jerk.

For the two-body unscented optimal control problem, a different cost function must be utilized than Case 15. For the three-body cases, the modal variables are coupled with the rigid-body dynamics and are integral to accurately describing the movement of the system. For the two-body dynamics, the modal variables are no longer coupled into the antenna dynamics but instead act as a sort of energy monitor, where each modal variable is an independent two-body system excited by the estimated acceleration of the un-modeled bus. Because the modal variables do not possess a physical interpretation with respect to the satellite model, placing the same bounds on the variables would be meaningless, so while Case 15 can minimize control jerk while maintaining bus vibration within the specified bounds, the same process cannot be used for Case 17.

Case 17 then seeks to minimize the modal energy of the system by integrating the inner-product of the modal variables, thus penalizing excessive vibration of the uncoupled system without necessitating direct bounds on the modal states. The optiml problem formulation in standard format is then,

$$
\begin{aligned}
\text{minimize} \quad & J[\cdot] = \int_{t_0}^{t_f} \eta^T \eta \, dt \\
\text{subject to} \quad & \dot{x}_i(t) = f(x_i(t), u(t); \hat{p}_i), \quad i = 1, ..., N_\Sigma, \\
& [x^0_{4,5}]_i = [0, 0] \; deg, \\
& [x^f_{4,5}]_i = [19, -20] \; deg, \\
& |\tau_{4-5}| \leq 0.23 \; Nm, \\
& |\dot{\tau}| \leq 0.3 \; Nm/s, \\
& \left| \sum_{i=1}^{N_\Sigma} w_i e(x_i(t_f, \hat{p}_i); \hat{p}_i) - x^f \right| = 0.0 \; deg, \\
& t_0 \leq t \leq 50s,
\end{aligned}
\tag{4.25}
$$

where the bounds on μ_x have been set to zero. This results in a solution with zero mean pointing error. The maneuver is simulated open-loop utilizing nominal parameter values with the resulting trajectories shown in Figures 4.55 through 4.57 while the open-loop Monte Carlo results are presented in Table 4.31. As with the previous two-body analysis, counter-steering control for the bus is calculated utilizing Equation (3.20). Due to the counter-steering controls being non-optimal for both antenna, this leads to a mean bus pointing error that is 20x larger than the three-body results from Case 15, but is similar to that exhibited by the standard maneuver. Despite the mean pointing errors of Case 17 being higher than Case 15, terminal system energy is reduced by an order of magnitude, and exhibits a similar control cost.

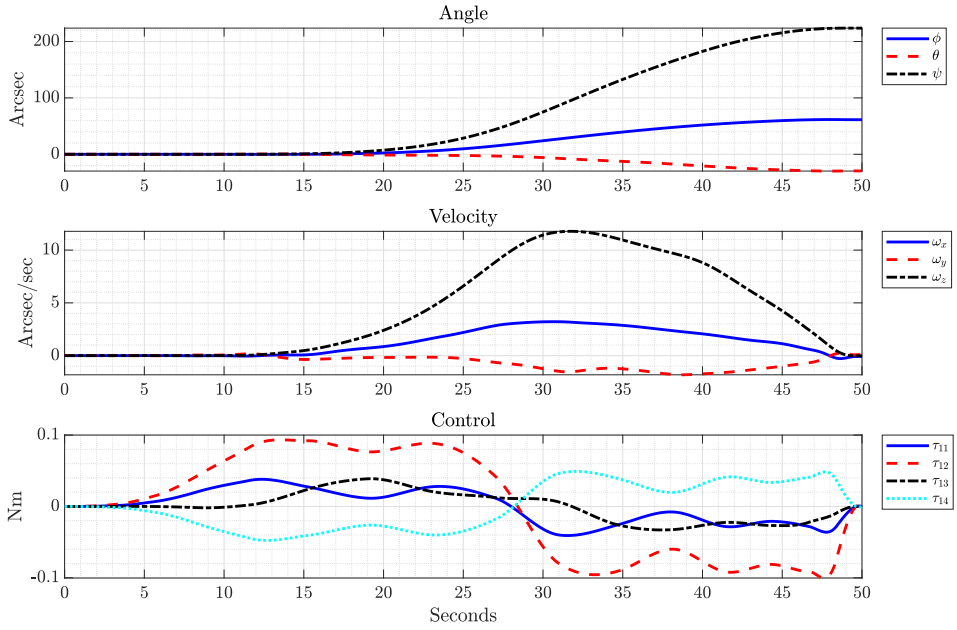

Figure 4.55: Case 17 Open-loop Maneuver: Bus States and Control

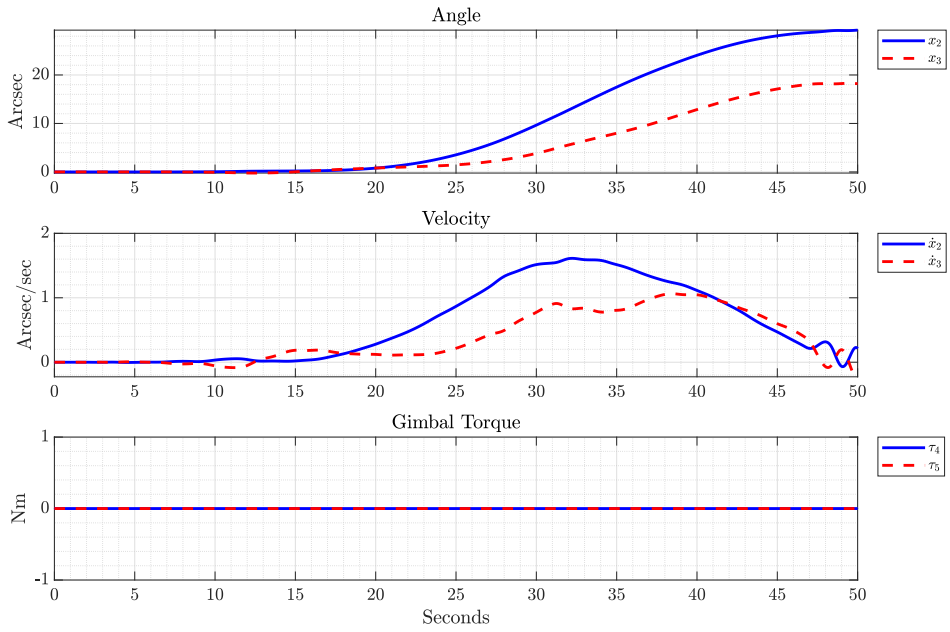

Figure 4.56: Case 17 Open-loop Maneuver: SAA-1 States and Control

Table 4.31: Case 17 Open-Loop Monte Carlo Results

Case #	Filter	# Bodies	t_f (s)	Mean Error (deg) Bus	SAA-1	SAA-2	Mean TE (J)	Control Cost
1a	Notch	1	84.3	0.064	0.026	0.19	1.3e-3	0.56
10	n/a	5	50	8.0e-3	0.017	0.092	3.2e-5	3.83
14	n/a	3	50	3.6e-3	1.5e-3	0.084	8.8e-7	1.96
17	n/a	2	50	0.065	0.028	0.18	4.4e-7	3.52

The results for the closed-loop simulation are shown in Table 4.32 which shows that even though Case 17 exhibited higher mean pointing errors open-loop, when the control loop is closed, pointing convergence is achieved 14 seconds faster than Case 15 while energy convergence is reduced by 12 seconds.

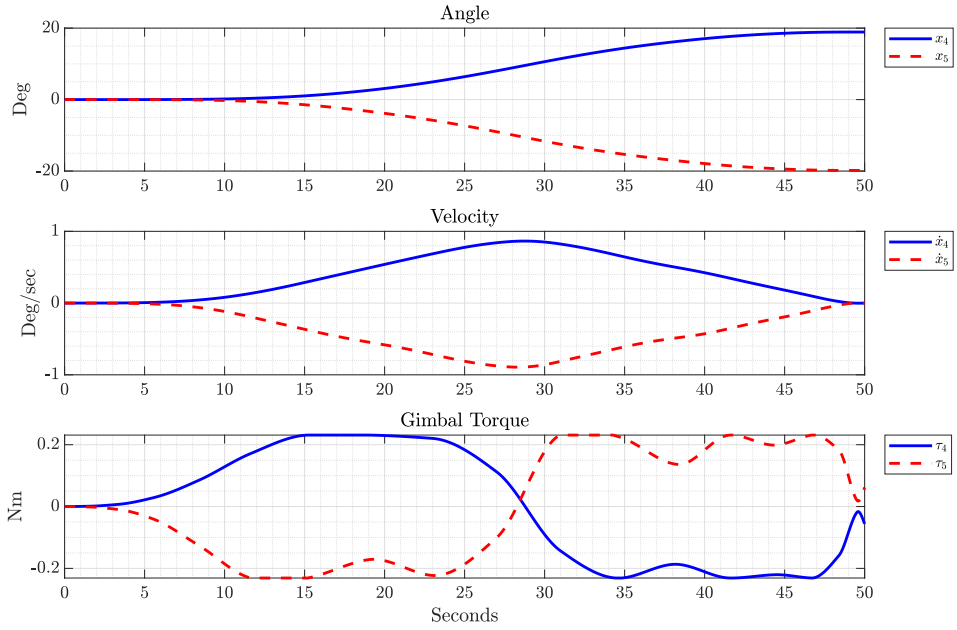

Figure 4.57: Case 17 Open-loop Maneuver: SAA-2 States and Control

Table 4.32: Case 17 Closed-Loop Convergence Results

		#	Planned	Convergence Time (s)			
Case #	Filter	Bodies	t_f	Bus	SAA-1	SAA-2	Total Energy
1a	Notch	1	84.3	89.3	–	131.6	145.2
10	n/a	5	50	39.15	–	50.0	110.3
14	n/a	3	50	–	–	54.8	65.7
17	n/a	2	50	–	–	50	60.32

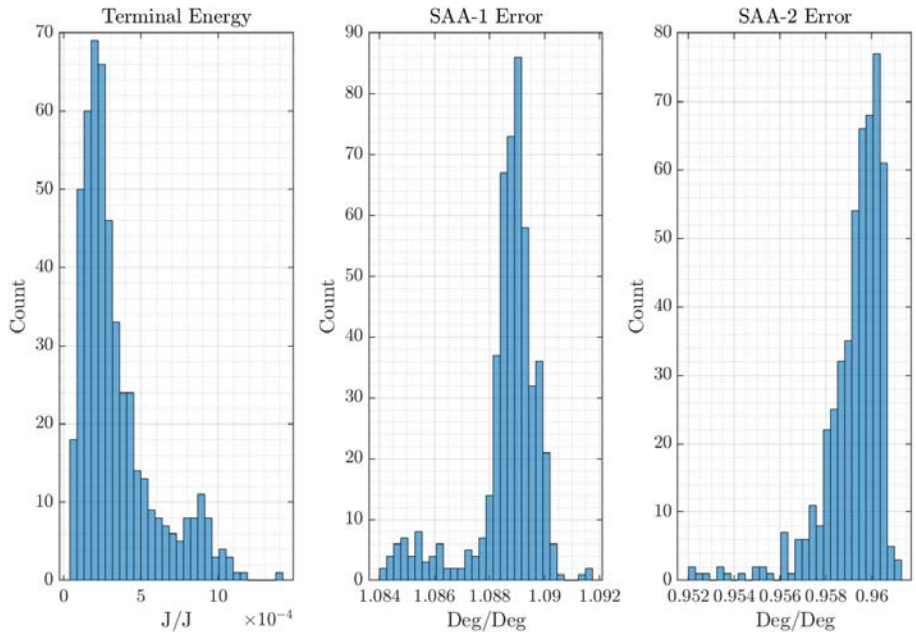

Figure 4.58: Case 17 Distribution of Normalized Terminal Residual Energy and SAA Pointing Error

V. Summary

5.1 Summary Results

The objective of this research is to leverage the previously developed robust optimal control techniques of desensitized optimal control and unscented optimal control, and extend the problem formulations to encompass the dynamics modeling an on-orbit configuration of a Tracking and Data Relay Satellite (TDRS) like multi-aperture system. While previous research was often restricted to a low number of articulated bodies, planar motion, or a single uncertain parameter, this research sought to extend the concepts to a higher fidelity model with multiple uncertain parameters. By leveraging these robust optimal control techniques, this manuscript demonstrates how conservative soft constraints on maximum gimbal velocity, used as a method of minimizing coupling between gimbal axes to reduce unwanted vibrational excitation, can be rolled back so long as the underlying dynamics of concern are properly modeled and constrained.

By developing a multi-body spacecraft model including both flexibility parameters within the gimbal motors, and leveraging the hybrid coordinate method to model bus structural modes, the underlying concern of unwanted interaction between neighboring apertures can be modeled, constrained, and minimized even in the face of parametric uncertainty. Once robust results were developed for the full five-body model, this research then incrementally reduced the fidelity of the model, decreasing the number of modeled states and formulated new robust optimal control problems to derive optimal results in a more computationally efficient manner.

Table 5.1 summarizes three of the desensitized optimal control cases representing five, three, and two-body problem formulations. The Case 5, five-body problem formulation exhibits the lowest mean pointing error for the bus and both Single Access Antenna (SAA) as well as the lowest mean terminal energy. As the number of bodies is decreased, the

Table 5.1: Open-loop Monte Carlo Results for Robust, Optimal Maneuvers

Case #	# Bodies	Robust Method	t_f (s)	Mean Error (deg) Bus	SAA-1	SAA-2	Mean TE (J)	Control Cost
1a	1	n/a	84.3	0.064	0.026	0.19	1.3e-3	0.56
5	5	Sensi	50	5.6e-4	5.5e-3	0.068	3.7e-7	3.75
11	3	Sensi	50	1.2e-3	1.6e-3	0.13	7.53e-7	13.5
16	2	Sensi	50	0.065	0.028	0.13	4.0e-7	3.4

mean pointing errors increase due to the inaccuracies in the dynamics. In particular, the bus pointing error increases as the number of bodies decreases, and is a primary driver for payload pointing error. This is due to the the process by which the bus counter-steering torques are derived utilizing linearized dynamic assumptions in Equation (3.4.1). The Case 16, two-body results exhibit the highest open-loop mean error and terminal energy for the desensitized optimal control cases, however, by minimizing the terminal sensitivity to parameter variability, Case 16 still reduces terminal system energy by four orders of magnitude while completing the maneuver 41% faster than the standard case.

Figure 5.1 contains the final pointing for the 500 Monte Carlo realizations for the sensitivity based cases from Table 5.1. No only is the mean pointing error decreased for all three optimal maneuvers, the standard deviation for the SAA-2 pointing error is improved by 86 to 95% compared to the standard maneuver. Similarly, Figure 5.2 illustrates SAA-1 versus SAA-2 terminal pointing error for each Monte Carlo realization again demonstrating the robustness improvements of the desensitized maneuvers.

Closed-loop convergence results (Table 5.2) for the desensitized optimal control maneuvers show all three maneuvers achieving pointing convergence at the pre-planned terminal maneuver time of 50 seconds, however, as the number of bodies is decreased, the convergence time for system energy increases, showing that increasing the accuracy

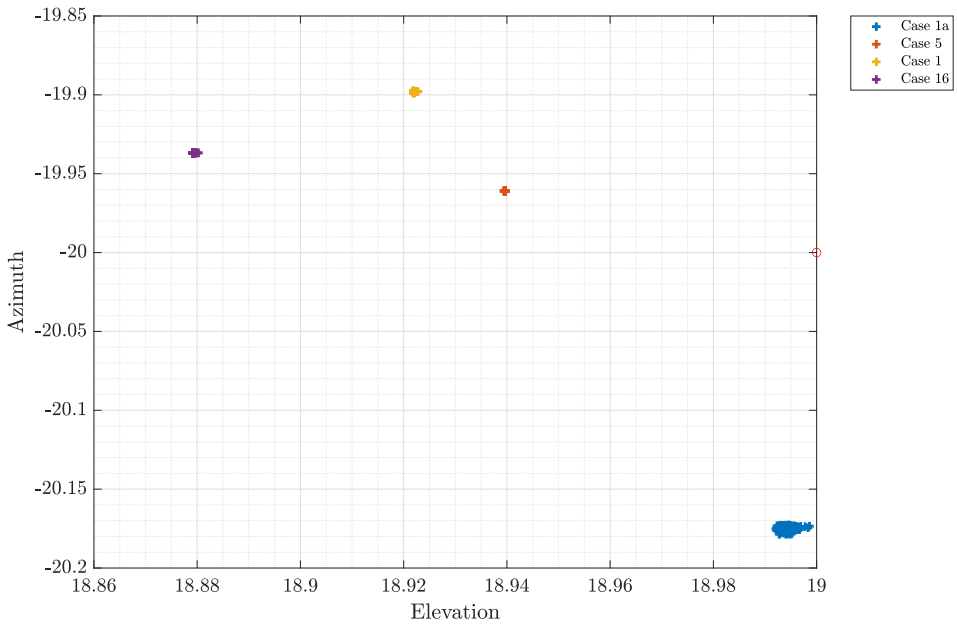

Figure 5.1: Open-loop Monte Carlo Realizations for SAA-2 for Select Sensitivity Cases

Table 5.2: Closed-loop Convergence Times for Robust, Optimal Maneuvers

		Robust	Convergence Time (s)			
Case #	Bodies	Method	Bus	SAA-1	SAA-2	Total Energy
1a	1	n/a	89.3	–	131.6	145.2
5	5	Sensi	37.2	–	50	57.8
11	3	Sensi	–	–	50	64
16	2	Sensi	–	–	50	68.7

of the flexible dynamics allows the method to better minimize system excitation. The two-body result still achieves a 56% reduction is energy convergence time, demonstrating that including the modal dynamics as a means of energy monitoring, and minimizing the systems terminal sensitivity to those dynamics, robust maneuvers can be achieved utilizing a reduced number of bodies.

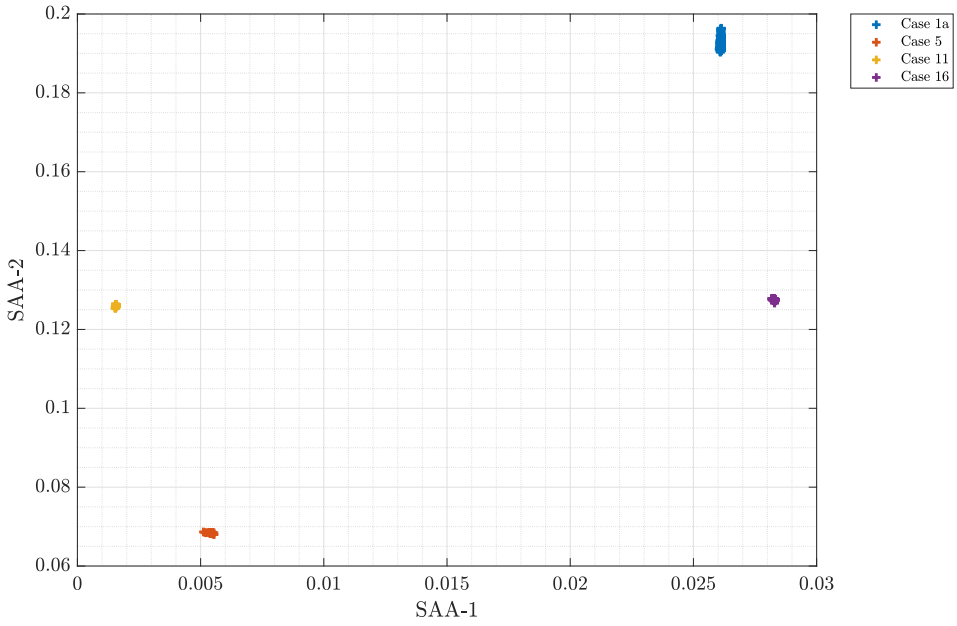

Figure 5.2: Open-loop, Mean Terminal SAA Pointing Error for Sensitivity Based Cases

Table 5.3: Open-loop Monte Carlo Results for Robust, Optimal Maneuvers

	#	Robust		Mean Error (deg)			Mean	Control
Case #	Bodies	Method	t_f (s)	Bus	SAA-1	SAA-2	TE (J)	Cost
1a	1	n/a	84.3	0.064	0.026	0.19	1.3e-3	0.56
10	5	Unc	50	8.0e-3	0.017	0.092	3.2e-5	3.83
14	3	Unc	50	3.6e-3	1.5e-3	0.084	8.8e-7	1.96
17	2	Unc	50	0.065	0.028	0.18	4.4e-7	3.52

Figure 5.3 contains the Monte Carlo realizations for SAA-2 terminal azimuth versus elevation states illustrating the robustness of the unscented optimal control maneuvers where mean pointing error is improved by 4 to 52% while the standard deviation is improved by 17 to 89%. Figure 5.3 illustrates terminal pointing error for SAA-1 versus SAA-2 for the Monte Carlo realizations demonstrating improvement in SAA-2 pointing error for all three optimal cases versus the standard maneuvers.

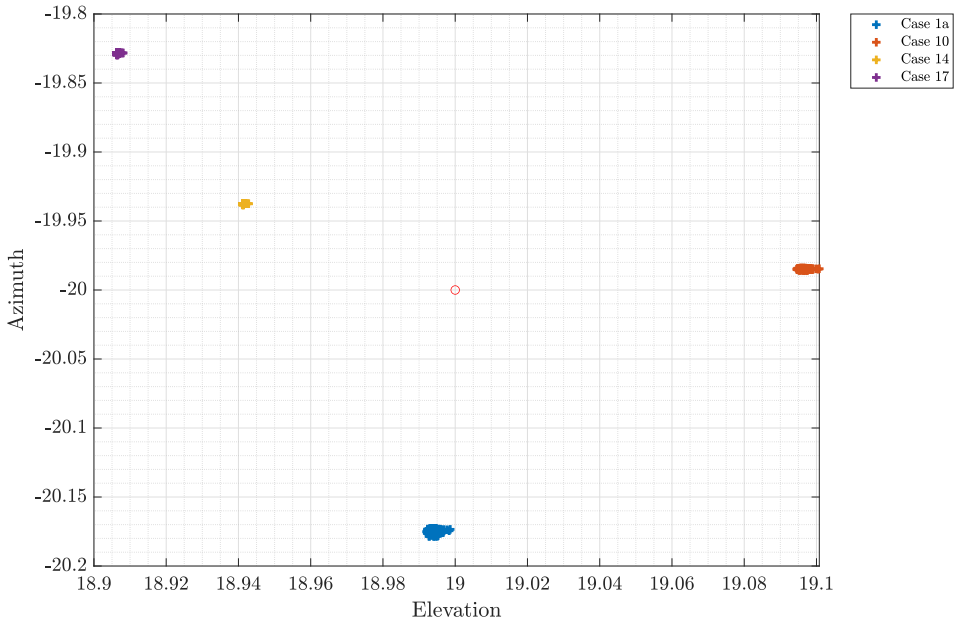

Figure 5.3: Open-loop Monte Carlo Realizations for SAA-2 for Select Unscented Cases

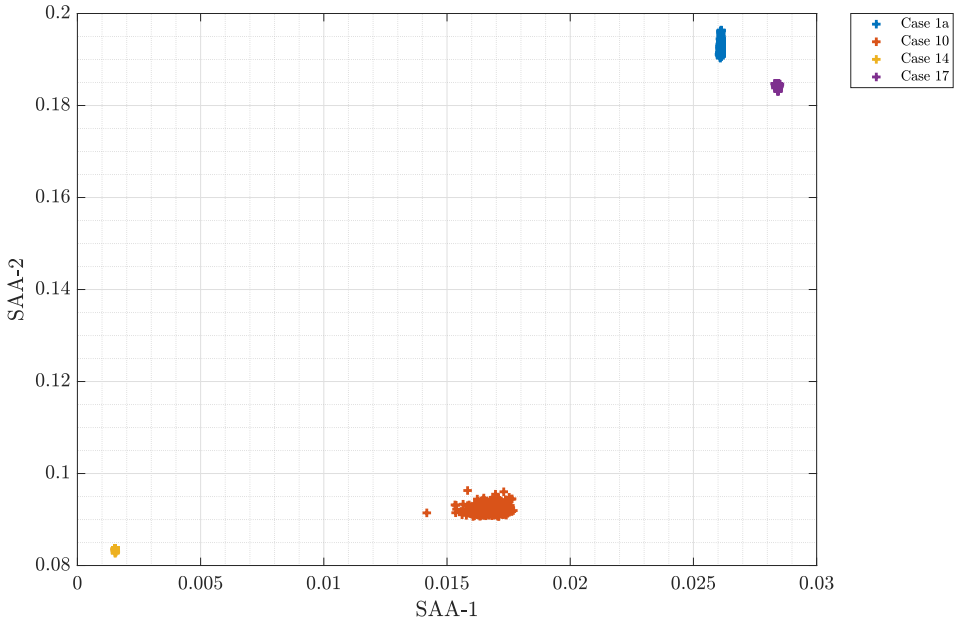

Figure 5.4: Open-loop, Mean Terminal SAA Pointing Error for Unscented Based Cases

Table 5.3 contains three cases for the unscented optimal control method representing a five, three, and two-body problem formulations. All three optimal maneuver exhibit significant improvement in open-loop mean pointing error and terminal energy, which is further supported by the closed-loop results in Table 5.4. Unlike with the desensitized results, the five-body unscented performance does not exhibit better energy convergence as compared to the three and two body results. This is largely due to the problem formulations and the ability of the Non-Linear Programming (NLP) solver to converge on an optimal results. For the three and two-body cases, the solver converges with lower allowable mean error (μ_x), so the solution accuracy lost utilizing a truncated model is compensated for by converging to solutions with lower mean error. There exists a trade-off then between model complexity, and the ability for the solver to converge to a lower mean error solution. For the cases analyzed herein, the bus and SAA-1 are largely desired to be nearly static. Their inclusion within the optimal dynamics increases the accuracy of the model, but also affects the solver's ability to converge by increasing the number of optimization variables. While the two-body model omits the dynamics of the bus and SAA-1, the solver is better able to converge to zero-mean error solutions. This is illustrated in Figure 5.4 where Case 10 exhibits significantly larger standard deviation than the three and two-body cases. While the five-body model exhibited worse energy convergence than the three and two-body models, it still represents a 62% improvement in pointing convergence, and a 24% improvement in energy convergence compared to the standard maneuver.

Table 5.4: Closed-loop Convergence Times for Robust, Optimal Maneuvers

		Robust	Convergence Time (s)			
Case #	Bodies	Method	Bus	SAA-1	SAA-2	Total Energy
1a	1	n/a	89.3	–	131.6	145.2
10	5	Unc	39.15	–	50.0	110.3
14	3	Unc	–	–	54.8	65.7
17	2	Unc	–	–	50	60.32

Table 5.5 compares the robustness method, number of optimization variables, and computation time for various cases analyzed. These results show that by utilizing robust optimal control techniques, such as desensitized and unscented optimal control, reduced-order models can be utilized producing results that are not only robust against parameter variability, but also provide significant performance improvements over the standard maneuver without resorting to artificial soft constraints on gimbal velocity. Reducing the number of modeled bodies has a large impact on the number of optimization variables submitted to the NLP solver and has a direct impact on computation times. By reducing the number of bodies modeled, while continuing to model the nonlinear and flexible dynamics of the remaining bodies, the desensitized and unscented optimal control techniques utilized herein produce maneuvers simultaneously increasing payload availability while remaining robust to parameter variability. Importantly for future operational implementation, the two-body problem formulations decreased computation time by 92.5 to 99% while still reducing pointing convergence times by 95 seconds and energy convergence times by 77 to 85 seconds.

Table 5.5: Closed-loop Convergence Times for Robust Optimal Control Maneuvers

		Robust	Convergence Time (s)				Compute	Optimization
Case #	Bodies	Method	Bus	SAA-1	SAA-2	Total Energy	Time (s)	Variables
1a	1	n/a	89.3	–	131.6	145.2	0.4	n/a
5	5	Sensi	37.2	–	50	57.8	3600	4960
10	5	Unc	39.15	–	50.0	110.3	2600	9020
11	3	Sensi	–	–	50	64	395	2760
14	3	Unc	–	–	54.8	65.7	365	4860
16	2	Sensi	–	–	50	68.7	29	1760
17	2	Unc	–	–	50	60.32	195	3160

Comparing the computation times of the desensitized optimal control technique versus the unscented method can be misleading. For desensitized optimal control, once

the necessary sensitivity dynamics have been formulated and appended to the system dynamics, the optimal control problem formulation is straight forward and issues of solution existence can largely be ignored. For the unscented optimal control method, it was often necessary to formulation multiple ancillary problem formulations, where allowable mean state error was successively tightened until an acceptable solution was calculated. So while the final computation time for Case 10 was only 2600 seconds compared to 3600 seconds for Case 5, this time does not take into account the multitude of iterations necessary for each ancillary problem.

5.2 Contributions

5.2.1 Research Question 1 Contributions.

Specific contributions from Research Question 1 include:

- A method for deriving optimal control maneuvers which rolling back "soft" constraints of maximum gimbal velocity utilized for standard maneuver planning and directly bounding the underlying vibrational modes to reduce maneuver time while minimizing system excitation
- Constraint formulation allowing for the optimal maneuver of one aperture while maintaining stringent pointing requirements of adjacent apertures
- A conference paper [97] containing the research for Research Question (RQ) 1: "Optimal Trajectory Generation for Multi-body Flexible Systems with Vibration Compensation via Pseudospectral Methods"

5.2.2 Research Question 2 Contributions.

Specific contributions from Research Question 2 include:

- Derivation of a first-order sensitivity function accounting for maneuver sensitivity to seven uncertain modeling parameters accounting for gimbal joint stiffness and bus modal frequency variations

- Formulation of a desensitized optimal control problem solved via pseudospectral methods reducing total maneuver time while minimizing terminal sensitivity to parameter variation

- Formulation of a novel multi-objective cost functional exploring the trade space between minimizing control jerk and maneuver terminal sensitivity as a means of further increasing maneuver robustness to vibrational excitation

- A draft journal article [98] containing the research for RQ 2: "Robust Slewing Trajectories for Flexible Multi-body Systems".

5.2.3 Research Question 3 Contributions.

Specific contributions from Research Question 3 include:

- A method for constructing an unscented optimal control problem formulation to be solved via pseudospectral methods minimizing mean terminal state error and total system energy

- A means of tightening optimization constraints as a means of ensuring the existence of the initial problem formulation while systematically stepping towards a zero-mean error solution

- A conference paper [99] containing the research for RQ 3: "Robust Multi-body Slewing Trajectories via Unscented Optimal Control".

5.2.4 Research Question 4 Contributions.

Specific contributions from Research Question 4 include:

- Derivation of a reduced order, three-body model assuming one antenna is static and modeled as a rigid body subsumed into the root body. The three-body dynamics are then utilized deriving desensitized and unscented optimal maneuvers

- Derivation of a truncated, two-body dynamic model, modeling the motion of a single antenna assuming an inertially fixed based. Derived method of stimulating the now decoupled modal dynamics, and utilizing their vibrational response as an energy monitor for the two-body system.

- Formulated a desensitized optimal control problem minimizing terminal sensitivity to parameter variation

- Monte Carlo simulations comparing the mean pointing error and mean terminal system energy for the three-body and two-body solutions comparing the results to the five-body results from RQ 2-3

- Provided comparison of maneuver performance versus computational time demonstrating how robust methods can be utilized to increase the performance of maneuvers derived with reduced fidelity models

5.3 Future Work

Future work for this area of research would involve experimenting with a larger problem set of slew maneuvers such as short 1-degree slews as well as investigating the ability of the robust methods to accommodate slew maneuvers of both antennas simultaneously. The problem utilized in this research included SAA-1 in an Auto Track (AT) mode where the maximum velocity was constrained to less than 0.02 deg/s where it contributes minimally to the excitation of the bus vibrational states. For real-world systems such as TDRS, there may be a desire to slew SAA-1 between User Satellites (USAT) while SAA-2 is mid-maneuver. This problem formulation would present a higher energy state

with both SAA in a Program Track (PT) mode, increasing the excitation of the system. Another case would be the ability to maintain AT or perform a PT maneuver while the satellite bus is simultaneously performing a slew maneuver demonstrating the ability to generate robust maneuvers maintaining mission while the bus performs station-keeping maneuvers.

Another area of future work would be to investigate the robust method's utility against different spacecraft models such as the International Space Station's Canadarm system, where flexibility of the long/slender members can also be modeled by the hybrid coordinate method or where the dynamic coupling matrix δ is not diagonal but contains cross-coupling terms. Similarly, additional parameters could be included within the uncertain parameter space such as system moment of inertia uncertainty due to fuel usage.

While this research utilized Legendre-Gauss-Lobatto (LGL) nodes, the convergence of Legendre-Gauss-Radau (LGR), Legendre-Gauss (LG) or alternative polynomials such as Chebyshev could be investigated and the computational time compared against commercially available solvers such as DIDO [100] and GPOPS II [101]. Similarly, the custom scripts utilized herein did utilize mesh refinement methods to increase convergence rates or solution optimality. The custom scripts utilized herein did not calculate the Hamiltonian evolution for the resulting optimal solutions, therefore the optimality of the resulting solutions was not verified other than through validation via simulation. If the custom scripts were used in future research, the Covector Mapping Principle (CMP) could be utilized to map the Karush-Kuhn-Tucker (KKT) multipliers from the NLP solver into the Lagrange multipliers necessary for calculating the Hamiltonian evolution in accordance with Equation (2.9).

The trade-off between maneuver length, the highest frequency of interest, and the number of collocation nodes utilized can be investigated. Based on the modeled modal frequencies, a minimum number of nodes must be utilized based on the corresponding

Nyquist frequency, however, the minimum sampling time traditionally corresponds to evenly space sampling points. Due to the Pseudospectral Methods (PSM) using variables spacing, how this impacts the number of nodes necessary to accurately model and accommodate the frequencies of interest should be investigated.

This research has demonstrated the ability for desensitized and unscented optimal control to accommodate a nonlinear, five-body model and derive maneuvers increasing system performance, however, and further showed the techniques can be used to increase the robustness of reduced-order models in order to decrease computation time. Even for the reduced-order models, the computation time is still untenable for real-time applications in which results must be provided to the Guidance, Navigation and Control subsystem often within milliseconds. Further research should investigate other methods of deriving the sensitivity function and/or methods of coding the resultant code so as to minimize computation time. The robust optimal control method could also be leverage by machine learning and artificial intelligence as a method of creating highly efficient trajectory derivation based upon the robust results.

Another means of reducing computation time could be by implementing a single-sided unscented transform where only $N_p + 1$ of of the $2N_p + 1$ sigma points are utilized and the resulting robustness compared to the full solution. By utilizing only half of the sigma vectors, the single-sided transform would no longer fully capture the statistical moments of the uncertain parameters but could still serve to increase the robustness of the maneuver. The trade-space between the increase in robustness versus reduction in computation time could be explored.

Bibliography

[1] Li Shunli, Xu Yang, and Di Yang. Active disturbance rejection control for high pointing accuracy and rotation speed. *Automatica*, 45(8):1854–1860, August 2009. URL: https://linkinghub.elsevier.com/retrieve/pii/S0005109809001721, doi:10.1016/j.automatica.2009.03.029.

[2] Bong Wie and Carl T. Plescia. Attitude stabilization of flexible spacecraft during stationkeeping maneuvers. *Journal of Guidance, Control, and Dynamics*, 7(4):430–436, July 1984. URL: https://arc.aiaa.org/doi/10.2514/3.19874, doi:10.2514/3.19874.

[3] Quang Tham, J. H. Ly, R. Y. Chiang, D. Bender, and B. N. Eyerly. Robust antenna pointing control for TDRS spacecraft. In *Proceedings of the 36th IEEE Conference on Decision and Control*, volume 5, pages 4938–4942. IEEE, 1997.

[4] H. Schmeichel and T. T. McElroy. TDRSS single-access antenna control system. In *Guidance and Control 1980*, pages 115–146, January 1980.

[5] Jennifer Donaldson, Gregory W. Heckler, Cheryl J. Gramling, Benjamin Ashman, Marco Toral, and Jeremy Lyon. Commissioning of NASA's 3 rd Generation Tracking and Data Relay Satellites (TDRS-KLM). In *15th International Conference on Space Operations*, Marseille, France, May 2018. American Institute of Aeronautics and Astronautics. URL: https://arc.aiaa.org/doi/10.2514/6.2018-2359, doi:10.2514/6.2018-2359.

[6] SpaceX. Starlink.com, 2019. URL: http://www.starlink.com.

[7] Paul Thomas. Blackjack: Military Space Pivot to LEO, August 2018. URL: https://satelliteobservation.files.wordpress.com/2019/03/thomas_8-22-18.pptx.

[8] Alexa Aguilar, Patrick Butler, Jennifer Collins, Markus Guerster, Bjarni Kristinsson, Patrick McKeen, Kerri Cahoy, and Edward F. Crawley. Tradespace Exploration of the Next Generation Communication Satellites. In *AIAA Scitech 2019 Forum*, page 30, San Diego, California, January 2019. American Institute of Aeronautics and Astronautics.

[9] NASA. Tracking and Data Relay Satellite (TDRS), September 2017. URL: https://www.nasa.gov/directorates/heo/scan/services/networks/tdrs_main.

[10] Marco A Toral. Third Generation Tracking and Data Relay Satellite (TDRS-KLM) TDRS Project Office, October 2017. URL: https://ntrs.nasa.gov/api/citations/20170010208/downloads/20170010208.pdf.

[11] Bernard L. Edwards and David J. Israel. A geosynchronous orbit optical communications relay architecture. In *2014 IEEE Aerospace Conference*, pages 1–7, Big Sky, MT, USA, March 2014. IEEE. URL: http://ieeexplore.ieee.org/document/6836521/, doi:10.1109/AERO.2014.6836521.

[12] Thomas R. Kane and David A. Levinson. *Dynamics: Theory and Applications*. McGraw-Hill College, New York, first edition edition, May 1985.

[13] Paul C. Mitiguy. MotionGenesis Kane: Symbolic Solutions for forces and motion, January 2019. URL: http://www.motiongenesis.com.

[14] Peter W. Likins. Dynamics and Control of Flexible Space Vehicles. Technical Report 32-1329, NASA Jet Propulsion Laboratory, February 1969.

[15] Philip E. Gill, Walter Murray, and Michael A. Saunders. SNOPT: An SQP Algorithm for Large-Scale Constrained Optimization. *SIAM Rev.*, 47(1):99–131, January 2005. URL: http://epubs.siam.org/doi/10.1137/S0036144504446096, doi:10.1137/S0036144504446096.

[16] Brian Bishop, Richard Gargano, Adam G. Sears, and Mark Karpenko. Rapid Maneuvering of Multi-Body Dynamic System with Motion Compensation. *Acta Astronautica*, 117:209–221, December 2015. URL: https://www.sciencedirect.com/science/article/pii/S0094576515003161.

[17] Peter Fortescue, Graham Swinerd, and John Stark. *Spacecraft Systems Engineering*. John Wiley & Sons, New York, 2011.

[18] Thomas P. Sarafin. *Spacecraft Structures and Mechanisms - From Concept to Launch*. Springer, New York, NY, 6th edition, 2011.

[19] P. Th. L. M. Van Woerkom and A.K. Misrab. Robotic Manipulators in Space: A Dynamis and Control Perspective. *Acta Astronautica*, 30(4-8):411–421, 1996.

[20] G. E. Fleischer and Peter W. Likins. Results of flexible spacecraft attitude control studies utilizing hybrid coordinates. *Journal of Spacecraft and Rockets*, 8(3):264–273, 1971. URL: http://dx.doi.org/10.2514/3.30258, doi:10.2514/3.30258.

[21] John T. Betts. Survey of Numerical Methods for Trajectory Optimization. *Journal of Guidance, Control, and Dynamics*, 21(2):193–207, March 1998. URL: https://arc.aiaa.org/doi/10.2514/2.4231, doi:10.2514/2.4231.

[22] Anil V Rao. A Survey of Numerical Methods for Optimal Control. *Advances in the Astronautical Sciences*, 135.1:32, 2009.

[23] Bruce A. Conway. A Survey of Methods Available for the Numerical Optimization of Continuous Dynamic Systems. *J Optim Theory Appl*, 152(2):271–306, February 2012. URL: http://link.springer.com/10.1007/s10957-011-9918-z, doi:10.1007/s10957-011-9918-z.

[24] I. Michael Ross and Fariba Fahroo. Legendre Pseudospectral Approximations of Optimal Control Problems. In *New Trends in Nonlinear Dynamics and Control and their Applications*, volume 295, pages 327–342. Springer Berlin Heidelberg, Berlin, Heidelberg, May 2004. URL: http://link.springer.com/10.1007/978-3-540-45056-6_21, doi:10.1007/978-3-540-45056-6_21.

[25] G. Elnagar, M.A. Kazemi, and M. Razzaghi. The pseudospectral Legendre method for discretizing optimal control problems. *IEEE Trans. Automat. Contr.*, 40(10):1793–1796, October 1995. URL: http://ieeexplore.ieee.org/document/467672/, doi:10.1109/9.467672.

[26] Fariba Fahroo and I. Michael Ross. Costate Estimation by a Legendre Pseudospectral Method. *Journal of Guidance, Control, and Dynamics*, 24(2):270–277, March 2001. URL: https://arc.aiaa.org/doi/10.2514/2.4709, doi:10.2514/2.4709.

[27] Nazareth S. Bedrossian, S Bhatt, Wei Kang, and I Michael Ross. Zero-propellant maneuver guidance. *IEEE Control Syst.*, 29(5):53–73, October 2009. URL: https://ieeexplore.ieee.org/document/5256357/, doi:10.1109/MCS.2009.934089.

[28] Mark Karpenko, Travis Lippman, I Michael Ross, Julie K Halverson, Timothy McClanahan, Michael Barker, Erwan Mazarico, Rebecca Besser, Cornelius J Dennehy, Tannen VanZwieten, and Aron Wolf. Fast Attitude Maneuvers for the Lunar Reconnaissance Orbiter. In *Guidance Navigation and Control*, page 17. American Astronautical Society, 2019.

[29] Mark Karpenko, Sagar Bhatt, Nazareth Bedrossian, and I. Michael Ross. Flight Implementation of Shortest-Time Maneuvers for Imaging Satellites. *Journal of Guidance, Control, and Dynamics*, 37(4):1069–1079, July 2014. URL: http://arc.aiaa.org/doi/10.2514/1.62867, doi:10.2514/1.62867.

[30] Jie Shen, Tao Tang, and Li-Lian Wang. *Spectral methods: algorithms, analysis and applications*, volume 41. Springer Science & Business Media, New York, 2011.

[31] L.S. Pontryagin, V.G. Boltyanskii, R.V. Gamkrelidze, and E.F. Mishchenko. *The Mathematical Theory of Optimal Processes*. John Wiley & Sons Inc, New York, 1962.

[32] Donald E. Kirk. *Optimal Control Theory: An Introduction*. Dover Publications, Inc, Mineola, New York, 1998.

[33] Arthur E. Bryson. *Dynamic optimization*. Addison Wesley Longman, Menlo Park, CA, 1999.

[34] Fariba Fahroo and I. Michael Ross. Advances in Pseudospectral Methods for Optimal Control. In *AIAA Guidance, Navigation and Control Conference and Exhibit*, Honolulu, Hawaii, August 2008. American Institute of Aeronautics and Astronautics. URL: http://arc.aiaa.org/doi/10.2514/6.2008-7309, doi:10.2514/6.2008-7309.

[35] Fariba Fahroo and I. Michael Ross. Pseudospectral Methods for Infinite-Horizon Nonlinear Optimal Control Problems. *Journal of Guidance, Control, and Dynamics*, 31(4):927–936, July 2008. URL: http://arc.aiaa.org/doi/10.2514/1.33117, doi:10.2514/1.33117.

[36] Divya Garg, Michael Patterson, William Hager, Anil Rao, David Benson, and Geoffrey Huntington. An overview of three pseudospectral methods for the numerical solution of optimal control problems. Technical report, University of Florida, 2017. URL: https://hal.archives-ouvertes.fr/hal-01615132/.

[37] Lloyd N. Trefethen. *Spectral Methods in Matlab*. SIAM, Philadelphia, PA, first edition, 2000.

[38] Philip E Gill, Elizabeth Wong, Walter Murray, and Michael A Saunders. User's Guide for SNOPT Version 7.7: Software for Large-Scale Nonlinear Programming. Center for Computational Mathematics Report CCoM 18-1, Department of Mathematics, University of California, San Diego, 2018.

[39] Richard Shaffer. *Two Degree of Freedom Optimal Control for Nonlinear Systems with Parameter Uncertainty*. Dissertation, University of California Santa Cruz, Santa Cruz, CA, 2019.

[40] Hassan K. Khalil and Jessy W. Grizzle. *Nonlinear Systems*, volume 3rd. Prentice Hall, Upper Saddle River, NJ, 2002.

[41] I Michael Ross, Ronald J Proulx, and Mark Karpenko. Unscented Optimal Control for Space Flight. In *24th International Symposium on Space Flight Dynamics*, page 12, 2014.

[42] I. Michael Ross, Ronald J. Proulx, and Mark Karpenko. Unscented guidance. In *2015 American Control Conference (ACC)*, pages 5605–5610, Chicago, IL, USA, July 2015. IEEE. URL: http://ieeexplore.ieee.org/document/7172217/, doi:10.1109/ACC.2015.7172217.

[43] Richard Shaffer, Mark Karpenko, and Qi Gong. Unscented guidance for waypoint navigation of a fixed-wing UAV. In *2016 American Control Conference (ACC)*, pages 473–478, Boston, MA, USA, July 2016. IEEE. URL: http://ieeexplore.ieee.org/document/7524959/, doi:10.1109/ACC.2016.7524959.

[44] Simon J. Julier and Jeffrey K. Uhlmann. New extension of the Kalman filter to nonlinear systems. In *Signal processing, sensor fusion, and target recognition VI*, volume 3068, pages 182–193. International Society for Optics and Photonics, Orlando, FL, 1997.

[45] I. Michael Ross, Ronald J. Proulx, Mark Karpenko, and Qi Gong. Riemann–Stieltjes Optimal Control Problems for Uncertain Dynamic Systems. *Journal of Guidance, Control, and Dynamics*, 38(7):1251–1263, July 2015. URL: http://arc.aiaa.org/doi/10.2514/1.G000505, doi:10.2514/1.G000505.

[46] I. Michael Ross, Ronald Proulx, and Mark Karpenko. Unscented Optimal Control for Orbital and Proximity Operations in an Uncertain Environment: A New Zermelo Problem. In *AIAA/AAS Astrodynamics Specialist Conference*, San Diego, CA, August 2014. American Institute of Aeronautics and Astronautics. URL: http://arc.aiaa.org/doi/10.2514/6.2014-4423, doi:10.2514/6.2014-4423.

[47] I. Michael Ross, Ronald Proulx, and Mark Karpenko. Unscented Optimal Control for Orbital and Proximity Operations in an Uncertain Environment: A New Zermelo Problem. In *AIAA/AAS Astrodynamics Specialist Conference*, San Diego, CA, August 2014. American Institute of Aeronautics and Astronautics. URL: http://arc.aiaa.org/doi/10.2514/6.2014-4423, doi:10.2514/6.2014-4423.

[48] E.A. Wan and R. Van Der Merwe. The unscented Kalman filter for nonlinear estimation. In *Proceedings of the IEEE 2000 Adaptive Systems for Signal Processing, Communications, and Control Symposium (Cat. No.00EX373)*, pages 153–158, Lake Louise, Alta., Canada, 2000. IEEE. URL: http://ieeexplore.ieee.org/document/882463/, doi:10.1109/ASSPCC.2000.882463.

[49] Shanzhong Duan. A Comparison Case Study For Dynamics Analysis Methods In Applied Multibody Dynamics. Technical Report 2006-1859, South Dakota State University, Brookings, SD, 2006.

[50] A. Purushotham and Mr J. Anjeneyulu. Kane's method for robotic arm dynamics: a novel approach. *IOSR Journal of Mechanical and Civil Engineering*, 6(4):7–13, 2013.

[51] Thomas R. Kane and David A. Levinson. Formulation of Equations of Motion for Complex Spacecraft. *Journal of Guidance, Control, and Dynamics*, 3(2):99–112, March 1980. URL: http://arc.aiaa.org/doi/10.2514/3.55956, doi:10.2514/3.55956.

[52] Thomas R. Kane and David A. Levinson. The Use of Kane's Dynamical Equations in Robotics. *The International Journal of Robotics Research*, 2(3):3–21, September 1983. URL: http://journals.sagepub.com/doi/10.1177/027836498300200301, doi:10.1177/027836498300200301.

[53] Eric Stoneking. Implementation of Kane's Method for a Spacecraft Composed of Multiple Rigid Bodies. In *AIAA Guidance, Navigation and Control Conference*, page 13, Boston, MA, August 2013. AIAA.

[54] M. W. Spong. Modeling and Control of Elastic Joint Robots. *Journal of Dynamic Systems, Measurement, and Control*, 109(4):310, 1987. URL: http://DynamicSystems.asmedigitalcollection.asme.org/article.aspx?articleid=1403980, doi:10.1115/1.3143860.

[55] Adam L Atwood, Martin J Griggs, Steven W Wojdakowski, and Mark Karpenko. Rapid Motion Control of Flexible Space Systems. *Advances in the Astronautical Sciences*, 18(012):17, 2018.

[56] Pengyu Wang, Zongming Liu, Chuanjiang Li, Yanchao Sun, and Chao Zhang. Time-Fuel Optimal Trajectory Based Attitude Maneuver Control for Flexible Spacecraft. In *2016 Sixth International Conference on Instrumentation & Measurement, Computer, Communication and Control (IMCCC)*, pages 197–201, Harbin, China, July 2016. IEEE. URL: http://ieeexplore.ieee.org/document/7774765/, doi:10.1109/IMCCC.2016.227.

[57] Qinglei Hu. Adaptive Nonlinear Proportional-Derivative Type Fault Tolerant Control for Flexible Spacecraft Attitude Maneuvers under Bounded Disturbances. *J. Aerosp. Eng.*, 25(2):178–190, April 2012. URL: http://ascelibrary.org/doi/10.1061/%28ASCE%29AS.1943-5525.0000107, doi:10.1061/(ASCE)AS.1943-5525.0000107.

[58] Ping Guan, Xiang-Jie Liu, and Ji-Zhen Liu. Adaptive fuzzy sliding mode control for flexible satellite. *Engineering Applications of Artificial Intelligence*, 18(4):451–459, June 2005. URL: https://linkinghub.elsevier.com/retrieve/pii/S0952197604001666, doi:10.1016/j.engappai.2004.11.003.

[59] N. Aouf, B. Boulet, and R. Botez. Model and controller reduction for flexible aircraft preserving robust performance. *IEEE Trans. Contr. Syst. Technol.*, 10(2):229–237, March 2002. URL: http://ieeexplore.ieee.org/document/987068/, doi:10.1109/87.987068.

[60] JB Burl. *Linear optimal control: H (2) and H (Infinity) methods*. Addison-Wesley Longman Publishing Co., Inc, 1998.

[61] Oyvind Hegrenaes, Jan Tommy Gravdahl, and Petter Tondel. Spacecraft attitude control using explicit model predictive control. *Automatica*, 41(12):2107–2114, December 2005. URL: https://linkinghub.elsevier.com/retrieve/pii/S0005109805002657, doi:10.1016/j.automatica.2005.06.015.

[62] M. Boerlage, M. Steinbuch, P. Lambrechts, and M. van de Wal. Model-based feedforward for motion systems. In *Proceedings of 2003 IEEE Conference on Control Applications, 2003. CCA 2003.*, volume 2, pages 1158–1163, Istanbul, Turkey, 2003. IEEE. URL: http://ieeexplore.ieee.org/document/1223174/, doi:10.1109/CCA.2003.1223174.

[63] S. Devasia, Degang Chen, and B. Paden. Nonlinear inversion-based output tracking. *IEEE Trans. Automat. Contr.*, 41(7):930–942, July 1996. URL: http://ieeexplore.ieee.org/document/508898/, doi:10.1109/9.508898.

[64] Paul Lambrechts, Matthijs Boerlage, and Maarten Steinbuch. Trajectory planning and feedforward design for electromechanical motion systems. *Control Engineering*

Practice, 13(2):145–157, February 2005. URL: https://linkinghub.elsevier.com/retrieve/pii/S0967066104000462, doi:10.1016/j.conengprac.2004.02.010.

[65] Yao Zhang and Jing-Rui Zhang. Combined control of fast attitude maneuver and stabilization for large complex spacecraft. *Acta Mech Sin*, 29(6):875–882, December 2013. URL: http://link.springer.com/10.1007/s10409-013-0080-8, doi:10.1007/s10409-013-0080-8.

[66] Shiyuan Jia and Jinjun Shan. Vibration control of gyroelastic spacecraft using input shaping and angular momentum devices. *Acta Astronautica*, 159, March 2019.

[67] W. Singhose and L. Pao. A comparison of input shaping and time-optimal flexible-body control. *Control Engineering Practice*, 5(4):459–467, April 1997. URL: https://linkinghub.elsevier.com/retrieve/pii/S0967066197000257, doi:10.1016/S0967-0661(97)00025-7.

[68] Mark Karpenko and Michael Ross. Implementation of Shortest-Time Maneuvers for Generic CMG Steering Laws. In *AIAA/AAS Astrodynamics Specialist Conference*, Minneapolis, Minnesota, August 2012. American Institute of Aeronautics and Astronautics. URL: http://arc.aiaa.org/doi/10.2514/6.2012-4959, doi:10.2514/6.2012-4959.

[69] Robert G. Melton. Hybrid methods for determining time-optimal, constrained spacecraft reorientation maneuvers. *Acta Astronautica*, 94(1):294–301, January 2014. URL: https://linkinghub.elsevier.com/retrieve/pii/S0094576513001574, doi:10.1016/j.actaastro.2013.05.007.

[70] E. Papadopoulos, I. Tortopidis, and K. Nanos. Smooth Planning for Free-floating Space Robots Using Polynomials. In *Proceedings of the 2005 IEEE International Conference on Robotics and Automation*, pages 4272–4277, Barcelona, Spain, 2005. IEEE. URL: http://ieeexplore.ieee.org/document/1570777/, doi:10.1109/ROBOT.2005.1570777.

[71] Wenfu Xu, Bin Liang, Cheng Li, Yangsheng Xu, and Wenyi Qiang. Path Planning of Free-Floating Robot in Cartesian Space Using Direct Kinematics. *International Journal of Advanced Robotic Systems*, 4(1):4, March 2007. URL: http://journals.sagepub.com/doi/10.5772/5713, doi:10.5772/5713.

[72] Alexander Crain and Steve Ulrich. Nonlinear Optimal Trajectory Planning for Free-Floating Space Manipulators using a Gauss Pseudospectral Method. In *AIAA/AAS Astrodynamics Specialist Conference*, Long Beach, California, September 2016. American Institute of Aeronautics and Astronautics. URL: http://arc.aiaa.org/doi/10.2514/6.2016-5272, doi:10.2514/6.2016-5272.

[73] Guangyan Xu, Changming Sun, Hongmei Zhang, Xia Chen, and Biao Zhou. Vibration suppressive control of flexible-joint space manipulators based on Legendre

pseudospectral method. In *The 26th Chinese Control and Decision Conference (2014 CCDC)*, pages 3322–3327, Changsha, China, May 2014. IEEE. URL: http://ieeexplore.ieee.org/document/6852748/, doi:10.1109/CCDC.2014.6852748.

[74] Steve Wojdakowski. Rapid Slewing of Flexible Space Structures. Master's thesis, Naval Postgraduate School, Monterey, CA, September 2015.

[75] Adam L. Atwood. *Flexible multi-body spacecraft simulator: design, construction, and experiments*. Thesis, Monterey, California: Naval Postgraduate School, December 2017. URL: https://calhoun.nps.edu/handle/10945/56795.

[76] Peter W. Likins. Dynamic analysis of a system of hinge-connected rigid bodies with nonrigid appendages. *International Journal of Solids and Structures*, 9(12):1473–1487, December 1973. URL: https://linkinghub.elsevier.com/retrieve/pii/0020768373900541, doi:10.1016/0020-7683(73)90054-1.

[77] Payam Zarafshan and S. Ali. A. Moosavian. Control of a space robot with flexible members. In *2011 IEEE International Conference on Robotics and Automation*, pages 2211–2216, Shanghai, China, May 2011. IEEE. URL: http://ieeexplore.ieee.org/document/5979882/, doi:10.1109/ICRA.2011.5979882.

[78] Arunava Banerjee, Syed Muhammad Amrr, and M. Nabi. Legendre-pseudospectral method based attitude control for tracking and regulation of rigid spacecraft. In *2019 Fifth Indian Control Conference (ICC)*, pages 347–352, New Delhi, India, January 2019. IEEE. URL: https://ieeexplore.ieee.org/document/8715563/, doi:10.1109/INDIANCC.2019.8715563.

[79] Arunava Banerjee, Syed Muhammad Amrr, and M. Nabi. A pseudospectral method based robust-optimal attitude control strategy for spacecraft. *Advances in Space Research*, 64(9):1688–1700, November 2019. URL: https://linkinghub.elsevier.com/retrieve/pii/S0273117719305745, doi:10.1016/j.asr.2019.08.008.

[80] S. H. Dai. The Implementation of Optimal Control with Sensitivity Reduction to Plant Parameter Variations. Master's thesis, Department of Engineering, McMaster University, Hamilton, Ontario, April 1970.

[81] Hans Seywald and Renjith R Kumar. Desensitized Optimal Trajectories. *Spaceflight Mechanics 1996*, page 19, 1996.

[82] Hans Seywald and Kevin L. Seywald. Intrinsic Desensitized Optimal Control Progress Report 1. In *2020 IEEE Aerospace Conference*, pages 1–33, Big Sky, MT, USA, March 2020. IEEE. URL: https://ieeexplore.ieee.org/document/9172693/, doi:10.1109/AERO47225.2020.9172693.

[83] Qiang Liu and Bong Wie. Robust time-optimal control of uncertain flexible spacecraft. *Journal of Guidance, Control, and Dynamics*, 15(3):597–604, May 1992. URL: https://arc.aiaa.org/doi/10.2514/3.20880, doi:10.2514/3.20880.

[84] Shin-Whar Liu and Tarunraj Singh. Robust Time-Optimal Control of Flexible Structures With Parametric Uncertainty. *Journal of Dynamic Systems, Measurement, and Control*, 119(4):743–748, December 1997. URL: https://asmedigitalcollection.asme.org/dynamicsystems/article/119/4/743/426490/Robust-TimeOptimal-Control-of-Flexible-Structures, doi:10.1115/1.2802386.

[85] Alex Ansari and Todd Murphey. Minimal parametric sensitivity trajectories for nonlinear systems. In *2013 American Control Conference*, pages 5011–5016, Washington, DC, June 2013. IEEE. URL: http://ieeexplore.ieee.org/document/6580616/, doi:10.1109/ACC.2013.6580616.

[86] Alex Ansari and Todd Murphey. Minimum sensitivity control for planning with parametric and hybrid uncertainty. *The International Journal of Robotics Research*, 35(7):823–839, June 2016. URL: http://journals.sagepub.com/doi/10.1177/0278364915600536, doi:10.1177/0278364915600536.

[87] Richard Shaffer, Mark Karpenko, and Qi Gong. Robust Control of a Flexible Double Gimbal Mechanism. In *2018 Annual American Control Conference (ACC)*, pages 1–4, Milwaukee, WI, June 2018. IEEE. URL: https://ieeexplore.ieee.org/document/8430958/, doi:10.23919/ACC.2018.8430958.

[88] Mark Karpenko and Ronald J. Proulx. Experimental Implementation of Riemann–Stieltjes Optimal Control for Agile Imaging Satellites. *Journal of Guidance, Control, and Dynamics*, 39(1):144–150, January 2016. URL: http://arc.aiaa.org/doi/10.2514/1.G001325, doi:10.2514/1.G001325.

[89] Bong Wie. *Space vehicle dynamics and control*. American Institute of Aeronautics and Astronautics, Reston, VA, 2008.

[90] I. Michael Ross, Mark Karpenko, and Ronald J. Proulx. Path constraints in tychastic and unscented optimal control: Theory, application and experimental results. In *2016 American Control Conference (ACC)*, pages 2918–2923, Boston, MA, USA, July 2016. IEEE. URL: http://ieeexplore.ieee.org/document/7525362/, doi:10.1109/ACC.2016.7525362.

[91] S. Mathavaraj and Radhakant Padhi. Unscented MPSP for Optimal Control of a Class of Uncertain Nonlinear Dynamic Systems. *Journal of Dynamic Systems, Measurement, and Control*, 141(6):065001, June 2019. URL: https://asmedigitalcollection.asme.org/dynamicsystems/article/doi/10.1115/1.4042549/472513/Unscented-MPSP-for-Optimal-Control-of-a-Class-of, doi:10.1115/1.4042549.

[92] Naoya Ozaki, Stefano Campagnola, and Ryu Funase. Tube Stochastic Optimal Control for Nonlinear Constrained Trajectory Optimization Problems. *Journal of Guidance, Control, and Dynamics*, 43(4):645–655, April 2020. URL: https://arc.aiaa.org/doi/10.2514/1.G004363, doi:10.2514/1.G004363.

[93] Peter Likins, Yoshiaki Ohkami, and Chung Wong. Appendage modal coordinate truncation criteria in hybrid coordinate dynamic analysis. *Journal of Spacecraft and Rockets*, 13(10):611–617, October 1976. URL: https://arc.aiaa.org/doi/10.2514/3.27933, doi:10.2514/3.27933.

[94] Quang Tham, F. Lee, J. Ly, and R. Chiang. Robust pointing control of spacecraft with large appendages. In *1997 IEEE Aerospace Conference*, volume 2, pages 369–375, Snowmass at Aspen, CO, USA, 1997. IEEE. URL: http://ieeexplore.ieee.org/document/577988/, doi:10.1109/AERO.1997.577988.

[95] Richard Béarée. New Damped-Jerk trajectory for vibration reduction. *Control Engineering Practice*, 28:112–120, July 2014. URL: https://linkinghub.elsevier.com/retrieve/pii/S0967066114001142, doi:10.1016/j.conengprac.2014.03.010.

[96] Jae Jun Kim and Brij Agrawal. Experiments on Jerk-Limited Slew Maneuvers of a Flexible Spacecraft. In *AIAA Guidance, Navigation, and Control Conference and Exhibit*, Keystone, Colorado, August 2006. American Institute of Aeronautics and Astronautics. URL: https://arc.aiaa.org/doi/10.2514/6.2006-6187, doi:10.2514/6.2006-6187.

[97] Brian W Bishop, Richard G Cobb, and Costantinos Zagaris. Optimal Trajectory Generation For Multi-Body Flexible Systems with Vibration Compensation via Pseudospectral Methods. In *To appear in proceedings of the AIAA/AAS Astrodynamics Specialist Conference*, page 20. American Institute of Aeronautics and Astronautics, 2020.

[98] Brian W Bishop, Richard G Cobb, Costantinos Zagaris, and Mark Karpenko. Robust Slewing Trajectories for Flexible Multi-body Systems. *in preparation - Acta Astronautica*, page 13, 2021.

[99] Brian W Bishop, Richard G Cobb, and Costantinos Zagaris. Robust Multi-Body Slewing Trajectories via Unscented Optimal Control. In *To appear in proceedings of the AIAA/AAS Spaceflight Mechanics Conference*, page 15, 2021.

[100] I. M. Ross. Enhancements to the DIDO Optimal Control Toolbox. *arXiv:2004.13112 [cs, math]*, April 2020. arXiv: 2004.13112. URL: http://arxiv.org/abs/2004.13112.

[101] Anil V Rao, David A Benson, Christopher Darby, Michael A Patterson, Camila Francolin, and Ilyssa Sanders. GPOPS: A MATLAB R Software for Solving Multiple-Phase Optimal Control Problems Using the Gauss Pseudospectral Method. page 36.

Appendix A: Lessons Learned

This appendix is intended to captures some of the general lessons learned during this research

When utilizing Matlab, it is beneficial to compile any computationally intensive scripts, such as the system dynamics, into MEX files. For the dynamics considered herein, Matlab it takes 27.4 seconds to compute 100,000 iterations of the dynamics in M-file format while only requiring 3.0 seconds for the MEX version. Utilizing the "Run and Time" command in Matlab allows one to identify the most time consuming functions which can then be converted to MEX in order to decrease total computation time.

For SNOPT (and many other NLP solvers), it is required to provide a bounds matrix for the optimization variables, and a constraints matrix. For problems where the initial or final state is known, there are multiple ways to inform the solver. The first is by setting the upper and lower bounds equal to the initial/final state. For example, setting the bounds at the final collocation point as: $x_L(t_f) = x^f = x_u(t_f)$ ensures that the only allowable values represent the final point. The second methods is to set identical state bounds for all collocation points, $x_L \leq x \leq x_u$, and create event conditions within the constraints matrix which enforce the beginning/final values exactly: $e_0 = x^0$, $e_f = x^f$. It was noted that for this problem formulation, using endpoint conditions within the constraints matrix provided faster computation times than bounding the states directly. This may not be true in general, but was the case for this problem.

When solving problem using the unscented method, ancillary formulations were used to incrementally approach zero-mean terminal error. Occasionally, setting the allowable mean to $\mu_x \leq 1x10^{-5}$ would not converge, but setting $\mu_x \leq 0$ would converge to a solution. While ancillary formulations proved useful and necessary many of the times, it could be

a smart strategy to always start with a zero-mean-error formulation to see if the solver converges before resorting to ancillary formulations.

The scaling of the states and controls has a direct correlation to the ability of the NLP solver to converge to an optimal solution. The modal variables are often constrained to be less than 0.01 degrees, which is $1.74E-04$ radians. If these values are squared in the dynamics, or multiplied by other similarly small values, the magnitude of the resulting state is below the convergence threshold of the solver. It is essential that the states be scaled such that their scaled values are larger than the convergence threshold of the solver otherwise, otherwise the return solution may not be valid. Proper scaling also has an impact on computation time where improper scaling and increase computation time by orders of magnitude.

Appendix B: Dynamics, 5-Body System

This page intentionally left blank. Dynamics code is inserted as a pdf on the following pages.

```
function [dxdt,COEF,As,Bs] = Dynamics_5B3D_LinkFlex9num(x,h,u,Z,p,ATe,ATw,SENSI)
% (U) The highest classification level of code contained within
% this MATLAB script is UNCLASSIFIED:

% Lt Col Brian Bishop, 2021
% Air Force Institute of Technology
% brian.bishop@afit.edu
%=========================================================================
% Dynamics for 5-Body system including joint flexibility
%=========================================================================
%% Error Check

if length(x) ~= 41
    if length(x) ~= 49
        disp('Incorrect state length')
        dxdt = 0;
        COEF = 0;
        As = zeros( 20, 41 );
    Bs = zeros( 20, 7 );
        return
    end
end

%=========================================================================
% Define Variables
%=========================================================================
As = zeros( 20, 41 );
    Bs = zeros( 20, 7 );
if SENSI == 0
    z = zeros( 1, 136 );
else
    As = zeros( 20, 41 );
    Bs = zeros( 20, 7 );
    z = zeros( 1, 302 );
end

%% Preamble
kB = p(1);
kC = p(2);
kD = p(3);
kE = p(4);
wx1 = p(5);
wx2 = p(6);
wx3 = p(7);
wy1 = p(8);
wy2 = p(9);
wy3 = p(10);
wz1 = p(11);
wz2 = p(12);
wz3 = p(13);
```



```
%% Unpack Inputs
% e0 = x(1);
% e1 = x(2);
% e2 = x(3);
% e3 = x(4);
xB = x(5);
xC = x(6);
xD = x(7);
xE = x(8);
xGB = x(9);
xGC = x(10);
xGD = x(11);
xGE = x(12);
qx1 = x(13);
qx2 = x(14);
qx3 = x(15);
qy1 = x(16);
qy2 = x(17);
qy3 = x(18);
qz1 = x(19);
qz2 = x(20);
qz3 = x(21);

wx = x(22);
wy = x(23);
wz = x(24);
xBDt = x(25);
xCDt = x(26);
xDDt = x(27);
xEDt = x(28);
xGBDt = x(29);
xGCDt = x(30);
xGDDt = x(31);
xGEDt = x(32);
qx1Dt = x(33);
qx2Dt = x(34);
qx3Dt = x(35);
qy1Dt = x(36);
qy2Dt = x(37);
qy3Dt = x(38);
qz1Dt = x(39);
qz2Dt = x(40);
qz3Dt = x(41);

if length(x) == 41
    % Convert RW (h=Jw) into [xyz] frame
    T = Z*u(1:4);
    TAx = T(1);
    TAy = T(2);
```



```
    TAz = T(3);
    % Commanded Gimbal Torques
    TB = u(5);
    TC = u(6);
    TD = u(7);
    TE = u(8);
else
    % Convert RW (h=Jw) into [xyz] frame
    T = Z*x(42:45);
    TAx = T(1);
    TAy = T(2);
    TAz = T(3);
    % Commanded Gimbal Torques
    TB = x(46);
    TC = x(47);
    TD = x(48);
    TE = x(49);
end

%% Lock Gimbals

% If a gimbal is locked, this removes the corresponding row/column from
% COEF and row from RHS; AT == 2 locks the gimbal but models link
% flexibility. AT == 3 locks both the gimbal motor and ignores link
% flexibility.
ind = [1:3,12:20];
%%{
switch ATe
    case 0
        ind = [ind,4,5,8,9];
    case 1
        ind = [ind,4,5,8,9];
    case 2
        ind = [ind,4,5];
end

switch ATw
    case 0
        ind = [ind,6,7,10,11];
    case 1
        ind = [ind,6,7,10,11];
    case 2
        ind = [ind,6,7];
end

ind = sort(ind);
%}

%% Autozee Variables
```



```
z(1) = sin(xC);
z(2) = cos(xC);
z(3) = -0.1 + 0.2*z(1) - 0.05*z(2);
z(4) = sin(xB);
z(5) = cos(xB);
z(6) = 1.5 + 0.1*z(4) + 0.1*z(5);
z(7) = z(4)*(z(1)+4*z(2));
z(8) = 0.05*z(5) + 0.05*z(2)*z(4);
z(9) = 0.05*z(1)*z(4) - 0.2*z(5);
z(10) = -0.1 + 0.1*z(4) - 0.1*z(5);
z(11) = z(5)*(z(1)+4*z(2));
z(12) = 0.05*z(4) - 0.05*z(2)*z(5);
z(13) = -0.2*z(4) - 0.05*z(1)*z(5);
z(14) = 0.05*z(4)*wx*wz + 0.05*z(5)*wx*wy + 0.05*z(5)*wx*wz + 0.15*z(4)*wz*xBDt + 0.15 ↙
*z(5)*wy*xBDt + 0.15*z(5)*wz*xBDt  ...
    + 0.1*wy*(wx-41.5*wy) + 1.5*wz*(wx-2.766666666666666*wz) + 0.05*(wx+xBDt)*(z(4) ↙
*wz+z(5)*wy) - 0.15*z(4)*wy*xBDt - 0.05*z(4)*wx*wy  ...
    - 0.05*(wx+xBDt)*(z(4)*wy-z(5)*wz);
z(15) = 4.15*wx*wy + 0.1*wz*(15*wy-wz) + 0.1*wz*(z(4)*wy+z(4)*wz+z(5)*wy-z(5)*wz) - 0.1 ↙
*wx^2;
z(16) = 4.15*wx*wz - 1.5*wx^2 - 0.1*wy*(15*wy-wz) - 0.1*wy*(z(4)*wy+z(4)*wz+z(5)*wy-z ↙
(5)*wz);
z(17) = 0.05*z(2)*z(5)*wz*xCDt + 0.2*z(1)*z(4)*wy*xCDt + 0.05*z(1)*xCDt*(wx+xBDt) + 0.2 ↙
*z(2)*xCDt*(wx+xBDt) - 0.2*z(1)*z(5)*wz*xCDt  ...
    - 0.2*z(2)*z(4)*wz*xBDt - 0.2*z(2)*z(5)*wy*xBDt - 0.1*(wx+xBDt)^2 - 0.05*z(1)*z(4) ↙
*wz*xBDt - 0.05*z(1)*z(5)*wy*xBDt - 0.05*z(2)*z(  ...
    4)*wy*xCDt - 0.05*(z(2)*z(4)*wy-z(2)*z(5)*wz-z(1)*(wx+xBDt))*(xCDt+z(4)*wz+z(5) ↙
*wy+z(2)*z(4)*wy-z(2)*z(5)*wz-z(1)*(wx+xBDt))  ...
    - 0.05*(z(1)*z(5)*wz-z(1)*z(4)*wy-z(2)*(wx+xBDt))*(4*xCDt+4*z(4)*wz+4*z(5)*wy+z(1) ↙
*z(5)*wz-z(1)*z(4)*wy-z(2)*(wx+xBDt));
z(18) = (wx+xBDt)^2;
z(19) = 0.05*z(5)*wz*xBDt + 0.05*z(1)*z(5)*wz*xCDt + 0.05*z(2)*z(4)*wz*xBDt + 0.05*z(2) ↙
*z(5)*wy*xBDt + 0.05*(z(2)*z(4)*wy-z(2)*z(  ...
    5)*wz-z(1)*(wx+xBDt))*(z(1)*z(5)*wz+4*z(2)*z(5)*wz+4*z(1)*(wx+xBDt)-4*z(2)*z(4)*wy- ↙
z(1)*z(4)*wy-z(2)*(wx+xBDt)) - 0.05*z(4)*wy*xBDt  ...
    - 0.05*z(1)*z(4)*wy*xCDt - 0.05*z(2)*xCDt*(wx+xBDt) - 0.05*(xCDt+z(4)*wz+z(5)*wy)* ↙
(4*xCDt+4*z(4)*wz+4*z(5)*wy+z(1)*z(5)*wz-z(1)*z(  ...
    4)*wy-z(2)*(wx+xBDt));
z(20) = 0.2*z(4)*wy*xBDt + 0.05*z(1)*z(4)*wz*xBDt + 0.05*z(1)*z(5)*wy*xBDt + 0.05*z(2) ↙
*z(4)*wy*xCDt - 0.2*z(5)*wz*xBDt  ...
    - 0.05*z(2)*z(5)*wz*xCDt - 0.05*z(1)*xCDt*(wx+xBDt) - 0.05*(xCDt+z(4)*wz+z(5)*wy)* ↙
(xCDt+z(4)*wz+z(5)*wy+z(2)*z(4)*wy-z(2)*z(5)*wz-  ...
    z(1)*(wx+xBDt)) - 0.05*(z(1)*z(5)*wz-z(1)*z(4)*wy-z(2)*(wx+xBDt))*(z(1)*z(5)*wz+4*z ↙
(2)*z(5)*wz+4*z(1)*(wx+xBDt)-4*z(2)*z(4)*wy-z(  ...
    1)*z(4)*wy-z(2)*(wx+xBDt));
z(21) = z(1)*z(4);
z(22) = z(2)*z(4);
z(23) = z(1)*z(5);
z(24) = z(2)*z(5);
z(26) = wz*xDDt;
```

```
z(27) = wy*xDDt;
z(28) = sin(xD);
z(29) = cos(xD);
z(30) = 1.5 + 0.05*z(28) + 0.05*z(29);
z(31) = -0.1 + 0.05*z(28) - 0.05*z(29);
z(32) = 0.1*wx*wy + 1.5*wx*wz + 4.05*wy^2 + 4.05*wz^2 + 0.05*z(28)*wz*xDDt + 0.05*z(29) ↙
*wy*xDDt + 0.05*z(29)*wz*xDDt + 0.05*(wx+xDDt)*(  ...
    z(28)*wz+z(29)*wy) - 0.05*z(28)*wy*xDDt - 0.05*(wx+xDDt)*(z(28)*wy-z(29)*wz);
z(33) = 0.1*wz*(15*wy-wz) + 0.05*wz*(z(28)*wy+z(28)*wz+z(29)*wy-z(29)*wz) - 4.05*wx*wy ↙
- 0.1*wx^2;
z(34) = -4.05*wx*wz - 1.5*wx^2 - 0.1*wy*(15*wy-wz) - 0.05*wy*(z(28)*wy+z(28)*wz+z(29) ↙
*wy-z(29)*wz);
z(35) = (wx+xDDt)^2;
z(36) = cos(xE);
z(37) = sin(xE);
z(38) = z(28)*z(37);
z(39) = z(29)*z(37);
z(40) = z(29)*z(36);
z(41) = z(28)*z(36);
z(42) = z(28)*z(37)*wz*xDDt + z(29)*z(37)*wy*xDDt + z(36)*xEDt*(z(28)*wy-z(29)*wz) - z ↙
(37)*xEDt*(wx+xDDt);
z(43) = xDDt*(z(28)*wy-z(29)*wz);
z(44) = z(36)*xEDt*(wx+xDDt) + z(37)*xEDt*(z(28)*wy-z(29)*wz) - z(28)*z(36)*wz*xDDt - z ↙
(29)*z(36)*wy*xDDt;
z(45) = z(36)*wx + z(36)*xDDt + z(38)*wy - z(39)*wz;
z(46) = xEDt + z(28)*wz + z(29)*wy;
z(47) = z(37)*wx + z(37)*xDDt + z(40)*wz - z(41)*wy;
z(48) = 0.0658*z(46) + 58.4038*z(45) - 1.9517*z(47);
z(49) = 0.0658*z(45) + 58.3947*z(46) - 1.8211*z(47);
z(50) = 112.3681*z(47) - 1.9517*z(45) - 1.8211*z(46);
z(51) = z(45)*z(49) - z(46)*z(48);
z(52) = z(47)*z(48) - z(45)*z(50);
z(53) = z(46)*z(50) - z(47)*z(49);
z(54) = -0.1 - 0.2*z(37) - 0.05*z(36);
z(55) = 1.5 + 0.1*z(28) + 0.1*z(29);
z(56) = z(28)*(4*z(36)-z(37));
z(57) = 0.05*z(29) + 0.05*z(28)*z(36);
z(58) = 0.2*z(29) + 0.05*z(28)*z(37);
z(59) = -0.1 + 0.1*z(28) - 0.1*z(29);
z(60) = z(29)*(4*z(36)-z(37));
z(61) = 0.05*z(28) - 0.05*z(29)*z(36);
z(62) = 0.2*z(28) - 0.05*z(29)*z(37);
z(63) = 0.1*wx*wy + 1.5*wx*wz + 4.15*wy^2 + 4.15*wz^2 + 0.05*z(28)*wx*wz + 0.05*z(29) ↙
*wx*wy + 0.05*z(29)*wx*wz + 0.15*z(28)*wz*xDDt  ...
    + 0.15*z(29)*wy*xDDt + 0.15*z(29)*wz*xDDt + 0.05*(wx+xDDt)*(z(28)*wz+z(29)*wy) - ↙
0.15*z(28)*wy*xDDt - 0.05*z(28)*wx*wy  ...
    - 0.05*(wx+xDDt)*(z(28)*wy-z(29)*wz);
z(64) = 0.1*wz*(15*wy-wz) + 0.1*wz*(z(28)*wy+z(28)*wz+z(29)*wy-z(29)*wz) - 4.15*wx*wy - ↙
0.1*wx^2;
z(65) = -4.15*wx*wz - 1.5*wx^2 - 0.1*wy*(15*wy-wz) - 0.1*wy*(z(28)*wy+z(28)*wz+z(29) ↙
```



```
*wy-z(29)*wz);
z(66) = 0.05*z(29)*z(36)*wz*xEDt + 0.2*z(28)*z(36)*wz*xDDt + 0.2*z(29)*z(36)*wy*xDDt + ↙
0.2*z(29)*z(37)*wz*xEDt + 0.05*z(37)*xEDt*(  ...
    wx+xDDt) - 0.2*z(28)*z(37)*wy*xEDt - 0.1*(wx+xDDt)^2 - 0.05*z(28)*z(36)*wy*xEDt - ↙
0.05*z(28)*z(37)*wz*xDDt - 0.05*z(29)*z(37)*wy*xDDt  ...
    - 0.2*z(36)*xEDt*(wx+xDDt) - 0.05*(z(28)*z(36)*wy-z(29)*z(36)*wz-z(37)*(wx+xDDt))* ↙
(xEDt+z(28)*wz+z(29)*wy+z(28)*z(36)*wy-z(29)*  ...
    z(36)*wz-z(37)*(wx+xDDt)) - 0.05*(z(29)*z(37)*wz-z(28)*z(37)*wy-z(36)*(wx+xDDt))*(z ↙
(29)*z(37)*wz-4*xEDt-4*z(28)*wz-4*z(29)*wy-  ...
    z(28)*z(37)*wy-z(36)*(wx+xDDt));
z(67) = 0.05*z(29)*wz*xDDt + 0.05*z(28)*z(36)*wz*xDDt + 0.05*z(29)*z(36)*wy*xDDt + 0.05 ↙
*z(29)*z(37)*wz*xEDt + 0.05*(z(28)*z(36)*wy-  ...
    z(29)*z(36)*wz-z(37)*(wx+xDDt))*(z(29)*z(37)*wz+4*z(28)*z(36)*wy-4*z(29)*z(36)*wz-z ↙
(28)*z(37)*wy-4*z(37)*(wx+xDDt)-z(36)*(wx+xDDt))  ...
    - 0.05*z(28)*wy*xDDt - 0.05*z(28)*z(37)*wy*xEDt - 0.05*z(36)*xEDt*(wx+xDDt) - 0.05* ↙
(xEDt+z(28)*wz+z(29)*wy)*(z(29)*z(37)*wz-4*xEDt-  ...
    4*z(28)*wz-4*z(29)*wy-z(28)*z(37)*wy-z(36)*(wx+xDDt));
z(68) = 0.2*z(29)*wz*xDDt + 0.05*z(28)*z(36)*wy*xEDt + 0.05*z(28)*z(37)*wz*xDDt + 0.05 ↙
*z(29)*z(37)*wy*xDDt - 0.2*z(28)*wy*xDDt  ...
    - 0.05*z(29)*z(36)*wz*xEDt - 0.05*z(37)*xEDt*(wx+xDDt) - 0.05*(xEDt+z(28)*wz+z(29) ↙
*wy)*(xEDt+z(28)*wz+z(29)*wy+z(28)*z(36)*wy-  ...
    z(29)*z(36)*wz-z(37)*(wx+xDDt)) - 0.05*(z(29)*z(37)*wz-z(28)*z(37)*wy-z(36)* ↙
(wx+xDDt))*(z(29)*z(37)*wz+4*z(28)*z(36)*wy-4*z(29)*  ...
    z(36)*wz-z(28)*z(37)*wy-4*z(37)*(wx+xDDt)-z(36)*(wx+xDDt));
z(69) = 49.8 + 2.2249*z(4) + 41.905*z(29) + 0.0658*z(29)*z(36) + 0.5*z(28)*z(56) + ↙
1.9517*z(36)*z(41) + 5*z(54)*z(56) + 7.5*z(5)*z(7)  ...
    + 10*z(9)*z(24) + 10*z(40)*z(58) + 15*z(2)*z(9) + 15*z(36)*z(58) + 20.75*z(36)*z ↙
(40) + 20.75*z(37)*z(39) + 58.4038*z(36)*z(38)  ...
    + 150*z(9)*z(22) + 150*z(41)*z(58) + 415*z(28)*z(54) + 1.9528*z(1)*(z(5) ↙
-7.681278164686606*z(8)-27.639031134780833*z(2)*z(4)-1.8638877509217753*  ...
    z(1)*z(4)) - 41.905*z(5) - 0.405*z(28) - 415*z(3)*z(4) - 150*z(8)*z(21) - 150*z(38) ↙
*z(57) - 112.3681*z(37)*z(41) - 20.75*z(1)*z(23)  ...
    - 20.75*z(2)*z(24) - 15*z(37)*z(57) - 10*z(8)*z(23) - 10*z(39)*z(57) - 7.5*z(29)*z ↙
(56) - 5*z(3)*z(7) - 1.9517*z(37)*z(38)  ...
    - 1.8211*z(29)*z(37) - 0.5*z(4)*z(7) - 0.0658*z(2)*z(5);
z(70) = 6760.0546 + 2.32*z(5) + 2.32*z(29) + 30.28*z(4) + 30.28*z(28) + 1*z(1)*z(23) + ↙
1*z(2)*z(24) + 1*z(36)*z(40) + 1*z(37)*z(39)  ...
    + 1.25*z(2)^2 + 15*z(1)*z(21) + 15*z(2)*z(22) + 15*z(36)*z(41) + 15*z(37)*z(38) + ↙
20*z(3)*z(4) + 20*z(28)*z(54) + 55.2235*z(1)^2  ...
    + 59.6538*z(36)^2 + 100*z(3)^2 + 100*z(54)^2 + 113.6181*z(37)^2 - 300*z(3)*z(5) - ↙
300*z(29)*z(54) - 3.9034*z(36)*z(37) - 3.6398*z(  ...
    1)*z(2);
z(71) = -61.3 + 0.405*z(29) + 41.905*z(28) + 0.0658*z(28)*z(36) + 0.5*z(4)*z(11) + ↙
1.9517*z(37)*z(39) + 5*z(3)*z(11) + 7.5*z(29)*z(60)  ...
    + 10*z(13)*z(24) + 10*z(40)*z(62) + 15*z(2)*z(13) + 15*z(36)*z(62) + 20.75*z(36)*z ↙
(41) + 20.75*z(37)*z(38) + 112.3681*z(37)*z(40)  ...
    + 150*z(13)*z(22) + 150*z(41)*z(62) + 415*z(3)*z(5) + 1.9528*z(1)*(z(4)+1. ↙
8638877509217753*z(1)*z(5)+27.639031134780882*z(2)*z(5))  ...
    - 41.905*z(4) - 2.2249*z(5) - 415*z(29)*z(54) - 150*z(12)*z(21) - 150*z(38)*z(61) - ↙
58.4038*z(36)*z(39) - 20.75*z(1)*z(21)  ...
```



```
    - 20.75*z(2)*z(22) - 15*z(1)*z(12) - 15*z(37)*z(61) - 10*z(12)*z(23) - 10*z(39)*z ↙
(61) - 7.5*z(5)*z(11) - 5*z(54)*z(60)  ...
    - 1.9517*z(36)*z(40) - 1.8211*z(28)*z(37) - 0.5*z(28)*z(60) - 0.0658*z(2)*z(4);
z(72) = 61.4046 + 1.16*z(5) + 15.14*z(4) + 0.5*z(1)*z(23) + 0.5*z(2)*z(24) + 1.25*z(2) ↙
^2 + 7.5*z(1)*z(21) + 7.5*z(2)*z(22)  ...
    + 10*z(3)*z(4) + 55.2235*z(1)^2 + 100*z(3)^2 - 150*z(3)*z(5) - 3.6398*z(1)*z(2);
z(73) = 1.2028*z(1) - 30*z(22) - 7.5*z(21) - 3.0658*z(2) - 2*z(24) - 0.5*z(23);
z(74) = 3.01 + 1.16*z(29) + 15.14*z(28) + 0.5*z(36)*z(40) + 0.5*z(37)*z(39) + 7.5*z(36) ↙
*z(41) + 7.5*z(37)*z(38) + 10*z(28)*z(54)  ...
    + 59.6538*z(36)^2 + 100*z(54)^2 + 113.6181*z(37)^2 - 150*z(29)*z(54) - 3.9034*z(36) ↙
*z(37);
z(75) = 2*z(40) + 3.0658*z(36) + 30*z(41) - 7.5*z(38) - 2.5711*z(37) - 0.5*z(39);
z(76) = 0.14*z(5)*(wx+xDDt)^2 + 958.1*wy*(wy+3.051163761611522*wz) + 0.14*wy*(z(4)*wy- ↙
2*z(5)*wz) + 0.005*z(5)*(81*wx*wz-32*wy^2-wy*(  ...
    z(5)*wy+4*z(4)*wz)) + 0.005*z(4)*(32*wx^2-81*wx*wy-z(4)*wz^2-28*wz*(wz+2. ↙
2857142857142857*wy)) + 0.0658*z(4)*wy*(887.59726443769*xCDt+  ...
    29.677811155015198*z(1)*wx+887.59726443769*z(4)*wz+887.59726443769*z(5)*wy-z(2)*wx- ↙
29.677811155015198*z(2)*z(4)*wy-z(1)*z(4)*wy)  ...
    + 1.8199*z(2)*(z(2)*z(4)*wz*xBDt+z(2)*z(5)*wy*xBDt-z(2)*xCDt*(wx+xBDt)-2*z(1)*xCDt* ↙
(z(4)*wy-z(5)*wz)) + 0.0658*z(5)*wz*(z(2)*wx+2*  ...
    z(1)*z(4)*wy+59.35562310030396*z(2)*z(4)*wy-887.59726443769*xCDt-887.59726443769*z ↙
(4)*wz-887.59726443769*z(5)*wy-29.677811155015198*  ...
    z(1)*wx-29.677811155015198*z(2)*z(5)*wz-z(1)*z(5)*wz) + 1.8199*z(2)*(xCDt+z(4)*wz+z ↙
(5)*wy)*(1.073025990439035*xCDt+1.073025990439035*  ...
    z(4)*wz+1.073025990439035*z(5)*wy+61.74410681905599*z(2)*z(5)*wz-61.74410681905599 ↙
*z(2)*z(4)*wy-2*z(1)*z(4)*wy-z(2)*(wx+xBDt))  ...
    + 0.2*z(34) + 10*z(16) + 10*z(65) + z(36)*z(53) + z(37)*z(51) + 0.1*z(29)*z(34) + ↙
1.8211*z(37)*z(43) + 10*z(4)*z(17) + 10*z(5)*z(16)  ...
    + 10*z(24)*z(20) + 10*z(28)*z(66) + 10*z(29)*z(65) + 10*z(40)*z(68) + 15*z(2)*z(20) ↙
+ 15*z(36)*z(68) + 58.4038*z(36)*z(42)  ...
    + 100*z(3)*z(17) + 100*z(54)*z(66) + 112.3681*z(37)*z(44) + 150*z(22)*z(20) + 150*z ↙
(41)*z(68) + 5*z(1)*z(23)*z(16) + 5*z(2)*  ...
    z(24)*z(16) + 5*z(36)*z(40)*z(65) + 5*z(37)*z(39)*z(65) + 100*z(3)*z(4)*z(16) + ↙
100*z(3)*z(5)*z(15) + 100*z(28)*z(54)*z(65)  ...
    + 100*z(29)*z(54)*z(64) - 958.1*wz^2 - 73.45*wx*wy - 48.99*wx*wz - 0.16*z(4)* ↙
(wx+xBDt)^2 - 0.005*z(4)*(81*wx*wz-z(4)*wy^2)  ...
    - 1.8199*z(1)^2*(z(4)*wz*xBDt+z(5)*wy*xBDt-xCDt*(wx+xBDt)) - 53.9735*z(1)*(z(2)*z ↙
(4)*wz*xBDt-2.0819124199838881*z(1)*xCDt*(z(4)*wy-  ...
    z(5)*wz)) - 0.005*z(5)*(28*wx^2+81*wx*wy-32*wz^2-z(5)*wz^2) - 53.9735*z(2)*(z(1)*z ↙
(5)*wy*xBDt-z(1)*xCDt*(wx+xBDt)-1.0819124199838881*  ...
    z(2)*xCDt*(z(4)*wy-z(5)*wz)) - 0.0658*z(1)*(xCDt+z(4)*wz+z(5)*wy)* ↙
(887.4559270516717*z(1)*z(4)*wy-xCDt-z(4)*wz-z(5)*wy-887.4559270516717*  ...
    z(1)*z(5)*wz-55.3161094224924*z(2)*z(5)*wz-820.2659574468087*z(2)*(wx+xBDt) ↙
-27.6580547112462*z(1)*(wx+xBDt)) - 150*z(15)  ...
    - 150*z(64) - 3*z(33) - z(18) - z(35) - 150*z(5)*z(17) - 150*z(21)*z(19) - 150*z ↙
(29)*z(66) - 150*z(38)*z(67) - 15.16*z(28)*z(35)  ...
    - 15*z(1)*z(19) - 15*z(37)*z(67) - 15*z(4)*z(18) - 10*z(23)*z(19) - 10*z(39)*z(67) ↙
- 10*z(4)*z(15) - 10*z(28)*z(64) - 1.9517*  ...
    z(36)*z(44) - 1.9517*z(37)*z(42) - z(5)*z(18) - 0.86*z(29)*z(35) - 0.1*z(28)*z(34) ↙
- 0.1*z(28)*z(33) - 0.1*z(29)*z(33)  ...
```



```
    - 0.0658*z(36)*z(43) - 5*z(1)*z(21)*z(15) - 5*z(2)*z(22)*z(15) - 5*z(36)*z(41)*z ↙
(64) - 5*z(37)*z(38)*z(64) - 0.5*z(1)^2*z(18)  ...
    - 0.5*z(2)^2*z(18) - 0.5*z(36)^2*z(35) - 0.5*z(37)^2*z(35);
z(77) = 49.8 + 2.2249*z(4) + 41.905*z(29) + 0.0658*z(29)*z(36) + 0.5*z(28)*z(56) + ↙
1.9517*z(36)*z(41) + 1.9528*z(1)*z(5)  ...
    + 5*z(54)*z(56) + 7.5*z(5)*z(7) + 10*z(9)*z(24) + 10*z(40)*z(58) + 15*z(2)*z(9) + ↙
15*z(36)*z(58) + 20.75*z(36)*z(40) + 20.75*  ...
    z(37)*z(39) + 58.4038*z(36)*z(38) + 150*z(9)*z(22) + 150*z(41)*z(58) + 415*z(28)*z ↙
(54) - 41.905*z(5) - 0.405*z(28) - 415*z(3)*z(4)  ...
    - 150*z(8)*z(21) - 150*z(38)*z(57) - 112.3681*z(37)*z(41) - 20.75*z(1)*z(23) - ↙
20.75*z(2)*z(24) - 15*z(1)*z(8) - 15*z(37)*z(57)  ...
    - 10*z(8)*z(23) - 10*z(39)*z(57) - 7.5*z(29)*z(56) - 5*z(3)*z(7) - 1.9517*z(37)*z ↙
(38) - 1.8211*z(29)*z(37) - 0.5*z(4)*z(7)  ...
    - 0.0658*z(2)*z(5) - 53.9735*z(1)*z(2)*z(4) - 3.6398*z(4)*z(1)^2;
z(78) = 958.4 + 0.0658*z(1) + 1.9528*z(2) + 0.0658*z(28)*z(38) + 1.8211*z(28)*z(41) + ↙
2*z(30)*z(31) + 58.3947*z(28)*z(29)  ...
    + 100*z(6)*z(10) + 100*z(8)*z(12) + 100*z(9)*z(13) + 100*z(55)*z(59) + 100*z(57)*z ↙
(61) + 100*z(58)*z(62) + 415*z(8)*z(21)  ...
    + 415*z(41)*z(58) + 415*z(12)*z(23) + 415*z(40)*z(62) + 100*z(1)*z(6)*z(13) + 100*z ↙
(1)*z(9)*z(10) + 100*z(2)*z(6)*z(12)  ...
    + 100*z(2)*z(8)*z(10) + 100*z(36)*z(55)*z(61) + 100*z(36)*z(57)*z(59) + 100*z(37)*z ↙
(55)*z(62) + 100*z(37)*z(58)*z(59) + 0.005*(30+  ...
    z(4)+z(5))*(-2+z(4)-z(5)) + 0.1316*z(4)*(443.798632218845*z(5)-157.6747720364742*z ↙
(11)-29.677811155015198*z(2)*z(4)-z(1)*z(4)-853.8609422492401*  ...
    z(5)*z(2)^2-27.6580547112462*z(1)*z(5)*(z(2)+16.043354030441233*z(1))) - 415*z(13)*z ↙
(24) - 415*z(39)*z(61) - 415*z(9)*z(22)  ...
    - 415*z(38)*z(57) - 112.3681*z(40)*z(41) - 58.4038*z(38)*z(39) - 20.75*z(28)*z(60) ↙
- 20.75*z(5)*z(7) - 20.75*z(29)*z(56)  ...
    - 1.9517*z(38)*z(40) - 1.9517*z(39)*z(41) - 1.8211*z(29)*z(40) - 0.25*z(7)*z(11) - ↙
0.25*z(56)*z(60) - 0.0658*z(29)*z(39);
z(79) = 8973.0139 + 0.1316*z(29)*z(38) + 0.25*z(7)^2 + 0.25*z(56)^2 + 2*z(30)^2 + ↙
3.6422*z(29)*z(41) + 3.9034*z(38)*z(41)  ...
    + 41.5*z(28)*z(56) + 58.3947*z(29)^2 + 58.4038*z(38)^2 + 100*z(6)^2 + 100*z(8)^2 + ↙
100*z(9)^2 + 100*z(55)^2 + 100*z(57)^2  ...
    + 100*z(58)^2 + 112.3681*z(41)^2 + 830*z(8)*z(23) + 830*z(40)*z(58) + 200*z(1)*z(6) ↙
*z(9) + 200*z(2)*z(6)*z(8) + 200*z(36)*z(55)*z(57)  ...
    + 200*z(37)*z(55)*z(58) + 0.005*(30+z(4)+z(5))^2 - 830*z(39)*z(57) - 830*z(9)*z(24) ↙
- 0.1316*z(4)*(443.798632218845*z(4)+z(1)*z(5)+  ...
    29.677811155015198*z(2)*z(5)-315.3495440729484*z(7)-853.8609422492401*z(4)*z(2)^2- ↙
27.6580547112462*z(1)*z(4)*(z(2)+16.043354030441233*  ...
    z(1)));
z(80) = 2.2249*z(4) + 1.9528*z(1)*z(5) + 15*z(2)*z(9) - 41.905*z(5) - 415*z(3)*z(4) - ↙
20.75*z(1)*z(23) - 20.75*z(2)*z(24)  ...
    - 15*z(1)*z(8) - 5*z(3)*z(7) - 0.0658*z(2)*z(5) - 53.9735*z(1)*z(2)*z(4) - 3.6398*z ↙
(4)*z(1)^2;
z(81) = 5*z(8) + 20.75*z(23) + 58.4039*z(5) + 83*z(24) + 5*z(2)*z(6) - 20*z(9) - 20*z ↙
(1)*z(6) - 1.9528*z(2)*z(4) - 0.0658*z(1)*z(4);
z(82) = 41.905*z(29) + 0.0658*z(29)*z(36) + 1.9517*z(36)*z(41) + 5*z(54)*z(56) + 15*z ↙
(36)*z(58) + 20.75*z(36)*z(40) + 20.75*  ...
    z(37)*z(39) + 58.4038*z(36)*z(38) + 415*z(28)*z(54) - 0.405*z(28) - 112.3681*z(37) ↙
```

```
*z(41) - 15*z(37)*z(57) - 1.9517*z(37)*z(38) -    ...
    1.8211*z(29)*z(37);
z(83) = 0.0658*z(38) + 1.8211*z(41) + 5*z(57) + 20*z(58) + 58.3947*z(29) + 83*z(40) + ↙
5*z(36)*z(55) + 20*z(37)*z(55) - 20.75*z(39);
z(84) = 2*wz*xBDt + 73.45*wx^2 + 0.405*z(4)*(wx+xBDt)^2 + 0.405*z(5)*(wx+xBDt)^2 + ↙
12.15*wy*(wy+4.032098765432099*wz) + 1.8199*z(   ...
    4)*xCDt*(z(4)*wy-z(5)*wz) + 1.9528*z(2)*z(4)*xBDt*(z(4)*wy-2*z(5)*wz) + 112.3681*z ↙
(4)*z(2)^2*xBDt*(z(4)*wz+z(5)*wy) + 0.405*wy*(z(   ...
    4)*wy+z(4)*wz+z(5)*wy-z(5)*wz) + 0.0658*z(2)*z(4)*xCDt*(27.6580547112462*z(2)*z(4) ↙
*wy+1640.531914893617*z(1)*z(5)*wz-xCDt-2*z(5)*   ...
    wy-z(4)*wz-1640.531914893617*z(1)*z(4)*wy-27.6580547112462*z(2)*z(5)*wz- ↙
820.2659574468087*z(2)*(wx+xBDt)-110.6322188449848*z(1)*(   ...
    wx+xBDt)) + 0.0658*z(1)*z(4)*(z(4)*wy*xBDt+55.31610942249 24*z(2)*z(4)*wz*xBDt+55. ↙
3161094224924*z(2)*z(5)*wy*xBDt+82.97416413373861*   ...
    z(1)*z(5)*wz*xCDt+887.4559270516717*z(1)*xBDt*(z(4)*wz+z(5)*wy)-29.67781155015198 ↙
*xCDt*(2.795831626238263*z(1)*z(4)*wy-xCDt-z(4)*wz-   ...
    27.639031134783083*z(1)*(wx+xBDt))) + 0.005*(30+z(4)+z(5))*(z(4)*wz*xBDt+z(5) ↙
*wy*xBDt+z(5)*wz*xBDt+2*wy*(wx-40.5*wy)+30*wz*(wx-2.7*   ...
    wz)+(wx+xBDt)*(z(4)*wz+z(5)*wy)-z(4)*wy*xBDt-(wx+xBDt)*(z(4)*wy-z(5)*wz)) + 2*z(26) ↙
+ 8.1*z(34) + 415*z(65) + z(29)*z(52)   ...
    + z(38)*z(53) + 0.0658*z(29)*z(42) + 1.9517*z(41)*z(42) + 2*z(30)*z(32) + 5*z(56)*z ↙
(66) + 41.5*z(5)*z(18) + 58.4038*z(38)*z(42)   ...
    + 100*z(6)*z(14) + 100*z(8)*z(19) + 100*z(9)*z(20) + 100*z(55)*z(63) + 100*z(57)*z ↙
(67) + 100*z(58)*z(68) + 415*z(23)*z(19)   ...
    + 415*z(28)*z(66) + 415*z(40)*z(68) + 5*z(29)*z(56)*z(64) + 5*z(28)*z(56)*z(65) + ↙
10*z(1)*z(8)*z(18) + 10*z(37)*z(57)*z(35)   ...
    + 100*z(1)*z(6)*z(20) + 100*z(1)*z(9)*z(14) + 100*z(2)*z(6)*z(19) + 100*z(2)*z(8)*z ↙
(14) + 100*z(8)*z(21)*z(15) + 100*z(9)*z(24)*z(16)   ...
    + 100*z(36)*z(55)*z(67) + 100*z(36)*z(57)*z(63) + 100*z(37)*z(55)*z(68) + 100*z(37) ↙
*z(58)*z(63) + 100*z(38)*z(57)*z(64)   ...
    + 100*z(40)*z(58)*z(65) - 2126.505*wx*wz - 958.4*wx*wy - 61.3*wz^2 - 58.4039*z(5) ↙
*xBDt*(z(4)*wy-z(5)*wz) - 1.9528*z(5)*(z(2)*z(5)*   ...
    wy*xBDt-z(1)*xCDt*(2*z(4)*wy-z(5)*wz)) - 0.0658*z(5)*(z(1)*z(5)*wy*xBDt+2*z(1)*z(4) ↙
*wz*xBDt-z(2)*z(5)*wz*xCDt) - 1.8199*z(1)*wz*(   ...
    z(1)*z(4)*wy-1.073025990439035*xCDt-1.073025990439035*z(4)*wz-1.073025990439035*z ↙
(5)*wy-z(1)*z(5)*wz-61.74410681905599*z(1)*(wx+xBDt))   ...
    - 0.0658*z(2)*wz*(xCDt+z(4)*wz+z(5)*wy+27.6580547112462*z(2)*z(5)*wz+820. ↙
2659574468087*z(1)*z(4)*wy+55.3161094224924*z(1)*(wx+xBDt)-   ...
    820.2659574468087*z(1)*z(5)*wz-27.6580547112462*z(2)*z(4)*wy-887.4559270516717*z(2) ↙
*(wx+xBDt)) - 0.0658*z(4)*(wx+xBDt)*(887.59726443769*   ...
    xCDt+887.59726443769*z(4)*wz+887.59726443769*z(5)*wy+2*z(1)*z(5)*wz+59. ↙
35562310030396*z(2)*z(5)*wz+29.67781155015198*z(1)*(wx+xBDt)-   ...
    29.67781155015198*z(2)*z(4)*wy-z(1)*z(4)*wz*(wx+xBDt)) - 0.0658*z(5)*(wx+xBDt) ↙
*(27.6580547112462*z(2)*(1.073025990439035*z(5)*   ...
    wy+61.74410681905599*z(2)*z(5)*wz-61.74410681905599*z(2)*z(4)*wy-2*z(1)*z(4)*wy-z ↙
(2)*(wx+xBDt))-z(1)*(887.4559270516717*z(1)*z(4)*   ...
    wy-z(5)*wy-887.4559270516717*z(1)*z(5)*wz-55.3161094224924*z(2)*z(5)*wz- ↙
820.2659574468086*z(2)*(wx+xBDt)-27.6580547112462*z(1)*(wx+   ...
    xBDt))) - 415*z(16) - 415*z(4)*z(17) - 415*z(24)*z(20) - 415*z(39)*z(67) - 112.3681 ↙
*z(41)*z(44) - 58.3947*z(29)*z(43) - 41.905*   ...
```



```
    z(29)*z(35) - 5*z(7)*z(17) - 1.9517*z(38)*z(44) - 1.8211*z(29)*z(44) - 1.8211*z(41) ↙
*z(43) - z(41)*z(51) - 0.405*z(28)*z(35)   ...
    - 0.0658*z(38)*z(43) - 100*z(8)*z(23)*z(16) - 100*z(9)*z(22)*z(15) - 100*z(39)*z ↙
(57)*z(65) - 100*z(41)*z(58)*z(64) - 10*z(2)*z(9)*z(18)   ...
    - 10*z(36)*z(58)*z(35) - 5*z(4)*z(7)*z(16) - 5*z(5)*z(7)*z(15);
z(85) = 958.4 + 0.0658*z(1) + 1.9528*z(2) + 0.0658*z(28)*z(38) + 1.8211*z(28)*z(41) + ↙
2*z(30)*z(31) + 58.3947*z(28)*z(29)   ...
    + 100*z(6)*z(10) + 100*z(8)*z(12) + 100*z(9)*z(13) + 100*z(55)*z(59) + 100*z(57)*z ↙
(61) + 100*z(58)*z(62) + 415*z(12)*z(23)   ...
    + 415*z(40)*z(62) + 415*z(8)*z(21) + 415*z(41)*z(58) + 100*z(1)*z(6)*z(13) + 100*z ↙
(1)*z(9)*z(10) + 100*z(2)*z(6)*z(12)   ...
    + 100*z(2)*z(8)*z(10) + 100*z(36)*z(55)*z(61) + 100*z(36)*z(57)*z(59) + 100*z(37)*z ↙
(55)*z(62) + 100*z(37)*z(58)*z(59) + 0.005*(30+   ...
    z(4)+z(5))*(-2+z(4)-z(5)) - 415*z(9)*z(22) - 415*z(38)*z(57) - 415*z(13)*z(24) - ↙
415*z(39)*z(61) - 112.3681*z(40)*z(41)   ...
    - 58.4038*z(38)*z(39) - 20.75*z(5)*z(7) - 20.75*z(28)*z(60) - 20.75*z(29)*z(56) - ↙
1.9517*z(38)*z(40) - 1.9517*z(39)*z(41)   ...
    - 1.8211*z(29)*z(40) - 0.25*z(7)*z(11) - 0.25*z(56)*z(60) - 0.0658*z(29)*z(39) - ↙
0.1316*z(4)*(157.6747720364742*z(11)+410.0623100303952*   ...
    z(5)+29.67781155015198*z(2)*z(4)-z(1)*(410.1329787234042*z(1)*z(5)-z(4) ↙
-27.6580547112462*z(2)*z(5)));
z(86) = 11842.41 + 0.25*z(11)^2 + 0.25*z(60)^2 + 2*z(31)^2 + 3.9034*z(39)*z(40) + 41.5 ↙
*z(5)*z(11) + 41.5*z(29)*z(60) + 58.3947*z(28)^2   ...
    + 58.4038*z(39)^2 + 58.4039*z(4)^2 + 100*z(10)^2 + 100*z(12)^2 + 100*z(13)^2 + ↙
100*z(59)^2 + 100*z(61)^2 + 100*z(62)^2   ...
    + 112.3681*z(40)^2 + 830*z(12)*z(21) + 830*z(41)*z(62) + 0.1316*z(1)*z(4)*z(5) + ↙
3.9056*z(2)*z(4)*z(5) + 200*z(1)*z(10)*z(13)   ...
    + 200*z(2)*z(10)*z(12) + 200*z(36)*z(59)*z(61) + 200*z(37)*z(59)*z(62) + 3.6398*z ↙
(1)*z(2)*z(5)^2 + 58.3946*z(1)^2*z(5)^2   ...
    + 112.3681*z(2)^2*z(5)^2 + 0.005*(-2+z(4)-z(5))^2 - 830*z(13)*z(22) - 830*z(38)*z ↙
(61) - 3.6422*z(28)*z(40) - 0.1316*z(28)*z(39);
z(87) = -61.3 + 0.405*z(29) + 41.905*z(28) + 0.0658*z(28)*z(36) + 0.5*z(4)*z(11) + ↙
1.9517*z(37)*z(39) + 5*z(3)*z(11) + 7.5*z(29)*z(60)   ...
    + 10*z(13)*z(24) + 10*z(40)*z(62) + 15*z(2)*z(13) + 15*z(36)*z(62) + 20.75*z(36)*z ↙
(41) + 20.75*z(37)*z(38) + 112.3681*z(37)*z(40)   ...
    + 150*z(13)*z(22) + 150*z(41)*z(62) + 415*z(3)*z(5) + 1.9528*z(1)*(z(4)+1. ↙
8638877509217 53*z(1)*z(5)+27.639031134780 83*z(2)*z(5))   ...
    - 41.905*z(4) - 2.2249*z(5) - 415*z(29)*z(54) - 150*z(12)*z(21) - 150*z(38)*z(61) - ↙
58.4038*z(36)*z(39) - 20.75*z(1)*z(21)   ...
    - 20.75*z(2)*z(22) - 15*z(1)*z(12) - 15*z(37)*z(61) - 10*z(12)*z(23) - 10*z(39)*z ↙
(61) - 7.5*z(5)*z(11) - 5*z(54)*z(60)   ...
    - 1.9517*z(36)*z(40) - 1.8211*z(28)*z(37) - 0.5*z(28)*z(60) - 0.0658*z(2)*z(4);
z(88) = 5*z(3)*z(11) + 15*z(2)*z(13) + 415*z(3)*z(5) + 1.9528*z(1)*(z(4)+1. ↙
8638877509217 53*z(1)*z(5)+27.639031134780 83*z(2)*z(5))   ...
    - 41.905*z(4) - 2.2249*z(5) - 20.75*z(1)*z(21) - 20.75*z(2)*z(22) - 15*z(1)*z(12) - ↙
0.0658*z(2)*z(4);
z(89) = 5*z(12) + 20.75*z(21) + 58.4039*z(4) + 83*z(22) + 0.0658*z(1)*z(5) + 1.9528*z ↙
(2)*z(5) + 5*z(2)*z(10) - 20*z(13) - 20*z(1)*z(10);
z(90) = 0.405*z(29) + 41.905*z(28) + 0.0658*z(28)*z(36) + 1.9517*z(37)*z(39) + 15*z(36) ↙
*z(62) + 20.75*z(36)*z(41) + 20.75*z(37)*z(38)   ...
```



```
    + 112.3681*z(37)*z(40) - 415*z(29)*z(54) - 58.4038*z(36)*z(39) - 15*z(37)*z(61) - ↙
5*z(54)*z(60) - 1.9517*z(36)*z(40) - 1.8211*   ...
    z(28)*z(37);
z(91) = 5*z(61) + 20*z(62) + 58.3947*z(28) + 83*z(41) + 5*z(36)*z(59) + 20*z(37)*z(59) ↙
- 20.75*z(38) - 1.8211*z(40) - 0.0658*z(39);
z(92) = 48.99*wx*(wx+19.56317615839967*wz) + 0.81*wz*(90.67901234567901*wy-wz) + 0.405 ↙
*wz*(z(4)*wy+z(4)*wz+z(5)*wy-z(5)*wz)   ...
    + 0.0658*z(2)*wy*(xCDt+z(4)*wz+z(5)*wy+27.6580547112462*z(2)*z(5)*wz- ↙
27.6580547112462*z(2)*z(4)*wy-887.4559270516717*z(2)*(wx+xBDt))   ...
    + 0.0658*z(5)*(wx+xBDt)*(887.59726443769*z(4)*wz+887.59726443769*z(5)*wy+z(1)*z(5) ↙
*wz+29.67781155015198*z(2)*z(5)*wz+29.67781155015198*   ...
    z(1)*(wx+xBDt)-z(2)*(wx+xBDt)) + 0.005*(-2+z(4)-z(5))*(z(4)*wz*xBDt+z(5)*wy*xBDt+z ↙
(5)*wz*xBDt+2*wy*(wx-40.5*wy)+30*wz*(wx-2.7*wz)+(   ...
    wx+xBDt)*(z(4)*wz+z(5)*wy)-z(4)*wy*xBDt-(wx+xBDt)*(z(4)*wy-z(5)*wz)) + 415*z(15) + ↙
z(28)*z(52) + z(40)*z(51) + 0.0658*z(28)*z(42)   ...
    + 0.0658*z(39)*z(43) + 0.405*z(29)*z(35) + 1.8211*z(40)*z(43) + 1.9517*z(39)*z(44) ↙
+ 2*z(31)*z(32) + 5*z(11)*z(17) + 100*z(10)*z(14)   ...
    + 100*z(12)*z(19) + 100*z(13)*z(20) + 100*z(59)*z(63) + 100*z(61)*z(67) + 100*z(62) ↙
*z(68) + 112.3681*z(40)*z(44) + 415*z(5)*z(17)   ...
    + 415*z(21)*z(19) + 415*z(41)*z(68) + 5*z(5)*z(11)*z(15) + 10*z(37)*z(61)*z(35) + ↙
100*z(1)*z(10)*z(20) + 100*z(1)*z(13)*z(14)   ...
    + 100*z(2)*z(10)*z(19) + 100*z(2)*z(12)*z(14) + 100*z(12)*z(21)*z(15) + 100*z(13)*z ↙
(24)*z(16) + 100*z(36)*z(59)*z(67) + 100*   ...
    z(36)*z(61)*z(63) + 100*z(37)*z(59)*z(68) + 100*z(37)*z(62)*z(63) + 100*z(38)*z(61) ↙
*z(64) + 100*z(40)*z(62)*z(65) - 801.295*wx*wy   ...
    - 49.8*wy^2 - 2*wy*xBDt - 0.405*z(5)*(wx+xBDt)^2 - 1.9528*z(2)*z(5)*xBDt*(2*z(4) ↙
*wy-z(5)*wz) - 53.9642*z(5)*(z(4)*wz*xBDt+2.082271209431438*   ...
    z(5)*wy*xBDt-2.082443545906361*xCDt*(wx+xBDt)) - 0.0658*z(2)*z(5)*xCDt* ↙
(55.3161094224924*z(2)*z(4)*wy-xCDt-2*z(4)*wz-z(5)*wy-55.3161094224924*   ...
    z(2)*z(5)*wz) - 415*z(64) - 8.1*z(33) - 2*z(27) - 415*z(22)*z(20) - 415*z(29)*z(66) ↙
- 415*z(38)*z(67) - 58.4038*z(39)*z(42)   ...
    - 58.3947*z(28)*z(43) - 41.905*z(28)*z(35) - 5*z(60)*z(66) - 1.9517*z(40)*z(42) - ↙
1.8211*z(28)*z(44) - z(39)*z(53) - 100*z(12)*   ...
    z(23)*z(16) - 100*z(13)*z(22)*z(15) - 100*z(39)*z(61)*z(65) - 100*z(41)*z(62)*z(64) ↙
- 10*z(2)*z(13)*z(18) - 10*z(36)*z(62)*z(35)   ...
    - 5*z(28)*z(60)*z(65) - 5*z(29)*z(60)*z(64) - 0.0658*z(1)*(z(5)*xBDt*(2*z(4)*wy-z ↙
(5)*wz)+29.67781155015198*z(5)*xCDt*(xCDt+z(5)*wy+   ...
    2*z(4)*wz+1.863887750921753*z(1)*z(5)*wz+55.27806226956165*z(2)*z(5)*wz+55. ↙
27806226956166*z(1)*(wx+xBDt)-55.27806226956165*z(2)*z(   ...
    4)*wy-1.863887750921753*z(1)*z(4)*wy-3.727775501843506*z(2)*(wx+xBDt)) ↙
-820.2659574468084*z(1)*z(5)*xBDt*(z(4)*wz+z(5)*wy)-27.6580547112462*   ...
    wy*(2*z(2)*wx+z(1)*z(4)*wy+29.65739875817353*z(2)*z(4)*wy-1.073025990439035*xCDt- ↙
1.073025990439035*z(4)*wz-1.073025990439035*z(5)*   ...
    wy-29.65739875817353*z(2)*z(5)*wz-61.74410681905599*z(1)*(wx+xBDt)) ↙
-151.9756838905775*z(12)*z(18)) - 0.0658*z(4)*(887.59726443769*   ...
    z(4)*wy*xBDt+55.3161094224924*z(1)*z(2)*z(5)*wz*xBDt+z(4)*(z(1)*wz*xBDt+z(2) ↙
*wy*xCDt)-6.15501519756839*(wx+xBDt)^2-55.3161094224924*   ...
    z(1)*z(2)*z(4)*wy*xBDt-29.67781155015198*z(4)*(z(1)*wy*xCDt-z(2)*wz*xBDt)-(wx+xBDt) ↙
*(z(1)*(887.4559270516717*z(1)*z(4)*wy-2*z(5)*   ...
    wy-z(4)*wz-887.4559270516717*z(1)*z(5)*wz-820.2659574468086*z(2)*(wx+xBDt) ↙
```



```
-27.6580547112462*z(1)*(wx+xBDt))-27.6580547112462*z(2)*(   ...
    1.073025990439035*z(4)*wz+2.146051980807*z(5)*wy+2*z(1)*z(5)*wz+61. ↙
74410681905599*z(2)*z(5)*wz-61.74410681905599*z(2)*z(4)*wy-2*   ...
    z(1)*z(4)*wy-z(2)*(wx+xBDt)))-630.6990881458967*z(18)-75.98784194528876*z(11)*z ↙
(16));
z(93) = 61.4046 + 1.16*z(5) + 15.14*z(4) + 0.5*z(1)*z(23) + 0.5*z(2)*z(24) + 1.25*z(2) ↙
^2 + 7.5*z(1)*z(21) + 7.5*z(2)*z(22)   ...
    + 10*z(3)*z(4) + 55.2235*z(1)^2 + 100*z(3)^2 - 150*z(3)*z(5) - 3.6398*z(1)*z(2);
z(94) = 61.4046 + 1.25*z(2)^2 + 55.2235*z(1)^2 + 100*z(3)^2 - 3.6398*z(1)*z(2);
z(95) = 2.2249*z(4) + 15*z(2)*z(9) + 1.9528*z(1)*(z(5)-7.681278164686606*z(8) ↙
-27.639031134780 83*z(2)*z(4)-1.863887750921753*z(1)*   ...
    z(4)) - 41.905*z(5) - 415*z(3)*z(4) - 20.75*z(1)*z(23) - 20.75*z(2)*z(24) - 5*z(3) ↙
*z(7) - 0.0658*z(2)*z(5);
z(96) = 5*z(3)*z(11) + 15*z(2)*z(13) + 415*z(3)*z(5) + 1.9528*z(1)*(z(4)+1. ↙
8638877509217 53*z(1)*z(5)+27.639031134780 82*z(2)*z(5))   ...
    - 41.905*z(4) - 2.2249*z(5) - 20.75*z(1)*z(21) - 20.75*z(2)*z(22) - 15*z(1)*z(12) - ↙
0.0658*z(2)*z(4);
z(97) = 1.2028*z(1) - 3.0658*z(2);
z(98) = 0.005*z(5)*(81*wx*wz-z(5)*wy^2-28*wy*(wz+1.071428571428572*wy)) + 0.005*z(4)* ↙
(32*wx^2-81*wx*wy-z(4)*wz^2-2*wz*(16*wy-wz))   ...
    + 0.005*z(5)*(2*wz^2-81*wx*wy-28*wx^2-wz*(4*z(4)*wy-z(5)*wz)) + 0.0658*z(4)*wy* ↙
(887.59726443769*xCDt+29.67781155015198*z(1)*wx+887.59726443769*   ...
    z(4)*wz+887.59726443769*z(5)*wy-z(2)*wx-29.67781155015198*z(2)*z(4)*wy-z(1)*z(4) ↙
*wy) + 1.8199*z(2)*(z(2)*z(4)*wz*xBDt+z(2)*z(5)*wy*   ...
    xBDt-z(2)*xCDt*(wx+xBDt)-2*z(1)*xCDt*(z(4)*wy-z(5)*wz)) + 0.0658*z(5)*wz*(z(2) ↙
*wx+2*z(1)*z(4)*wy+59.35562310030396*z(2)*z(4)*wy-   ...
    887.59726443769*xCDt-887.59726443769*z(4)*wz-887.59726443769*z(5)*wy- ↙
29.67781155015198*z(1)*wx-29.67781155015198*z(2)*z(5)*wz-z(1)*   ...
    z(5)*wz) + 1.8199*z(2)*(xCDt+z(4)*wz+z(5)*wy)*(1.073025990439035*xCDt+1. ↙
073025990439035*z(4)*wz+1.073025990439035*z(5)*wy+61.74410681905599*   ...
    z(2)*z(5)*wz-61.74410681905599*z(2)*z(4)*wy-2*z(1)*z(4)*wy-z(2)*(wx+xBDt)) + 10*z ↙
(5)*z(16) + 15*z(2)*z(20) + 100*z(3)*z(17)   ...
    + 5*z(1)*z(23)*z(16) + 5*z(2)*z(24)*z(16) + 100*z(3)*z(4)*z(16) + 100*z(3)*z(5)*z ↙
(15) - 0.005*z(4)*(81*wx*wz-30*wy^2-z(4)*wy^2)   ...
    - 1.8199*z(1)^2*(z(4)*wz*xBDt+z(5)*wy*xBDt-xCDt*(wx+xBDt)) - 53.9735*z(1)*(z(2)*z ↙
(4)*wz*xBDt-2.081912419983881*z(1)*xCDt*(z(4)*wy-   ...
    z(5)*wz)) - 53.9735*z(2)*(z(1)*z(5)*wy*xBDt-z(1)*xCDt*(wx+xBDt)-1.081912419983881*z ↙
(2)*xCDt*(z(4)*wy-z(5)*wz)) - 0.0658*z(1)*(xCDt+   ...
    z(4)*wz+z(5)*wy)*(887.4559270516717*z(1)*z(4)*wy-xCDt-z(4)*wz-z(5)*wy- ↙
887.4559270516717*z(1)*z(5)*wz-55.3161094224924*z(2)*z(5)*wz-   ...
    820.2659574468087*z(2)*(wx+xBDt)-27.6580547112462*z(1)*(wx+xBDt)) - z(18) - 15*z(1) ↙
*z(19) - 10*z(4)*z(15) - 5*z(1)*z(21)*z(15)   ...
    - 5*z(2)*z(22)*z(15) - 0.5*z(1)^2*z(18) - 0.5*z(2)^2*z(18);
z(99) = 5*z(8) + 20.75*z(23) + 58.4039*z(5) + 83*z(24) + 5*z(2)*z(6) - 20*z(9) - 20*z ↙
(1)*z(6) - 1.9528*z(2)*z(4) - 0.0658*z(1)*z(4);
z(100) = 1.2028*z(1) - 30*z(22) - 7.5*z(21) - 3.0658*z(2) - 2*z(24) - 0.5*z(23);
z(101) = 5*z(12) + 20.75*z(21) + 58.4039*z(4) + 83*z(22) + 0.0658*z(1)*z(5) + 1.9528*z ↙
(2)*z(5) + 5*z(2)*z(10) - 20*z(13) - 20*z(1)*z(10);
z(102) = 58.4039*z(5)*wz*xBDt + 0.0658*z(1)*xCDt*(wx+xBDt) + 1.9528*z(2)*xCDt*(wx+xBDt) ↙
+ 1.9528*z(1)*xCDt*(z(4)*wy-z(5)*wz)   ...
```

```
    + 0.0658*(z(2)*z(4)*wy-z(2)*z(5)*wz-z(1)*(wx+xBDt))*(xCDt+z(4)*wz+z(5)*wy+27. ↙
6580547112462*z(2)*z(5)*wz+887.4559270516717*z(1)*z(   ...
    5)*wz+27.6580547112462*z(1)*(wx+xBDt)-887.4559270516717*z(1)*z(4)*wy- ↙
27.6580547112462*z(2)*z(4)*wy-887.4559270516717*z(2)*(wx+xBDt))   ...
    + 1.8199*(z(1)*z(5)*wz-z(1)*z(4)*wy-z(2)*(wx+xBDt))*(1.073025990439035*xCDt+1. ↙
073025990439035*z(4)*wz+1.073025990439035*z(5)*wy+z(   ...
    1)*z(5)*wz+61.74410681905599*z(2)*z(5)*wz+61.74410681905599*z(1)*(wx+xBDt) ↙
-61.74410681905599*z(2)*z(4)*wy-z(1)*z(4)*wy-z(2)*(wx+xBDt))   ...
    + 5*z(19) + 0.5*z(1)*z(18) + 2*z(2)*z(18) + 5*z(2)*z(14) + 5*z(21)*z(15) + 20*z(22) ↙
*z(15) - 58.4039*z(4)*wy*xBDt - 1.9528*z(2)*z(   ...
    4)*wz*xBDt - 1.9528*z(2)*z(5)*wy*xBDt - 0.0658*z(1)*z(4)*wz*xBDt - 0.0658*z(1)*z(5) ↙
*wy*xBDt - 0.0658*z(2)*xCDt*(z(4)*wy-z(5)*wz)   ...
    - 20*z(20) - 20*z(24)*z(16) - 20*z(1)*z(14) - 5*z(23)*z(16);
z(103) = 3.01 + 1.16*z(29) + 15.14*z(28) + 0.5*z(36)*z(40) + 0.5*z(37)*z(39) + 7.5*z ↙
(36)*z(41) + 7.5*z(37)*z(38) + 10*z(28)*z(54)   ...
    + 59.6538*z(36)^2 + 100*z(54)^2 + 113.6181*z(37)^2 - 150*z(29)*z(54) - 3.9034*z(36) ↙
*z(37);
z(104) = 3.01 + 59.6538*z(36)^2 + 100*z(54)^2 + 113.6181*z(37)^2 - 3.9034*z(36)*z(37);
z(105) = 41.905*z(29) + 0.0658*z(29)*z(36) + 1.9517*z(36)*z(41) + 5*z(54)*z(56) + 15*z ↙
(36)*z(58) + 20.75*z(36)*z(40) + 20.75*   ...
    z(37)*z(39) + 58.4038*z(36)*z(38) + 415*z(28)*z(54) - 0.405*z(28) - 112.3681*z(37) ↙
*z(41) - 15*z(37)*z(57) - 1.9517*z(37)*z(38) -    ...
    1.8211*z(29)*z(37);
z(106) = 0.405*z(29) + 41.905*z(28) + 0.0658*z(28)*z(36) + 1.9517*z(37)*z(39) + 15*z ↙
(36)*z(62) + 20.75*z(36)*z(41) + 20.75*z(37)*z(38)   ...
    + 112.3681*z(37)*z(40) - 415*z(29)*z(54) - 58.4038*z(36)*z(39) - 15*z(37)*z(61) - ↙
5*z(54)*z(60) - 1.9517*z(36)*z(40) - 1.8211*   ...
    z(28)*z(37);
z(107) = 3.0658*z(36) - 2.5711*z(37);
z(108) = z(36)*z(53) + z(37)*z(51) + 0.1*z(29)*z(34) + 1.8211*z(37)*z(43) + 10*z(29)*z ↙
(65) + 15*z(36)*z(68) + 58.4038*z(36)*z(42)   ...
    + 100*z(54)*z(66) + 112.3681*z(37)*z(44) + 5*z(36)*z(40)*z(65) + 5*z(37)*z(39)*z ↙
(65) + 100*z(28)*z(54)*z(65) + 100*z(29)*z(54)*z(64)   ...
    - z(35) - 15*z(37)*z(67) - 10*z(28)*z(64) - 1.9517*z(36)*z(44) - 1.9517*z(37)*z(42) ↙
- 0.1*z(28)*z(34) - 0.1*z(28)*z(33)   ...
    - 0.1*z(29)*z(33) - 0.0658*z(36)*z(43) - 5*z(36)*z(41)*z(64) - 5*z(37)*z(38)*z(64) ↙
- 0.5*z(36)^2*z(35) - 0.5*z(37)^2*z(35);
z(109) = 2*z(40) + 3.0658*z(36) + 30*z(41) - 7.5*z(38) - 2.5711*z(37) - 0.5*z(39);
z(110) = 0.0658*z(38) + 1.8211*z(41) + 5*z(57) + 20*z(58) + 58.3947*z(29) + 83*z(40) + ↙
5*z(36)*z(55) + 20*z(37)*z(55) - 20.75*z(39);
z(111) = 5*z(61) + 20*z(62) + 58.3947*z(28) + 83*z(41) + 5*z(36)*z(59) + 20*z(37)*z(59) ↙
- 20.75*z(38) - 1.8211*z(40) - 0.0658*z(39);
z(112) = z(52) + 0.0658*z(42) + 5*z(67) + 20*z(68) + 0.5*z(37)*z(35) + 5*z(36)*z(63) + ↙
5*z(38)*z(64) + 20*z(37)*z(63) + 20*z(40)*z(65)   ...
    - 58.3947*z(43) - 1.8211*z(44) - 20*z(41)*z(64) - 5*z(39)*z(65) - 2*z(36)*z(35);
z(113) = 117*xGBDt - kB*(xB-xGB) - 117*xBDt;
z(114) = 117*xGCDt - kC*(xC-xGC) - 117*xCDt;
z(115) = 117*xGDDt - kD*(xD-xGD) - 117*xDDt;
z(116) = 117*xGEDt - kE*(xE-xGE) - 117*xEDt;
z(117) = TB + kB*(xB-xGB) + 117*xBDt - 117*xGBDt;
```



```
z(118) = TC + kC*(xC-xGC) + 117*xCDt - 117*xGCDt;
z(119) = TD + kD*(xD-xGD) + 117*xDDt - 117*xGDDt;
z(120) = TE + kE*(xE-xGE) + 117*xEDt - 117*xGEDt;
z(121) = wx1*(200*wx1*qx1+qx1Dt);
z(122) = wx2*(200*wx2*qx2+qx2Dt);
z(123) = wx3*(200*wx3*qx3+qx3Dt);
z(124) = wy1*(200*wy1*qy1+qy1Dt);
z(125) = wy2*(200*wy2*qy2+qy2Dt);
z(126) = wy3*(200*wy3*qy3+qy3Dt);
z(127) = wz1*(200*wz1*qz1+qz1Dt);
z(128) = wz2*(200*wz2*qz2+qz2Dt);
z(129) = wz3*(200*wz3*qz3+qz3Dt);
z(130) = z(76) - TAx;
z(131) = z(84) - TAy;
z(132) = z(92) - TAz;
z(133) = z(98) - z(113);
z(134) = z(102) - z(114);
z(135) = z(108) - z(115);
z(136) = z(112) - z(116);

%% Define COEF and RHS
COEF = zeros( 20, 20 );
COEF(1,1) = z(70);
COEF(1,2) = z(69);
COEF(1,3) = z(71);
COEF(1,4) = z(72);
COEF(1,5) = z(73);
COEF(1,6) = z(74);
COEF(1,7) = z(75);
COEF(1,12) = 35;
COEF(1,13) = 5;
COEF(1,14) = 2.75;
COEF(2,1) = z(77);
COEF(2,2) = z(79);
COEF(2,3) = z(78);
COEF(2,4) = z(80);
COEF(2,5) = z(81);
COEF(2,6) = z(82);
COEF(2,7) = z(83);
COEF(2,15) = 8.5;
COEF(2,16) = 1.75;
COEF(2,17) = 0.7;
COEF(3,1) = z(87);
COEF(3,2) = z(85);
COEF(3,3) = z(86);
COEF(3,4) = z(88);
COEF(3,5) = z(89);
COEF(3,6) = z(90);
COEF(3,7) = z(91);
COEF(3,18) = 22.45;
```



```
COEF(3,19) = 6.9;
COEF(3,20) = 3.5;
COEF(4,1) = z(93);
COEF(4,2) = z(95);
COEF(4,3) = z(96);
COEF(4,4) = z(94);
COEF(4,5) = z(97);
COEF(5,1) = z(100);
COEF(5,2) = z(99);
COEF(5,3) = z(101);
COEF(5,4) = z(97);
COEF(5,5) = 62.6539;
COEF(6,1) = z(103);
COEF(6,2) = z(105);
COEF(6,3) = z(106);
COEF(6,6) = z(104);
COEF(6,7) = z(107);
COEF(7,1) = z(109);
COEF(7,2) = z(110);
COEF(7,3) = z(111);
COEF(7,6) = z(107);
COEF(7,7) = 62.6447;
COEF(8,8) = 200;
COEF(9,9) = 200;
COEF(10,10) = 200;
COEF(11,11) = 200;
COEF(12,1) = 35;
COEF(12,12) = 1;
COEF(13,1) = 5;
COEF(13,13) = 1;
COEF(14,1) = 2.75;
COEF(14,14) = 1;
COEF(15,2) = 8.5;
COEF(15,15) = 1;
COEF(16,2) = 1.75;
COEF(16,16) = 1;
COEF(17,2) = 0.7;
COEF(17,17) = 1;
COEF(18,3) = 22.45;
COEF(18,18) = 1;
COEF(19,3) = 6.9;
COEF(19,19) = 1;
COEF(20,3) = 3.5;
COEF(20,20) = 1;

RHS = zeros( 1, 20 )';
RHS(1) = -z(130);
RHS(2) = -z(131);
RHS(3) = -z(132);
RHS(4) = -z(133);
```



```
RHS(5) = -z(134);
RHS(6) = -z(135);
RHS(7) = -z(136);
RHS(8) = z(117);
RHS(9) = z(118);
RHS(10) = z(119);
RHS(11) = z(120);
RHS(12) = -0.005*z(121);
RHS(13) = -0.005*z(122);
RHS(14) = -0.005*z(123);
RHS(15) = -0.005*z(124);
RHS(16) = -0.005*z(125);
RHS(17) = -0.005*z(126);
RHS(18) = -0.005*z(127);
RHS(19) = -0.005*z(128);
RHS(20) = -0.005*z(129);
%=========================================================================
% Add Reaction Wheel Dynamics
%=========================================================================
RHS(1:3,1) = RHS(1:3,1) - skew([wx;wy;wz])*(Z*h);
%=========================================================================
% Lock degreese of freedom based on AT settings
%=========================================================================
COEF_lock = COEF(ind,ind);
RHS = RHS(ind);

%% Create dxdt
dxdt = zeros(20,1);
dxdt(ind) = COEF_lock\RHS;

COEF = zeros(20);
COEF(ind,ind) = COEF_lock;

%% Sensitivity Calculations
if SENSI == 1
    %% Autozee for Sensitivity

    z(137) = wy*(z(4)*wy-z(4)*wz-z(5)*wy-z(5)*wz);
    z(138) = 0.05*z(1)*z(4)*wy*xBDt + 0.2*z(1)*z(4)*wz*xCDt + 0.2*z(1)*z(5)*wy*xCDt + ↙
0.2*z(2)*z(4)*wy*xBDt + 0.05*(z(2)*z(4)*wy-z(2)*   ...
        z(5)*wz-z(1)*(wx+xBDt))*(z(4)*wy-z(5)*wz-z(2)*z(4)*wz-z(2)*z(5)*wy) - 0.2*z(2) ↙
*z(5)*wz*xBDt - 0.05*z(1)*z(5)*wz*xBDt - 0.05*z(2)*   ...
        z(4)*wz*xCDt - 0.05*z(2)*z(5)*wy*xCDt - 0.05*z(2)*(z(4)*wz+z(5)*wy)*(xCDt+z(4) ↙
*wz+z(5)*wy+z(2)*z(4)*wy-z(2)*z(5)*wz) - 0.05*z(1)*(   ...
        z(4)*wz+z(5)*wy)*(z(1)*z(4)*wy-4*xCDt-4*z(4)*wz-4*z(5)*wy-z(1)*z(5)*wz) - 0.05* ↙
(z(1)*z(5)*wz-z(1)*z(4)*wy-z(2)*(wx+xBDt))*(4*z(5)*   ...
        wz-4*z(4)*wy-z(1)*z(4)*wz-z(1)*z(5)*wy);
    z(139) = 0.2*z(4)*wz*xBDt + 0.2*z(5)*wy*xBDt + 0.05*z(1)*z(5)*wz*xBDt + 0.05*z(2)*z ↙
(4)*wz*xCDt + 0.05*z(2)*z(5)*wy*xCDt   ...
        + 0.05*(xCDt+z(4)*wz+z(5)*wy)*(z(4)*wy-z(5)*wz-z(2)*z(4)*wz-z(2)*z(5)*wy) + ↙
```

REPORT DOCUMENTATION PAGE

Form Approved
OMB No. 0704–0188

1. REPORT DATE *(DD–MM–YYYY)*	2. REPORT TYPE	3. DATES COVERED *(From — To)*
12–09–2021	Doctoral Dissertation	Sep 2018–Sep 2021

4. TITLE AND SUBTITLE

Robust optimal motion planning for multi-aperture space systems via Pseudospectral Methods

5a. CONTRACT NUMBER

5b. GRANT NUMBER

5c. PROGRAM ELEMENT NUMBER

6. AUTHOR(S)

Bishop, Brian W., Lieutenant Colonel, USSF

5d. PROJECT NUMBER

5e. TASK NUMBER

5f. WORK UNIT NUMBER

7. PERFORMING ORGANIZATION NAME(S) AND ADDRESS(ES)

Air Force Institute of Technology
Graduate School of Engineering and Management (AFIT/EN)
2950 Hobson Way
WPAFB, OH 45433-7765

8. PERFORMING ORGANIZATION REPORT NUMBER

AFIT-ENY-21-DS-090

9. SPONSORING / MONITORING AGENCY NAME(S) AND ADDRESS(ES)

Intentionally Left Blank

10. SPONSOR/MONITOR'S ACRONYM(S)

11. SPONSOR/MONITOR'S REPORT NUMBER(S)

12. DISTRIBUTION / AVAILABILITY STATEMENT

DISTRIBUTION STATEMENT A:
APPROVED FOR PUBLIC RELEASE; DISTRIBUTION UNLIMITED.

13. SUPPLEMENTARY NOTES

14. ABSTRACT

For multi-body, flexible systems, the ability to achieve rapid reorientation maneuvers can be impacted by nonlinear dynamics and uncertainty in the model parameters. Trajectory sensitivity to parameter variations increases final pointing error and residual vibrational energy in the system. This dissertation explores using desensitized optimal control and unscented optimal control methods to generate trajectories robust against parameter variations while decreasing total maneuver time, pointing error, and system excitation. A five-body, flexible model representing a communications satellite is developed, and utilizing robust problem formulations solved via pseudospectral techniques, maneuvers are generated decreasing maneuver time by 62% and terminal system energy by up to 60%. Lastly, reduced fidelity, three-body and two-body models are developed achieving similar robust performance to the five-body model but with an up to 99% reduction in computation time.

15. SUBJECT TERMS

pseudospectral optimal control, trajectory planning, spacecraft

16. SECURITY CLASSIFICATION OF:			17. LIMITATION OF ABSTRACT	18. NUMBER OF PAGES	19a. NAME OF RESPONSIBLE PERSON
a. REPORT	b. ABSTRACT	c. THIS PAGE			Dr. Richard Cobb (ENY)
U	U	U	U	208	19b. TELEPHONE NUMBER *(include area code)* (937) 255-3636 x4559